**Author**: Schakenraad, K.K.
**Title**: Anisotropy in cell mechanics
**Issue Date**: 2020-05-13

# Anisotropy in cell mechanics

Proefschrift

ter verkrijging van
de graad van Doctor aan de Universiteit Leiden,
op gezag van Rector Magnificus prof. mr. C.J.J.M. Stolker,
volgens besluit van het College voor Promoties
te verdedigen op woensdag 13 mei 2020
klokke 16:15 uur

door

**Koenraad Keith Schakenraad**

geboren te Venray
in 1990

Promotor: Prof. dr. R.M.H. Merks
Co-promotor: Dr. L. Giomi

Promotiecommissie: Prof. dr. M. Alber (UCR, Riverside, VS)
Dr. L.M.C. Janssen (TU Eindhoven)
Prof. dr. A. Doelman
Prof. dr. T. Schmidt
Prof. dr. P. Stevenhagen

Casimir PhD series, Delft-Leiden, 2020-07
ISBN 978-90-8593-434-9
An electronic version of this thesis can be found at openaccess.leidenuniv.nl.

The work described in this thesis was carried out at Leiden University within the Leiden Institute of Physics (LION) and the Mathematical Institute (MI). It was funded by a Leiden/Huygens PhD fellowship.

The cover shows an artist's impression of a cell with an anisotropic internal structure, inspired by the visualization of stress fiber orientations in Chapters 3 and 4. Drawing by Dorien de Wit, design by Marijn de Wit.

# Contents

## CHAPTER 1

# INTRODUCTION

Physics and biology have traditionally been completely separated fields within the natural sciences. This started to change in the twentieth century, when state-of-the-art optical and electronic imaging technologies were first used to obtain a better understanding of biology at the scale of single molecules. The most well-known example is probably the discovery of the double-helix structure of DNA, using X-ray radiation, by Watson and Crick in 1953 [1] (see Figure 1.1a). Other examples include fluorescence microscopy [2], optical tweezers [3], magnetic tweezers [4], atomic force microscopy [5], and combinations of these methods [6]. Around the same time, physics and biology also started to get entangled at a theoretical level due to the introduction of mathematics in biology. Whereas the language of mathematics has always played a crucial role in physics since Sir Isaac Newton published his *Principia* in the seventeenth century, biology has traditionally been a purely experimental science. In the twentieth century this changed with the emergence of *mathematical biology*, a field that theoretically studies biological systems using mathematical tools. Applications of mathematical biology include pattern formation [7], population dynamics [8], and physical models of cells and tissues [9, 10].

More recently, physics and (mathematical) biology got further entangled when people started to realize that both fields could profit from closer collaborations. On the one hand, the enormous complexity of biological systems serves as an inspiration for both engineering and fundamental physics. From an engineering perspective, the ingenuity of biological materials serves as an inspiration for designing new man-made materials, with applications in robotics [11] and tissue engineering [12]. In fundamental physics, new theories are required to describe biological systems. Living entities, such as cells or entire organisms, actively consume energy to move, exert forces on their environment, and perform various other tasks. The challenge of understanding the physics of these living systems inspired the emergence of new areas of physics and mathematics, such as non-equilibrium statistical mechanics [13], pattern formation [7], and active matter [14].

On the other hand, insights from physics have greatly helped in getting a better understanding of experimental and mathematical biology at various scales. On the smallest length scales, the mechanical properties of DNA molecules have been elucidated both

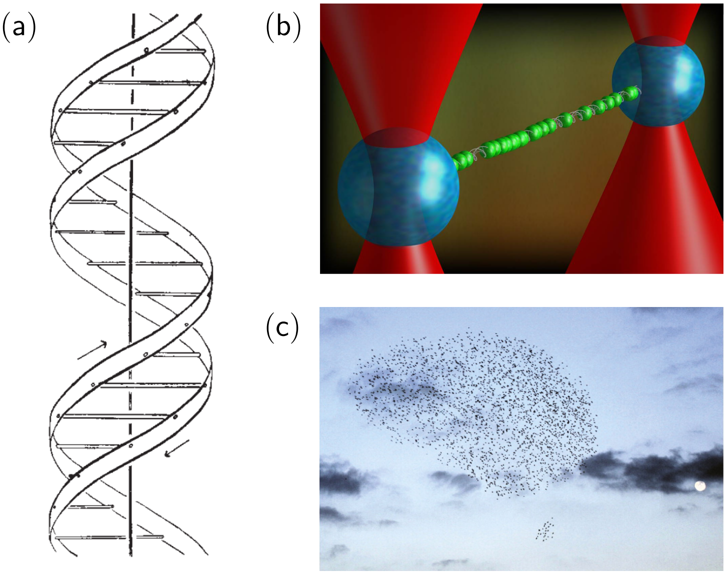

**Figure 1.1.** Examples of the interplay between physics and biology. (a) The double-helix structure of DNA was discovered by Watson and Crick using X-ray radiation. (b) Physical techniques and theories have helped to eludicate the mechanical propertiees of DNA. In this illustration, a DNA molecule is attached to two beads (blue) and stretched by moving two optical tweezers (red) apart. (c) Groups of living entities, such as a flock of birds, have inspired the field of active matter, a field in physics that studies matter that can actively consume energy to move and exert forces. Figure (a) was reprinted from Ref. [1] with permission from Springer Nature, copyright 1953. Figure (b) was printed with permission from Iddo Heller. Figure (c) was adapted from Ref. [15] with permission from Annual Reviews, copyright 2014.

experimentally, using stretching and twisting experiments [16–18] (see Figure 1.1b), and theoretically, using statistical mechanics [19]. On much larger length scales, mathematical models have shown that mechanical interactions are crucial in, for instance, the formation of new blood vessels [20, 21] and embryonic development [22–24]. On even larger length scales, insights from active matter have helped to understand the collective behaviour of animal groups, such as schools of fish or flocks of birds [25–27] (Figure 1.1c).

At intermediate biological scales, between those of single molecules and those of entire organisms, we find cells, the basic biological units that make up all life. It is at this intermediate length scale of a single cell that the importance of physics in biology has become most apparent in the past decades. A good example is given by the seminal experiment by Engler *et al.* [28]. In this experiment the authors studied differentiation of stem cells, a process in which stem cells specialize by becoming, for instance, nerve cells, muscle cells, or bone cells. Although stem cell differentiation is traditionally believed to be triggered chemically by the detection of signaling molecules [29], Engler *et al.* showed that this process is also affected by the mechanical properties of the cell's environment. In particular, they showed that cells lying on a soft surface (mimicking the brain) have a large probability of differentiating into nerve cells, whereas those on top of surfaces of intermediate stiffness (mimicking muscles) differentiate most likely into muscle cells and those on stiff surfaces (mimicking bone) differentiate into bone cells. Other research has shown that the influence of physics on stem cell differentiation is not limited to the rigidity of the underlying surface, as stem cell differentiation is also affected by, for instance, the internal structure of the underlying surface [30], the spreading area [31] and the shape [32, 33] of the cell itself, and the geometry of and the mechanical tension in the cell's internal cytoskeleton [32, 33]. These results by no means disprove the importance of biochemistry in cell biology, but they clearly demonstrate the need to understand cell biology from the perspective of physics as well.

The interplay between physics, mathematics, and biology in the emerging field of *cell mechanics* ranges much further than stem cell differentiation alone. For instance, the shape of cells plays a role in cell division, growth, death, nuclear deformation, and gene expression [34–37], and the migration of cells strongly depends on the mechanical properties of their environment [38]. From a biomedical perspective, mechanical interactions between cells and their environment play an important role in processes such as wound healing [39] and in diseases such as asthma [40] and cancer [41, 42]. In particular, several studies have shown that the mechanical properties of cancer cells change when they become metastatic [43–45], demonstrating that a fundamental understanding of cell mechanics is required for successful future cancer treatments and other biomedical applications. In this thesis we take a step back from these biological and biomedical applications, and focus on expanding the fundamental understanding of cell mechanics.

## 1.1 The cytoskeleton

In **Part I** of this thesis we study how the cell's *cytoskeleton* affects, and is affected by, the cell shape and how it influences the forces that cells exert on their surroundings. The cytoskeleton is a complex network of filaments and proteins inside the cell with many different functionalities [29]. It gives the cell structural integrity, determines the positions of organelles inside the cell, directs intracellular transport, splits a dividing cell into two, and allows the cell to regulate its shape and motion. Loosely speaking, the cytoskeleton is for a cell what the combination of muscles and bones is for the human body. The cytoskeleton of most animal cells consists of three different types of filaments. *Microtubules* are hollow cylindrical structures made from the polymer tubulin, making them the most rigid filaments. They are responsible for the internal structure of the cell, determine the positions of several organelles, organize intracellular transport of materials, and form the mitotic spindle that accurately divides the genetic material between two daughter cells during cell division. *Intermediate filaments* are a family of filaments that bend easily, making them much less rigid than microtubules. Networks of cross-linked intermediate filaments provide the cell with mechanical stability [29]. The third type of cytoskeletal filaments are *actin filaments*, also called microfilaments, which play an important role in the generation of cellular forces and in cell migration. In this thesis we focus on the role of actin in cell mechanics.

Actin filaments consist of two strands of polymers of the protein actin which are helically twisted around each other. Actin filaments have a diameter of 5-9 nm, and their bending rigidity is between those of microtubules and intermediate filaments, with a persistence length of about 10 μm. Actin filaments, in collaboration with many cross-linking proteins, self-organize into many different structures inside the cell. In the *cell cortex*, the layer just beneath the cell membrane, they support the membrane and regulate the shape and movement of the cell boundary. In cells under tension, this *cortical actin* can be highly contractile, minimizing the length of the cell boundary. During cell division, cortical actin forms a contractile ring that splits the cell into two. Actin in the cell cortex is also responsible for *filopodia* and *lamellipodia*, thin and wide protrusions of the cell membrane, respectively, that are crucial during cell migration [29]. In the cell interior, away from the edge, actin filaments form gel-like branched networks as well as linear bundles called *stress fibers* [46, 47]. A crucial property of actin filaments is that they are polar, meaning that their head (called *barbed end*) is different from their tail (called *pointed end*). This polarization allows motor proteins called *myosin* to move along actin filaments, always toward the barbed end, by consuming energy using ATP hydrolysis. In bundles of oppositely aligned filaments present in stress fibers and the actin cortex, this property allows myosin motors, that bind simultaneously to two opposite filaments, to exert forces in opposite directions on these filaments, thereby contracting the actin bundle.

### 1.1.1 Adherent cells

In **Part I** of this thesis we investigate individual cells that adhere to an adhesive surface, which we refer to as the substrate. These adhesive surfaces lack the realism of the complex three-dimensional environment of cells *in vivo*, but they are an excellent platform for exploring the key mechanisms in cell mechanics in a controlled and reproducible setting [48]. For instance, the response of cells to the mechanical properties of their environment can be studied by varying the substrate stiffness. This stiffness does not only affect stem cell differentiation, as we discussed above, but it also has prominent consequences for the shape and actin cytoskeleton of the cell. On soft substrates, cells have a round shape, a small spreading area, and an isotropic actin cytoskeleton. On stiffer substrates, the cell's aspect ratio [49] and spreading area [49–52] increase, and stress fibers are formed [51, 53]. Consequently, cells adhering to stiff surfaces obtain an essentially flat, two-dimensional shape. They adhere to the substrate using adhesion receptors called *focal adhesions* [54], large protein complexes in the cell membrane that mechanically connect intracellular actin bundles with the outside world, in this case the

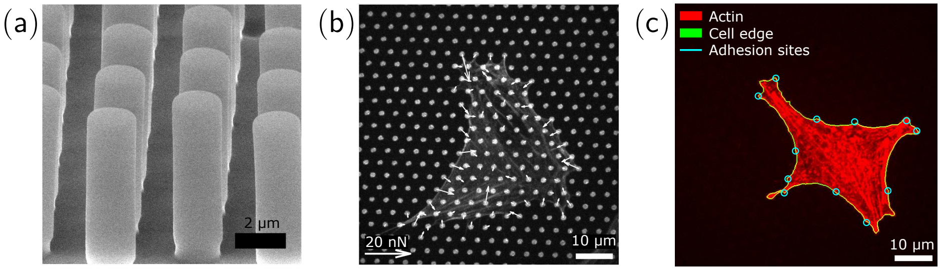

**Figure 1.2.** Cells on top of an array of stiff microfabricated pillars. (a) Scanning electron microscopy image of micropillars. The micropillars have a 2 µm diameter and a height of 6.9 µm. Scalebar corresponds to 2 µm. (b) A cell (3T3 fibroblast) on top of a two-dimensional array of micropillars. The arrows indicate the orientations and magnitudes of the forces that the cell exerts on the micropillars. Scalebar is 10 µm and the arrow in the bottom left corresponds to a force of 20 nN. (c) A cell (epithelioid GE$\beta$3) adhering to a micropillar array assumes a concave (i.e., curved inwards) shape. The cell boundary (green) consists of cellular arcs that connect two sites of strong adhesion to the substrate (cyan circles). The actin in the cell is visualized in red using tetramethyl isothiocyanate rhodamine phalloidin. Scalebar is 10 µm. Figures (a) and (b) were adapted from Ref. [55]. Copyright (2014) American Chemical Society.

substrate. Because these focal adhesions keep them in place, cells on stiff substrates are under considerable mechanical tension and the cytoskeleton generates mainly contractile forces due to contraction of actin bundles [48].

The adhesive surfaces that are used in experimental studies on adherent cells can be divided into two main types. One of these types is a *microfabricated elastomeric pillar array* [55–57], shown in Figure 1.2a. This substrate consists of a lattice of pillars with a diameter in the µm range, whose tops are coated with fibronectin, a protein which is also present in the natural environment of cells and to which focal adhesions can bind. Cells deposited on a stiff micropillar array lie on top of a bed of micropillars and adhere to a limited number of them, mainly distributed along the cell boundary. At these *adhesion sites*, the cell exerts forces on the substrate, often referred to as *traction forces*, which can be measured by observing the deflections of the micropillars [55–57] (see Figure 1.2b). Due to the contractility of the actin cytoskeleton, adherent cells on stiff micropillar arrays assume a typical concave (i.e., curved inwards) shape, with the cell boundary consisting of *cellular arcs* connecting two consecutive adhesion sites (see, for example, the cell in Figure 1.2c). *Micropatterned substrates* are an often used alternative to micropillar arrays. These are flat surfaces coated with a specific pattern of fibronectin [58]. Although less straightforward than on micropillar arrays, traction forces can be measured on micropatterned substrates using a technique called traction force microscopy [59–61]. The big advantage of micropatterned substrates, with respect to micropillar arrays, is that the well-defined shape of the adhesive part of the surface ensures predictable and reproducible cell shapes, facilitating an easier comparison between experimental findings and

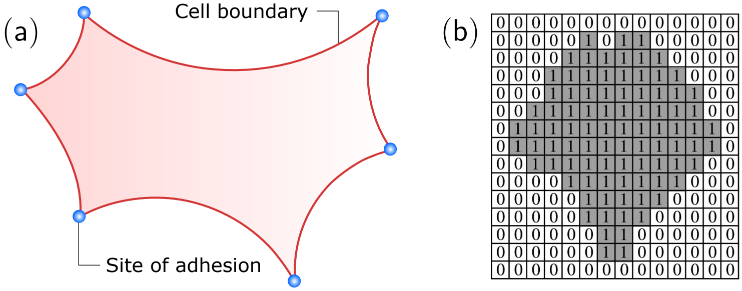

| | | | | | | | | | | | | | |
|---|---|---|---|---|---|---|---|---|---|---|---|---|---|
| 0 | 0 | 0 | 0 | 0 | 0 | 0 | 0 | 0 | 0 | 0 | 0 | 0 | 0 |
| 0 | 0 | 0 | 0 | 0 | 1 | 0 | 1 | 1 | 0 | 0 | 0 | 0 | 0 |
| 0 | 0 | 0 | 0 | 1 | 1 | 1 | 1 | 1 | 1 | 0 | 0 | 0 | 0 |
| 0 | 0 | 0 | 1 | 1 | 1 | 1 | 1 | 1 | 1 | 1 | 0 | 0 | 0 |
| 0 | 0 | 0 | 1 | 1 | 1 | 1 | 1 | 1 | 1 | 1 | 1 | 0 | 0 |
| 0 | 0 | 1 | 1 | 1 | 1 | 1 | 1 | 1 | 1 | 1 | 1 | 0 | 0 |
| 0 | 1 | 1 | 1 | 1 | 1 | 1 | 1 | 1 | 1 | 1 | 1 | 1 | 0 |
| 0 | 1 | 1 | 1 | 1 | 1 | 1 | 1 | 1 | 1 | 1 | 1 | 1 | 0 |
| 0 | 0 | 1 | 1 | 1 | 1 | 1 | 1 | 1 | 1 | 1 | 1 | 0 | 0 |
| 0 | 0 | 0 | 0 | 1 | 1 | 1 | 1 | 1 | 1 | 1 | 0 | 0 | 0 |
| 0 | 0 | 0 | 0 | 0 | 1 | 1 | 1 | 1 | 1 | 0 | 0 | 0 | 0 |
| 0 | 0 | 0 | 0 | 0 | 1 | 1 | 1 | 1 | 0 | 0 | 0 | 0 | 0 |
| 0 | 0 | 0 | 0 | 0 | 0 | 1 | 1 | 0 | 0 | 0 | 0 | 0 | 0 |
| 0 | 0 | 0 | 0 | 0 | 0 | 1 | 1 | 0 | 0 | 0 | 0 | 0 | 0 |
| 0 | 0 | 0 | 0 | 0 | 0 | 0 | 0 | 0 | 0 | 0 | 0 | 0 | 0 |

**Figure 1.3.** Models for cell shape used in this thesis. (a) In a contour model, the shape of a cell is modelled by describing the location of the one-dimensional cell boundary. The cell boundary adheres to the underlying substrate at sites of adhesion, indicated by the blue circles. Contour models are used in Chapters 2 and 3 of this thesis. (b) In the Cellular Potts Model, space is represented by a discrete lattice of pixels and the cell is represented by the collection of pixels that are labelled with the number 1. The Cellular Potts Model is used in Chapter 4 of this thesis. Figure (b) was reprinted from Ref. [69] with permission from Elsevier.

the predictions of mathematical models.

Mathematical models complement experimental approaches because they can help to interpret experimental findings and often raise questions that inspire new experiments. Several types of these mathematical models have been proposed to study the shape of adherent cells and the traction forces they exert on the substrate [48]. The simplest type of model is a two-dimensional *contour model* [62–67], in which the shape of a cell is fully described by the location of the one-dimensional cell boundary (see Figure 1.3a). Each contour model predicts this location based on a particular choice of intracellular forces. For cells adhering to a small number of discrete adhesion sites, such as cells on micropillar arrays, the cell boundary is a collection of cellular arcs that connect two adjacent adhesion sites. The simplest contour model is the Simple Tension Model (STM), first proposed by Bar-Ziv *et al.* [62] and later expanded by Bischofs *et al.* [63, 64]. This model assumes that the locations of the adhesion sites are fixed and known, and calculates the resulting shape of a cellular arc by considering the competition between contractile forces in the cell bulk, which model the contractility of the internal actin cytoskeleton, and contractile forces in the cell contour, which model the contractility of the actin cortex. The STM predicts that cellular arcs are curved inwards and have a circular shape, and succesfully describes cellular shape and traction forces observed in experiments of several cell types on adhesive surfaces [63, 64]. The STM was extended in more advanced contour models by inclusion of other intracellular forces, such as bending elasticity of the cell membrane [65, 68] or an elastic contribution to the contractility of the actin cortex [63, 64].

An alternative to contour models is given by *whole-cell models* [48], which explicitly define the two-dimensional shape of the cell by modeling the cell interior. An example is given by cable network models [70, 71], which describe the actin cytoskeleton as a network of cables that pull on the cell edge. When these cables are contracting due to myosin activity [72], this model reproduces the circular arcs predicted by contour models [62–64]. Many whole-cell models are rooted in *continuum mechanics* and describe the cytoskeleton as a continuous medium rather than by explicitly modeling its discrete constituents. In these models, the cytoskeleton can be represented as an elastic [68, 73] or viscoelastic medium [74], or by more sophisticated models that include several biomechanical and biochemical aspects [75–79]. The *Cellular Potts Model* (CPM), on the other hand, is a computational model that discretizes space and represents a cell as a collection of lattice sites on an often two-dimensional lattice (see Figure 1.3b). During a CPM simulation, lattice sites can be added to or subtracted from the cell, allowing it to grow, shrink, change shape, and move. This dynamics is governed by a *Hamiltonian*, an energy functional which describes the various intracellular and intercellular forces in the model. The Cellular Potts Model was developed in 1992 by Glazier and Graner to describe the demixing of two types of cells [80, 81]. Later, the CPM has been extended with many biomechanical and biochemical aspects to describe a wide range of multicellular processes [9], such as embryonic development [22, 23], tumor growth [82], and blood vessel formation [20, 21]. More recently, the Cellular Potts Model has been employed to model the shape of single cells. For instance, Vianay *et al.* used the CPM to successfully predict a variety of shapes for cells on a dotlike micropattern [83], whereas Albert and Schwarz developed a CPM based on the Simple Tension Model to describe the shape and traction forces of cells adhering to continuous micropatterns of arbitrary shape [69, 84].

### 1.1.2 Liquid crystals

Most mathematical models on shape and traction forces of adherent cells, including many models discussed above, are *isotropic*, meaning that the cytoskeleton in those models contracts in all directions equally. However, many cells on stiff adhesive substrates develop actin stress fibers [51, 53], which are often oriented parallel to other stress fibers in their vicinity (see Figure 1.4a). Therefore, the cytoskeleton of these cells is *anisotropic* and experimental studies have demonstrated that both cell shape [85–88] and traction forces [89, 90] are strongly affected by this cytoskeletal anisotropy. In **Part I** of this thesis, we develop anisotropic models for the actin cytoskeleton employing the theory of *nematic liquid crystals* [91]. Liquid crystals are materials whose smallest constituents are anisotropic particles, giving them mechanical and optical properties intermediate between those of simple liquids and those of solid crystals. Liquid crystals have many applications [92], but are best known for the technological development of the Liquid Crystal Display (LCD) [93]. *Nematic* liquid crystals consist of elongated particles that, like in liquids, have no long-range positional order and can freely flow. However, due to their anisotropy, the particles align with one another, giving them long-range directional order as is the case in solid crystals [94], see Figure 1.4b. An extensive continuum mechanics framework has been developed to describe the physics of nematic liquid crys-

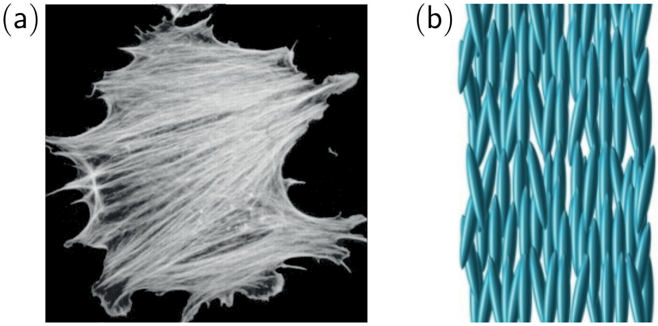

**Figure 1.4.** The anisotropy of the actin cytoskeleton can be modeled by using the theory of nematic liquid crystals. (a) An adherent cell (3T3 fibroblast) with visualized actin stress fibers. The stress fibers are oriented parallel to other stress fibers in their vicinity, making the actin cytoskeleton anisotropic. (b) Nematic liquid crystals consist of elongated particles that have long-range directional order but no long-range positional order. Their anisotropic nature makes them perfectly suitable for modeling the actin cytoskeleton. Figure (a) is reprinted from Ref. [112] with permission from AAAS, and Figure (b) was adapted from Ref. [113].

tals [91], including the interactions with confining boundaries [95] and the emergence of *topological defects* [96], locations where the particle orientation is ill-defined. This theoretical framework has been applied to a variety of systems, ranging from polymer solutions [97] and droplets of elongated colloidal particles [98] to rod-like viruses [99] and the mitotic spindle [100]. More recently, liquid crystal theory has been extended to describe *active* nematic liquid crystals [101], which consist of anisotropic particles that actively exert forces by consuming energy. These active constituents collectively give rise to an active bulk stress [102, 103], and lead to new phenomena such as active turbulence [104, 105] and complex dynamics of topological defects [106]. The active nature of this theory makes it a natural framework to describe various biological systems such as collections of swimming microorganisms [102], mixtures of cytoskeletal filaments and molecular motor proteins [107, 108], growing bacterial colonies [109], and confluent cell layers [110, 111].

## 1.2 Cell migration

In **Part II** of this thesis we shift our focus from the shape of non-motile cells to the process of cell migration, which is essential for many biological processes. For instance, *neutrophils*, a type of white blood cell, move to locations of infections where they attack hostile invaders such as bacteria. *Fibroblasts* migrate toward damaged tissue where they play a crucial role in wound healing. Cell migration also plays a crucial role in cancer metastasis, a process in which cancer cells leave a primary tumor and migrate to a distant organ to form a secondary tumor. Some animal cells, such as sperm cells, achieve migration by swimming through a fluid using a *flagellum*, a tail that is used for propulsion. However, most animal cells migrate by crawling over a surface rather than by swimming. Although the detailed mechanisms of the crawling process are different for each cell type, the general idea behind the mechanism is the same for most of them. First, the leading edge of the cell moves forward because actin polymerization in the cell cortex, in the form of filopodia, lamellipodia, or pseudopodia, pushes the cell membrane forward. Then, the cell forms adhesions to the surface at this leading edge and, finally, contractile forces in the cytoskeleton pull the rest of the cell along [29]. Various mathematical models have been proposed to describe this process [114, 115]. These models vary both in numerical techniques and in the biological phenomena they describe. A relatively simple approach uses Langevin equations to model the stochastic dynamics of the cell position based on experimental data [116, 117]. More complex models explicitly model individual focal adhesions and stress fibers [118, 119], or describe cell shape and the dynamics of the actin cytoskeleton using phase-field models [120, 121], hydrodynamic models [122, 123], or Cellular Potts Models [124, 125].

Both *in vivo* and in experiments on surfaces, the direction of cellular migration can be biased by so-called *directional cues*, asymmetries in the surroundings of the cell that stimulate the cell to move in a specific direction. The most well-known directional cue is *chemotaxis*, the ability of cells to sense and respond to local gradients in the concentration of certain chemicals. Both prokaryotic cells (such as bacteria) [126] and eukaryotic cells (such as animal cells) [127] can perform chemotaxis, which can be positive (i.e., motion toward large concentrations) or negative (i.e., motion toward small concentrations). Chemotaxis has been extensively studied, both experimentally [128] and theoretically [129, 130], and plays a crucial role in many processes in the human body, such as in the above-mentioned migration of neutrophils toward sites of infection [29]. However, similar to what we discussed earlier for stem cell differentiation, it has become increasingly clear in the last decades that cell migration is not solely dictated by biochemistry. Instead, many mechanical cues have been found that play an important role in dictating the direction of cell migration. The most well-known examples of these are *haptotaxis*, the migration of cells from small to large densities of adhesion sites, and *durotaxis*, the migration of cells from soft to rigid mechanical environments [131–136].

In **Chapter 5** we study a recently discovered mechanical cue called *topotaxis*, the directed migration of cells due to asymmetries in the local topographical properties of the environment. Several kinds of topographically anisotropic substrates have been shown to direct cell migration, including surfaces with asymmetric adhesive patterns [137–139], substrates with spatial gradients in the density of micropillars [140, 141], and substrates with tilted micropillars [137, 142]. In all of these examples, cell motion is biased due to topographical cues at sub-cellular length scales. These small-scale directional cues cause an anisotropic response of the cytoskeleton, thereby biasing the direction of migration. Wondergem and coworkers demonstrated, however, that topotaxis can also be achieved by topographical cues at length scales larger than the cell itself [143]. They studied highly motile cells, moving on a substrate that contains cell-sized obstacles that force the cells to move around them, and showed that cells migrate from regions of large obstacle densities to regions of low obstacle densities. In **Chapter 5** we zoom out from the cell's internal structure and cytoskeleton, which we studied in Part I. Inspired by the experiments on cells by Wondergem *et al.* [143], we study topotaxis of active Brownian particles (ABPs), a simple model for structureless self-propelled particles that is extensively studied in the field of active matter [144, 145]. Despite their simplicity, directed motion of ABPs has been demonstrated using asymmetric periodic potentials [146–148], arrays of asymmetric obstacles [149, 150], and asymmetric channels [151–154]. ABPs have even been demonstrated to perform chemotaxis [155, 156], durotaxis [157], and phototaxis [158], making them an excellent model system for identifying the basic physical principles behind directed cell migration.

## 1.3 Outline of the thesis

In this thesis we investigate the role of anisotropy in cell mechanics. The thesis is organized as follows. In **Part I** we combine analytical calculations, computer simulations and *in vitro* experiments to study cells adhering to stiff adhesive substrates. We investigate the mechanical interplay between the shape of these cells, the orientation of their actin stress fibers, and the traction forces that they exert on the underlying substrate. In **Chapter 2** we develop a theory for the shape of cells adhering to adhesive micropillar arrays. We extend previous isotropic contour models of cellular adhesion by explicitly introducing the directed contractile forces generated by actin stress fibers. Given the orientations of stress fibers in adherent cells, we predict cell shape as well as the directions of cellular traction forces, and we compare these predictions to experimental observations on epithelioid and fibroblastoid cells. We demonstrate that the arcs of cells with an anisotropic cytoskeleton are well described by segments of an ellipse. The aspect ratio of this ellipse is dictated by the degree of anisotropy of the internal cell stresses, and the orientation of the ellipse is dictated by the orientations of the stress fibers. Our work shows that cells can control the anisotropy of their shape by regulating the anisotropy of their cytoskeleton.

In **Chapter 3** we reverse this question, and ask how the shape of a cell influences the orientations of its stress fibers. We study the interplay between cell shape and stress fiber orientation by combining the model for cell shape, developed in Chapter 2, with a model for the cytoskeleton based on liquid crystal theory. We perform numerical simulations that predict both cell shape and the orientations of stress fibers, and again compare our results to experimental observations on epithelioid and fibroblastoid cells adhering to a micropillar array. We find that stress fiber orientation is determined by a competition between alignment with the cell edge and alignment with one another in the bulk of the cell. Our work highlights the importance of the boundary conditions, imposed by cell shape, in understanding the internal structure of the actin cytoskeleton.

In **Chapter 4** we study the interplay between cell shape, stress fiber orientation and traction forces on stiff micropatterned surfaces. To be able to model cells with continuous adhesion with the substrate, rather than through a limited number of adhesion sites on top of micropillars, we implement the concepts developed in Chapters 2 and 3 into the Cellular Potts Model (CPM). As was the case for pre-existing contour models, previous CPM implementations model the contractility of the cytoskeleton using isotropic forces. In **Chapter 4**, we introduce the anisotropic contractility of the cytoskeleton in the Cellular Potts Model, and validate our model by comparing our numerical results on stress fiber distributions and traction forces to previously reported experimental data. Our numerical results show that traction forces are strongly biased by the local stress fiber orientation, and reproduce previously reported anisotropic traction force distributions. Our findings demonstrate that an anisotropic model for the actin cytoskeleton is required for accurately predicting cellular traction forces.

In **Part II** of this thesis we study cell migration on a substrate that contains cell-sized obstacles. We zoom out from the internal structure of the cell, which we studied in Part I, and investigate the motion of active Brownian particles (ABPs) in **Chapter 5**. Using a combination of numerical simulations and analytical arguments, we study the motion of ABPs in obstacle lattices of both constant and non-constant densities, and demonstrate the emergence of topotaxis of active Brownian particles. This finding demonstrates that persistent migration of cells is sufficient to obtain topotaxis, even in the absence of any more complex mechanical or biochemical mechanisms.

Finally, in **Chapter 6** we summarize the most important findings of the research presented in this thesis. We discuss the implications of our results on the field of cell mechanics and suggest the most promising directions for future research.

# Part I

# Mechanics of the cytoskeleton

Chapter 2

# CYTOSKELETAL ANISOTROPY CONTROLS GEOMETRY AND FORCES OF ADHERENT CELLS

This chapter is the result of a collaboration with Wim Pomp, Hayri E. Balcıoğlu, Hedde van Hoorn, Erik H.J. Danen, and Thomas Schmidt, who performed the experiments and analyzed the experimental data. The chapter is reprinted with permission, copyright 2018 by the American Physical Society. The chapter is published as:

Wim Pomp*, Koen Schakenraad*, Hayri E. Balcıoğlu, Hedde van Hoorn, Erik H.J. Danen, Roeland M.H. Merks, Thomas Schmidt, and Luca Giomi, 'Cytoskeletal Anisotropy Controls Geometry and Forces of Adherent Cells', Physical Review Letters **121**, 178101 (2018)

## Abstract

We investigate the geometrical and mechanical properties of adherent cells characterized by a highly anisotropic actin cytoskeleton. Using a combination of theoretical work and experiments on micropillar arrays, we demonstrate that the shape of the cell edge is accurately described by elliptical arcs, whose eccentricity expresses the degree of anisotropy of the internal cell stresses. This results in a spatially varying tension along the cell edge, that significantly affects the traction forces exerted by the cell on the substrate. Our work highlights the strong interplay between cell mechanics and geometry and paves the way toward the reconstruction of cellular forces from geometrical data.

---

*These authors contributed equally to this work

## 2.1 Introduction

Cells, from simple prokaryotes to the more complex eukaryotes, are capable of astonishing mechanical functionalities. They can repair wounded tissues by locally contracting the extracellular matrix [159], move in a fluid or on a substrate [160], and generate enough force to split themselves in two while remaining alive [161]. Conversely, cell behavior and fate crucially depend on mechanical cues from outside the cell [162–166]. Examples include rigidity-dependent stem cell differentiation [28, 30], protein expression regulated by internal stresses [167], mechanical cell-cell communication [168] and durotaxis [132, 169]. In all these biomechanical processes, cells rely on their shape [64, 170, 171] to gauge the mechanical properties of their microenvironment [172] and direct the traction forces exerted on their surroundings.

In recent years, experiments on adhesive surfaces have contributed to explore such mechanical complexity in a controlled setting [48]. Immediately after coming into contact with such a surface, many animal cells spread and develop transmembrane adhesion receptors. This induces the actin cytoskeleton to reorganize into cross-linked networks and bundles (i.e., stress fibers [46, 47]), whereas adhesion becomes limited to a number of sites, distributed mainly along the cell contour (i.e., focal adhesions [54]). At this stage, cells are essentially flat and assume a typical shape characterized by arcs which span between the sites of adhesion, while forces are mainly contractile [48]. On timescales much shorter than those required by a cell to change its shape (i.e., minutes), the cell can be considered in mechanical equilibrium at any point of its interface. These observations have opened the way to the use of theoretical concepts inspired by the physics of fluid interfaces [48, 62–64], but limited to the case of cells with an isotropic cytoskeleton.

In this chapter, we overcome this limitation and explore the geometry and the mechanical properties of adherent cells characterized by a highly anisotropic actin cytoskeleton. Using a combination of theoretical modeling, spinning disk confocal microscopy, and traction-force microscopy of living cells cultured on microfabricated elastomeric pillar arrays [55–57], we demonstrate that both the shape of and the traction forces exerted by adherent cells are determined by the anisotropy of their actin cytoskeleton. In particular, by comparing different cell types [173], we demonstrate that the cell contour consists of arcs of a unique ellipse, whose eccentricity expresses the degree of anisotropy of the internal stresses.

## 2.2 The model

We model adherent cells as two-dimensional contractile films [65, 66], and we focus on the shape of the cell edge connecting two consecutive adhesion sites. Mechanical equilibrium requires the difference between the internal and external stresses acting on the cell edge to balance the contractile forces arising in the cortex:

$$\frac{\mathrm{d}\boldsymbol{F}_{\mathrm{cortex}}}{\mathrm{d}s} + (\hat{\boldsymbol{\Sigma}}_{\mathrm{out}} - \hat{\boldsymbol{\Sigma}}_{\mathrm{in}}) \cdot \boldsymbol{N} = \boldsymbol{0} \; . \tag{2.1}$$

Here $\hat{\boldsymbol{\Sigma}}_{\rm out}$ and $\hat{\boldsymbol{\Sigma}}_{\rm in}$ are the stress tensors outside and inside the cell and $\boldsymbol{F}_{\rm cortex}$ is the stress resultant along the cell cortex. The latter is parametrized as a one-dimensional curve spanned by the arc-length $s$ and oriented along the inward pointing normal vector $\boldsymbol{N}$. A successful approach, initially proposed by Bar-Ziv *et al.* in the context of cell pearling [62] and later expanded by Bischofs *et al.* [63, 64], consists of modeling bulk contractility in terms of an isotropic pressure $\hat{\boldsymbol{\Sigma}}_{\rm out} - \hat{\boldsymbol{\Sigma}}_{\rm in} = \sigma \hat{\boldsymbol{I}}$, with $\hat{\boldsymbol{I}}$ the identity matrix, and peripheral contractility as an interfacial tension of the form $\boldsymbol{F}_{\rm cortex} = \lambda \boldsymbol{T}$, with $\boldsymbol{T}$ a unit vector tangent to the cell edge. The quantities $\sigma$ and $\lambda$ are material constants that embody the biomechanical activity of myosin motors in the actin cytoskeleton. This competition between bulk and peripheral contractility along the cell boundary results in the formation of arcs of constant curvature $1/R = \sigma/\lambda$, through a mechanism analogous to the Young-Laplace law for fluid interfaces. The shape of the cell boundary is then approximated by a sequence of circular arcs, whose radius $R$ might or might not be uniform across the cell, depending on how the cortical tension $\lambda$ varies from arc to arc. The possibility of an elastic origin of the cortical tension was also explored in Ref. [63] to account for an apparent correlation between the curvature and length $L$ of the cellular arcs. In this case $\lambda = k(L - L_0)/L_0$, with $k$ an elastic constant and $L_0$ a rest length. Both models successfully describe the geometry of adherent cells in the presence of strictly isotropic forces.

Yet, many cells, including the fibroblastoids (GDβ1, GDβ3) and epithelioids (GEβ1, GEβ3) [173] studied here [Figure 2.1a], develop directed forces by virtue of the strong anisotropic cytoskeleton originating from the actin stress fibers [46, 47]. This scenario is, evidently, beyond the scope of models based on isotropic contractility. Indeed, long cellular arcs appear prominently non-circular, as indicated by the fact that their curvature smoothly varies along the arc up to a factor ten [Figure 2.5a in the Appendix]. Furthermore, whereas the shape of the cell edge in Figure 2.1a can in principle be approximated by circular arcs, a survey of a sample of 285 cells [Figure 2.5b in the Appendix] did not allow conclusive statements about a possible correlation between the arc's length and curvature, required to justify the variance in $\lambda$ [63, 64]. On the other hand, our data show a significant correlation between the radius of curvature of the cellular arcs and their orientation with respect to the stress fibers [Figure 2.1b]. In particular, the radius of curvature decreases as the stress fibers become more perpendicular to the cell cortex [Figure 2.1c]. This correlation is intuitive as the bulk contractile stress focuses in the direction of the stress fibers.

The anisotropy of the actin cytoskeleton can be incorporated into the mechanical framework summarized by Eq. (2.1), by modeling the stress fibers as contractile force dipoles. This collectively gives rise to a directed contractile bulk stress, such that $\hat{\boldsymbol{\Sigma}}_{\rm out} - \hat{\boldsymbol{\Sigma}}_{\rm in} = \sigma \hat{\boldsymbol{I}} + \alpha \boldsymbol{n}\boldsymbol{n}$ [102, 103, 174], with $\boldsymbol{n} = (\cos\theta_{\rm SF}, \sin\theta_{\rm SF})$ the average direction of the stress fibers [Figure 2.1b]. The quantity $\alpha > 0$ represents the magnitude of the directed contractile stresses and is proportional to the local degree of alignment between the fibers. The higher the alignment, the larger $\alpha$, whereas in the case of randomly oriented fibers $\alpha = 0$, thus recovering the isotropic case. The ratio between isotropic contractility

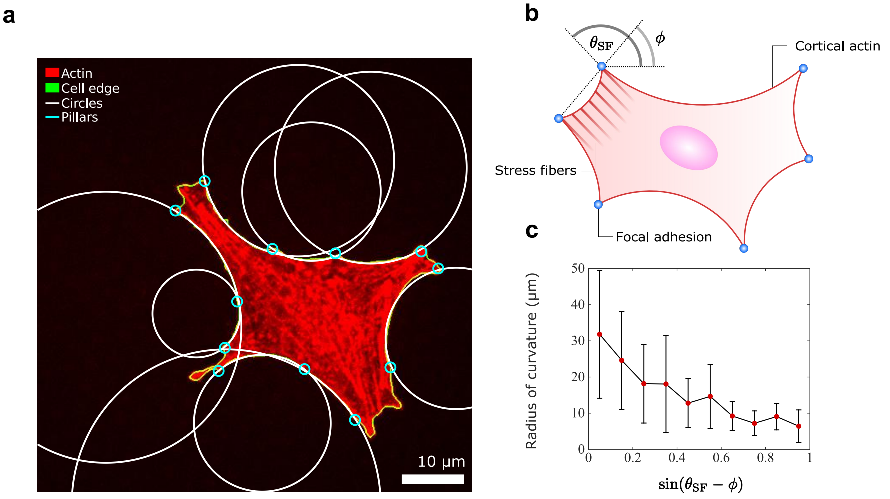

**Figure 2.1.** (a) A cell with an anisotropic actin cytoskeleton (epithelioid GEβ3) with circles (white) fitted to its edges (green). The end points of the arcs (cyan) are identified based on the forces exerted on the pillars, see Materials and Methods in Section 2.5. The actin cytoskeleton is visualized with tetramethyl isothiocyanate rhodamine phalloidin (red). Scale bar is 10 μm. (b) The cell cortex (red line) is spanned in segments between fixed adhesion sites (blue). (c) Arc radius as a function of the sine of the angle $\theta_{\mathrm{SF}} - \phi$, between the local orientation of the stress fibers and that of the distance between the adhesion sites (data correspond to a sample of 285 cells and show the mean $\pm$ standard deviation).

$\sigma$ and directed contractility $\alpha$ measures the degree of anisotropy of the bulk stress. With this stress tensor the force balance [Eq. (2.1)] becomes

$$\frac{\mathrm{d}\lambda}{\mathrm{d}s}\boldsymbol{T} + (\lambda\kappa + \sigma)\boldsymbol{N} + \alpha(\boldsymbol{n}\cdot\boldsymbol{N})\boldsymbol{n} = \boldsymbol{0}\,, \tag{2.2}$$

where we use $\mathrm{d}\boldsymbol{T}/\mathrm{d}s = \kappa\boldsymbol{N}$, with $\kappa$ the curvature of the cell edge. This implies that, in the presence of an anisotropic cytoskeleton, the cortical tension $\lambda$ is no longer constant along the cell cortex, as long as the directed stress has a non-vanishing tangential component (i.e., $\boldsymbol{n}\cdot\boldsymbol{T} \neq 0$). As shown by Kassianidou *et al.* [175], isolated stress fibers can also exert localized contractile forces on the cell contour, leading to kinks and piecewise constant curvature. Consistent with our experiments, here we consider the case in which the density of the stress fibers is sufficiently high and uniform to approximate their mechanical effect in terms of a continuous anisotropic stress.

## 2.3 Results and discussion

In the following, we introduce a number of simplifications that make the problem analytically tractable. As the orientation of the stress fibers varies only slightly along a single cellular arc [Figure 2.2a, and Figures 2.7 and 2.8 in the Appendix], we assume $\theta_{\rm SF}$ to be constant along each arc, but different, in general, from arc to arc. Furthermore, as all the arcs share the same bulk, we assume the bulk stresses $\sigma$ and $\alpha$ uniform throughout the cell. Under these assumptions a general solution of Eq. (2.2) can be readily obtained. Taking $\boldsymbol{T} = (\cos\varphi, \sin\varphi)$, $\boldsymbol{N} = (-\sin\varphi, \cos\varphi)$, with $\varphi$ the orientation of the tangent vector $\boldsymbol{T}$ with respect to an axis perpendicular to the stress fibers [Figure 2.2a], and $\tan\varphi = {\rm d}y/{\rm d}x$, with $(x, y)$ the position of the cell contour, yields:

$$\begin{aligned}\frac{\sigma^2}{\gamma\lambda_{\rm min}^2}\left[(x-x_c)\sin\theta_{\rm SF} - (y-y_c)\cos\theta_{\rm SF}\right]^2 \\ + \frac{\sigma^2}{\lambda_{\rm min}^2}\left[(x-x_c)\cos\theta_{\rm SF} + (y-y_c)\sin\theta_{\rm SF}\right]^2 = 1 \;, \quad (2.3)\end{aligned}$$

where $\gamma = \sigma/(\sigma+\alpha)$ and $\lambda_{\rm min}$ is an integration constant related with cortical tension and whose physical interpretation will become clear later. Eq. (2.3) describes an ellipse of semiaxes $a = \sqrt{\gamma}\,\lambda_{\rm min}/\sigma$ and $b = \lambda_{\rm min}/\sigma$, centered at the point $(x_c, y_c)$ and whose major axis is parallel to the stress fibers, hence tilted by an angle $\theta_{\rm SF}$ with respect to the $x$ axis (Figure 2.2). The dimensionless quantity $\gamma$ highlights the anisotropy of the forces acting on the cell contour. Thus, $\gamma = 0$ corresponds to the case in which the directed forces outweigh the isotropic ones, whereas $\gamma = 1$ reflects the purely isotropic case. Further details can be found in Section 2.6.1 in the Appendix and in Chapter 3.

The key prediction of our model is illustrated in Figure 2.2b, where we have fitted the contour of the same cell shown in Figure 2.1a with ellipses. More examples are shown in Figures 2.7 and 2.8 in the Appendix. Whereas large variations in the circles' radii were required in Figure 2.1a, a *unique* ellipse ($\gamma = 0.52$, $\lambda_{\rm min}/\sigma = 13.4\,\mu{\rm m}$) faithfully describes all the arcs in the cell. The directions of the major axes were fixed to be parallel to the local orientations of the stress fibers in the fit. To test the accuracy of this latter choice, we fitted unconstrained and independent ellipses to all cellular arcs in our database. The distribution of the difference between the orientation $\theta_{\rm ellipse}$ of the major axis of the fitted ellipse and the measured orientation $\theta_{\rm SF}$ of the stress fibers is shown in Figure 2.2c. The distribution peaks at $0^\circ$ and has a width of $36^\circ$, demonstrating that the orientation of the ellipses is parallel, on average, to the local orientation of the stress fibers as predicted by our model.

Eq. (2.2) further allows to analytically calculate the cortical tension $\lambda$. Namely,

$$\lambda(\varphi) = \lambda_{\rm min}\sqrt{\frac{1+\tan^2\varphi}{1+\gamma\tan^2\varphi}}\;. \qquad (2.4)$$

The function $\lambda$ attains its minimum value at the point along the cellular arc where $\varphi = 0$ and $\lambda(0) = \lambda_{\rm min}$, see also Figure 2.6 in the Appendix. Here, the cortical tension has no

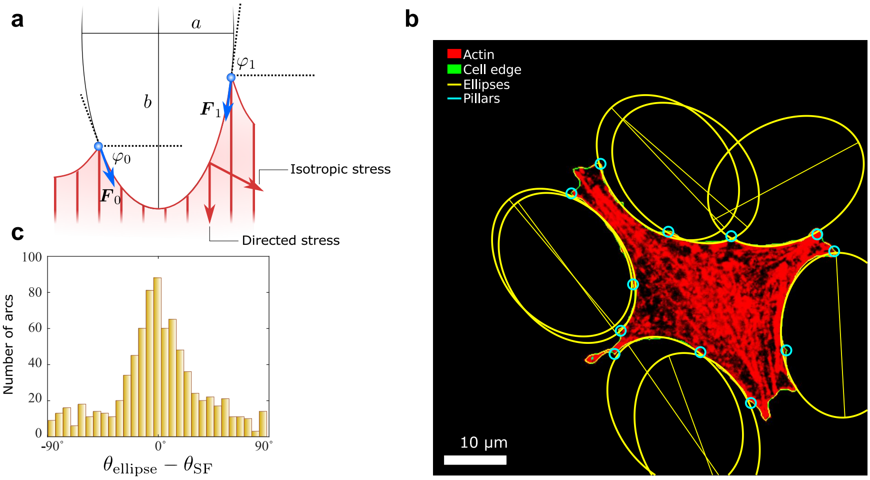

**Figure 2.2.** (a) Schematic representation of our model for $\theta_{\text{SF}} = \pi/2$. All cellular arcs are part of a unique ellipse of aspect ratio $a/b = \sqrt{\gamma}$. The cell exerts forces $\boldsymbol{F}_0$ and $\boldsymbol{F}_1$ on the adhesion sites (blue) with magnitude $\lambda(\varphi_0)$ and $\lambda(\varphi_1)$. (b) An epithelioid cell (GEβ3; same cell as in Figure 2.1a) with a unique ellipse (yellow) fitted to its edges (green). The end points of the arcs (cyan) are identified based on the forces exerted on the pillars, see Materials and Methods in Section 2.5. The fitted values of the ellipses' major and minor axes are, respectively, $13.38 \pm 0.04$ μm and $9.65 \pm 0.02$ μm. The major axes (yellow lines) are parallel to the stress fibers. Their orientations are found to be, in counterclockwise order from the nearly vertical ellipse in the bottom right corner, $\theta_{\text{SF}} = 93 \pm 4^\circ$, $28 \pm 5^\circ$, $110 \pm 2^\circ$, $139 \pm 6^\circ$, $127 \pm 3^\circ$, $125 \pm 2^\circ$, $133 \pm 2^\circ$, $130 \pm 3^\circ$ with respect to the horizontal axis of the image. Scalebar is 10 μm. (c) Histogram of $\theta_{\text{ellipse}} - \theta_{\text{SF}}$, with $\theta_{\text{ellipse}}$ the orientation of the major axis of the fitted ellipse and $\theta_{\text{SF}}$ the measured orientation of the stress fibers. The mean of this distribution is $0^\circ$ and the standard deviation is $36^\circ$.

contribution from the directed stress (i.e., $\boldsymbol{n} \cdot \boldsymbol{T} = 0$), thus $\lambda_{\text{min}}$ represents the minimal tension withstood by the cortical actin. Although the latter could, in principle, be arc-dependent, for instance in the presence of substantial variations in the actin densities [63], here we approximate $\lambda_{\text{min}}$ as a constant. Thus $\sigma$, $\alpha$ and $\lambda_{\text{min}}$ represent the material parameters of our model.

Eqs. (2.3) and (2.4) are combined to predict the traction force exerted by the cell at a specific adhesion site by adding the cortical tension $\lambda \boldsymbol{T}$ along the two cellular arcs joining at the adhesion site. We emphasize that this analysis yields information on cellular forces solely based on the analysis of cell shape. For example, the direction of the traction forces is calculated without additional fitting parameters. We compare the result with the direction of the traction force measured with a micropillar array technology [55–57]. An example is shown in Figure 2.3a for one of the adhesion sites of the cell in Figure 2.2b; more examples are shown in Figures 2.7 and 2.8 in the Appendix. The

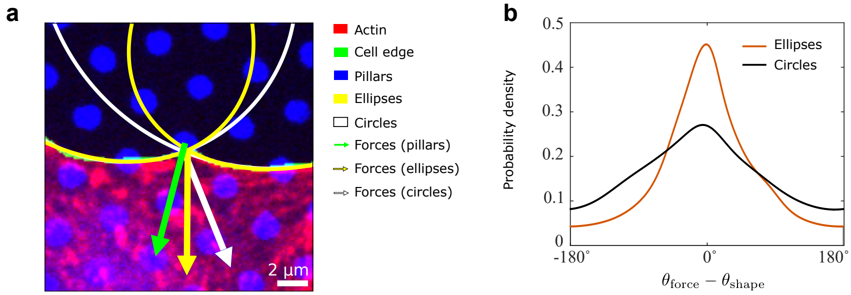

**Figure 2.3.** (a) Enlargement of one adhesion site of the cell in the previous figures. Actin is shown in red, the cell edge in green, and the tops of the micropillars in blue. The lines represent the fitted circle (white) and ellipse (yellow). The arrows correspond to the measured forces (green) and the predicted directions (but not magnitudes) of the forces in the presence of isotropic ($\alpha = 0$, white arrow) and anisotropic ($\alpha \neq 0$, yellow arrow) contractile stresses. Scale bar is 2 µm. (b) Histogram (shown as a probability density) of $\theta_{\mathrm{force}} - \theta_{\mathrm{shape}}$ for isotropic (black) and anisotropic (orange) contractile stresses. Both the distributions are centered around $0^\circ$, the standard deviations are $60^\circ$ and $40^\circ$ for the isotropic and anisotropic models, respectively.

arrows mark the direction of the measured traction force (green) and that calculated by approximating the cell shape with ellipses (yellow). As a comparison, Figure 2.3a also shows a prediction based on circles from the isotropic model (white) [63, 64].

In Figure 2.3b, we show the distribution of the difference $\theta_{\mathrm{force}} - \theta_{\mathrm{shape}}$ between the measured orientation of the traction forces and that calculated from our model, across the entire cell population. The predicted distribution is centered at $0^\circ$ and has a width of $40^\circ$. As a comparison, we also plot the result for the isotropic model, which displays a larger standard deviation of about $60^\circ$. This shows that not only cell shape, but also adhesion forces are profoundly affected by the anisotropy of the cytoskeleton.

Finally, our model allows us to obtain quantitative information on the relative magnitude of isotropic and anisotropic stresses. In Tables 2.1 and 2.2 (Appendix) we report a survey of the material parameters over a sample of 285 cells. Despite the large variability among the cell population, the directed stress $\alpha$ is consistently larger than the isotropic stress $\sigma$, reflecting the high anisotropy of the adherent cell types used here.

**Table 2.1.** Survey of the average material parameters in a sample of 285 fibroblastoid and epithelioid cells.

| $\gamma$ | $\lambda_{\mathrm{min}}$ (nN) | $\sigma$ (nN/µm) | $\alpha$ (nN/µm) |
|---|---|---|---|
| $0.33 \pm 0.20$ | $7.6 \pm 5.6$ | $0.87 \pm 0.70$ | $1.7 \pm 1.7$ |

## 2.4 Conclusion

In conclusion, we have investigated the geometrical and mechanical properties of adherent cells characterized by an anisotropic actin cytoskeleton, by combining experiments on micropillar arrays with simple mechanical modeling. We have predicted and tested that the shape of the cell edge consists of arcs that are described by a unique ellipse, whose major axis is parallel to the orientation of the stress fibers. The model allowed us to obtain quantitative information on the values of the isotropic and anisotropic contractility of cells. In the future, we plan to use our model in combination with experiments on micropatterns (see, e.g., Refs. [58, 176]), where cellular shape can be controlled, thus allowing higher reproducibility of the results and more systematic statistical analysis of the data.

## 2.5 Materials and methods

### 2.5.1 Cell culture and fluorescent labeling

Epithelioid GE11 and fibroblastoid GD25 cells [173] expressing either $\alpha5\beta1$ or $\alpha v\beta3$ (GD$\beta$1, GD$\beta$3, GE$\beta$1 and GE$\beta$3) have been cultured as described before [172]. GD$\beta$1, GD$\beta$3, GE$\beta$1 and GE$\beta$3 are approximately equally represented among the 285 cells in the data presented here. Cells have cultured in medium (DMEM; Dulbecco's Modified Eagle's Medium, Invitrogen/Fisher Scientific) supplemented with 10% fetal bovine serum (HyClone, Etten-Leur, The Netherlands), 25 U/ml penicillin and 25 μg/ml streptomycin (Invitrogen/Fisher Scientific cat. # 15070-063). Cells were fixed in 4% formaldehyde and then permeabilised with 0.1% Triton-X and 0.5% BSA in PBS. Tetramethylrhodamine (TRITC)-Phalloidin (Fisher Emergo B.V. cat. # A12380, Thermo Fisher) was subsequently used to stain F-actin.

### 2.5.2 Micropillar arrays

Micropillar arrays were made out of a soft elastomeric material (PDMS) using a negative silicon wafer as a mask as described before [55, 57]. Briefly, the 2 μm diameter micropillars are arranged in a hexagonal pattern with a 4 μm center-to-center distance. The micropillars have a height of 6.9 μm, resulting in a stiffness of 16.2 nN/μm. The pillar tops were fluorescently labelled using an Alexa 405-fibronectin conjugate (Alexa Fluor®, Invitrogen/Fisher Scientific, Breda, The Netherlands; Fibronectin cat. #1141, Sigma Aldrich, Zwijndrecht, The Netherlands). Pillar deflections were determined with ∼30 nm precision using a specifically designed Matlab script resulting in a ∼0.5 nN precision in force [55].

### 2.5.3 Imaging

High-resolution imaging was performed on an in-house constructed spinning disk confocal microscope based on an Axiovert200 microscope body with a Zeiss Plan-Apochromat 100× 1.4NA objective (Zeiss, Sliedrecht, The Netherlands) and a CSU-X1 spinning disk unit (CSU-X1, Yokogawa, Amersfoort, The Netherlands). Imaging was done using an emCCD camera (iXon 897, Andor, Belfast, UK). Alexa405 and TRITC were exited using 405 nm (Crystalaser, Reno, NV) and 561 nm (Cobolt, Stockholm, Sweden) lasers, respectively. This results in a resolution of approximately 150 nm and 200 nm respectively, enough to distinguish separate stress fibers which are typically separated by about 1.5 µm.

### 2.5.4 Image analysis

All image analysis and ellipse fitting are performed using Matlab®, except the determination of the stress fiber orientation, for which ImageJ with the OrientationJ plugin [177] was used. The micropillar array allows measuring forces that the cell exerts on the substrate. We selected the pillars used for the force calculations and the geometrical fit shown in Figures 2.7 and 2.8 according to the following criteria. *1)* They are within 10 pixels (1.38 µm) from the edge of the cell. *2)* They are subject to a force that is at least 3 times larger than the average force on all the pillars or the tangent vector along the cell contour rotates by an angle equal or larger than 30° at the location of that pillar. *3)* The distance between two pillars delimiting the same ellipse is larger than 50 pixels (6.9 µm). Figure 2.9 shows examples of the pillars identified with these criteria for the six cells displayed in Figures 2.7 and 2.8.

### 2.5.5 Ellipse fitting

Ellipses are fitted, using Matlab, to the part of the cell edge delimited by two consecutive pillars, provided the pillars satisfy the three criteria listed in Section 2.5.4. Each ellipse is described by five parameters: the two coordinates of the center, the two semi-axes and the orientation of the ellipse's longitudinal direction. In fitting ellipses to cellular arcs, the orientation of the longitudinal direction of a given ellipse is constrained to be equal to the local orientation of stress fibers along that cellular arc, consistent with our predictions [Eq. (2.3)]. This local stress fiber orientation is measured from the channel with TRITC-Phalloidin (Actin) using the OrientationJ plugin for ImageJ [177]. The average orientation per cell edge segment is calculated over all pixels between 15 and 50 pixels ($2.07\ \mu\mathrm{m}$ and $6.9\ \mu\mathrm{m}$) away from the corresponding cell edge and whose coherency is larger than 0.15. See also Section 2.5.7. Then, each cellular arc is fitted separately to obtain the coordinates of the center and the lengths of the two semi-axes of the ellipse, and the resulting lengths are averaged over the $N$ ellipses in the cell that meet the criteria listed above. The resulting numbers serve as initial parameters for a global fit, which simultaneously fits $N$ cellular arcs to a unique ellipse. This global fit then finds optimal values for the coordinates of the center of each ellipse, and for the length of the two semi-axes of the unique ellipse, by minimizing the distance between fitted ellipses and the cellular arcs using $\chi^2$. All reported ellipse parameters are obtained using this global fit. Ellipses whose $\chi^2$ is greater than 10 were discarded, which occurs in case of membrane ruffling and other out-of-equilibrium events.

### 2.5.6 Force analysis

For both isotropic and anisotropic cells, traction forces can be calculated by summing the cortical tension $\boldsymbol{F} = \lambda \boldsymbol{T}$ of the two arcs meeting at a specific adhesion site. In the anisotropic case, this is conveniently done by first rotating the ellipse in such a way the minor and major axes are parallel to the $x-$ and $y-$direction respectively. Then two forces $\boldsymbol{F}_1$ and $\boldsymbol{F}_0$ are calculated by combining Eqs. (2.3) and (2.4) and defined in such a way that they are pointing clockwise and counter-clockwise around the ellipse:

$$\frac{\boldsymbol{F}_0}{\lambda_{\min}} = \left(\frac{d}{2b}\sin\phi + \frac{\rho}{b}\cos\phi\right)\hat{\boldsymbol{x}} + \left(-\frac{1}{\gamma}\frac{d}{2b}\cos\phi + \frac{\rho}{b}\sin\phi\right)\hat{\boldsymbol{y}}\ , \tag{2.5a}$$

$$\frac{\boldsymbol{F}_1}{\lambda_{\min}} = \left(\frac{d}{2b}\sin\phi - \frac{\rho}{b}\cos\phi\right)\hat{\boldsymbol{x}} + \left(-\frac{1}{\gamma}\frac{d}{2b}\cos\phi - \frac{\rho}{b}\sin\phi\right)\hat{\boldsymbol{y}}\ , \tag{2.5b}$$

where $d$ is the distance between the positions of both forces on the ellipse, $b$ is the major semi-axis of the ellipse and $\phi$ is the angle that the line through both points makes with the $x-$axis (see Figure 2.4). The length scale $\rho$ is defined as:

$$\rho = \sqrt{b^2\left(\frac{1+\tan^2\phi}{1+\gamma\tan^2\phi}\right) - \frac{1}{\gamma}\left(\frac{d}{2}\right)^2}\ . \tag{2.6}$$

Then, $\boldsymbol{F}_0$ and $\boldsymbol{F}_1$ are rotated back to the coordinate system of the image and summed to give the force, scaled by $\lambda_{\min}$, acting on the cell edge on the location of a particular intersection of two ellipses.

The magnitude of the traction forces is required for the calculation of the minimal line tension $\lambda_{\min}$ and the isotropic and directed stresses $\sigma$ and $\alpha$. We get this from the micropillar array. A measured force usually is the sum of two forces exerted by two different cell edge segments. Therefore, we first decompose the traction force into two forces pointing along tangents to the two cell edge segments adjacent to the position of the force. Then, per cell, we take any combination of two clockwise and counter-clockwise forces and calculate:

$$\lambda_{\min} = \sqrt{\frac{F_{1x}^2 F_{0y}^2 - F_{0x}^2 F_{1y}^2}{F_{0y}^2 - F_{1y}^2}}\ , \quad \sigma = \frac{|\boldsymbol{F}_0 - \boldsymbol{F}_1|}{d}\frac{F_{0x}+F_{1x}}{F_{0y}-F_{1y}}\ , \quad \alpha = \sigma\left(\frac{1}{\gamma} - 1\right)\ . \tag{2.7}$$

Here $\boldsymbol{F}_0$ and $\boldsymbol{F}_1$ are defined in the coordinate system where the $x-$ and $y-$axes are the minor and major axes of the ellipse. Furthermore, $F_{nx}$ and $F_{ny}$ are the components of

$\boldsymbol{F}_n$ in the x and y-directions respectively. To calculate values for these quantities, we average all the different tensions and stresses we get for all possible combinations in all cells, taking the errors on these values into account as weights while averaging.

### 2.5.7 Orientational analysis of the stress fibers

The local orientation of the stress fibers and their degree of alignment (see, also, Figure 2.10 in the Appendix) have been calculated using the ImageJ plugin OrientationJ [177]. The local alignment has been calculated through the following procedure. Let $I(x_0, y_0)$ be the intensity of the image at the point $(x_0, y_0)$ and $I_u = \boldsymbol{u} \cdot \nabla I$, the projection on the gradient of $I$ along the arbitrary $\boldsymbol{u}$ direction. The amount of anisotropy of the image can be quantified by introducing the extrema of the squared norm of $I_u$, namely:

$$\Lambda_{\text{max}} = \max_{\boldsymbol{u}} \|I_u\|^2 \,, \qquad \Lambda_{\text{min}} = \min_{\boldsymbol{u}} \|I_u\|^2 \,, \tag{2.8}$$

where $\| \cdots \| = \int w(x,y) \mathrm{d}x\, \mathrm{d}y\, (\cdots)$ represents the norm of a weighted average with $w(x,y)$ a Gaussian with a standard deviation of five pixels ($0.69\,\mu$m) centered at $(x_0, y_0)$. The amount of anisotropy is then naturally quantified in terms of the coherence parameter:

$$C = \frac{\Lambda_{\text{max}} - \Lambda_{\text{min}}}{\Lambda_{\text{max}} + \Lambda_{\text{min}}} \,. \tag{2.9}$$

In case of isotropic distributions, $\Lambda_{\text{max}} = \Lambda_{\text{min}}$ and $C = 0$. On the other hand, in case of strongly aligned stress fibers $\Lambda_{\text{max}} \gg \Lambda_{\text{min}}$ and $C \approx 1$. From the right column of Figure 2.10, we see that the stress fibers are highly aligned in the periphery of the cell, consistent with our theoretical model.

## 2.6 Appendix

### 2.6.1 Angular coordinates of the adhesion sites

As we explained in Section 2.3, the ratios $b = \lambda_{\text{min}}/\sigma$ between the peripheral and bulk contractility and $\gamma = \sigma/(\sigma+\alpha)$ between isotropic and directed stresses set, respectively, the major semi-axis and the aspect ratio $a/b = \sqrt{\gamma}$ of the ellipse approximating the shape of the cellular arcs, whereas the orientation of the ellipse is determined by the direction of the stress fibers. These quantities uniquely identify the shape and the orientation of the ellipse, but not which portion of the ellipse corresponds to a given cellular arc. In order for this to be uniquely determined, one needs to specify the relative position $\boldsymbol{d} = d(\cos\phi, \sin\phi)$ of the adhesion sites (Figure 2.4a), where the stress fibers are assumed, without loss of generality, parallel to the $y-$axis.

Then, using Eq. (2.3) with $\theta_{\text{SF}} = \pi/2$, one can straightforwardly calculate the coordinates of the center of the ellipse in the reference frame centered at the first adhesion

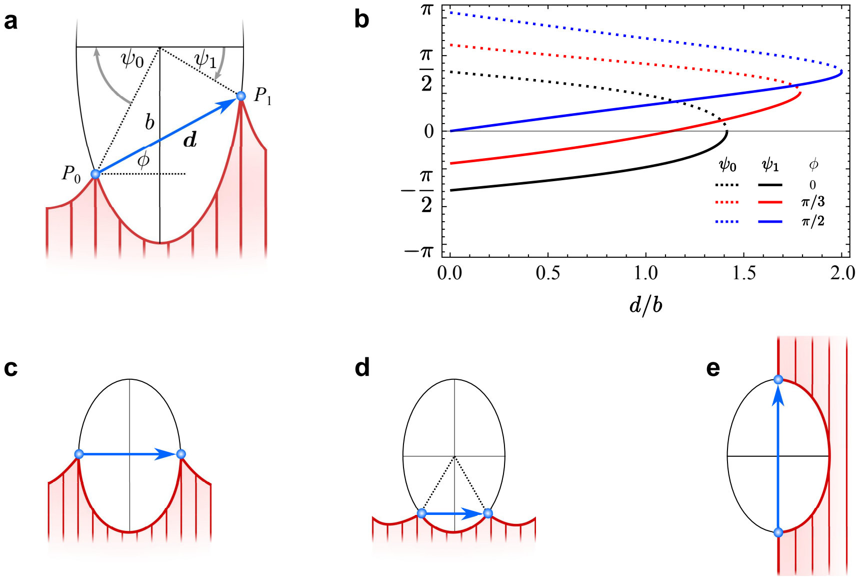

$d = 2b\sqrt{\gamma}$
$\psi_0 = \psi_1 = 0$

$d = b\sqrt{\gamma}$
$\psi_0 = -\psi_1 = \pi/3$

$d = 2b$
$\psi_0 = \psi_1 = \pi/2$

**Figure 2.4.** Angular coordinates of the adhesion sites. (a) Schematic illustration of a cellular arc and the approximating ellipse. The angular coordinates $\psi_0$ and $\psi_1$ are measured with respect to the negative and positive $x-$direction respectively. Thus, in the displayed configuration $\psi_0 > 0$ and $\psi_1 < 0$. The ellipse major semi-axis is set by the ratio between peripheral and bulk contractile stresses, i.e., $b = \lambda_{\min}/\sigma$. (b) Angular coordinates $\psi_0$ (dotted line) and $\psi_1$ (solid line) as a function of the rescaled distance between the adhesion sites, i.e., $d/b$, for various choices of the tilt angle $\phi$ and $\sigma = \alpha$ (hence $\gamma = 1/2$). (c), (d) and (e) Examples of specific configurations for various choices of $d$ and $\phi$.

site ($P_0$ in Figure 2.4a), namely:

$$x_c = \frac{d}{2}\cos\phi - \gamma\rho\sin\phi\ , \tag{2.10a}$$

$$y_c = \frac{d}{2}\sin\phi + \rho\cos\phi\ , \tag{2.10b}$$

with the distance $\rho$ defined in Eq. (2.6). From Eqs. (2.10), standard algebraic manipulations allow us to express the angular coordinate $\psi$ of the adhesion sites in the frame of the ellipse (Figure 2.4a), namely:

$$\tan \psi_0 = \frac{d \sin \phi + 2\rho \cos \phi}{d \cos \phi - 2\gamma\rho \sin \phi} \;, \tag{2.11a}$$

$$\tan \psi_1 = \frac{d \sin \phi - 2\rho \cos \phi}{d \cos \phi + 2\gamma\rho \sin \phi} \;. \tag{2.11b}$$

Illustrations of the possible configurations described by Eqs. (2.11) are shown in Figures 2.4b-e. When $\rho$ becomes imaginary, the two adhesion sites are as far apart as possible along the ellipse. This sets the position of the extremum of the curves displayed in Figure 2.4b.

### 2.6.2 Material parameters for different cell types

Section 2.3 gives the material parameters $\gamma$, $\lambda_{\mathrm{min}}$, $\sigma$ and $\alpha$ for a set of 285 cells. These cells, in fact, come from a pool of two different cell types. The GE11 cells used exhibit an epithelioid morphology whereas the GD25 cells exhibit a fibroblastoid morphology. Both cell types are deficient of the fibronectin receptor integrin β1. In both cell types then either α5β1 was reexpressed, or αvβ3 was expressed. These cells are designated GEβ1, GEβ3, GDβ1 and GDβ3. The differing cell and integrin types result in a different cell-substrate coupling leading to different material parameters for each cell and integrin expression type. It is outside the scope of this chapter to examine these differences in detail, therefore initially only the average of each parameter over all 285 cells is given. For completeness, we give the same parameters per cell type in Table 2.2. As can be expected [172], cells expressing β1 exert higher traction forces than cells expressing β3, which is reflected in a lower $\lambda_{\mathrm{min}}$ for the latter.

**Table 2.2.** Survey of the average material parameters per cell type in a sample of 285 fibroblastoid and epithelioid cells. Shown are the mean and standard deviation. Whereas $\gamma$ does not vary significantly, there is some variance observed in especially $\lambda_{\mathrm{min}}$, which appears larger for cells expressing β-integrin.

| Cell type | number of cells | $\gamma$ | $\lambda_{\mathrm{min}}$ (nN) | $\sigma$ (nN/μm) | $\alpha$ (nN/μm) |
|---|---|---|---|---|---|
| GEβ1 | 59 | $0.32 \pm 0.14$ | $9.8 \pm 6.9$ | $1.4 \pm 1.0$ | $2.6 \pm 2.2$ |
| GEβ3 | 112 | $0.31 \pm 0.19$ | $5.5 \pm 3.4$ | $0.62 \pm 0.41$ | $1.3 \pm 1.1$ |
| GDβ1 | 56 | $0.38 \pm 0.26$ | $10.6 \pm 9.4$ | $0.92 \pm 0.78$ | $1.5 \pm 1.7$ |
| GDβ3 | 58 | $0.34 \pm 0.25$ | $7.9 \pm 6.0$ | $1.0 \pm 0.8$ | $2.0 \pm 2.2$ |
| All | 285 | $0.33 \pm 0.20$ | $7.6 \pm 5.6$ | $0.87 \pm 0.70$ | $1.7 \pm 1.7$ |

### 2.6.3 Supporting figures

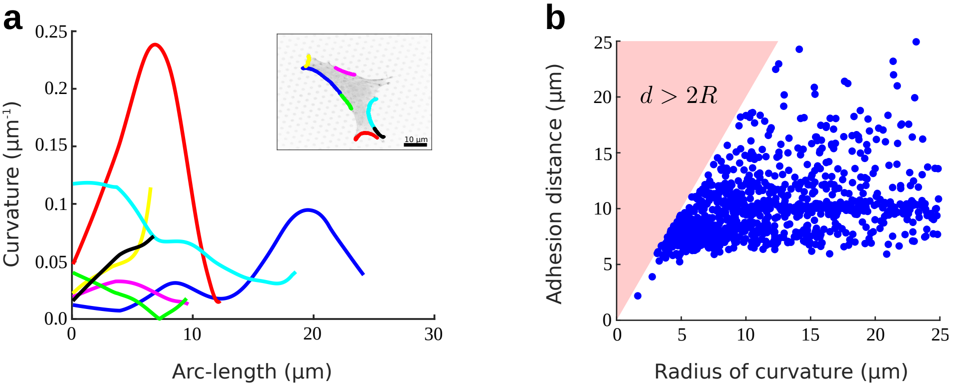

**Figure 2.5.** (a) Curvature versus arc-length for a specific cell (inset). The blue, red, cyan, yellow and black arcs are evidently non-circular as indicated by the smooth curvature variation. Because any smooth plane curve can be locally approximated by a circle of radius $R = 1/\kappa$, longer arcs are more likely to exhibit appreciable curvature variations. The large curvature variation of the yellow arc is instead caused by the fact that the arc is roughly perpendicular to the stress fibers, hence it experiences the largest anisotropy in the force distribution. (b) Average radius of curvature of a cellular arc versus the distance between the end-points of the arc (i.e., adhesion sites). The radius of curvature is obtained by fitting cellular arcs with circles (see Figures 2.1 and 2.7). The data points correspond to a sample of 285 cells and do not allow conclusive statements about a possible correlation between the arc's length and curvature.

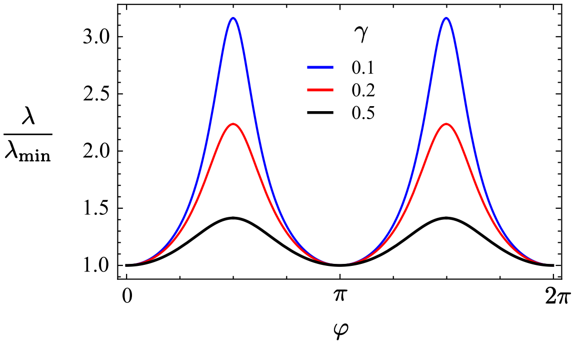

**Figure 2.6.** Normalized cortical tension $\lambda/\lambda_{\min}$, calculated as expressed by Eq. (2.4), versus the turning angle $\varphi$ (see Figure 2.2) for $\theta_{\text{SF}} = \pi/2$ and various $\gamma$ values. Upon increasing the anisotropy (decreasing $\gamma$), the cortical tension becomes progressively less uniform across the arc. The isotropic limit is recovered when $\gamma = 1$ and $\lambda = \lambda_{\min}$ along the entire cellular arc. Maximal tension is attained when $\varphi = \pi/2$ and the tangent vector $\boldsymbol{T}$ is parallel to the stress fibers.

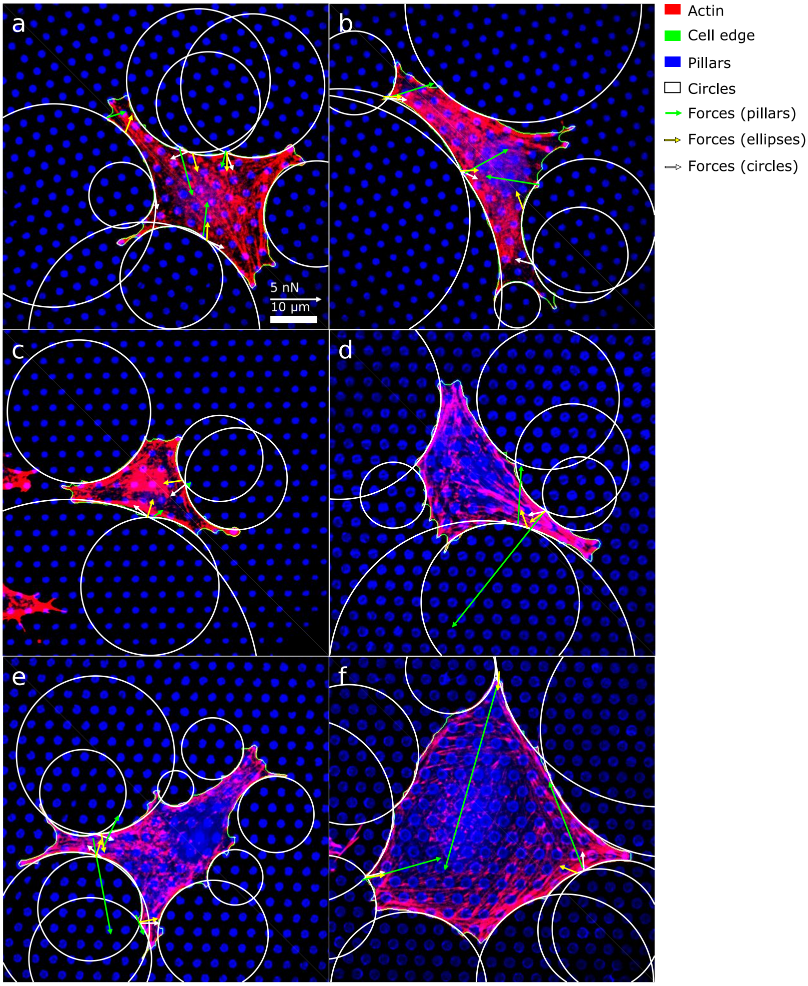

**Figure 2.7.** Six examples of cells with circles fitted to the cell edges. The actin, cell edge and micropillar tops are in the red, green and blue channels respectively. Circles (white) are fitted to the edge of the cells. The arrows correspond to the measured forces (green) and predicted directions (but not magnitudes) of the forces in the presence of isotropic ($\alpha = 0$, white arrow) and anisotropic ($\alpha \neq 0$, yellow arrow) contractile stresses. The length of the green arrows indicates the magnitude of the force. Green arrows originate from the center of the micropillar, while yellow and white arrows originate from the intersections of ellipses and circles respectively, therefore, arrows do not necessarily originate from the same point. Yellow and white arrows are only plotted for adhesion sites under an intersection of ellipses or circles respectively. Panels (a) to (c) show epithelioid cells and (d) to (f) show fibroblastoid cells.

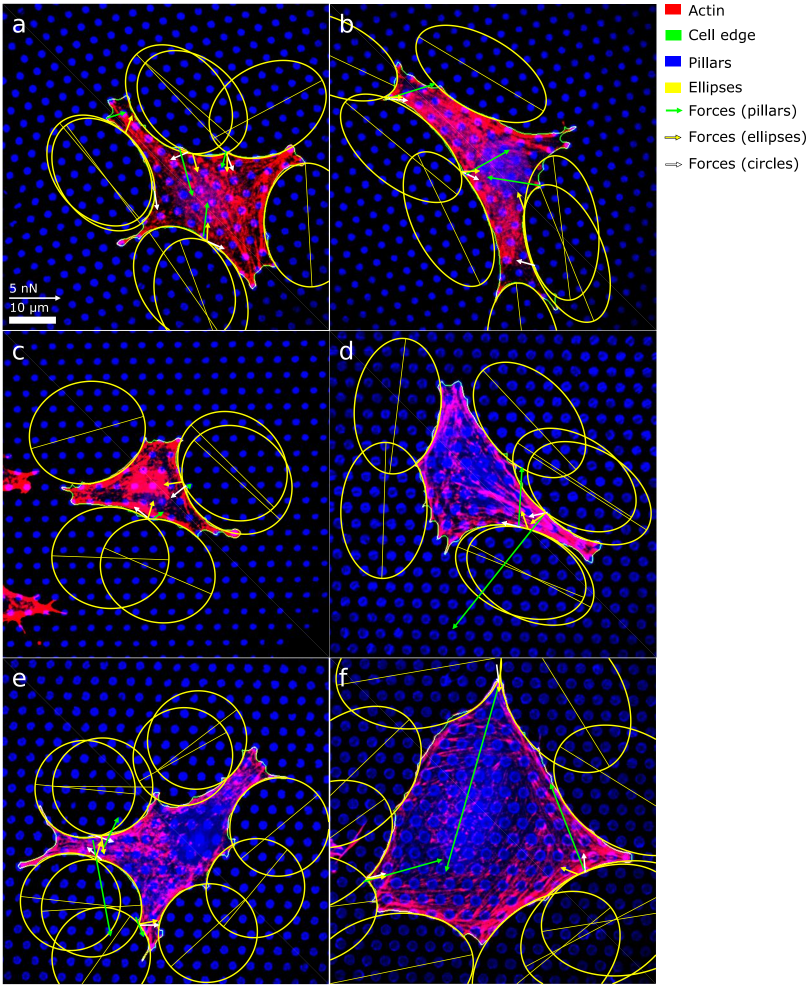

**Figure 2.8.** Six examples of cells (same as in Figure 2.7) with ellipses fitted to the cell edges. The actin, cell edge and micropillar tops are in the red, green and blue channels respectively. Ellipses (yellow, including the major axis) are fitted to the edge of the cells. The arrows correspond to the measured forces (green) and predicted directions (but not magnitudes) of the forces in the presence of isotropic ($\alpha = 0$, white arrow) and anisotropic ($\alpha \neq 0$, yellow arrow) contractile stresses. The length of the green arrows indicates the magnitude of the force. Green arrows originate from the center of the micropillar, while yellow and white arrows originate from the intersections of ellipses and circles respectively, therefore, arrows do not necessarily originate from the same point. Yellow and white arrows are only plotted for adhesion sites under an intersection of ellipses or circles respectively. Panels (a) to (c) show epithelioid cells and (d) to (f) show fibroblastoid cells. Fit values for the ellipses in panels (a) to (f) respectively: $\gamma$: 0.52; 0.25; 0.75; 0.40; 0.95; 0.46, $\lambda_{\min}/\sigma$ (µm): 13.4; 15.7; 12.6; 14.7; 10.8; 18.0.

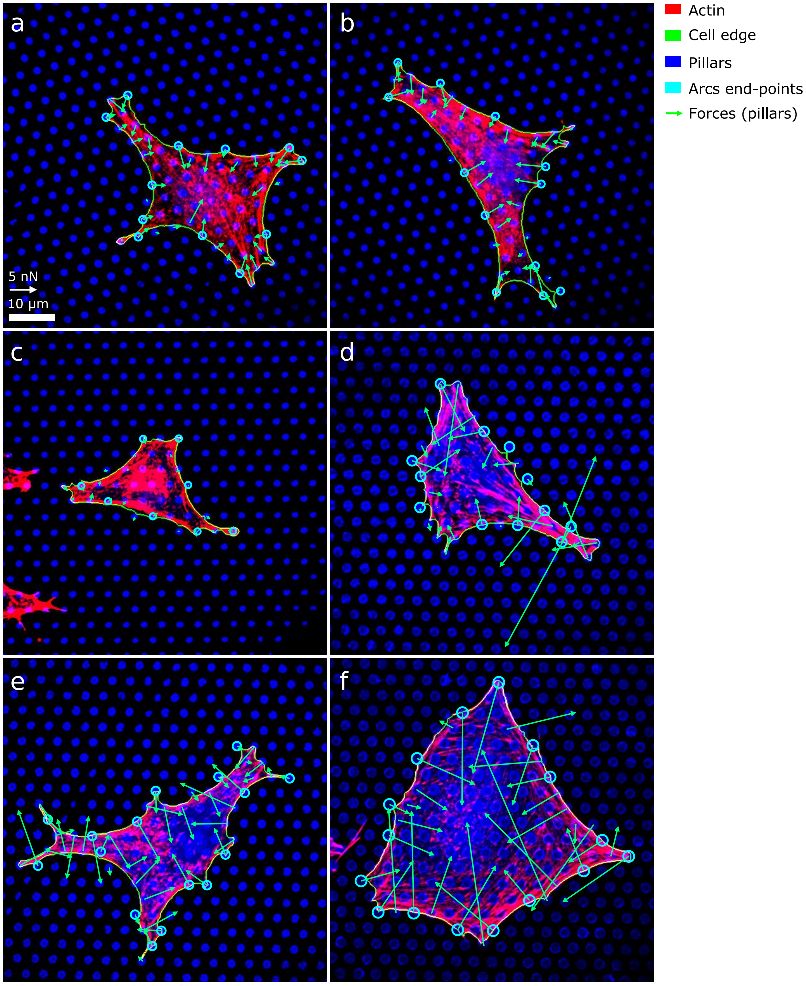

**Figure 2.9.** Six examples of cells (same as in Figures 2.7 and 2.8) with all the traction forces measured along the contour explicitly indicated. The actin, cell edge and micropillar tops are in the red, green and blue channels respectively. The length of the green arrows indicates the magnitude of the force and the pillars used for the geometrical fits, illustrated in Figures 2.7 and 2.8, are highlighted. Panels (a) to (c) show epithelioid cells and (d) to (f) show fibroblastoid cells.

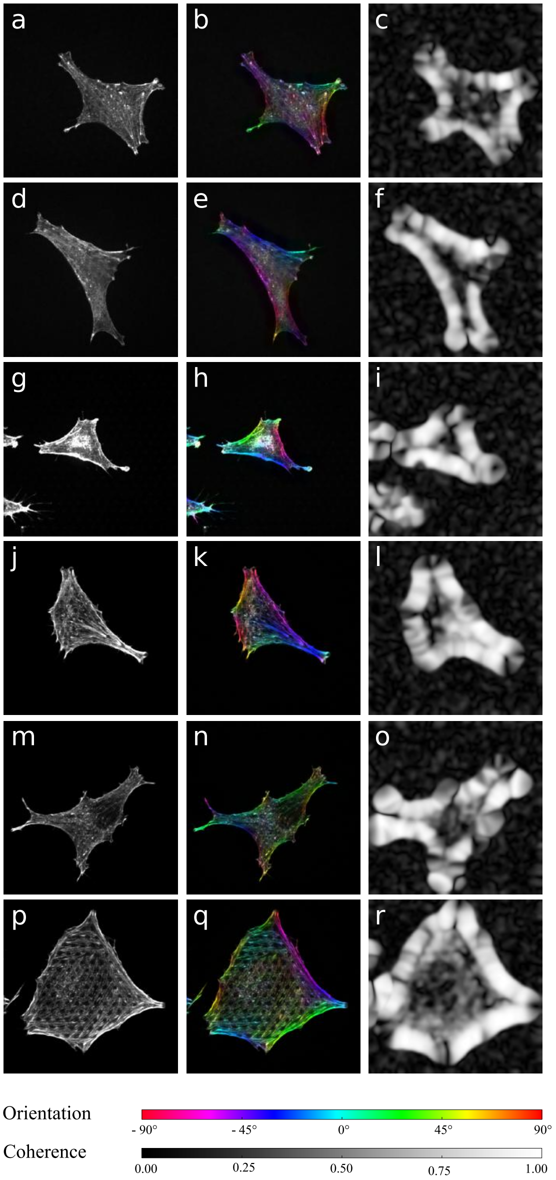

**Figure 2.10.** Orientational analysis of the stress fibers. On the left column, optical micrographs of the six example cells displayed in Figures 2.7, 2.8 and 2.9. On the center column, color survey of the stress fibers orientation. On the right column, density plot of the orientational coherence of the stress fibers, computed via OrientationJ [177]. Along the cell periphery, stress fibers are highly aligned and the calculated coherence is close to one (see Section 2.5.7).

## Chapter 3

# MECHANICAL INTERPLAY BETWEEN CELL SHAPE AND ACTIN CYTOSKELETON ORGANIZATION

The experimental data presented in this chapter was kindly provided by Wim Pomp, Erik H.J. Danen, and Thomas Schmidt. The chapter is available on arXiv as:

Koen Schakenraad, Jeremy Ernst, Wim Pomp, Erik H.J. Danen, Roeland M.H. Merks, Thomas Schmidt, and Luca Giomi, 'Mechanical interplay between cell shape and actin cytoskeleton organization', arXiv:1905.09805

## Abstract

We investigate the mechanical interplay between the spatial organization of the actin cytoskeleton and the shape of animal cells adhering on micropillar arrays. Using a combination of analytical work, computer simulations and *in vitro* experiments, we demonstrate that the orientation of the stress fibers strongly influences the geometry of the cell edge. In the presence of a uniformly aligned cytoskeleton, the cell edge can be well approximated by elliptical arcs, whose eccentricity reflects the degree of anisotropy of the cell's internal stresses. Upon modeling the actin cytoskeleton as a nematic liquid crystal, we further show that the geometry of the cell edge feeds back on the organization of the stress fibers by altering the length scale at which these are confined. This feedback mechanism is controlled by a dimensionless number, the anchoring number, representing the relative weight of surface-anchoring and bulk-aligning torques. Our model allows to predict both cellular shape and the internal structure of the actin cytoskeleton and is in good quantitative agreement with experiments on fibroblastoid (GDβ1,GDβ3) and epithelioid (GEβ1, GEβ3) cells.

## 3.1 Introduction

Mechanical cues play a vital role in many cellular processes, such as durotaxis [132, 169], cell-cell communication [168], stress-regulated protein expression [167] or rigidity-dependent stem cell differentiation [28, 30]. Whereas mechanical forces can directly activate biochemical signaling pathways, via the mechanotransduction machinery [178], their effect is often mediated by the cortical cytoskeleton, which, in turn, affects and can be affected by the geometry of the cell envelope.

By adjusting their shape, cells can sense the mechanical properties of their microenvironment and regulate traction forces [64, 170, 171], with prominent consequences on bio-mechanical processes such as cell division, differentiation, growth, death, nuclear deformation and gene expression [32–37]. On the other hand, the cellular shape itself depends on the mechanical properties of the environment. Experiments on adherent cells have shown that the stiffness of the substrate strongly affects cell morphology [49, 50] and triggers the formation of stress fibers [51, 53]. The cell spreading area increases with the substrate stiffness for several cell types, including cardiac myocytes [49], myoblasts [50], endothelial cells and fibroblasts [51], and mesenchymal stem cells [52].

In Chapter 2 we have investigated the shape and traction forces of concave cells, adhering to a limited number of discrete adhesion sites and characterized by a highly anisotropic actin cytoskeleton. Using a contour model of cellular adhesion [48, 62–64, 67], we demonstrated that the edge of these cells can be accurately approximated by a collection of elliptical arcs obtained from a unique ellipse, whose eccentricity depends on the degree of anisotropy of the contractile stresses arising from the actin cytoskeleton. Furthermore, our model quantitatively predicts how the anisotropy of the actin cytoskeleton determines the magnitudes and directions of traction forces. Both predictions were tested in experiments on highly anisotropic fibroblastoid and epithelioid cells [173] supported by stiff microfabricated elastomeric pillar arrays [55–57], finding good quantitative agreement.

Whereas these findings shed light on how cytoskeletal anisotropy controls the geometry and forces of adherent cells, they raise questions on how anisotropy emerges from the three-fold interplay between isotropic and directed stresses arising within the cytoskeleton, the shape of the cell envelope and the geometrical constraints introduced by focal adhesions. It is well known that the orientation of the stress fibers in elongated cells strongly correlates with the polarization direction of the cell [85–88]. Consistently, our results indicate that, in highly anisotropic cells, stress fibers align with each other and with the cell's longitudinal direction (see, e.g., Figures 3.1A and 2.10). However, the physical origin of these alignment mechanisms is less clear and inevitably leads to a chicken-and-egg causality dilemma: do the stress fibers align along the cell's axis or does the cell elongate in the direction of the stress fibers?

The biophysical literature is not scarce of cellular processes that might possibly contribute to alignment of stress fibers with each other and with the cell edge. Mechanical feedback between the cell and the extracellular matrix or substrate, for instance, has been shown to play an important role in the orientation and alignment of stress fibers [52, 76, 179–181]. Molecular motors have also been demonstrated to produce an aligning effect on cytoskeletal filaments, both in mesenchymal stem cells [182] and in purified cytoskeletal extracts [183], where the observation is further corroborated by agent-based simulations [184]. A similar mechanism has been theoretically proposed for microtubules-kinesin mixtures [185]. Studies in microchambers demonstrated that steric interactions can also drive alignment of actin filaments with each other and with the microchamber walls [186–188]. Theoretical studies have highlighted the importance of the stress fibers' assembly and dissociation dynamics [75, 76], the dynamics of focal adhesion complexes [136, 189], or both [77, 79]. Also the geometry of actin nucleation sites has been shown to affect the growth direction of actin filaments, thus promoting alignment [190, 191]. Finally, mechanical coupling between the actin cytoskeleton and the plasma membrane has been theoretically shown to lead to fiber alignment, as bending moments arising in the membrane result into torques that reduce the amount of splay within the filaments [192]. Despite such a wealth of possible mechanisms, it is presently unclear which one or which combination is ultimately responsible for the observed alignment of stress fibers between each other and with the cell's longitudinal direction. Analogously, it is unclear to what extent these mechanisms are sensitive to the specific mechanical and topographic properties of the environment, although some mechanisms rely on specific environmental conditions that are evidently absent in certain circumstances (e.g., the mechanical feedback between the cell and the substrate discussed in Refs. [76, 136, 180, 193] relies on deformations of the substrate and is unlikely to play an important role in experiments performed on stiff micro-pillar arrays).

In this chapter we investigate the interplay between the anisotropy of the actin cytoskeleton and the shape of cells adhering to stiff microfabricated elastomeric pillar arrays [55–57]. Rather than pinpointing a specific alignment mechanism, among those reviewed above, we focus on the *interplay* between cell shape and the spatial organization of the actin cytoskeleton. This is achieved by means of a phenomenological treatment of the stress fiber orientation based on the continuum description of nematic liquid crystals, coupled with the contour model of the cell edge that we developed in Chapter 2. The chapter is organized as follows: in Section 3.2 we introduce our contour model for cells with anisotropic cytoskeleton. We first review the key theoretical results, already reported in Chapter 2, followed by an in-depth and previously unreported analysis of the model. In Section 3.3 we further generalize this approach by studying the mechanical interplay between the shape of the cell, described by our contour model, and the orientation of the actin cytoskeleton, modeled as a nematic liquid crystal confined by the cell edge, and we compare our results to experimental data on highly anisotropic cells. In both sections we assume that the coordinates of the adhesion sites along the cell contour are constant in time and known. A theoretical description of the dynamics of these adhesion sites, as a result of focal adhesion dynamics, is beyond the scope of this study and can be found, for example, in Refs. [136, 189].

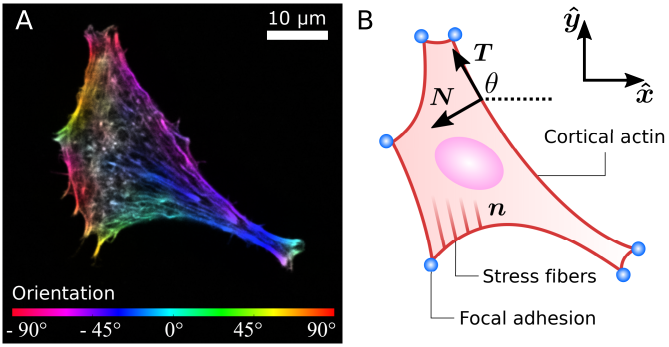

**Figure 3.1.** (A) A fibroblastoid cell with an anisotropic actin cytoskeleton cultured on a stiff microfabricated elastomeric pillar array. The color scale indicates the measured orientation of the actin stress fibers. (B) Schematic representation of a contour model for the cell in (A). The cell contour consists of a collection of concave cellular arcs (red lines) that connect pairs of adhesion sites (blue dots). These arcs are parameterized as curves spanned counterclockwise around the cell by the arc length $s$, and are entirely described via the tangent unit vector $\boldsymbol{T} = (\cos\theta, \sin\theta)$ and the normal vector $\boldsymbol{N} = (-\sin\theta, \cos\theta)$, with $\theta$ the turning angle. The unit vector $\boldsymbol{n} = (\cos\theta_{\mathrm{SF}}, \sin\theta_{\mathrm{SF}})$ describes the local orientation $\theta_{\mathrm{SF}}$ of the stress fibers.

## 3.2 Equilibrium configuration of the cell contour

Many animal cells spread out after coming into contact with a stiff adhesive surface. They develop transmembrane adhesion receptors at a limited number of adhesion sites that lie mainly along the cell contour (i.e., focal adhesions [54]). These cells are then essentially flat and assume a typical concave shape characterized by arcs which span between the sites of adhesion, while forces are mainly contractile [48]. This makes it possible to describe adherent cells as two-dimensional contractile films, whose shape is unambiguously identified by the position $\boldsymbol{r} = (x, y)$ of the cell contour [62–67, 194]. Figure 3.1B illustrates a schematic representation of the cell (fibroblastoid) in Figure 3.1A, where the cell contour consists of a collection of curves, referred to as “cellular arcs”, that connect two consecutive adhesion sites. These arcs are parameterized by the arc length $s$ as curves spanned counterclockwise around the cell, oriented along the tangent unit vector $\boldsymbol{T} = \partial_s \boldsymbol{r} = (\cos\theta, \sin\theta)$, with $\theta = \theta(s)$ the turning angle of the arc with respect to the horizontal axis of the frame of reference. The normal vector $\boldsymbol{N} = \partial_s \boldsymbol{r}^{\perp} = (-\sin\theta, \cos\theta)$, with $\boldsymbol{r}^{\perp} = (-y, x)$, is directed toward the interior of the cell. The equation describing the shape of a cellular arc is obtained upon balancing all the conservative and dissipative forces experienced by the cell contour. These are:

$$\xi_t \partial_t \boldsymbol{r} = \partial_s \boldsymbol{F}_{\mathrm{cortex}} + (\hat{\boldsymbol{\Sigma}}_{\mathrm{out}} - \hat{\boldsymbol{\Sigma}}_{\mathrm{in}}) \cdot \boldsymbol{N} \,, \tag{3.1}$$

where $t$ is time and $\xi_t$ is a (translational) drag coefficient measuring the resistance, arising from cell-substrate interactions, against motion of the cell contour. $\hat{\boldsymbol{\Sigma}}_{\mathrm{out}}$ and

$\hat{\boldsymbol{\Sigma}}_{\rm in}$ are the stress tensors on the two sides of the cell boundary and $\boldsymbol{F}_{\rm cortex}$ is the stress resultant along the cell contour [48, 63–65, 67, 194]. We assume the substrate to be rigid and the adhesion sites, lying along the cell contour, to be stationary. For theoretical models of cell adhesion on compliant substrates, see, e.g., Refs. [64, 65, 67]. The temporal evolution of the cell contour is then dictated by a competition between internal and external bulk stresses acting on the cell boundary and the tension arising within the cell cortex. The former give rise to a contractile (i.e., inward-directed) force on the cell contour and tend to decrease the cell area. By contrast, cortical tension decreases the cell perimeter, thus resulting in an extensile (i.e., outward-directed) force, as a consequence of the cell concavity. As the planar contour represents the two-dimensional projection of the full three-dimensional body of the cell, changes in the area affect neither the density of the cytoplasm nor the internal pressure. Finally, we assume the dynamics of the cell contour to be overdamped.

The stress tensor can be modeled upon taking into account isotropic and directed stresses. The latter are constructed by treating the stress fibers as contractile force dipoles, whose average orientation $\theta_{\rm SF}$ is parallel to the unit vector $\boldsymbol{n} = (\cos\theta_{\rm SF}, \sin\theta_{\rm SF})$ (see Figure 3.1B). This gives rise to an overall contractile bulk stress of the form [102, 103]:

$$\hat{\boldsymbol{\Sigma}}_{\rm out} - \hat{\boldsymbol{\Sigma}}_{\rm in} = \sigma\hat{\boldsymbol{I}} + \alpha\boldsymbol{n}\boldsymbol{n} \;, \tag{3.2}$$

where $\hat{\boldsymbol{I}}$ is the identity matrix, $\sigma > 0$ embodies the magnitude of all isotropic stresses (passive and active) experienced by the cell edge and $\alpha > 0$ is the magnitude of the directed contractile stresses and is proportional to the local degree of alignment between the stress fibers, in such a way that $\alpha$ is maximal for perfectly aligned fibers, and vanishes if these are randomly oriented. In Section 3.3 we will explicitly account for the local orientational order of the stress fibers using the language of nematic liquid crystals. Furthermore, since $\hat{\boldsymbol{I}} = \boldsymbol{n}\boldsymbol{n} + \boldsymbol{n}^{\perp}\boldsymbol{n}^{\perp}$, the nematic director $\boldsymbol{n}$ and its normal $\boldsymbol{n}^{\perp} = (-\sin\theta_{\rm SF}, \cos\theta_{\rm SF})$ correspond to the principal stress directions, whereas $\sigma_{\rm max} = \sigma + \alpha$ and $\sigma_{\rm min} = \sigma$ are, respectively, the maximal and minimal principal stresses. The degree of anisotropy of the bulk stress is thus determined by the ratio between the isotropic contractility $\sigma$ and the directed contractility $\alpha$. Finally, the tension within the cell cortex is modeled as $\boldsymbol{F}_{\rm cortex} = \lambda\boldsymbol{T}$, where the line tension $\lambda$ embodies the contractile forces arising from myosin activity in the cell cortex. This quantity varies, in general, along an arc and can be expressed as a function of the arc length $s$. In the presence of anisotropic bulk stresses, in particular, $\lambda(s)$ cannot be constant, as we will see in Section 3.2.1. The force balance condition, Eq. (3.1), becomes then

$$\xi_t \partial_t \boldsymbol{r} \;=\; \partial_s(\lambda\boldsymbol{T}) + \sigma\boldsymbol{N} + \alpha(\boldsymbol{n}\cdot\boldsymbol{N})\boldsymbol{n} \;. \tag{3.3}$$

In this section we describe the position of the cell boundary under the assumption that the timescale required for the equilibration of the forces in Eq. (3.3) is much shorter than the typical timescale of cell migration on the substrate (i.e., minutes). Under this assumption, $\partial_t\boldsymbol{r} = \boldsymbol{0}$ and Eq. (3.3) can be cast in the form:

$$\boldsymbol{0} \;=\; (\partial_s\lambda)\,\boldsymbol{T} + (\lambda\kappa + \sigma)\boldsymbol{N} + \alpha(\boldsymbol{n}\cdot\boldsymbol{N})\boldsymbol{n} \;, \tag{3.4}$$

where we have used $\partial_s \boldsymbol{T} = \kappa \boldsymbol{N}$, with $\kappa = \partial_s \theta$ the curvature of the cell edge. In the following, we review (Section 3.2.1) and extend (Sections 3.2.2, 3.2.3 and 3.2.4) the results reported in Chapter 2 about the geometry and mechanics of anisotropic cells adhering to micropillar arrays.

### 3.2.1 Equilibrium cell shape and line tension

In this section we review the results previously reported in Chapter 2. A derivation of the main equations can be found in Section 3.6.1 in the Appendix.

For $\alpha = 0$, Eq. (3.4) describes the special case of a cell endowed with a purely isotropic cytoskeleton [62–64]. Force balance requires $\lambda$ to be constant along a single cellular arc (i.e., $\partial_s \lambda = 0$), whereas the bulk and cortical tension compromise along an arc of constant curvature, i.e., $\kappa = -\sigma/\lambda$, with the negative sign of $\kappa$ indicating that the arcs are curved inwards. The cell edge is then described by a sequence of circular arcs, whose radius $R = 1/|\kappa| = \lambda/\sigma$ depends on the local cortical tension $\lambda$ of the arc. This model successfully describes the shape of adherent cells in the presence of strictly isotropic forces. However, as we showed in Chapter 2, isotropic models are not suited for describing cells whose anisotropic cytoskeleton develops strong directed forces originating from actin stress fibers [46, 47]. In the presence of an anisotropic cytoskeleton, $\alpha > 0$ and the cell contour is no longer subject to purely normal forces. As a consequence, the cortical tension $\lambda$ varies along a given cellular arc to balance the tangential component of the contractile forces arising from the actin cytoskeleton. In order to highlight the physical mechanisms described, in this case, by Eq. (3.4), we introduce a number of simplifications that make the problem analytically tractable. These will be lifted in Section 3.3, where we will consider the most general scenario. First, because the orientation of the stress fibers typically varies only slightly along a single arc, we assume the orientation of the stress fibers, $\theta_{\mathrm{SF}}$, to be constant along a single cellular arc, but different from arc to arc. Furthermore, without loss of generality, we orient the reference frame such that the stress fibers are parallel to the $y-$axis. Thus, $\theta_{\mathrm{SF}} = \pi/2$ and $\boldsymbol{n} = \hat{\boldsymbol{y}}$. Then, solving Eq. (3.4) with respect to $\lambda$ yields:

$$\lambda(\theta) = \lambda_{\min} \sqrt{\frac{1 + \tan^2 \theta}{1 + \gamma \tan^2 \theta}} \;, \tag{3.5}$$

where the constant $\gamma = \sigma/(\sigma + \alpha)$ quantifies the anisotropy of the bulk contractile stress. The quantity $\lambda_{\min}$ represents the minimal cortical tension attained along each cellular arc, where the stress fibers are perpendicular to the cell contour (i.e., $\theta = 0$). By contrast, the actin cortex exerts maximal tension when the stress fibers are parallel to the cell contour, i.e., $\lambda_{\max} = \lambda(\pi/2) = \lambda_{\min}/\sqrt{\gamma}$. We note that these variations in line tension along a single arc do not necessarily have to be regulated by the cell. Instead, they could simply be a result of passive mechanical forces in a way very similar to the space-dependent tension in a simple cable hanging under gravity. Although the minimal line tension $\lambda_{\min}$ could, in principle, be arc-dependent, for example if the cell

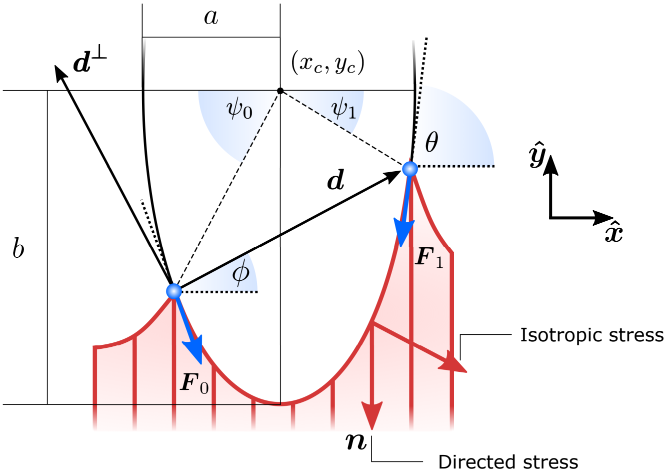

**Figure 3.2.** Schematic representation of a cellular arc, described by Eq. (3.6), for $\boldsymbol{n} = (\cos\theta_{\text{SF}}, \sin\theta_{\text{SF}}) = \hat{\boldsymbol{y}}$, hence $\theta_{\text{SF}} = \pi/2$. A force balance between isotropic stress, directed stress and line tension results in the description of each cell edge segment (red curve) as part of an ellipse of aspect ratio $a/b = \sqrt{\gamma}$ and with major semi-axis $b = \lambda_{\text{min}}/\sigma$. The cell exerts forces $\boldsymbol{F}_0$ and $\boldsymbol{F}_1$ on the adhesion sites (blue). The vector $\boldsymbol{d} = d(\cos\phi, \sin\phi)$ describes the relative position of the two adhesion sites, $\boldsymbol{d}^\perp = d(-\sin\phi, \cos\phi)$ is a vector perpendicular to $\boldsymbol{d}$, and $\theta$ is the turning angle of the cellular arc. The coordinates of the ellipse center $(x_c, y_c)$ and the angular coordinates of the adhesion sites along the ellipse $\psi_0$ and $\psi_1$ are given in Section 2.5.7.

cortex displays substantial variations in the myosin densities [63], here we approximate $\lambda_{\text{min}}$ as a constant. This approximation is motivated by the fact that our previous *in vitro* observations of anisotropic epithelioid and fibroblastoid cells did not identify a correlation between the arc length and curvature (see Figure 2.6b), which, on the other hand, is expected if $\lambda_{\text{min}}$ was to vary significantly from arc to arc [63]. Hence, $\alpha$, $\sigma$ and $\lambda_{\text{min}}$ represent the independent material parameters of our model.

The shape of a cellular arc is given by a segment of an ellipse, which is given by:

$$\frac{\sigma^2}{\lambda_{\text{min}}^2}\left[(x-x_c)\cos\theta_{\text{SF}} + (y-y_c)\sin\theta_{\text{SF}}\right]^2 + \frac{\sigma^2}{\gamma\lambda_{\text{min}}^2}\left[-(x-x_c)\sin\theta_{\text{SF}} + (y-y_c)\cos\theta_{\text{SF}}\right]^2 = 1\ . \quad (3.6)$$

The longitudinal direction of the ellipse is always parallel to the stress fibers, hence tilted by an angle $\theta_{\text{SF}}$ with respect to the $x$−axis, as illustrated in Figure 3.2 for $\boldsymbol{n} = \hat{\boldsymbol{y}}$. The direct relation between the contractile forces arising from the cytoskeleton and the shape of the cell is highlighted by the dimensionless parameter $\gamma = \sigma/(\sigma + \alpha)$: on the one hand, $\gamma$ defines the anisotropy of the contractile bulk stress, on the other hand it dictates the anisotropy of the cell shape. This, in turn, does not depend on the positions of the adhesion sites, which instead affect the traction forces experienced by the substrate (see Section 3.2.3). Both these properties arise from the fact that, in our model, cellular arcs have no preferred length, and are consistent with experimental observations on fibroblastoids and epithelioids (see Chapter 2). The coordinates of the center of the ellipse $(x_c, y_c)$ and the angular coordinates of the adhesion sites along the ellipse, $\psi_0$ and $\psi_1$ in Figure 3.2, can be calculated using standard algebraic manipulation and are given in Section 2.5.7.

Figure 3.3 shows an example of a fibroblastoid cell with ellipses fitted to its arcs. Because ellipse fitting is very sensitive to noise on the cell shape, only the longer arcs are considered here (see Section 2.5). We stress that, as long as the contractile stresses arising from the actin cytoskeleton are roughly uniform across the cell (i.e., $\alpha$, $\sigma$ and $\lambda_{\rm min}$ are constant), all cellular arcs of sufficient length are approximated by a *unique* ellipse (see Figure 3.3). The parameters that describe this ellipse are, in general, different for each individual cell. A survey of these parameters over a sample of 285 fibroblastoid and epithelioid cells yielded $\gamma = 0.33 \pm 0.20$, $\lambda_{\rm min} = 7.6 \pm 5.6$ nN, $\sigma = 0.87 \pm 0.70$ nN/µm, and $\alpha = 1.7 \pm 1.7$ nN/µm (see Chapter 2). Evidently, the variance in the parameter values is in part due to the natural variations across the cell population, and in part to possible statistical fluctuations in the experiments. Further insight about the distribution of material parameters can be obtained in the future by combining our model with experiments of cells adhering to micropatterned substrates, which impose reproducible cell shapes [58]. Finally, we note that some of the smaller cellular arcs, such as those in the bottom left corner of Figure 3.3, cannot be approximated by the same ellipse as the longer arcs. This may be due to local fluctuations in the density and orientation of stress fibers at the small scale or to other effects that are not captured by our model. For a description of the selection of the fitted arcs and of the endpoints of the arcs, see Section 2.5. For more experimental data on the elliptical fits, see Figure 2.8.

### 3.2.2 Curvature

One of the most striking consequences of the elliptical shape of the cellular arcs is that the local curvature is no longer constant, consistent with experimental observations on epithelioid and fibroblastoid cells in Figure 2.6a. This can be calculated from Eq. (3.6) in the form:

$$\kappa = -\frac{1}{\gamma b}\left(\frac{1+\gamma\,\tan^2\theta}{1+\tan^2\theta}\right)^{\frac{3}{2}}\,, \tag{3.7}$$

with $b = \lambda_{\rm min}/\sigma$ the major semi-axis of the ellipse and with the negative sign indicating that the arcs are curved inwards. A cellular arc thus attains its maximal (minimal) absolute curvature where $\theta = 0$ ($\theta = \pi/2$) and the stress fibers are parallel (perpendicular)

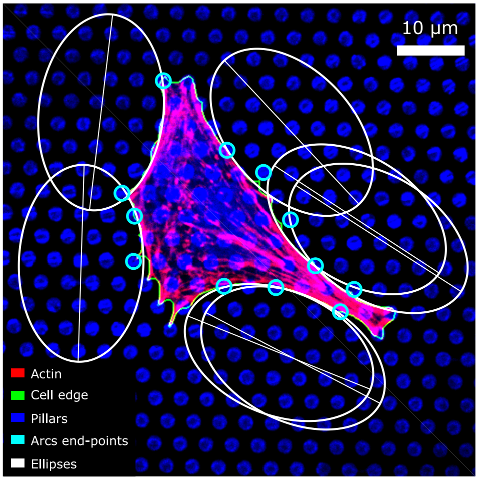

**Figure 3.3.** A fibroblastoid cell with an anisotropic actin cytoskeleton on a microfabricated elastomeric pillar array (same cell as in Figure 3.1A), with a unique ellipse (white) fitted to its arcs of sufficient length (see Section 2.5). The actin, cell edge, and micropillar tops are in the red, green, and blue channels respectively. The endpoints of the arcs (cyan) are identified based on the forces that the cell exerts on the pillars (Section 2.5). Scale bar is 10 μm.

to the arc tangent vector, namely

$$\kappa_{\text{min}} = \kappa\left(\theta = \frac{\pi}{2}\right) = -\frac{\sqrt{\gamma}}{b}\,, \tag{3.8a}$$

$$\kappa_{\text{max}} = \kappa\left(\theta = 0\right) = -\frac{1}{\gamma b}\,. \tag{3.8b}$$

Consistent with experimental evidence, the radius of curvature of arcs perpendicular to stress fibers is smaller than the radius of curvature of arcs parallel to the stress fiber direction. Thus, regions of the cell edge having higher and lower local curvature correspond to different portions of the same ellipse, depending on the relative orientation of the local tangent vector and the stress fibers. For a more detailed comparison between theory and experiment, see Chapter 2.

### 3.2.3 Traction forces

With the expressions for shape of the cellular arcs [Eq. (3.6)] and cortical tension [Eq. (3.5)] in hand, we now calculate the traction forces exerted by the cell via the focal adhesions positioned at the end-points of a given cellular arc (Figure 3.2). Calling these $\boldsymbol{F}_0$ and $\boldsymbol{F}_1$ and recalling that the cell edge is oriented counter-clockwise, we have $\boldsymbol{F}_0 = -\lambda(\theta_0)\boldsymbol{T}(\theta_0)$ and $\boldsymbol{F}_1 = \lambda(\theta_1)\boldsymbol{T}(\theta_1)$, where $\theta_0$ and $\theta_1$ are the turning angles at the end-points of the arc. For practical applications, it is often convenient to express the position of the adhesion sites in terms of their relative distance $\boldsymbol{d} = d(\cos\phi, \sin\phi)$ (Figure 3.2). This yields

$$\boldsymbol{F}_0 = \lambda_{\min}\left[-\left(\frac{d}{2b}\sin\phi + \frac{\rho}{b}\cos\phi\right)\boldsymbol{n}^{\perp} + \left(-\frac{1}{\gamma}\frac{d}{2b}\cos\phi + \frac{\rho}{b}\sin\phi\right)\boldsymbol{n}\right], \tag{3.9a}$$

$$\boldsymbol{F}_1 = \lambda_{\min}\left[-\left(\frac{d}{2b}\sin\phi - \frac{\rho}{b}\cos\phi\right)\boldsymbol{n}^{\perp} + \left(-\frac{1}{\gamma}\frac{d}{2b}\cos\phi - \frac{\rho}{b}\sin\phi\right)\boldsymbol{n}\right], \tag{3.9b}$$

where the length scale $\rho$ is defined as

$$\rho = \sqrt{b^2\left(\frac{1+\tan^2\phi}{1+\gamma\tan^2\phi}\right) - \frac{1}{\gamma}\left(\frac{d}{2}\right)^2}\,. \tag{3.10}$$

The total traction force exerted by the cell can be calculated by summing the two forces associated with the arcs joining at a given adhesion site, while taking into account that the the orientation $\boldsymbol{n}$ of the stress fibers is generally different from arc to arc.

Another interesting quantity is obtained by adding the forces $\boldsymbol{F}_0$ and $\boldsymbol{F}_1$ from the same arc. Although these two forces act on two different adhesion sites, their sum represents the total net force that a single cellular arc exerts on the substrate. This is given by

$$\begin{aligned}\boldsymbol{F}_0 + \boldsymbol{F}_1 &= -d\sigma\sin\phi\,\boldsymbol{n}^{\perp} - d(\sigma+\alpha)\cos\phi\,\boldsymbol{n}\ ,\\ &= -\left(\sigma\hat{\boldsymbol{I}} + \alpha\,\boldsymbol{n}\boldsymbol{n}\right)\cdot\boldsymbol{d}^{\perp}\ ,\end{aligned} \tag{3.11}$$

where $\boldsymbol{d}^{\perp} = d(-\sin\phi, \cos\phi)$ (Figure 3.2). Eq. (3.11) presents the force resulting from the integrated contractile bulk stress [see Eq. (3.1)], which is independent of the line tension $\lambda_{\min}$ but scales linearly with the distance between adhesions. This implies that the total traction increases with the cell size, consistent with earlier contour models [64, 65] and various experimental observations [195–197]. Because the cell size is expected to be larger on stiffer substrates, as these stretch only slightly in response to the cell contraction, the total amount of traction also increases with substrate stiffness.

### 3.2.4 Mechanical invariants

We conclude this section by highlighting two mechanical invariants, local quantities that are constant along a cellular arc, thus showing the intimate relation between the geometry of the cell and the mechanical forces it exerts on the environment. From Eqs. (3.9) we find

$$F_{\perp}^2 + \gamma F_{\parallel}^2 = \text{const.}, \tag{3.12}$$

where $F_{\parallel}$ and $F_{\perp}$ are the components of the force, parallel and perpendicular to $\boldsymbol{n}$, at any point along a same cellular arc. Furthermore, by inspection of Eqs. (3.7) and (3.5) we observe that

$$\lambda^3\kappa = -\lambda_{\min}^2(\alpha+\sigma) = \text{const}\ . \tag{3.13}$$

From this, we find that the normal component of the cortical force, $\lambda\kappa$ [see Eq. (3.4)], is then given by

$$\lambda\kappa = -\left(\frac{\lambda_{\min}}{\lambda}\right)^2 (\alpha + \sigma) \ . \tag{3.14}$$

This relation is an analog of the Young-Laplace law for our anisotropic system. In the isotropic limit, $\alpha = 0$ and $\lambda_{\min} = \lambda$, thus we recover the standard force-balance expression $\lambda\kappa = -\sigma$. Eq. (3.14) shows that the normal force $\lambda\kappa$ decreases with increasing line tension $\lambda$, because an increase in line tension is accompanied by an even stronger decrease in the curvature $\kappa$.

## 3.3 Interplay between orientation of the cytoskeleton and cellular shape

In this section we generalize our approach by allowing the orientation of the stress fibers to vary along individual cellular arcs. This is achieved by combining the contour model for the cell shape, reviewed in Section 3.2, with a continuous phenomenological model of the actin cytoskeleton, rooted into the hydrodynamics of nematic liquid crystals [91]. This setting can account for the mechanical feedback between the orientation of the stress fibers and the concave cellular shape and allows us to predict both these features starting from the positions of the adhesion sites along the cell edge alone. Although experimental studies have shown the biophysical importance of substrate adhesions in the cell interior [56, 198, 199], here we only describe a limited number of discrete adhesion sites at the cell periphery, where the largest traction stresses are found [200–202]. A treatment of the dynamics of focal adhesions is beyond the scope of this chapter and can be found elsewhere, e.g., in Refs. [136, 189].

As mentioned in Section 3.1, experimental observations, by us (Chapter 2) and others [85–88], have indicated that stress fibers tend to align with each other and with the cell's longitudinal direction. As we discussed, several cellular processes might contribute to these alignment mechanisms, such as mechanical cell-matrix feedback [52, 76, 179–181], motor-mediated alignment [182–185], steric interactions [186–188], stress fiber formation and dissociation [75–77, 79], focal adhesion dynamics [77, 79, 136, 189], the geometry of actin nucleation sites [190, 191], or membrane-mediated alignment [192], but it is presently unclear which combination of mechanisms is ultimately responsible for the orientational correlation observed in experiments. Our phenomenological description of the actin cytoskeleton allows us to focus on the *interplay* between cellular shape and the orientation of the stress fibers, without the loss of generality that would inevitably result from selecting a specific alignment mechanism among those listed above.

This phenomenological description necessitates a number of simplifying assumptions that can be addressed in future work. First, we again assume the typical timescale associated with the equilibration of the forces (hence the reorientation of the actin filaments) to be much shorter than that associated with cell motility (see also Section 3.2.1).

Consequently, experiments on migrating cells [203] or cells subject to cyclic mechanical loading [204, 205] are outside of the scope of the present chapter. Moreover, our model does not take into account dynamical effects, such as actin filament turnover and the viscoelasticity of stress fibers [206, 207]. Additionally, as we did with in Section 3.2, we restrict our model to effectively two-dimensional cells. This is not unreasonable, as cells adhering to a stiff surface have a largely flat shape [48], but it does imply that our model cannot capture three-dimensional stress fiber structures around the nucleus, such as the actin cap [208], or distinguish between the orientations of apical and basal stress fibers [209]. Third, we do not model signaling pathways, thus our approach cannot account for variations of myosin activity (thus contractile stress) in response to the substrate stiffness and other mechanical cues, but, as already discussed in Section 3.2, it can describe the modulation of traction forces originating from the mechanical coupling between the cell and the substrate [195–198] (see Section 3.2.3). Fourth, our model describes the overall cell-scale structure of the actin cytoskeleton and does not include local effects such as the interactions of individual stress fibers with focal adhesions in the cell interior [56, 198, 199]. Finally, we assume a uniform density of actin. Therefore our model does not account for local density variations that have been found experimentally on several cell types, where stress fibers occur most prominently along concave cell edges [176, 196, 210, 211].

### 3.3.1 Model of the actin cytoskeleton

The actin cytoskeleton is modeled as a nematic liquid crystal confined within the cellular contour. This is conveniently represented in terms of the two-dimensional nematic tensor (see, e.g., Ref. [91]):

$$Q_{ij} = S\left(n_i n_j - \frac{1}{2}\,\delta_{ij}\right)\,, \tag{3.15}$$

where $\delta_{ij}$ is the Kronecker delta and $S = \sqrt{2\,\mathrm{tr}\,\hat{\boldsymbol{Q}}^2}$ is the so called nematic order parameter, measuring the amount of local nematic order. Here, $0 \leq S \leq 1$, where $S = 1$ represents perfect nematic order and $S = 0$ represents randomly oriented stress fibers. In the standard $\{\hat{\boldsymbol{x}}, \hat{\boldsymbol{y}}\}$ Cartesian basis, Eq. (3.15) yields

$$\hat{\boldsymbol{Q}} = \begin{bmatrix} Q_{xx} & Q_{xy} \\ Q_{xy} & -Q_{xx} \end{bmatrix} = \frac{S}{2}\begin{bmatrix} \cos 2\theta_{\mathrm{SF}} & \sin 2\theta_{\mathrm{SF}} \\ \sin 2\theta_{\mathrm{SF}} & -\cos 2\theta_{\mathrm{SF}} \end{bmatrix}. \tag{3.16}$$

The preferred orientation of stress fibers within the cell is captured by the Landau-de Gennes free-energy $F_{\mathrm{cyto}}$ [91]:

$$\begin{aligned} F_{\mathrm{cyto}} = \frac{1}{2}\,K \int \mathrm{d}A\, \left[|\nabla\hat{\boldsymbol{Q}}|^2 + \frac{1}{\delta^2}\,\mathrm{tr}\,\hat{\boldsymbol{Q}}^2(\mathrm{tr}\,\hat{\boldsymbol{Q}}^2 - 1)\right] \\ + \frac{1}{2}\,W \oint \mathrm{d}s\,\mathrm{tr}\left[(\hat{\boldsymbol{Q}} - \hat{\boldsymbol{Q}}_0)^2\right]\,. \end{aligned} \tag{3.17}$$

The first integral in Eq. (3.17) corresponds to a standard mean-field free-energy, favoring perfect nematic order (i.e., $S = 1$), while penalizing gradients in the orientation of the stress fibers and their local alignment. For simplicity, we neglect the dependence on the nematic order parameter on the density of actin (here assumed to be uniform). The quantity $K$ is known as Frank's elastic constant and, in this context, expresses the stiffness of the actin cytoskeleton with respect to both splay and bending deformations, on a scale larger than that of the individual actin filaments. The length scale $\delta$ sets the size of the boundary layer in regions where the order parameter drops to zero to compensate a strong distortion of the nematic director $\boldsymbol{n}$, such as in proximity of topological defects. Hence, $\delta$ measures the typical size of regions where stress fibers are randomly oriented.

The second integral, which is extended over the cell contour, is the Nobili-Durand anchoring energy [95] and determines the orientation of the stress fibers along the edge of the cell, with the tensor $\hat{\boldsymbol{Q}}_0$ representing their preferential orientation. Experimental evidence form our (Figures 3.3 and 2.10) and other's work (e.g., Refs. [85–88]), suggests that, in highly anisotropic cells, peripheral stress fibers are preferentially parallel to the cell edge. The same trend is recovered in experiments with purified actin bundles confined in microchambers [186, 187]. In the language of Landau-de Gennes theory, this effect can be straightforwardly reproduced by setting

$$Q_{0,ij} = S_0 \left( T_i T_j - \frac{1}{2}\, \delta_{ij} \right) , \tag{3.18}$$

with $\boldsymbol{T}$ the tangent unit vector of the cell edge. Along concave edges the local orientation of stress fibers tends to be well defined [176, 210], so we further assume a large nematic order along the contour: $S_0 = 1$. The phenomenological constant $W > 0$ measures the strength of this parallel anchoring, hence it is a measure for the preference of stress fibers to align parallel to the cell boundary. Although stress fiber formation is affected by the pre-existing cytoskeletal tension [51, 53], here we treat our bulk parameters $K$, $W$, and $\delta$ independently from $\alpha_0$, $\sigma$, and $\lambda_{\min}$ which model the tension at the cell boundary.

In order to generate stationary configurations of the actin cytoskeleton, we numerically integrate the following overdamped equation:

$$\partial_t Q_{ij} = -\frac{1}{\xi_r} \frac{\delta F_{\text{cyto}}}{\delta Q_{ij}} , \tag{3.19}$$

where $\xi_r$ is a rotational drag coefficient, controlling the relaxation rate of the system, but without affecting the steady-state configurations. Eq. (3.19) is numerically integrated with Neumann boundary conditions:

$$K \boldsymbol{N} \cdot \nabla Q_{ij} - 2W \left( Q_{ij} - Q_{0,ij} \right) = 0 . \tag{3.20}$$

This guarantees the steady-state configurations to be energy-minimizing, but without imposing a specific non-physical orientation of the stress fibers along the contour of the cell.

### 3.3.2 The dynamics of the cell contour

The relaxational dynamics of the cell contour are governed, in our model, by Eq. (3.3), which is now lifted from the assumption that the orientation $\boldsymbol{n}$ of the stress fibers is uniform along individual cellular arcs. Furthermore, the contractile stress given by Eq. (3.2) can now be generalized as:

$$\begin{aligned}\hat{\boldsymbol{\Sigma}}_{\mathrm{out}} - \hat{\boldsymbol{\Sigma}}_{\mathrm{in}} &= \sigma \hat{\boldsymbol{I}} + \alpha_0 S \boldsymbol{n}\boldsymbol{n} \\ &= \left(\sigma + \frac{1}{2}\,\alpha_0 S\right) \hat{\boldsymbol{I}} + \alpha_0 \hat{\boldsymbol{Q}}\ , \end{aligned} \tag{3.21}$$

with $\alpha_0$ a constant independent on the local order parameter. Comparing Eqs. (3.2) and (3.21) yields $\alpha = \alpha_0 S$, thus the formalism introduced in this section allows us to explicitly account for the effect of the local orientational order of the stress fibers on the amount of contractile stress that they exert.

Next, we decompose Eq. (3.3) along the normal and tangent directions of the cell contour. Since the cells considered here are pinned at the adhesion sites, which we again assume to be rigid, and the density of actin along the cell contour is assumed to be constant, tangential motion is suppressed, i.e., $\boldsymbol{T} \cdot \partial_t \boldsymbol{r} = 0$. Together with Eq. (3.21) this yields:

$$0 = \partial_s \lambda\ + \alpha_0\, \boldsymbol{T} \cdot \hat{\boldsymbol{Q}} \cdot \boldsymbol{N}\ , \tag{3.22a}$$

$$\xi_t \boldsymbol{N} \cdot \partial_t \boldsymbol{r} = \lambda \kappa + \sigma\ + \frac{1}{2}\,\alpha_0 S + \alpha_0\, \boldsymbol{N} \cdot \hat{\boldsymbol{Q}} \cdot \boldsymbol{N}\ . \tag{3.22b}$$

Eq. (3.22a) describes then the relaxation of tension $\lambda$ within the cell edge, given its shape, whereas Eq. (3.22b) describes the relaxation of the cellular shape itself. The variations in the cortical tension might result from a regulation of the myosin activity or simply form a passive response of the cortical actin to the tangential stresses.

Integrating Eq. (3.22a) then yields the cortical tension along an arc:

$$\lambda(s) = \lambda(0) - \alpha_0 \int_0^s \mathrm{d}s'\, \boldsymbol{T} \cdot \hat{\boldsymbol{Q}} \cdot \boldsymbol{N}\ , \tag{3.23}$$

where $\hat{\boldsymbol{Q}} = \hat{\boldsymbol{Q}}(s)$ varies, in general, along an individual cellular arc. The integration constant $\lambda(0)$, which represents the cortical tension at one of the adhesion sites, is related to the minimal tension $\lambda_{\mathrm{min}}$ withstood by the cortical actin which we used, in Section 3.2, as material parameter of the problem. In practice, we first calculate $\lambda$ over an entire arc using a arbitrary guess for $\lambda(0)$. Then, we apply a uniform shift in such a way that the minimal $\lambda$ value coincides with $\lambda_{\mathrm{min}}$.

Combining the dynamics of the cell contour and that of the cell bulk, we obtain the following coupled differential equations:

$$\partial_t \boldsymbol{r} = \frac{1}{\xi_t}\left[\lambda\kappa + \sigma + \frac{1}{2}\,\alpha_0 S + \alpha_0\,\boldsymbol{N}\cdot\hat{\boldsymbol{Q}}\cdot\boldsymbol{N}\right]\boldsymbol{N}\,, \tag{3.24a}$$

$$\partial_t \hat{\boldsymbol{Q}} = \frac{K}{\xi_r}\left[\nabla^2\hat{\boldsymbol{Q}} - \frac{2}{\delta^2}\,(S^2-1)\hat{\boldsymbol{Q}}\right]\,. \tag{3.24b}$$

These are complemented by the condition that $\boldsymbol{r}$ is fixed in a number of specific adhesion sites, the boundary condition given by Eq. (3.20) for the nematic tensor $\hat{\boldsymbol{Q}}$ and the requirement that $\min_s \lambda(s) = \lambda_{\text{min}}$ on each arc.

## 3.4 Numerical results

Eqs. (3.24) are numerically solved using a finite difference integration scheme with moving boundary. As we detail in Section 3.6.2 in the Appendix, the time-integration is performed iteratively using the forward Euler algorithm by alternating updates of the cell contour and of the bulk nematic tensor. This process is iterated until both the cell shape and the orientation reach a steady state.

To highlight the physical meaning of our numerical results, we introduce two dimensionless numbers, namely the *contractility* number, *Co*, and the *anchoring* number, *An*. *Co* is defined as the ratio between the typical distance between two adhesion sites $d$ and the major semi-axis of the ellipse approximating the corresponding cellular arc ($b = \lambda_{\text{min}}/\sigma$, see Section 3.2.1):

$$Co = \frac{\sigma d}{\lambda_{\text{min}}}\,, \tag{3.25}$$

and provides a dimensionless measure of the cell contraction (thus of the cell average curvature). The anchoring number, on the other hand, is defined as the ratio between a typical length scale $R$ in which the internal cell structure is confined (not necessarily equal to the distance $d$) and the length scale $K/W$, which sets the size of the boundary layer where $\hat{\boldsymbol{Q}}$ crosses over from its bulk configuration to $\hat{\boldsymbol{Q}}_0$:

$$An = \frac{WR}{K}\,. \tag{3.26}$$

This number expresses the ratio between the anchoring energy, which scales as $WR$ [i.e., last term in Eq. (3.17)], and the bulk energy, which scales as $K$, thus independently on cell size [i.e., first term in Eq. (3.17)]. Hence, *An* represents the competition between boundary alignment (with strength $W$) and bulk alignment (strength $K$) within the length scale of the cell $R$. For *An* $\ll 1$, bulk elasticity dominates over boundary anchoring and the orientation of the stress fibers in the bulk propagates into the boundary, resulting into a uniform orientation throughout the cell and large deviations from parallel anchoring in proximity of the edge. Conversely, for *An* $\gg 1$, boundary anchoring dominates bulk elasticity and the orientation of the stress fibers along the cell edge propagates into the bulk, leading to non-uniform alignment in the interior of the cell.

To get insight on the effect of the combinations of these dimensionless parameters on the spatial organization of the cell, we first consider the simple case in which the adhesion sites are located at the corners of squares and rectangles (Section 3.4.1). In Section 3.4.2 we consider more realistic adhesion geometries and compare our numerical results with experimental observations on highly anisotropic cells adhering to a small number of discrete adhesions.

### 3.4.1 Rectangular cells

Figure 3.4 shows the possible configurations of a model cell whose adhesion sites are located at the vertices of a square, obtained upon varying *An* and *Co*, while keeping $\gamma = \sigma/(\sigma + \alpha_0)$ constant. Figure 3.10 in the Appendix shows the effect of varying the ratio between $\sigma$ and $\alpha_0$ for this model cell. The thick black line represents the cell boundary, the black lines in the interior of the cells represent the orientation field $\boldsymbol{n}$ of the stress fibers and the background color indicates the local nematic order parameter $S$, or equivalently, the magnitude of the maximal principal stress $\sigma_{\max} = \sigma + \alpha_0 S$.

As expected, for low *Co* values (left column), cells with large *An* exhibit better parallel anchoring than cells with small *An* values, but lower nematic order parameter $S$ in the cell interior (spatial average of $S$ decreases from 1.0 at the bottom left to 0.80 at the top left, see Figure 3.4). Interestingly, the alignment of stress fibers with the walls in the configuration with large *An* value (top left) resembles the configurations found by Deshpande *et al.* [75, 76], who specifically accounted for the assembly and dissociation dynamics of the stress fibers. More strikingly, the structure reported in the top left of Figure 3.4 appears very similar to those found in experiments of dense suspensions of pure actin in cell-sized square microchambers [186, 187], simulations of hard rods in quasi-2D confinement [186], and results based on Frank elasticity [212], even though these systems are very different from living cells. As is the case in our simulations, in these studies the tendency of the filaments to align along the square edges competes with that of aligning along the diagonal.

For large *Co* values (right column of Figure 3.4), the cell deviates from the square shape. Interestingly, although the contractile stresses ($\sigma$ and $\alpha_0$) do not directly affect the configuration of the cytoskeleton, they do it indirectly by influencing the shape of the cell. This results into an intricate interplay between shape and orientation, controlled by the numbers *An* and *Co*. In particular, for constant *Co*, i.e., for fixed stress fiber contractility, increasing *An* leads to higher tangential alignment of the stress fibers with the cell edge, thus increasing *An* decreases the contractile force experienced by the cell edge, which is proportional to $(\boldsymbol{n} \cdot \boldsymbol{N})^2$ [Eq. (3.24a)]. Conversely, for constant *An*, increasing *Co* leads to a more concave cell shape which forces the stress fibers to bend more. Consequently, the average order parameter in the cell decreases with increasing *Co* (see Figure 3.4).

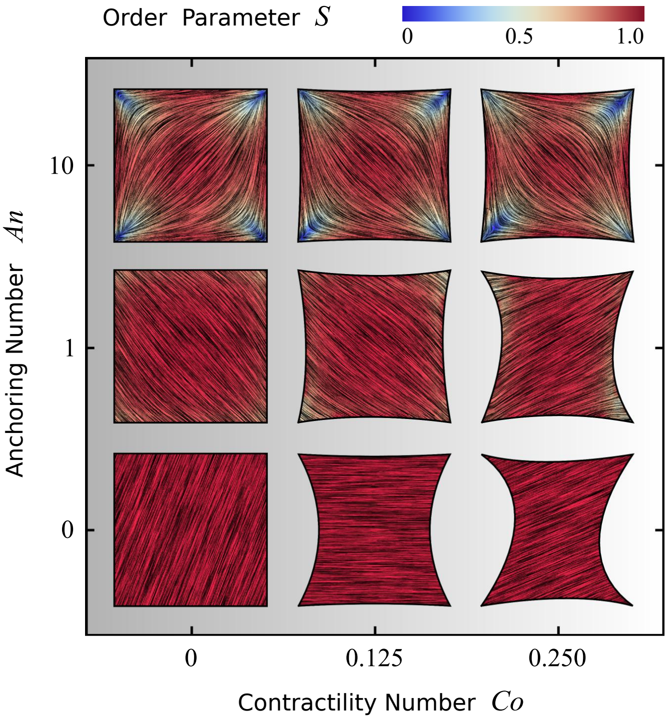

**Figure 3.4.** Configurations of cells whose adhesion sites are located at the vertices of a square. The thick black line represents the cell boundary, the black lines in the interior of the cells represent the orientation field $\boldsymbol{n} = (\cos\theta_{\mathrm{SF}}, \sin\theta_{\mathrm{SF}})$ of the stress fibers and the background color indicates the local nematic order parameter $S$. The spatial averages of the order parameter $S$ are given, from left to right, by: $0.80; 0.80; 0.77$ (top row), $0.94; 0.92; 0.92$ (middle row), and $1.0; 1.0; 1.0$ (bottom row). The vertical axis corresponds to the anchoring number *An* $= WR/K$ and the horizontal axis to the contractility number *Co* $= \sigma d/\lambda_{\mathrm{min}}$. The cells shown correspond to values of *An* $= 0, 1, 10$ and *Co* $= 0, 0.125, 0.25$, where we take both $d$ and $R$ equal to the length of the square side. The ratios $\sigma/(\sigma+\alpha_0) = 1/9$, $\lambda_{\mathrm{min}}\Delta t/(\xi_t R^2) = 2.8\cdot 10^{-6}$, and $K\Delta t/(\xi_r R^2) = 2.8\cdot 10^{-6}$, and the parameters $\delta = 0.15R$, $N_{\mathrm{arc}} = 20$, and $\Delta x = R/19$ are the same for all cells. The number of iterations is $5.5\cdot 10^5$. For definitions of $\Delta t$, $\Delta x$, and $N_{\mathrm{arc}}$, see Section 3.6.2 in the Appendix.

Finally, we note that all configurations in Figure 3.4 display a broken rotational and/or chiral symmetry. For *An* $= 0$ the stress fibers are uniformly oriented, but any direction is equally likely. For non-zero *An*, the stress fibers tend to align along either of the diagonals (with the same probability) to reduce the amount of distortion. Upon increasing *Co*, chirality emerges in the cytoskeleton and in the cell contour (see, e.g., the cell in the middle of the right column in Figure 3.4). In light of the recent interest in chiral symmetry breaking in single cells [213] and in multicellular environments [214], we find it particularly interesting that chiral symmetry breaking can originate from the natural interplay between the orientation of the stress fibers and the shape of the cell.

To conclude this section, we focus on four-sided cells whose adhesion sites are located at the vertices of a rectangle and explore the effect of the cell aspect ratio (i.e., height/width). Figure 3.5 displays three configurations having fixed maximal width and aspect ratio varying from 1 to 2. Figure 3.11 in the Appendix shows the effect of increasing the aspect ratio while keeping instead the area of the rectangle fixed. Upon increasing the cell aspect ratio, the mean orientation of the stress fibers switches from the diagonal (aspect ratio 1) to longitudinal (aspect ratio 2), along with an increase in the order parameter in the cell bulk, as can be seen in Figure 3.5 by the slightly more red-shifted cell interior (spatial average of $S$ increases from 0.92 to 0.96). This behavior originates from the competition between bulk and boundary effects. Whereas the bulk energy favors longitudinal alignment, as this reduces the amount of bending of the nematic director, the anchoring energy favors alignment along all four edges alike, thus favoring highly bent configurations at the expense of the bulk elastic energy. When the aspect ratio increases, the bending energy of the bulk in the diagonal configuration increases, whereas the longitudinal state only pays the anchoring energy at the short edges, hence independently on the aspect ratio. Therefore, elongating the cell causes the stress fibers to transition from tangential to longitudinal alignment, with a consequent increase of the nematic order parameter. Interestingly, similar observations were made in experiments on pure actin filaments in cell-sized microchambers [186, 187]. More importantly, the longitudinal orientation of the stress fibers in cells of aspect ratio 2 is consistent with several experimental studies of cells adhering on adhesive stripes and elongated adhesive micropatterns [87–89, 196, 211]. Figures 3.12 and 3.13 in the Appendix show the effect of the anchoring number *An*, the contractility number *Co*, and the ratio between $\sigma$ and $\alpha_0$ on a cell with aspect ratio 2.

### 3.4.2 Cells on micropillar arrays

In order to validate our model experimentally, we compare our numerical results with experiments on fibroblastoid and epithelioid cells [173] plated on stiff micropillar arrays [55–57]. The cells are imaged using spinning disk confocal microscopy (see, e.g., Figure 3.6A) and the images are then processed in order to detect the orientation of the stress fibers. Upon coarse-graining the local gradients of the image intensity, we reconstruct both the nematic director $\boldsymbol{n}$ (black lines, representing the orientation of the stress fibers) and order parameter $S$ (background color, representing the degree of alignment), as visualized in Figure 3.6B. Because of this coarse-graining, which takes place on a length scale comparable to the radius of the micropillars ($\sim 1$ µm) (see Section 2.5), local variations in orientations and densities of stress fibers are smoothened out and the influence of individual micropillars under the cell interior, as visible in Figure 3.6A, is no longer visible in Figure 3.6B. Regions in the cell with low actin expression, that do not show a clear structural orientation, have a low order parameter $S$. Hence, in the experimental data, a low $S$ value might result from either a low local density of stress fibers, or from a

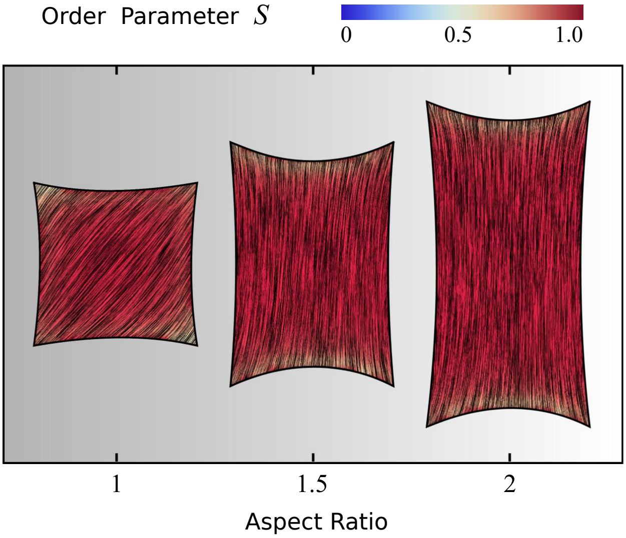

**Figure 3.5.** Effect of the aspect ratio of the cell, ranging from 1 to 2, on cytoskeletal organization for cells whose four adhesion sites are located at the vertices of a rectangle. The thick black line represents the cell boundary, the black lines in the interior of the cells represent the orientation field $\boldsymbol{n} = (\cos\theta_{\mathrm{SF}}, \sin\theta_{\mathrm{SF}})$ of the stress fibers and the background color indicates the local nematic order parameter $S$. The spatial averages of the order parameter $S$ are given, from left to right, by: $0.92; 0.95; 0.96$. The simulations shown are performed with $\mathit{An} = WR/K = 1$ where $R$ is equal to the short side of the rectangle, and $\mathit{Co} = \sigma d/\lambda_{\min}$ equal to 0.125, 0.1875, and 0.25 respectively, where $d$ is equal to the long side of the rectangle. The ratios $\sigma/(\sigma + \alpha_0) = 1/9$, $\lambda_{\min}\Delta t/(\xi_t R^2) = 2.8 \cdot 10^{-6}$, and $K\Delta t/(\xi_r R^2) = 2.8 \cdot 10^{-6}$, and the parameters $\delta = 0.15R$ and $\Delta x = R/19$ are the same for all cells. $N_{\mathrm{arc}} = 20, 30, 40$ from left to right and the number of iterations is $5.5 \cdot 10^5$. For definitions of $\Delta t$, $\Delta x$, and $N_{\mathrm{arc}}$, see Section 3.6.2 in the Appendix.

high density of randomly oriented stress fibers. See Section 3.6.3 for more detail on the construction of the nematic director and order parameter from experimental data.

Consistent with our results on rectangular cells (Figure 3.5), the stress fibers align parallel to the cell's longitudinal direction and perpendicularly to the cell's shorter edges. Furthermore, the nematic order parameter is close to unity in proximity of the cell contour, indicating strong orientational order near the cell edge, but drops in the interior. This behavior is in part originating from the lower density of stress fibers around the center of mass of the cell, and in part from the presence of $\pm 1/2$ nematic disclinations away from the cell edge. These topological defects naturally arise from the tangential orientation along the boundary. Albeit not uniform throughout the whole cell contour, thus not sufficient to impose hard topological constraints on the configuration of the director in the bulk (i.e., Poincaré-Hopf theorem), this forces a non-zero winding of the stress fibers, which in turn is accommodated via the formation of one or more disclinations. As a consequence of the concave shape of the cell boundary, these defects have most commonly strength $-1/2$. The average order parameter in the cell is $S = 0.54$.

To compare our theoretical and experimental results, we extract the locations of the adhesion sites from the experimental data by selecting micropillars that are close to the cell edge and experience a significant force (for details, see Section 2.5), and use them as input parameters for the simulations. In Figures 3.6C-E we show results of simulations of the cell in Figures 3.6A,B for increasing *An* values, thus decreasing magnitude of the length scale $K/W$. Here, we take the length scale $R = 23.6$ µm to be the square root of the cell area and we use constant values for the ratios $\lambda_{\min}/\sigma = 14.7$ µm and $\sigma/(\sigma+\alpha_0) = 0.40$ as found by an analysis of the elliptical shape of this cell (see Chapter 2). Figure 3.6C shows the results of a simulation where bulk alignment dominates over boundary alignment (*An* = 0.33, $K/W = 71$ µm), resulting in an approximately uniform cytoskeleton oriented along the cell's longitudinal direction. The nematic order parameter is also approximatively uniform and close to unity (spatial average of the order parameter is $S = 0.85$). For larger *An* values (Figure 3.6D, *An* = 1.7 and $K/W = 14$ µm), anchoring effects become more prominent, resulting in distortions of the bulk nematic director, a lower nematic order parameter (spatial average $S = 0.60$), and the emergence of a $-1/2$ disclination in the bottom left side of the cell. Upon further increasing *An* (Figure 3.6E, *An* = 8.0 and $K/W = 2.9$ µm), the $-1/2$ topological defect moves toward the interior, as a consequence of the increased nematic order along the boundary. This results in a decrease in nematic order parameter in the bulk of the cell, consistent with our experimental data. The spatial average is $S = 0.56$, close to the experimental average of $S = 0.54$.

A qualitative comparison between our in *vitro* (Figure 3.6B) and *in silico* cells (Figure 3.6E) highlights a number of striking similarities, such as the overall structure of the nematic director, the large value of the order parameter along the cell edge and in the thin neck at the bottom-right of the cell and the occurrence of a $-1/2$ disclination on the bottom-left side. The main difference is the order parameter away from the cell edges, which is lower in the experimental data than in the numerical prediction. The lower order parameter also results in an additional $-1/2$ disclination at the top-left of the cell in Figure 3.6B which is absent in Figure 3.6E. We hypothesize that this discrepancy is caused by a lower actin density in the cell interior, as observed before in many other experimental studies [176, 196, 210, 211]. As a consequence of the actin depletion, the nematic order parameter can decrease, and potentially vanish, in a way that cannot be described by our model, where the density of the actin fibers is, by contrast, assumed to be uniform across the cell.

In order to make this comparison quantitative and infer the value of the phenomenological parameters introduced in this section, we have further analyzed the residual function

$$\Delta^2 = \frac{1}{N}\sum_{i=1}^{N}\frac{1}{2}\,\mathrm{tr}\left[(\hat{\boldsymbol{Q}}_{\mathrm{sim},i}-\hat{\boldsymbol{Q}}_{\mathrm{exp},i})^2\right] , \tag{3.27}$$

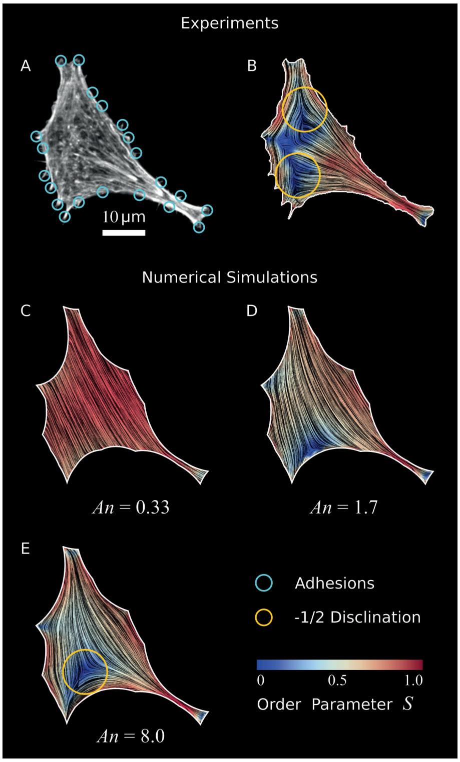

**Figure 3.6.** Validation of our model to experimental data. (A) Optical micrograph (TRITC-Phalloidin) of a fibroblastoid cell (same cell as in Figures 3.1 and 3.3). The adhesions (cyan circles) are determined by selecting micropillars that are close to the cell edge and experience a significant force (Section 2.5). (B) Experimental data of cell shape and coarse-grained cytoskeletal structure of this cell. The white line represents the cell boundary, black lines in the interior of the cells represent the orientation field $\boldsymbol{n} = (\cos\theta_{\mathrm{SF}}, \sin\theta_{\mathrm{SF}})$ of the stress fibers and the background color indicates the local nematic order parameter $S$. The spatial average of the order parameter is $S = 0.54$. (C-E) Configurations obtained from a numerical solution of Eqs. (3.24) using the adhesion sites of the experimental data (cyan circles) as input, and with various anchoring number (*An*) values. This is calculated from Eq. (3.26), with $R = 23.6$ µm the square root of the cell area. The corresponding values of the length scale $K/W$ are 71 µm (C), 14 µm (D), and 2.9 µm (E) respectively. The spatial averages of the order parameter $S$ are given by: 0.85 (C), 0.60 (D), and 0.56 (E) respectively. The values for $\lambda_{\mathrm{min}}/\sigma = 14.7$ µm and $\sigma/(\sigma + \alpha_0) = 0.40$ are found by an analysis of the elliptical shape of this cell (see Chapter 2). The ratios $\lambda_{\mathrm{min}}\Delta t/\xi_t = 1.2 \cdot 10^{-3}\mu\mathrm{m}^2$ and $K\Delta t/\xi_r = 1.2 \cdot 10^{-3}\mu\mathrm{m}^2$, and the parameters $\delta = 11$ µm, $N_{\mathrm{arc}} = 20$, and $\Delta x = 1.1$ µm are the same for figures (C-E). The number of iterations is $2.1 \cdot 10^6$. For definitions of $\Delta t$, $\Delta x$, and $N_{\mathrm{arc}}$, see Section 3.6.2 in the Appendix.

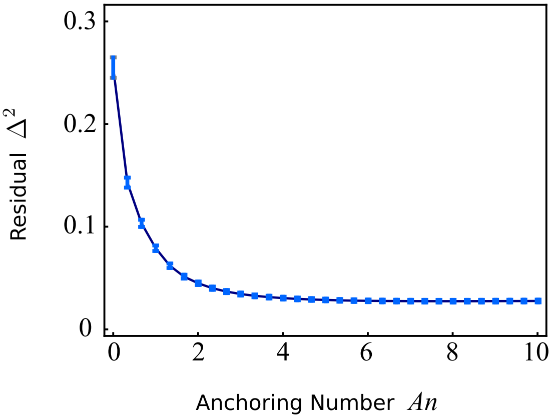

**Figure 3.7.** Residual function $\Delta^2$, defined in Eq. (3.27), as a function of the anchoring number *An* [Eq. (3.26) with $R = 23.6$ µm] for the cell displayed in Figure 3.6. The error bars display the standard deviation obtained using jackknife resampling. For large *An* values the residual flattens, indicating that the actual value of *An* becomes unimportant once the anchoring torques (with magnitude $W$), which determine the tangential alignment of the stress fibers in the cell's periphery, outcompete the bulk elastic torques (with magnitude $K$). The minimum ($\Delta^2 = 0.027$) is found for $An = 8.0$.

expressing the departure of the predicted configurations of the nematic tensor, $\hat{\boldsymbol{Q}}_{\rm sim}$, from the experimental ones, $\hat{\boldsymbol{Q}}_{\rm exp}$. The index $i$ identifies a pixel in the cell and $N$ is the total number of pixels common to both numerical and experimental configurations. By construction, $\Delta^2$ captures both differences in the nematic director $\boldsymbol{n}$ and in the order parameter $S$ [see Eq. (3.15)], and $0 \le \Delta^2 \le 1$, with 0 representing perfect agreement. Figure 3.7 shows a plot of $\Delta^2$ versus the anchoring number *An* for the cell shown in Figure 3.6. Consistent with the previous qualitative comparison, the agreement is best at large *An* values, indicating a substantial preference of the stress fibers for parallel anchoring along the cell edge. For the cell in Figure 3.6, $\Delta^2$ is minimized for $An = 8.0$ ($\Delta^2 = 0.027$), corresponding to a boundary layer $K/W = 2.9$ µm. The corresponding numerically calculated configuration is shown in Figure 3.6E. However, the flattening of $\Delta^2$ for large *An* values implies that the actual value of *An* becomes unimportant once the anchoring torques (with magnitude $W$), which determine the tangential alignment of the stress fibers in the cell's periphery, outcompete the bulk elastic torques (with magnitude $K$). Therefore, we conclude that the cell illustrated in Figure 3.6 is best described by $An \gtrsim 5$, corresponding to a boundary layer $K/W \lesssim 5$ µm. The corresponding value of $\Delta^2 = 0.027$ indicates good quantitative agreement between the experimental (Figure 3.6B) and simulated (Figure 3.6E) data, despite the difference in order parameter away from the cell edges. This quantitative agreement indicates that, although oversimplified in comparison with the complexity of living cells, our model satisfactorily describes the stationary configuration of both the nematic order parameter and the stress fibers orientation.

The same analysis presented above has been repeated for five other cells (Figure 3.8). The first column shows the raw experimental data, the second column shows the coarse-grained experimental data, and the third column shows the simulations. For these we used the values of $\lambda_{\text{min}}/\sigma$ and $\sigma/(\sigma + \alpha_0)$ obtained from a previous analysis of the cell morphology (see Chapter 2) and the *An* values found by a numerical minimization of $\Delta^2$ (see Figure 3.14 in the Appendix). Also for these cells $\Delta^2$ flattens for large *An* values, and we estimate *An* $\gtrsim$ 3 and $K/W \lesssim 7$ µm. The minima of $\Delta^2$ are given, from top to bottom, by 0.016, 0.058, 0.057, 0.034, and 0.037. This indicates reasonable quantitative agreement between experiment and simulation for all cells, even though the agreement is significantly better for the cell in Figure 3.8F than for those in Figures 3.8G and 3.8H. Similar to the cell in Figure 3.6, we observe that the main discrepancies are the order parameter in the cell interior, which is smaller in the experimental data than in the numerical results, and a number of topological defects in this low nematic order region of the experimental data that are absent in the numerical data. The cell in Figure 3.8F shows good agreement between the average order parameter in the experimental ($S = 0.54$) and numerical ($S = 0.52$) data, but for the other cells the average order parameter is overestimated by the simulations. We again attribute this discrepancy to actin density variations in the experiments that are not captured by the theory. On the other hand, we note that the overall structure of the stress fiber orientation, including the emergence of a number of $-1/2$ topological defects (see, e.g., Figures 3.8F and 3.8K), is captured well by our approach.

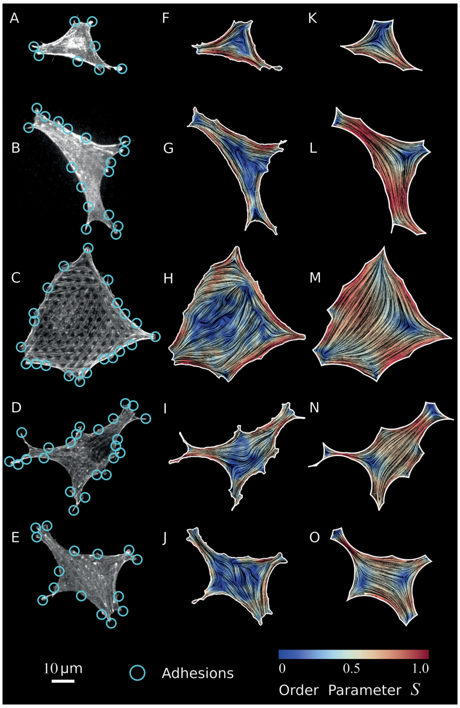

**Figure 3.8.** Comparison of experimental data on five anisotropic cells with the results of computer simulations. (A-E) Optical micrographs (TRITC-Phalloidin) of epithelioid (A,B,E) and fibroblastoid (C,D) cells on a microfabricated elastomeric pillar array. The adhesions (cyan circles) are determined by selecting micropillars that are close to the cell edge and experience a significant force (Section 2.5). (F-J) Experimental data of cell shape and coarse-grained cytoskeletal structure on a square lattice of these cells. The white line represents the cell boundary, the black lines in the interior of the cells represent the orientation field $\boldsymbol{n} = (\cos\theta_{\mathrm{SF}}, \sin\theta_{\mathrm{SF}})$ of the stress fibers and the background color indicates the local nematic order parameter $S$. The spatial averages of the order parameter $S$ are given, from top to bottom, by: $0.54; 0.44; 0.45; 0.46; 0.37$. (K-O) Simulations with the adhesion sites of the experimental data as input. The spatial averages of the order parameter $S$ are given, from top to bottom, by: $0.52; 0.68; 0.61; 0.59; 0.53$. The values for $\lambda_{\mathrm{min}}/\sigma = 12.6; 15.7; 18.0; 10.8; 13.4\,\mu\mathrm{m}$ and $\sigma/(\sigma+\alpha_0) = 0.75; 0.25; 0.46; 0.95; 0.52$ are found by an analysis of the elliptical shape of these cells (see Chapter 2). The values of *An* $= 4.4; 4.1; 19; 4.6; 4.7$, where $R = 17.3; 24.4; 39.9; 24.9; 25.3$ µm is defined as the square root of the cell area, are determined by minimizing $\Delta^2$, with the minima given by $\Delta^2 = 0.016; 0.058; 0.057; 0.034; 0.037$. These *An* values correspond to $K/W = 3.9; 5.9; 2.1; 5.4; 5.4$ µm. The ratios $\lambda_{\mathrm{min}}\Delta t/\xi_t = 1.2 \cdot 10^{-3}\mu\mathrm{m}^2$ and $K\Delta t/\xi_r = 1.2 \cdot 10^{-3}\mu\mathrm{m}^2$, and the parameters $\delta = 11$ µm, $N_{\mathrm{arc}} = 20$, and $\Delta x = 1.1$ µm are the same for all cells. The number of iterations is $2.1 \cdot 10^6$. For definitions of $\Delta t$, $\Delta x$, and $N_{\mathrm{arc}}$, see Section 3.6.2 in the Appendix.

## 3.5 Discussion and conclusions

In this chapter we investigated the spatial organization of cells adhering on a rigid substrate at a discrete number of points. Our approach is based on a contour model for the cell shape [48, 62–64, 67] coupled with a continuous phenomenological model for the actin cytoskeleton, inspired by the physics of nematic liquid crystals [91]. This approach can be carried out at various levels of complexity, offering progressively insightful results. Assuming that the orientation of the stress fibers is uniform along individual cellular arcs (but varies from arc to arc), it is possible to achieve a complete analytical description of the geometry of the cell, in which all arcs are approximated by different portions of a unique ellipse. The eccentricity of this ellipse depends on the ratio between the isotropic and directed stresses arising in the actin cytoskeleton, and the orientation of the major axis of this ellipse is parallel to the stress fibers. This parallel alignment highlights the ability of cells to employ their actin cytoskeleton to regulate their shape. The method further allows to analytically calculate the traction forces exerted by the cell on the adhesion sites and compare them with traction force microscopy data.

Lifting the assumption that the stress fibers are uniformly oriented along individual cellular arcs allows one to describe the mechanical interplay between cellular shape and the configuration of the actin cytoskeleton. Using numerical simulations and inputs from experiments on fibroblastoid and epithelioid cells plated on stiff micropillar arrays, we identified a feedback mechanism rooted in the competition between the tendency of stress fibers to align uniformly in the bulk of the cell, but tangentially with respect to the cell edge. Our approach enables us to predict both the shape of the cell and the orientation of the stress fibers and can account for the emergence of topological defects and other distinctive morphological features. The predicted stress fiber orientations are in good agreement with the experimental data and further offer an indirect way to estimate quantities that are generally precluded to direct measurement, such as the cell's internal stresses and the orientational stiffness of the actin cytoskeleton. The main discrepancy between our predictions and the experimental data is the overestimation of the nematic order parameter in the cell interior, which should be addressed in future work by explicitely accounting for actin density variations.

The success of this relatively simple approach is remarkable given the enormous complexity of the cytoskeleton and the many physical, chemical, and biological mechanisms associated with stress fiber dynamics and alignment [52, 75–77, 79, 136, 179–192]. Yet, the agreement between our theoretical and experimental results suggests that, on the scale of the whole cell, the myriad of complex mechanisms that govern the dynamics of the stress fibers in adherent cells can be effectively described in terms of simple entropic mechanisms, as those at the heart of the physics of liquid crystals. Moreover, this quantitative agreement further establishes the fact that the dynamics and alignment of stress fibers in cells cannot be understood from dynamics at the sub-cellular scale alone, and highlights the crucial role of the boundary conditions inferred by cellular shape [176, 210].

In addition, our analysis demonstrates that chiral symmetry breaking can originate from the natural interplay between the orientation of the stress fibers and the shape of the cell. A more detailed investigation of this mechanism is beyond the scope of this study, but will represent a challenge in the near future with the goal of shedding light on the fascinating examples of chiral symmetry breaking observed both in single cells [213] and tissues [214].

In the future, we plan to use our model to investigate the mechanics of cells adhering to micropatterned substrates that impose reproducible cell shapes [58], with special emphasis to the interplay between cytoskeletal anisotropy and the geometry of the adhesive patches. These systems are not new to theoretical research, but previous studies have focused on either the cytoskeleton [77] or on cell shape [69], rather than on their interaction. This will enable us to more rigorously compare our model predictions with existing experimental data on stress fiber orientation in various adhesive geometries [33, 43, 176, 210, 211], including convex shapes such as circles or stadium-shapes [196, 213, 215], see Chapter 4. Additionally, we will extend our model for the cytoskeleton (Section 3.3.1) to account for variations of myosin activity, which will allow us to study the increase of cytoskeletal tension with substrate stiffness [198] or substrate area [195–197], as well as the interactions of stress fibers with micropillars in the cell interior [56, 198, 199]. Furthermore, our framework could be extended to study the role of cytoskeletal anisotropy in cell motility, for instance by taking into account the dynamics of focal adhesions [136, 189], biochemical pathways in the actin cytoskeleton [124], actin filament turnover and the viscoelasticity of stress fibers [206, 207], or cellular protrusions and retractions [216]. Finally, our approach could be extended to computational frameworks such as vertex models, Cellular Potts Models (see Chapter 4), or phase field models [84], and could provide a starting point for exploring the role of anisotropy in multicellular environments such as tissues [111, 217–223].

## 3.6 Appendix

### 3.6.1 Derivation of Eqs. (3.5) and (3.6)

In this section, we show how Eqs. (3.5) and (3.6) in Section 3.2.1 follow from Eq. (3.4). Without loss of generality, we orient the reference frame such that the stress fibers are parallel to the $y-$axis. Thus, $\theta_{\mathrm{SF}} = \pi/2$ and $\boldsymbol{n} = \hat{\boldsymbol{y}}$ (see Figure 3.2). Since we assume $\alpha$, $\sigma$ and $\boldsymbol{n}$ to be constant along an arc, Eq. (3.4) can be expressed as a total derivative and integrated directly. This yields

$$\lambda \boldsymbol{T} + (\sigma \hat{\boldsymbol{I}} + \alpha \boldsymbol{n}\boldsymbol{n}) \cdot \boldsymbol{r}^{\perp} = \boldsymbol{C}_1 \ , \tag{3.28}$$

where $\boldsymbol{C}_1 = (C_{1x}, C_{1y})$ is an integration constant. Decomposing Eq. (3.28) into $x-$ and $y-$directions yields

$$\lambda \cos\theta = C_{1x} + \sigma y \tag{3.29a}$$

$$\lambda \sin\theta = C_{1y} - (\alpha + \sigma) x \ . \tag{3.29b}$$

Next, taking the ratio of Eqs. (3.29), using $\tan\theta = \mathrm{d}y/\mathrm{d}x$ and integrating, we obtain a general solution for the shape of the cellular arc subject to a non-vanishing isotropic stress (i.e., $\sigma \neq 0$), namely

$$\frac{1}{\gamma}(x-x_c)^2 + (y-y_c)^2 = C_2 \ , \tag{3.30}$$

where $C_2$ is another integration constant and we have set

$$x_c = \frac{C_{1y}}{\sigma+\alpha} \ , \qquad y_c = -\frac{C_{1x}}{\sigma} \ , \qquad \gamma = \frac{\sigma}{\sigma+\alpha} \ .$$

Eq. (3.30) describes an ellipse centered at $(x_c, y_c)$ and whose minor and major semi-axis are $a = \sqrt{\gamma C_2}$ and $b = \sqrt{C_2}$. Using again Eqs. (3.29), we further obtain an expression for the line tension $\lambda$ as a function of $x$ and $y$:

$$\lambda^2 = \sigma^2(y-y_c)^2 + (\sigma+\alpha)^2(x-x_c)^2 \ . \tag{3.31}$$

Using Eqs. (3.29) and (3.30), this can be also expressed as a function of the turning angle $\theta$, namely

$$\frac{\lambda^2}{\sigma^2} = C_2\,\frac{1+\tan^2\theta}{1+\gamma\tan^2\theta} \ . \tag{3.32}$$

This expression highlights the physical meaning of the integration constant $C_2$. The right-hand side of Eq. (3.32) attains its minimal value ($C_2$) where $\theta = 0$, hence when the tangent vector is perpendicular to the stress fibers (i.e., $\boldsymbol{n}\cdot\boldsymbol{T} = 0$). Thus $C_2 = \lambda_{\mathrm{min}}^2/\sigma^2$, where $\lambda_{\mathrm{min}}$ is the minimal tension withstood by the cortical actin. Substituting $C_2$ in Eq. (3.32) then yields Eq. (3.5). The maximum value of the line tension is found at $\theta = \pi/2$, where the stress fibers are parallel to the arc, and is given by $\lambda_{\mathrm{max}} = \lambda_{\mathrm{min}}/\sqrt{\gamma}$.

Substituting $C_2$ in Eq. (3.30) yields an implicit representation of the plane curve approximating individual cellular arcs, namely

$$\frac{\sigma^2}{\gamma\lambda_{\mathrm{min}}^2}\,(x-x_c)^2 + \frac{\sigma^2}{\lambda_{\mathrm{min}}^2}\,(y-y_c)^2 = 1 \ . \tag{3.33}$$

This equation describes an ellipse centered at the point $(x_c, y_c)$ and oriented along the $y-$direction, whose minor and major semi-axes are $a = \lambda_{\mathrm{min}}\sqrt{\gamma}/\sigma$ and $b = \lambda_{\mathrm{min}}/\sigma$ respectively (Figure 3.2). For arbitrary stress fiber orientation $\theta_{\mathrm{SF}}$, Eq. (3.33) can be straightforwardly generalized to find Eq. (3.6).

### 3.6.2 Numerical methods

**Integration scheme** Here we describe step by step the integration scheme that we use to generate the results shown in Figures 3.4-3.8.

**1)** Initialization.

**1a)** Define the positions of the adhesion sites. In Figures 3.4 and 3.5 these are the four corners of a square or rectangle. For the comparison to experimental data (Figures 3.6-3.8), the locations of the adhesion sites are directly determined from the experiments by detecting the pillars along the cell contour that are subject to the largest traction forces (see Section 2.5). These adhesion sites are fixed during the simulation.

**1b)** Define the initial cell boundary, consisting of cellular arcs that connect adjacent adhesion sites. Cellular arcs are parameterized in terms of a discrete number of vertices connected by straight edges in a chain-like manner. The initial cellular arcs are straight lines connecting two adhesion sites. Hence, at $t = 0$ the cell boundary is an irregular polygon.

**1c)** Define the initial cell bulk, which represents the cytoskeleton, as the region enclosed by the initial cell boundary. The bulk is discretized as a regularly spaced two-dimensional square lattice with $\hat{\boldsymbol{Q}}$ defined at every lattice point. Each lattice point initially obtains random values for the orientation $-\pi/2 \leq \theta_{\mathrm{SF}} \leq \pi/2$ and the nematic order parameter $0 \leq S \leq 1$, from which $\hat{\boldsymbol{Q}}$ is calculated using Eq. (3.16). Evidently, the initial configuration bears no resemblance to a real cell, but it reduces the risk of a possible bias in the final configuration.

**2)** Cell configuration updates. Perform the following steps for a predefined number of iterations, which is chosen such that both the cell edge and the cell bulk reach a steady-state configuration.

**2a)** Update the cell boundary for a single time step $\Delta t$ by discretizing Eqs. (3.23) and (3.24a). For details, see below.

**2b)** Update the cell bulk. First, the bulk is redefined as the region enclosed by the updated cell boundary (step 2a). In case of inclusion of a new lattice point that was previously located outside the cell, the associated $Q_{xx}$ and $Q_{xy}$ values are generated by averaging over the nearest neighbours (horizontally and vertically, not diagonally) that were inside the cell during the previous time step. In case of removal of a lattice point, the data at that lattice point are discarded. Then, $\hat{\boldsymbol{Q}}$ is updated at every lattice point for a single time step $\Delta t$ by discretizing Eq. (3.24b). For details, see below.

**3)** The final configurations are plotted in Figures 3.4-3.6 and 3.8. The cytoskeleton has been visualized with Mathematica Version 11.3 (Wolfram Research, Champaign, IL) using the line integral convolution tool. When using this tool we define $S = 1$ outside the cell, while $\theta_{\mathrm{SF}}$ is not defined outside the cell. In some cases this can lead to small artefacts in the visualisation near the cell edge.

**Cell contour update** In order to update the position of the cell contour, we first calculate the line tension $\lambda$ by discretizing Eq. (3.23) as follows:

$$\lambda_k = \lambda_0 - \alpha_0 \sum_{n=1}^{k} \Delta s_n \, \boldsymbol{T}_n \cdot \left\langle \hat{\boldsymbol{Q}}_n \right\rangle \cdot \boldsymbol{N}_n \ , \quad k = 1, 2 \ldots N_{\mathrm{arc}} \ , \tag{3.34}$$

where $\lambda_0$ is the line tension at the adhesion site at $s = 0$ (position $\boldsymbol{r}_0$) and $\lambda_k$ is the line tension at vertex $k$ (position $\boldsymbol{r}_k$). $N_{\mathrm{arc}}$ is the total number of vertices in which cellular arcs are discretized, and $\lambda_{N_{\rm arc}}$ represents the line tension at the other adhesion site. Furthermore, $\Delta s_n = |\boldsymbol{r}_n - \boldsymbol{r}_{n-1}|$, $\boldsymbol{T}_n = (\boldsymbol{r}_n - \boldsymbol{r}_{n-1})/\Delta s_n$, $\boldsymbol{N}_n = \boldsymbol{T}_n^{\perp}$ and

$$\left\langle \hat{\boldsymbol{Q}}_n \right\rangle = \frac{\hat{\boldsymbol{Q}}_n + \hat{\boldsymbol{Q}}_{n-1}}{2} \, , \tag{3.35}$$

with $\hat{\boldsymbol{Q}}_n$ and $\hat{\boldsymbol{Q}}_{n-1}$ the nematic tensor at the vertices $n$ and $n-1$. These are set equal to $\hat{\boldsymbol{Q}}$ at the closest bulk lattice point inside the cell among the four points, delimiting the unit cell of the bulk lattice, containing the edge vertices $n$ and $n-1$ respectively. If none of these is inside the cell, we set $Q_{xx,n} = Q_{xy,n} = 0$. The quantity $\lambda_0$ is calculated in such a way that the minimal $\lambda$ value along an arc equates the input parameter $\lambda_{\rm min}$, representing the minimal tension withstood by the cortical actin.

Next, the position of the vertices $\boldsymbol{r}_k$, $k = 0, 1 \ldots N_{\rm arc}$ is updated upon integrating Eq. (3.24a) using the forward Euler method with time step $\Delta t$. The curvature and normal vector at vertex $k$, $\kappa_k$ and $\boldsymbol{N}_k$, are found by constructing a circle with radius $R$ through vertices $k-1$, $k$, and $k+1$. The vector from vertex $k$ to the center of the circle is then equated to $\pm R\boldsymbol{N}_k$, with the sign such that $\boldsymbol{N}_k$ is an inward pointing normal vector, and $\kappa_k = \pm 1/R$, with a negative sign for a concave shape and a positive sign for a convex shape. Along each arc, $\boldsymbol{r}_0$ and $\boldsymbol{r}_{N_{\rm arc}}$ represent the positions of the adhesion sites and are kept fixed during simulations.

**Cell bulk update** Eq. (3.24b) is numerically solved at each lattice point inside the cell via a finite-difference scheme. Time integration is performed using the forward Euler method with time step $\Delta t$, whereas spatial derivatives are calculated using the centered difference approximation. In order to calculate derivatives at lattice points located in proximity of the edge, we use the boundary conditions, specified in Eq. (3.20), to express the values of $Q_{xx}$ and $Q_{xy}$ in a number of *ghost points* located outside the cell. This is conveniently done upon identifying three possible scenarios, illustrated in Figure 3.9. *1)* There is a single ghost point on the $x-$ or $y-$axis (Figure 3.9A). *2)* There are two ghost points, one on each axis (Figure 3.9B). *3)* There are two ghost points on the same axis and possibly a third one on the other axis (Figure 3.9C). In the following, we explain how to address each of these cases.

*1)* Using the centered difference approximation for the first derivative yields the following expression of the nematic tensor at a ghost point located at $(x \pm \Delta x, y)$ or $(x, y \pm \Delta y)$, with $\Delta x = \Delta y$ the lattice spacing:

$$Q_{ij}(x \pm \Delta x, y) = Q_{ij}(x \mp \Delta x, y) \pm 2\Delta x \, \partial_x Q_{ij}(x, y) \, , \tag{3.36a}$$

$$Q_{ij}(x, y \pm \Delta y) = Q_{ij}(x, y \mp \Delta y) \pm 2\Delta y \, \partial_y Q_{ij}(x, y) \, . \tag{3.36b}$$

The derivative with respect to $x$ in Eq. (3.36a) can be calculated from Eq. (3.20), upon taking $\boldsymbol{N} = \pm\hat{\boldsymbol{x}}$, where the plus (minus) sign correspond to a ghost point located on the left (right) of the central edge point. Thus $\boldsymbol{N} \cdot \nabla Q_{ij} = \pm\partial_x Q_{ij}$. Analogously, the derivative with respect to $y$ in Eq. (3.36b), is approximated as $\boldsymbol{N} \cdot \nabla Q_{ij} = \pm\partial_y Q_{ij}$,

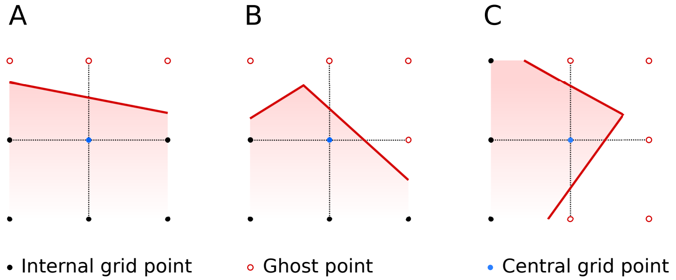

**Figure 3.9.** Schematic overview of the three geometrical situations described in Section 3.6.2. (A) There is a single ghostpoint on the $x-$ or $y-$axis. (B) There are two ghost points, one on each axis. (C) There are two ghost points on the same axis and possibly a third one on the other axis.

where the plus (minus) sign corresponds to a ghost point located below (above) the central edge point. Combining this with Eq. (3.20), yields:

$$Q_{ij}(x \pm \Delta x, y) = Q_{ij}(x \mp \Delta x, y) - 4\Delta x \frac{W}{K}\left[Q_{ij}(x,y) - Q_{0,ij}(x,y)\right] , \tag{3.37a}$$

$$Q_{ij}(x, y \pm \Delta y) = Q_{ij}(x, y \mp \Delta y) - 4\Delta y \frac{W}{K}\left[Q_{ij}(x,y) - Q_{0,ij}(x,y)\right] . \tag{3.37b}$$

The tensor $Q_{0,ij}$ is evaluated via Eq. (3.18) using the local orientation of the cell edge.

*2)* If a given lattice point is linked to ghost points in both the $x-$ and $y-$directions, we evaluate equation (3.37) for both directions independently as explained in the previous paragraph.

*3)* If a given lattice point is linked to two ghost points in either the $x-$ or $y-$direction, we employ a forward or backward finite difference approximation for the first spatial derivative of $Q_{ij}$ to evaluate $Q_{ij}$ at the ghost points. This yields:

$$Q_{ij}(x \pm \Delta x, y) = Q_{ij}(x, y) - 2\Delta x \frac{W}{K}\left[Q_{ij}(x,y) - Q_{0,ij}(x,y)\right] , \tag{3.38a}$$

$$Q_{ij}(x, y \pm \Delta y) = Q_{ij}(x, y) - 2\Delta y \frac{W}{K}\left[Q_{ij}(x,y) - Q_{0,ij}(x,y)\right] . \tag{3.38b}$$

Finally, if the given lattice point is also linked to a ghost point on the other axis, this is evaluated independently using Eq. (3.37).

### 3.6.3 Estimate of the nematic order parameter via OrientationJ

In this section, we demonstrate how the nematic director and order parameter can be estimated from experimental data. First, the locations of the cell interior and the cell edge were found by applying a low-pass filter on the images using Matlab. The interior of the cell was then sampled by overlaying a square lattice of 512 × 512 pixels

($1\,\text{pixel} = 0.138 \times 0.138\ \mu\text{m}^2$) on the microscope field-of-view (Figures 3.6A and 3.8A-E). For all pixels that are inside the cell, the nematic tensor was calculated using ImageJ with the OrientationJ plugin [177] in the following way. Given the intensity $I(x_0, y_0)$ of the image (channel with TRITC-Phalloidin) at the point $(x_0, y_0)$, we defined the symmetric $2 \times 2$ matrix $\hat{\boldsymbol{J}} = \langle \nabla I \nabla I \rangle$, where $\langle \cdots \rangle = \int w(x,y) \mathrm{d}x\, \mathrm{d}y\, (\cdots)$ represents a weighted average with $w(x,y)$ a Gaussian with a standard deviation of five pixels (0.69 µm) centered at $(x_0, y_0)$. The $\hat{\boldsymbol{J}}$ matrix can be expressed as:

$$\hat{\boldsymbol{J}} = (\Lambda_{\text{min}} - \Lambda_{\text{max}}) \left( \boldsymbol{e}_{\text{min}} \boldsymbol{e}_{\text{min}} - \frac{1}{2} \hat{\boldsymbol{I}} \right) + \frac{\Lambda_{\text{max}} + \Lambda_{\text{min}}}{2}\, \hat{\boldsymbol{I}}\ , \tag{3.39}$$

where $\Lambda_{\text{max}}$ and $\Lambda_{\text{min}}$ are the largest and smallest eigenvalues of $\hat{\boldsymbol{J}}$, $\boldsymbol{e}_{\text{min}}$ the eigenvector corresponding to $\Lambda_{\text{min}}$, and $\hat{\boldsymbol{I}}$ the two-dimensional identity matrix. The $\hat{\boldsymbol{J}}$ matrix was then used to estimate the average stress fiber direction $\boldsymbol{u}$:

$$\frac{\langle \nabla I \nabla I \rangle}{\langle |\nabla I|^2 \rangle} = \hat{\boldsymbol{I}} - \langle \boldsymbol{u}\boldsymbol{u} \rangle\ . \tag{3.40}$$

Here, the quantity $\hat{\boldsymbol{I}} - \langle \boldsymbol{u}\boldsymbol{u} \rangle$ reflects that the largest gradients in intensity are perpendicular to the orientation of the stress fibers and $\langle |\nabla I|^2 \rangle = \operatorname{tr} \hat{\boldsymbol{J}} = \Lambda_{\text{max}} + \Lambda_{\text{min}}$. Combining Eqs. (3.39) and (3.40), we obtain

$$\left\langle \boldsymbol{u}\boldsymbol{u} - \frac{1}{2} \hat{\boldsymbol{I}} \right\rangle = \frac{\Lambda_{\text{max}} - \Lambda_{\text{min}}}{\Lambda_{\text{max}} + \Lambda_{\text{min}}} \left( \boldsymbol{e}_{\text{min}} \boldsymbol{e}_{\text{min}} - \frac{1}{2} \hat{\boldsymbol{I}} \right)\ . \tag{3.41}$$

Comparing this with the definition of the nematic tensor:

$$\hat{\boldsymbol{Q}} = \left\langle \boldsymbol{u}\boldsymbol{u} - \frac{1}{2} \hat{\boldsymbol{I}} \right\rangle = S \left( \boldsymbol{n}\boldsymbol{n} - \frac{1}{2} \hat{\boldsymbol{I}} \right)\ , \tag{3.42}$$

we found the nematic order parameter $S$ and the nematic director $\boldsymbol{n}$ at each pixel:

$$S = \frac{\Lambda_{\text{max}} - \Lambda_{\text{min}}}{\Lambda_{\text{max}} + \Lambda_{\text{min}}}\ , \qquad \boldsymbol{n} = (\cos\theta_{\text{SF}}, \sin\theta_{\text{SF}}) = \boldsymbol{e}_{\text{min}}\ . \tag{3.43}$$

We note that the order parameter is identical to the coherence parameter defined in Chapter 2: $S = C$. If a pixel has zero actin expression, $I(x_0, y_0) = 0$, and consequently $S = 0$.

The data were further coarse-grained in blocks of $8 \times 8$ pixels corresponding to regions of size $1.104 \times 1.104\,\mu m^2$ in real space. This results in a new $64 \times 64$ lattice. The value of the nematic tensor in the new coarse-grained pixels was obtained from an average over those of the original $8 \times 8$ pixels located inside the cell. In turn, the coarse-grained pixels were considered inside the cell if more than half of the original pixels were inside the cell.

### 3.6.4 Supporting figures

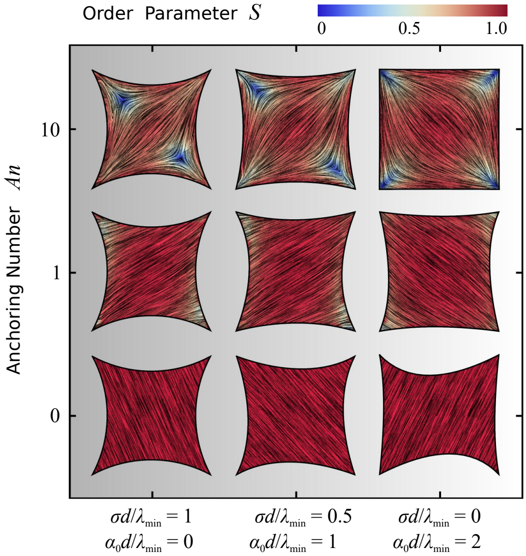

**Figure 3.10.** Configurations of cells whose adhesion sites are located at the vertices of a square. The thick black line represents the cell boundary, the black lines in the interior of the cells represent the orientation field $\boldsymbol{n} = (\cos\theta_{\rm SF}, \sin\theta_{\rm SF})$ of the stress fibers and the background color indicates the local nematic order parameter $S$. The spatial averages of the order parameter $S$ are given, from left to right, by: $0.74; 0.76; 0.80$ (top row), $0.90; 0.91; 0.92$ (middle row), and $1.0; 1.0; 1.0$ (bottom row). On the vertical axis the anchoring number *An* $= WR/K$ is varied (*An* $= 0, 1, 10$, with $R$ the length of the square side) and on the horizontal axis the ratio between the isotropic bulk stress $\sigma$ and the directed bulk stress $\alpha_0$ $((\sigma d/\lambda_{\rm min} = 1, \alpha_0 d/\lambda_{\rm min} = 0)$, $(\sigma d/\lambda_{\rm min} = 0.5, \alpha_0 d/\lambda_{\rm min} = 1)$, and $(\sigma d/\lambda_{\rm min} = 0, \alpha_0 d/\lambda_{\rm min} = 2)$, while $\lambda_{\rm min}$ is constant, and with $d$ equal to the square side. The ratios $\lambda_{\rm min}\Delta t/(\xi_t R^2) = 2.8 \cdot 10^{-6}$ and $K\Delta t/(\xi_r R^2) = 2.8 \cdot 10^{-6}$, and the parameters $\delta = 0.15R$, $N_{\rm arc} = 20$, and $\Delta x = R/19$ are the same for all cells. The number of iterations is $5.5 \cdot 10^5$.

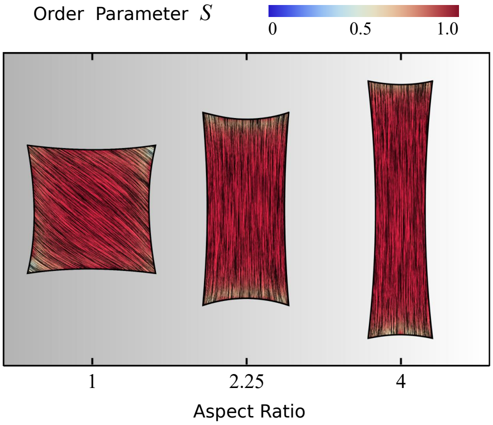

**Figure 3.11.** Effect of the aspect ratio of the cell, ranging from 1 to 4, on cytoskeletal organization for cells whose four adhesion sites are located at the vertices of rectangles with the same area $A$. The thick black line represents the cell boundary, the black lines in the interior of the cells represent the orientation field $\boldsymbol{n} = (\cos\theta_{\mathrm{SF}}, \sin\theta_{\mathrm{SF}})$ of the stress fibers and the background color indicates the local nematic order parameter $S$. The spatial averages of the order parameter $S$ are given, from left to right, by: $0.92; 0.95; 0.96$. The simulations shown are performed with *An* $= WR/K$ equal to 1, 0.67, and 0.5 respectively, where $R$ is equal to the short side of the rectangle, and *Co* $= \sigma d/\lambda_{\min}$ equal to 0.125, 0.1875, and 0.25 respectively, where $d$ is equal to the long side of the rectangle. The ratios $\sigma/(\sigma + \alpha_0) = 1/9$, $\lambda_{\min}\Delta t/(\xi_t A) = 2.8 \cdot 10^{-6}$, and $K\Delta t/(\xi_r A) = 2.8 \cdot 10^{-6}$, and the parameters $\delta = 0.15R$ and $\Delta x = R/19$ are the same for all cells. $N_{\mathrm{arc}} = 20, 30, 40$ from left to right and the number of iterations is $5.5 \cdot 10^5$.

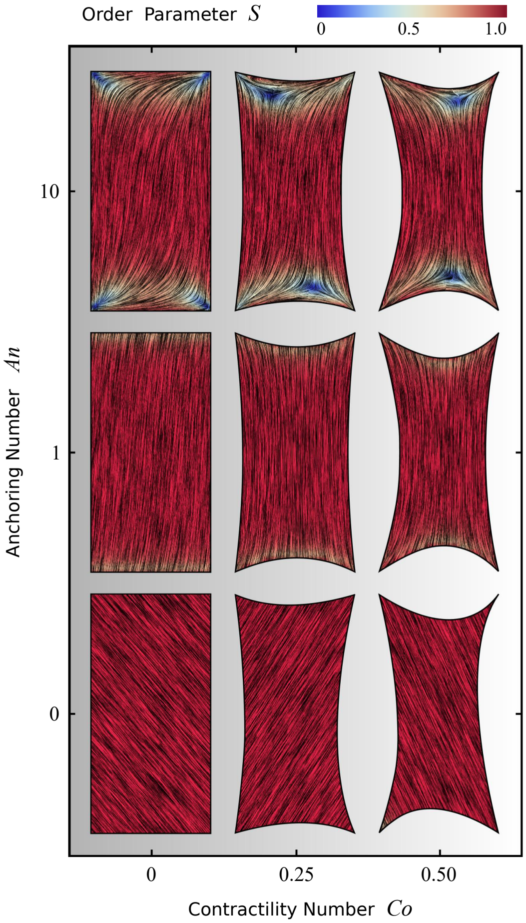

**Figure 3.12.** Configurations of cells whose adhesion sites are located at the vertices of a rectangle of aspect ratio 2. The thick black line represents the cell boundary, the black lines in the interior of the cells represent the orientation field $\boldsymbol{n} = (\cos\theta_{\mathrm{SF}}, \sin\theta_{\mathrm{SF}})$ of the stress fibers and the background color indicates the local nematic order parameter $S$. The spatial averages of the order parameter $S$ are given, from left to right, by: $0.88; 0.86; 0.87$ (top row), $0.97; 0.96; 0.96$ (middle row), and $1.0; 1.0; 1.0$ (bottom row). The vertical axis corresponds to the anchoring number $An = WR/K$ and the horizontal axis to the contractility number $Co = \sigma d/\lambda_{\mathrm{min}}$. The cells shown correspond to values of $An = 0, 1, 10$ and $Co = 0, 0.25, 0.50$, with $R$ the short side of the rectangle and $d$ the long side of the rectangle. The ratios $\sigma/(\sigma+\alpha_0) = 1/9$, $\lambda_{\mathrm{min}}\Delta t/(\xi_t R^2) = 2.8 \cdot 10^{-6}$, and $K\Delta t/(\xi_r R^2) = 2.8 \cdot 10^{-6}$, and the parameters $\delta = 0.15R$, $N_{\mathrm{arc}} = 40$, and $\Delta x = R/19$ are the same for all cells. The number of iterations is $5.5 \cdot 10^5$.

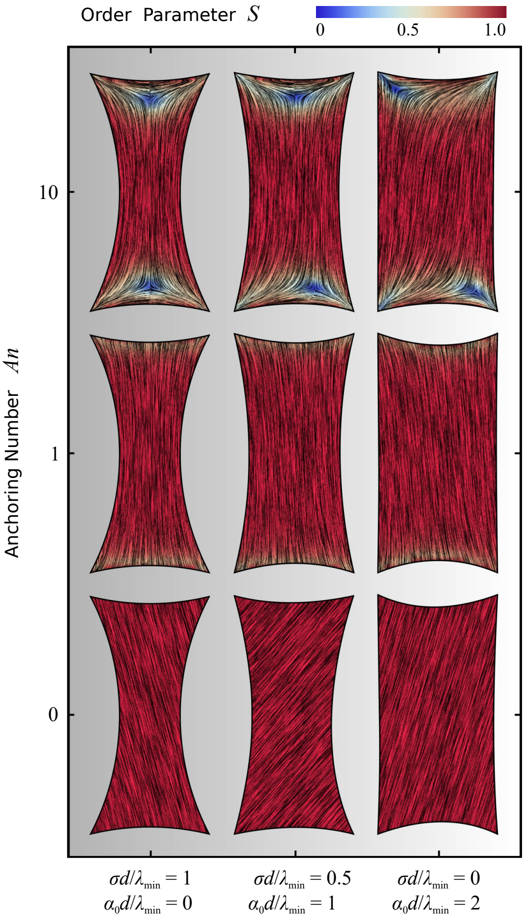

**Figure 3.13.** Configurations of cells whose adhesion sites are located at the vertices of a rectangle of aspect ratio 2. The thick black line represents the cell boundary, the black lines in the interior of the cells represent the orientation field $\boldsymbol{n} = (\cos\theta_{\mathrm{SF}}, \sin\theta_{\mathrm{SF}})$ of the stress fibers and the background color indicates the local nematic order parameter $S$. The spatial averages of the order parameter $S$ are given, from left to right, by: $0.84; 0.85; 0.87$ (top row), $0.94; 0.96; 0.96$ (middle row), and $1.0; 1.0; 1.0$ (bottom row). On the vertical axis the anchoring number $An = WR/K$ is varied ($An = 0, 1, 10$, with $R$ the short side of the rectangle) and on the horizontal axis the ratio between the isotropic bulk stress $\sigma$ and the directed bulk stress $\alpha_0$ $((\sigma d/\lambda_{\min} = 1, \alpha_0 d/\lambda_{\min} = 0), (\sigma d/\lambda_{\min} = 0.5, \alpha_0 d/\lambda_{\min} = 1)$, and $(\sigma d/\lambda_{\min} = 0, \alpha_0 d/\lambda_{\min} = 2)$, while $\lambda_{\min}$ is constant, and with $d$ equal to the long side of the rectangle. The ratios $\lambda_{\min}\Delta t/(\xi_t R^2) = 2.8 \cdot 10^{-6}$ and $K\Delta t/(\xi_r R^2) = 2.8 \cdot 10^{-6}$, and the parameters $\delta = 0.15R$, $N_{\mathrm{arc}} = 40$, and $\Delta x = R/19$ are the same for all cells. The number of iterations is $5.5 \cdot 10^5$.

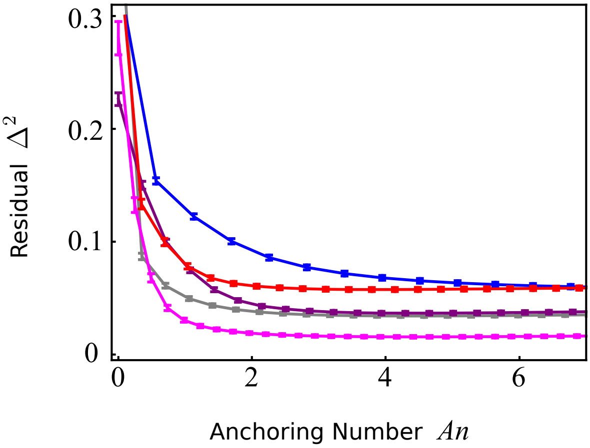

**Figure 3.14.** Residual function $\Delta^2$, defined in Eq. (3.27), as a function of the anchoring number *An* [Eq. (3.26)] for the cells displayed in Figures 3.8A-E, which correspond to the magenta, red, blue, grey, and purple data respectively. The minima are given by $\Delta^2 = 0.016; 0.058; 0.057; 0.034; 0.037$ for the cells displayed in Figures 8A-E, at values of $An = 4.4; 4.1; 19; 4.6; 4.7$, where $R = 17.3; 24.4; 39.9; 24.9; 25.3$ µm is defined as the square root of the cell area. These *An* values correspond to $K/W = 3.9; 5.9; 2.1; 5.4; 5.4$ µm. Error bars display the standard deviation obtained using jackknife resampling. For large *An* values the residual flattens for all cells, indicating that the actual value of *An* becomes unimportant once the anchoring torques (with magnitude $W$), which determine the tangential alignment of the stress fibers in the cell's periphery, outcompete the bulk elastic torques (with magnitude $K$).

## CHAPTER 4

# A HYBRID CELLULAR POTTS MODEL PREDICTS STRESS FIBER ORIENTATIONS AND TRACTION FORCES ON MICROPATTERNED SUBSTRATES

This chapter is in preparation as:

Koen Schakenraad, Bente H. Bakker, Gaia I. Martorana, Luca Giomi, and Roeland M.H. Merks, 'A hybrid Cellular Potts Model predicts stress fiber orientations and traction forces on micropatterned substrates'

## Abstract

Adherent cells exert traction forces on the underlying substrate. We numerically investigate the intimate relation between traction forces, the structure of the actin cytoskeleton, and the shape of cells adhering to adhesive micropatterned substrates. By combining the Cellular Potts Model with a model on stress fiber contractility, we reproduce prominent anisotropic features in previously published experimental data on fibroblasts, endothelial cells, and epithelial cells on adhesive micropatterned substrates. Our work highlights the role of cytoskeletal anisotropy in the generation of cellular traction forces, and provides a computational strategy for investigating stress fiber anisotropy in dynamical and multicellular settings.

## 4.1 Introduction

The mechanical properties of the environment play a crucial role in many cellular processes, such as stem cell differentiation [28, 30], durotaxis [132, 169] and protein expression [167]. Conversely, cells mechanically influence their environment by applying traction forces, with direct biomedical consequences in, for example, cancer metastasis [43–45] or asthma [40]. These traction forces are intimately related with the cell shape [64, 69, 90, 195, 196] and the presence of actin stress fibers [89, 90, 194]. For instance, the total traction [56, 195, 197, 224, 225] and the total amount of mechanical work that the cell does [132, 196, 226, 227] on the substrate increase with the cell spreading area.

The distribution of traction forces within the cell has also been extensively studied, showing, e.g., that traction forces are larger further away from the centroid of the cell [200, 228] and accumulate at the cell periphery [201, 202], as a consequence of contractility throughout the whole cell [229]. Many studies focus on the magnitudes of the traction forces only [45, 197, 230–232], but the directions of these forces are important for understanding, for instance, cell migration [233]. Many theoretical models consider cell contractility to be isotropic and homogeneous [68, 73, 196, 197, 232]. Although successful in explaining experimental observations on the scale of the whole cell, these models cannot describe the anisotropic contractility caused by actin stress fibers, which strongly influence the direction of traction forces [89, 90, 194]. In fact, in many contractility models the traction forces are always normal to the surface because they are calculated using only local information on the cell shape [69, 196, 234, 235], although experimental studies on micropatterns [89, 196] and during cell spreading [224] clearly show that traction forces have significant tangential components. Other models take the opposite limit in which the local cell shape and stress fiber orientation are not taken into account and traction forces generally point to the centroid of the cell [73, 228].

In this chapter we overcome these limitations and develop a hybrid model combining a finite difference method for the cytoskeleton based on liquid crystal (LC) theory, developed in Chapter 3, with a Cellular Potts Model (CPM) for cell shape. Using this hybrid LC-CPM method, we calculate the distribution and orientation of traction forces at the cell periphery by taking into account both the local cell shape and the structure of the actin cytoskeleton. We theoretically study single cells adhering to adhesive micropatterns [58], and find qualitative agreement between our simulations and previously published experimental data on fibroblasts, endothelial cells, and epithelial cells, demonstrating the importance of cytoskeletal anisotropy in determining the magnitudes and orientations of cellular traction forces.

To understand the complex interplay between cellular mechanics and geometry, cells are often studied *in vitro* on an adhesive substrate [48]. Traction forces can be measured using microfabricated elastomeric pillar arrays [55–57] or traction force microscopy [59–61]. The latter is often combined with micropatterned substrates [58] to ensure reproducible cell shapes which allows for a more systematic analysis of the data. On stiff substrates, most animal cells spread out and adhere to the substrate, via focal adhesions [54], at adhesion sites mainly lying along the cell contour. This results in flat cells with a large area that exert mainly contractile forces [48].

Several types of mathematical models have been developed to interpret experimental findings and predict the shapes of adherent cells [48]. The simplest among those are two-dimensional contour models [62–67, 194], in which the cell is completely described by the position of a one-dimensional cell contour. For adherent cells with a limited number of discrete adhesion sites, for instance cells on micropillar arrays, this contour consists of a collection of curves, called “cellular arcs”, that connect two consecutive adhesion sites. Different contour models predict the shapes of these cellular arcs given different intracellular forces.

The simplest contour model, often referred to as the “Simple Tension Model” (STM), describes the total force per unit length along the cell contour, $\boldsymbol{f}_{\text{tot}}$, as the competition between a simple line tension in the cell contour, $\lambda\boldsymbol{T}$, and an isotropic bulk contractility with magnitude $\sigma$ [62–64]:

$$\boldsymbol{f}_{\text{tot}} = \partial_s(\lambda\boldsymbol{T}) + \sigma\boldsymbol{N} \ . \tag{4.1}$$

Here, $\boldsymbol{T}$ is the tangent unit vector of the cell, $\boldsymbol{N}$ the inward pointing normal unit vector, and $\partial_s$ is a derivative along the arc length $s$. Here, $\sigma > 0$ models the isotropic contractility of the internal cytoskeleton, and $\lambda$ describes the contractile forces arising from myosin activity in the cell cortex. The term $\partial_s(\lambda\boldsymbol{T})$ describes the net force on the cell contour originating from spatial variations in the cortical tension $\lambda$ or in the orientation $\boldsymbol{T}$ of the cell contour. Solving $\boldsymbol{f}_{\text{tot}} = \boldsymbol{0}$ shows that, at mechanical equilibrium, the balance between bulk contractility and line tension leads to concave circular arcs with radius $R = \lambda/\sigma$ [62–64]. Extensions to the STM include an elastic contribution to the line tension [63, 64], bending elasticity of the cell membrane [65, 68], and anisotropic bulk contractility (Chapters 2 and 3 of this thesis), which we discuss below.

In Chapters 2 and 3, we extended the existing contour models by incorporating a directed, anisotropic, contractile bulk stress into the Simple Tension Model. This anisotropic contractility originates from actin stress fibers [46, 47], which we treat as contractile force dipoles with average local orientation $\theta_{\text{SF}}$ [102, 103]. Together with the isotropic contribution [Eq. (4.1)] this leads to an overall force per unit length along the contour given by

$$\boldsymbol{f}_{\text{tot}} = (\partial_s\lambda)\boldsymbol{T} + (\lambda\kappa + \sigma)\boldsymbol{N} + \alpha(\boldsymbol{n}\cdot\boldsymbol{N})\boldsymbol{n} \ , \tag{4.2}$$

with $\boldsymbol{n} = (\cos\theta_{\text{SF}}, \sin\theta_{\text{SF}})$ a unit vector parallel to the average local stress fiber orientation, $\kappa$ the local curvature of the cell boundary, $\alpha > 0$ the magnitude of the directed contractile stresses, and where we used $\partial_s\boldsymbol{T} = \kappa\boldsymbol{N}$. Here, $\alpha$ is treated as a constant, but in Section 4.2.2 we will use the language of nematic liquid crystals to make $\alpha$ proportional to the local degree of alignment between the stress fibers. Upon again solving $\boldsymbol{f}_{\text{tot}} = \boldsymbol{0}$, the equilibrium shape of the concave cellular arcs is found, in the presence of anisotropic contractility, to be given by a segment of an ellipse with aspect ratio $\sqrt{\sigma/(\sigma+\alpha)}$ and whose longitudinal direction is parallel to the local orientation of the stress fibers $\theta_{\text{SF}}$. These predictions were experimentally verified by an analysis of the shapes of anisotropic fibroblastoid (GDβ1, GDβ3) and epithelioid (GEβ1, GEβ3) cells (see Chapter

2). Because of the discrete nature of the adhesion sites in this contour model, cells are always concave and comparisons to experimental data are limited to cells adhering to substrates at a small number of adhesion sites.

In recent years, the Cellular Potts Model (CPM) framework, best known for studies of multicellular systems (see, e.g., Refs. [9, 81]), has emerged as a computational alternative for studying the shape [69, 83, 84] and motility [124, 125] of single cells. In the CPM, the cell is represented by a collection of occupied lattice sites on an often two-dimensional square lattice. The dynamics is inspired by a Monte Carlo method using the Metropolis algorithm [236]. During each step of the simulation, the state (occupied or not occupied) of a randomly chosen lattice site is copied into a random neighbor lattice site. Using a predefined energy functional, called the Hamiltonian $H$, the energy change $\Delta H$ as a result of the copy is calculated. Then, the copy is accepted if $\Delta H < 0$ and accepted with probability $\mathrm{e}^{-\Delta H/\mu}$ if $\Delta H > 0$, where the reference energy $\mu$ is called the "motility energy" and is a measure for the activity of the cell. Each term in the Hamiltonian describes a particular cellular force field $\boldsymbol{F}$ via the relation $\boldsymbol{F} = -\nabla H$, which can be calculated for every configuration of the cell [237].

Albert and Schwarz [69] used a CPM approach to apply the Simple Tension Model, as well as the more extended "tension-elasticity model" [63, 64], to cells adhering to micropatterns of arbitrary shape. Here, we focus on the STM, for which the Hamiltonian is given by

$$H = \sigma A + \lambda P - \frac{E_0}{A_{\mathrm{ref}} + A_{\mathrm{ad}}} A_{\mathrm{ad}} \,, \tag{4.3}$$

with $A$ the cell area, $P$ the length of cell perimeter, and $A_{\mathrm{ad}}$ represents the area of the adhesive pattern covered by the cell. Minimization of the first two terms in Eq. (4.3) is equivalent to applying the force field given in Eq. (4.1) [64]. The last term represents the adhesion energy of the cell with the substrate, with strength $E_0$. Because the number of adhesion molecules in a cell is finite, the adhesion energy saturates with the covered area as determined by the reference area $A_{\mathrm{ref}}$.

Here, we develop an anisotropic hybrid liquid crystal-Cellular Potts Model (LC-CPM) framework to apply the contour model in Eq. (4.2) to cells adhering to micropatterns. The chapter is organized as follows: in Section 4.2.1 we theoretically study how stress fibers affect cell shape, in Section 4.2.2 how cell shape affects the orientations of stress fibers, and in 4.2.3 we study the interplay between shape and cytoskeleton. We demonstrate that our results are consistent with earlier analytical and numerical approaches, and our simulations reproduce cell shape and orientations of stress fibers of previously published experimental data on fibroblasts, endothelial cells, and epithelial cells on adhesive micropatterned substrates. In Section 4.2.4 we predict how the anisotropy of stress fibers affects the traction forces that the cell boundary exerts on the adhesive substrate, and we reproduce prominent anisotropic features in experimentally observed traction force patterns of fibroblasts, endothelial cells and epithelial cells.

## 4.2 Results

### 4.2.1 Cytoskeletal organization controls cell shape

Following Albert and Schwarz [69], we apply our anisotropic model to micropatterns of arbitrary shape by implementing it in the Cellular Potts Model. In order to do so, we need to translate the anisotropic contractile force density $\boldsymbol{f}_a = \alpha(\boldsymbol{n} \cdot \boldsymbol{N})\boldsymbol{n}$ to an energy description. However, unlike the forces in Eq. (4.1), the force considered here is derived from inherently non-equilibrium processes [102, 103] and is a non-conservative, *active*, force. Consequently, $\boldsymbol{f}_a$ cannot be derived from a Hamiltonian. For a review on non-equilibrium forces and active matter, see, e.g., Ref. [14]. Instead, we follow the lines of earlier works who have incorporated other non-equilibrium processes, such as chemotaxis and durotaxis, in the Cellular Potts Model by calculating directly the energy difference $\Delta H$ associated with a CPM copy [220, 238]. This energy difference is given by minus the work done on the cell by the stress fibers: $\Delta H_a = -W_a$, where the negative sign indicates that the total energy of the cell, $H$, decreases when the stress fibers do (contractile) work. For a given displacement of the cell boundary, i.e., the addition or removal of one lattice site from the cell, the total work $W_a$ is obtained by integrating the force density $\boldsymbol{f}_a$ over a displacement $\mathbf{d}\boldsymbol{x}$ (to obtain the work per unit length along the boundary) and over a distance $\mathrm{d}s$ along the cell boundary:

$$W_a = \int \mathrm{d}s \int \boldsymbol{f}_a \cdot \mathbf{d}\boldsymbol{x}. \tag{4.4}$$

As only normal displacements of the boundary change the cell shape, we write $\mathbf{d}\boldsymbol{x} = -\mathrm{d}x\boldsymbol{N}$, where $\mathrm{d}x > 0$ if the displacement is opposite to $\boldsymbol{N}$, i.e., when the boundary moves outwards. Upon further assuming that $\boldsymbol{n}$ and $\boldsymbol{N}$ change slowly on the scale of the CPM lattice site that is added or removed, we can take them out of the integrals and find

$$W_a = -\alpha(\boldsymbol{n} \cdot \boldsymbol{N})^2 \iint \mathrm{d}s\mathrm{d}x. \tag{4.5}$$

Finally, given that the displacements $\mathrm{d}x$ (along $-\boldsymbol{N}$) and $\mathrm{d}s$ (along $\boldsymbol{T}$) are perpendicular, the double integral is equal to the change in area of the cell, $\iint \mathrm{d}x\mathrm{d}s = \Delta A$, which yields

$$\Delta H_a = -W_a = \alpha(\boldsymbol{n} \cdot \boldsymbol{N})^2 \Delta A. \tag{4.6}$$

with $\boldsymbol{n}$ and $\boldsymbol{N}$ evaluated at the boundary lattice site of the cell that is copied (in case of an extension) or that is copied into (in case of a retraction), and where $\Delta A = 1$ for an extension and $\Delta A = -1$ for a retraction.

To obtain the total energy change for a given CPM copy, we introduce two further simplifications. First, we assume the line tension to be constant (i.e., $\partial_s \lambda = 0$), although previous work has shown that $\lambda$ can in general be different between different cellular arcs [63, 64] or even vary within a single arc (Chapters 2 and 3 in this thesis). Second, we take the limit in which the reference area $A_{\mathrm{ref}}$ [Eq. (4.3)] is much larger than the

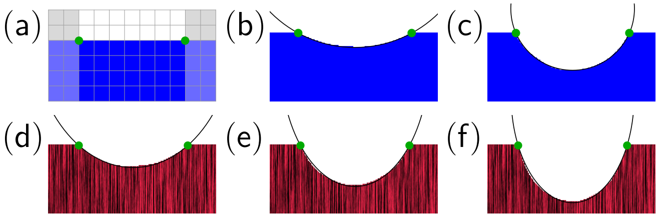

**Figure 4.1.** Single cellular arcs are well described by circles and ellipses. (a) Schematic of the simulation setup for studying the shape of a single arc. The initial condition is a rectangular "cell" (blue lattice sites) that occupies the lower half of the lattice sites in the simulation. Two adhesion sites (green circles), placed 100 lattice sites apart, pin the cell to the substrate. In practice, all lattice sites that are not in between the adhesion sites (grey areas) are frozen and are not updated during the simulation. A Cellular Potts Model (CPM) simulation is then performed using the Hamiltonian in Eq. (4.7), with $\gamma_{\text{ad}} = 0$, to find the shape of the arc. (b,c) Configurations of single arcs for $\mu/\lambda = 1/10$ lattice sites and $\alpha = 0$ are well approximated by circles. The theoretical radii of the circles, $R = \lambda/\sigma$, are 50 and 100 lattice sites respectively, whereas the approximating circles have radii of 54.5 and 105 lattice sites. (d-f) Configurations of single arcs for $\alpha \neq 0$ are well approximated by ellipses. The black lines in the cell interior represent the vertically oriented stress fibers (i.e., $\theta_{\text{SF}} = \pi/2$ and $\boldsymbol{n} = \hat{\boldsymbol{y}}$). The approximating ellipses have aspect ratios given by $\sqrt{\sigma/(\sigma+\alpha)}$ and are vertically oriented, as theoretically predicted. The lengths of the major semi-axes are given by: (d) 134 lattice sites (approximation) versus 120 lattice sites (theory), (e) 119 lattice sites (approximation) versus 120 (theory), (f) 98 lattice sites (approximation) versus 100 (theory). Parameters are given by: (d) $\alpha = \sigma$, $\lambda/\sigma = 120$ lattice sites, and $\mu/\lambda = 1/12$ lattice sites, (e) $\alpha = 2\sigma$, $\lambda/\sigma = 120$ lattice sites, and $\mu/\lambda = 1/12$ lattice sites, and (f) $\alpha = 2\sigma$, $\lambda/\sigma = 100$ lattice sites, and $\mu/\lambda = 1/10$ lattice sites.

adhesion area, such that the adhesion energy is simplified to $\gamma_{\text{ad}} A_{\text{ad}}$, with $\gamma_{\text{ad}} < 0$ a negative surface tension of the adhesion area. The total energy change for a copy is then given by

$$\Delta H = \Big(\sigma + \alpha(\boldsymbol{n} \cdot \boldsymbol{N})^2\Big)\Delta A + \lambda \Delta P + \gamma_{\text{ad}} \Delta A_{\text{ad}} \,. \tag{4.7}$$

See Section 4.4.1 in the Appendix for the numerical methods used for determining the normal vector $\boldsymbol{N}$ and the length of the perimeter $P$.

Before we study cells on micropatterned substrates, we first test the validity of our CPM model by comparing the shapes of non-adhering (i.e., $\gamma_{\text{ad}} = 0$) single cellular arcs to previously published analytical predictions [62–64, 194]. To do so, we define as initial condition a rectangular "cell" to occupy all lattice sites in the lower half of the simulation space. This is schematically illustrated in Figure 4.1a, where the lattice sites that are part of the cell are displayed in blue. Then, we define two adhesion sites (green circles in Figure 4.1a), placed 100 lattice sites apart, where the cell is pinned to the substrate. All lattice sites that are not in between the adhesion sites (grey areas) are frozen and are not allowed to be updated during the simulation. The region in between the adhesion sites then forms a cellular arc whose shape we study.

First, we study a cell with an isotropic cytoskeleton, i.e., $\alpha = 0$. The Hamiltonian then reduces to $H = \sigma A + \lambda P$, which is equivalent to a force per unit length along the contour given by Eq. 4.1 [64]. Hence, we expect to find a concave circular arc with radius $R = \lambda/\sigma$ [62–64]. In Figures 4.1b,c we show the results of two simulations with the same line tension $\lambda$ but with different values of the isotropic bulk stress $\sigma$. As expected, the arcs are concave and the arc with the larger bulk stress (Figure 4.1c) is more curved. The arcs are well approximated by circles (black lines in Figures 4.1b,c), as was also observed before for this Hamiltonian in Ref. [69]. The radii of the circles shown in Figures 4.1b,c are, however, slightly larger (5%-10%) than expected based on the theoretical prediction $R = \lambda/\sigma$. This slight underestimation of the observed radius is consistently found for all choices of the parameters $\lambda$ and $\sigma$. We hypothesize that this is a consequence of random fluctuations in the CPM due to the finite motility energy $\mu$. These random fluctuations favor states of the system that can be realized in many different ways (i.e., shapes with large *entropy*), leading to slightly less curved cellular arcs, and consequently bigger circles than expected based on the theory.

Next, we include the directed bulk stress (i.e., $\alpha \neq 0$), and assume a predefined and constant orientation of the cytoskeleton $\boldsymbol{n} = \hat{\boldsymbol{y}}$ (i.e, $\theta_{\mathrm{SF}} = \pi/2$). The resulting Hamiltonian [first two terms in Eq. (4.7)] is equivalent to a force per unit length described by the second and third term of Eq. (4.2). Hence, we expect the cellular arcs to approximate a segment of an ellipse with aspect ratio $\sqrt{\sigma/(\sigma+\alpha)}$ and whose long semi-axis of size $\lambda/\sigma$ is oriented vertical, parallel to the stress fiber orientation $\theta_{\mathrm{SF}}$ (see Chapters 2 and 3), although we do not expect the agreement to be perfect because we ignore the first term in Eq. (4.2) by assuming the line tension $\lambda$ to be constant. Figures 4.1d-f show the cellular arcs together with segments of ellipses matching the arcs. The thin black lines in the interior of the cells visualize the vertical orientation of the stress fibers. Figure 4.1d shows a cellular arc for $\sigma = \alpha$ and $\lambda/\sigma = 120$ lattice sites. In Figure 4.1e the directed bulk contractility is increased to $\alpha = 2\sigma$ resulting in a more curved shape and a narrower (larger aspect ratio) ellipse. In Figure 4.1f the line tension is additionally decreased such that $\lambda/\sigma = 100$ lattice sites, resulting in an even more curved shape and a smaller ellipse than in Figure 4.1e. The orientations and aspect ratios of the ellipses shown in Figures 4.1d-f exactly match those predicted by the theory, but the size of the ellipse in Figure 4.1d is, similar to what we observed for the circles, larger than expected based on the theory. Interestingly, for large values of the directed bulk stress $\alpha$ (Figures 4.1e and 4.1f) the size of the ellipses matches the theoretical predictions surprisingly well. This is because in the analytical results (for details, see Chapters 2 and 3), the average line tension along the arc increases as a result of the directed bulk stress. Because we assume the line tension to be constant here, the simulated ellipses are smaller than expected by the theory, which compensates for the fact that circles and ellipses become too large due to random CPM fluctuations.

Summarizing, although the correspondence between the theoretical predictions [62–64, 194, 239] and our simulations on the shapes of single cellular arcs is not exact, the lattice-based CPM approximates the continuous curves predicted by the theory remarkably well. For a numerical treatment of these models that explicitly describes the cell boundary, and therefore produces even more accurate shapes, we refer to Chapter 3. Here, we take advantage of the possibilities of the CPM to study cells adhering to continuous micropatterned geometries in Sections 4.2.2, 4.2.3, and 4.2.4.

### 4.2.2 Cell shape controls cytoskeletal organization

In order to apply the method introduced in Section 4.2.1 to entire cells, we require a theoretical description of the cytoskeleton to define the non-constant stress fiber orientation $\boldsymbol{n}$ at every lattice site. For this purpose we employ a continuous phenomenological model of the actin cytoskeleton, using the language of nematic liquid crystals [91], that we discussed in Chapter 3. We emphasize, however, that our method of anisotropic cytoskeletal contractility in the CPM, as summarized by Eq. (4.6), can, in principle, be combined with any theoretical description of the cytoskeleton (e.g., Ref. [77]).

As we detail in Chapter 3, the configuration of the stress fibers in the actin cytoskeleton is described by the two-dimensional nematic tensor:

$$\hat{\boldsymbol{Q}} = \begin{bmatrix} Q_{xx} & Q_{xy} \\ Q_{xy} & -Q_{xx} \end{bmatrix} = \frac{S}{2} \begin{bmatrix} \cos 2\theta_{\mathrm{SF}} & \sin 2\theta_{\mathrm{SF}} \\ \sin 2\theta_{\mathrm{SF}} & -\cos 2\theta_{\mathrm{SF}} \end{bmatrix}. \tag{4.8}$$

where $\theta_{\mathrm{SF}}$ describes the local orientation of the stress fibers and $0 \leq S \leq 1$ is the so called nematic order parameter. $S$ measures the amount of orientational order of the stress fibers, where $S = 1$ represents perfect local alignment between stress fibers, and $S = 0$ represents randomly oriented stress fibers. As $\hat{\boldsymbol{Q}}$ does not describe the local density of actin, our model does not predict experimentally observed actin density variations within the cell [176, 196, 210, 211].

The general idea behind our cytoskeleton model is based on the experimental observation, by us (see, e.g., Figure 2.10) and others [85–89], that stress fibers in highly anisotropic cells preferentially align with each other and with the cell's edges. For an overview of the physical, chemical, and biological mechanisms that are possibly involved in these aligning interactions, see Chapter 3. The alignment is phenomenologically captured by a minimization of the Landau-de Gennes free-energy $F_{\mathrm{cyto}}$ [91]:

$$F_{\mathrm{cyto}} = \frac{K}{2} \int \mathrm{d}A \, \left[ |\nabla \hat{\boldsymbol{Q}}|^2 + \frac{1}{\delta^2} \operatorname{tr} \hat{\boldsymbol{Q}}^2 (\operatorname{tr} \hat{\boldsymbol{Q}}^2 - 1) \right] + \frac{W}{2} \oint \mathrm{d}s \operatorname{tr} \left[ (\hat{\boldsymbol{Q}} - \hat{\boldsymbol{Q}}_0)^2 \right] . \tag{4.9}$$

The first integral in Eq. (4.9) is responsible for the alignment of stress fibers with one another, as it penalizes gradients in the orientation of the stress fibers and in their degree of alignment (first term). The constant $K$ expresses the stiffness of the average stress fiber orientation $\boldsymbol{n}$ with respect to splay and bending deformations, see also Chapter 3. The second term equals $S^2(S^2/2 - 1)/(2\delta^2)$, which favors perfect orientational order (i.e., $S = 1$), where the length scale $\delta$ defines the energy penalty associated with a low $S$ value. Consequently, $\delta$ determines the typical size of regions where the order parameter $S$ drops to zero to compensate for a strong local gradient in the stress fiber orientation $\theta_{\mathrm{SF}}$. The second integral is the Nobili-Durand anchoring energy [95], a contour integral which is responsible for the alignment of stress fibers with, and a large $S$ value along, the cell's edges. This is achieved by defining the tensor $\hat{\boldsymbol{Q}}_0$ as

$$\hat{\boldsymbol{Q}}_0 = \frac{S_0}{2}\begin{bmatrix}\cos 2\theta & \sin 2\theta \\ \sin 2\theta & -\cos 2\theta\end{bmatrix}. \tag{4.10}$$

where $\theta$ is an angle parallel to the cell edge, such that $\boldsymbol{T} = (\cos\theta, \sin\theta)$. In addition to stress fibers aligning to the cell edge, we assume that they do so with large nematic order: $S_0 = 1$. The phenomenological constant $W > 0$ [Eq. (4.9)] measures the strength of the parallel anchoring, i.e., it measures to what extent stress fibers align with the cell edge. For a description of the numerical methods employed for minimizing the energy, see Section 4.4.2 in the Appendix.

As we mentioned in Section 4.1, the directed bulk contractility $\alpha$ [Eq. (4.2)] is proportional to the local alignment between stress fibers. Having introduced the nematic order parameter $S$, we now make this relation quantitative by setting $\alpha = \alpha_0 S$, with $\alpha_0$ a constant (see also Chapter 3). Apart from this, we treat the contractility parameters $\alpha_0$, $\sigma$, and $\lambda$, which model the tension at the cell edge, independent from the parameters $K$, $W$, and $\delta$, which model the interior of the cell.

We combine this model for the cytoskeleton with the Cellular Potts Model for cell shape described in Section 4.2.1. We alternatingly update the CPM, using the Hamiltonian given by Eq. (4.7) with $\gamma_{\mathrm{ad}} \neq 0$, and the structure of the cytoskeleton by minimization of the free energy $F_{\mathrm{cyto}}$ [Eq. (4.9)], until both the cell shape and the cytoskeleton reach a steady state. For details, see Section 4.4.2 in the Appendix. Before we study the interplay between cytoskeleton and cell shape in Section 4.2.3, in this section we illustrate how cell shape affects the cytoskeleton and compare our model predictions to previously published experimental data. Figure 4.2 shows the results of simulations performed on three convex micropatterns (Figure 4.2a), namely a rectangle of aspect ratio 2, a stadium-shape of aspect ratio 2 and a circle. For cells adhering to these convex patterns, all contractile forces described by the first two terms in the Hamiltonian of Eq. (4.7) are directed inwards. Hence, the steady-state shape of these cells is, independent of the exact values of $\alpha_0$, $\sigma$, and $\lambda$, identical to the convex micropatterns that they adhere to, making these shapes very suited for studying the effect of cell shape on cytoskeletal organization. In Figure 4.2b we study the cytoskeleton for increasing parallel anchoring of the stress fibers with the cell edge. The importance of this parallel boundary anchoring, quantified by $W$, relative to parallel alignment in the bulk, quantified by $K$, is described by the *anchoring number An*, a dimensionless number which we introduced in Chapter 3 and is given by

$$\mathit{An} = \frac{WR}{K}, \tag{4.11}$$

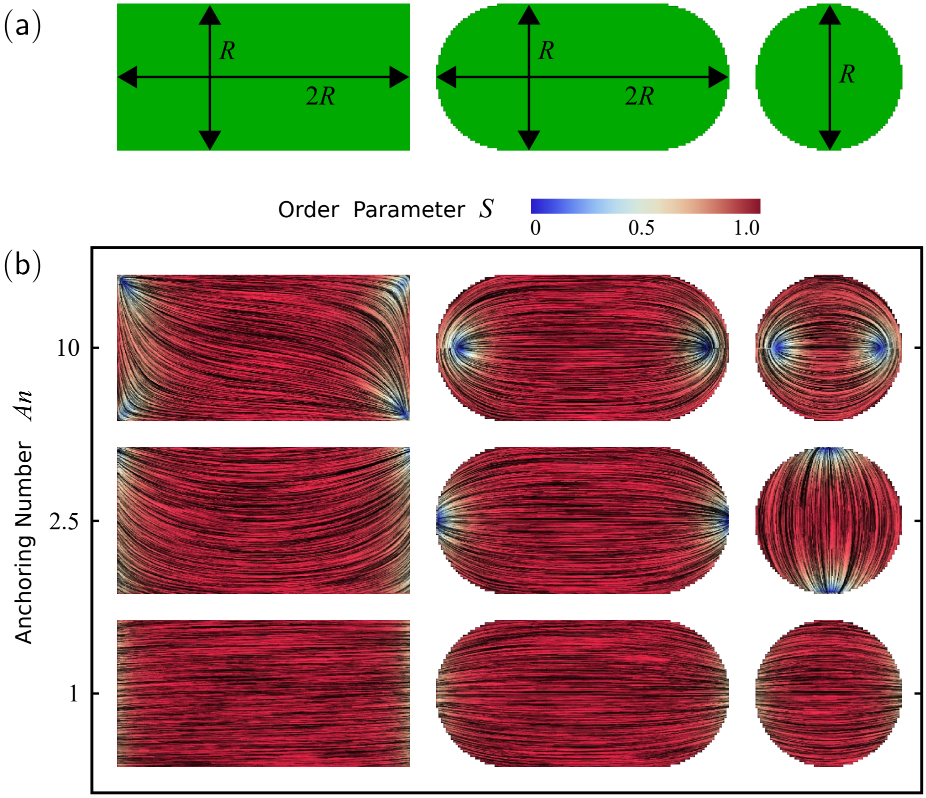

**Figure 4.2.** Cytoskeletal structure of cells on adhesive micropatterns with convex shapes. (a) Adhesive micropatterns with the shape of a rectangle of aspect ratio 2, a stadium of aspect ratio 2, and a circle. The length scale $R = 60$ lattice sites is used to calculate the anchoring number *An*, defined in Eq. (4.11). (b) Cells with increasing anchoring number (*An* $= 1$, *An* $= 2.5$, and *An* $= 10$) on the adhesive micropatterns shown in (a). The black lines in the interior of the cells represent the orientation field $\boldsymbol{n} = (\cos\theta_{\mathrm{SF}}, \sin\theta_{\mathrm{SF}})$ of the stress fibers and the background color indicates the nematic order parameter $S$. The spatial averages of the order parameter are given, from top to bottom, by: 0.90; 0.94; 0.97 (rectangles), 0.92; 0.94; 0.97 (stadiums), and 0.81; 0.87; 0.94 (circles). For all cells, $\delta = 9$ lattice sites, $\lambda/\sigma = 300$ lattice sites, $\alpha_0/\sigma = 2$, $\mu/\lambda = 1/30$ lattice sites, $\mu/|\gamma_{\mathrm{ad}}| = 1/20$ of the area of a lattice site, and $K\Delta t/(\xi_r R^2) = 2.5 \cdot 10^{-6}$. For definitions of $\Delta t$ and $\xi_r$, see Section 4.4.2 in the Appendix.

with $R$ a typical length scale in which the cytoskeleton is confined, see Figure 4.2a. For *An* $\ll 1$ bulk elasticity dominates boundary anchoring, resulting in a uniformly oriented cytoskeleton with large deviations form parallel anchoring with the cell's edges. On the other hand, for *An* $\gg 1$, boundary anchoring dominates, leading to perfect alignment of the stress fibers with the boundary.

The left column of Figure 4.2b shows the cytoskeleton of a cell, adhering to the rectangular micropattern, for *An* $= 10$, *An* $= 2.5$ and *An* $= 1$ respectively, where $R$ is the short side of the rectangle (see Figure 4.2a). The black lines in the interior of the cells represent the orientation field $\boldsymbol{n} = (\cos\theta_{\mathrm{SF}}, \sin\theta_{\mathrm{SF}})$ of the stress fibers and the background color indicates the nematic order parameter $S$. Consistent with our previous results on rectangular geometries (Figure 3.12), stress fibers align with all edges for large boundary anchoring (*An* $= 10$), but they align only with the rectangle's long edges for small boundary anchoring (*An* $= 1$). This longitudinal alignment of stress fibers is consistent with various experimental observations on cells adhering to elongated adhesive micropatterns and adhesive stripes [87–89, 196, 211]. We note that for configurations with sufficiently large anchoring numbers (*An* $= 2.5$ and *An* $= 10$), the random initial configuration of the simulation determines, independent of the anchoring number, whether the stress fibers at the short edges of the rectangle bend in opposite directions, leading to an "S"-shaped cytoskeleton (*An* $= 10$ in Figure 4.2), or in the same direction, leading to a "U"-shaped cytoskeleton (*An* $= 2.5$ in Figure 4.2).

Next, we focus on shapes distinct from those of cells adhering to a small number of discrete adhesion sites, which we studied in Chapter 3, and investigate the actin cytoskeleton on convex micropatterns with curved edges. The middle column of Figure 4.2b shows the cytoskeleton, for identical values of *An* as in the left column, for a cell adhering to a stadium-shaped micropattern of aspect ratio 2, where $R$ is again the short axis of the pattern. For *An* $= 1$ the cytoskeleton aligns parallel to the long axis of the stadium with large order parameter throughout the cell (spatial average is 0.97), similarly to what we observed for the rectangle. However, different from the rectangular shape, the more gentle curvature of the stadium causes the stress fiber orientation at the circular caps to deflect toward the middle. This effect becomes more pronounced for *An* $= 2.5$, where two topological defects start to form at the ends of the circular caps, as can be seen from the more blue-shifted color. For a review on topological defects in nematic liquid crystal systems, see, e.g., Ref. [96]. For the largest value of *An*, the stress fibers align with the edge throughout the complete cell, causing the topological defects to move inwards and the average order parameter to decrease to 0.92. Unlike the topological defects found in the stress fiber orientation in concavely shaped cells in Chapter 3, which have topological charge $-1/2$, these topological defects have charge $+1/2$ due to the convex cell shape. The observed cytoskeletal structures agree qualitatively with experimentally observed stress fiber distributions in fibroblasts on micropatterns of spherocylindrical shape in Ref. [196], where structures similar to our theoretical results for *An* $= 10$ (for relatively wide stadium-shapes, hence large $R$ and large *An*) and for *An* $= 1$ (for narrow stadium-shapes, small $R$ and *An*) are found. In Section 4.2.4, where we study traction forces, we compare in more detail with the experimental data in Ref. [196].

Finally, we decrease the aspect ratio to 1 while keeping the micropattern curvature constant. The right column of Figure 4.2b shows the cytoskeleton for a cell adhering to a circular micropattern (with $R$ the diameter of the circle). The resulting configurations

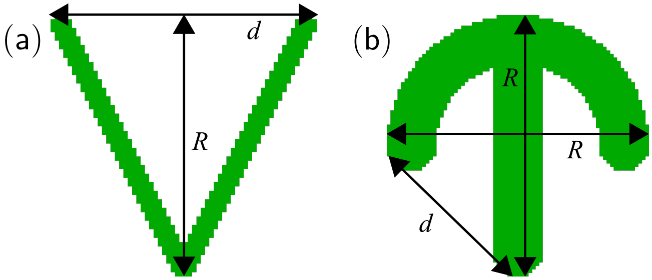

**Figure 4.3.** Adhesive micropatterns to study the interplay between cell shape and the orientation of the actin cytoskeleton. (a) Pattern in the shape of the letter V, where $R = 60$ lattice sites [Eq. (4.11)] and $d = 60$ lattice sites [Eq. (4.12)]. (b) Pattern in the shape of a crossbow, where $R = 60$ lattice sites and $d = 42$ lattice sites.

are qualitatively similar to those observed for the stadium shapes: for $An = 1$ the stress fibers align largely uniformly with small deflections inwards (average order parameter is 0.94), for $An = 2.5$ the structure bends more and topological defects start to form near the edge (average order parameter 0.87), and for $An = 10$ the stress fibers align with the cell edge everywhere, causing the defects to move inwards (average order parameter 0.81). The most important difference between circles and stadiums is that the main orientation is no longer biased toward a specific direction due to the symmetry of the shape, although the symmetry of the square lattice of the Cellular Potts Model appears to favor either horizontal or vertical configurations. The linear stress fiber structure for $An = 1$ closely resembles the actin cytoskeleton of fibroblasts found in Refs. [213, 215] and in simulations by Pathak *et al.* [77], but this linear pattern is not found for fibroblasts in Ref. [196] or for non-keratinocyte epitheliocytes or keratinocytes in Ref. [215], where mostly isotropic configurations that lack stress fibers are found. Hence, our cytoskeleton model qualitatively reproduces experimentally found stress fiber configurations for lower $An$ values, but is not applicable to describe cells that have not formed stress fibers.

### 4.2.3 Cytoskeleton and shape interplay on micropatterns

In previous sections we studied how the cytoskeleton affects cell shape (Section 4.2.1) and how the shape affects the orientation of the cytoskeleton (Section 4.2.2). Before demonstrating that stress fibers play an important role in directing traction forces in Section 4.2.4, we first study the interplay between stress fiber orientation and cell shape. We previously studied this interplay for concave cells adhering to a small number of discrete adhesion sites in Chapter 3, but here we take advantage of the Cellular Potts Model to study shapes that have both convex and concave features and again compare our predictions to previously published experimental data. We use two frequently studied micropattern shapes to illustrate the phenomenology of our model, a pattern in the shape of the letter V [69, 77, 210] and a pattern in the shape of a crossbow [43, 69, 176], see Figure 4.3. We measure the magnitude of the bulk contractility of the cells with respect to their line tension using another dimensionless number which we introduced in Chapter 3, the *contractility number Co*:

$$Co = \frac{\sigma d}{\lambda}, \tag{4.12}$$

with $d$ the typical distance between the ends of a non-adherent cellular arc (see Figure 4.3). For $Co \ll 1$ line tension dominates bulk contractility, resulting in straight non-adherent cellular edges, whereas $Co \gg 1$ leads to highly curved non-adherent cellular edges.

Figure 4.4 shows cells on the V-pattern as a function of the anchoring number *An* (on the vertical axis) and as a function of the contractility number *Co* (on the horizontal axis). For $Co = 0$, the cell has a triangular shape, whereas for nonzero *Co* the free edge at the top curves inwards. Similarly to what we observed in Figure 4.2b, for $An = 10$ the stress fibers align with the edge throughout the complete cell, leading to topological defects in the cell interior. Different from the circular and spherocylindrical shapes in Figure 4.2b, in the triangle these defects have topological charge $-1/2$. For smaller *An*, however, the boundary anchoring is too small to bend the stress fibers sufficiently to align with all edges. Consequently, the cytoskeleton aligns in the vertical direction, leading to perpendicular alignment with the non-adherent cell edge. We note that *An* indirectly also influences the cell shape: for nonzero constant stress fiber contractility (i.e., constant $Co > 0$), increasing *An* leads to more tangential alignment of the stress fibers with the cell edge. Because the directed contractile bulk force is proportional to $(\boldsymbol{n} \cdot \boldsymbol{N})^2$ [Eq. (4.6)], stress fibers exert a larger contractile force on the cell edge when they are oriented perpendicular to the edge than when they are parallel. Consequently, increasing *An* decreases the contractile force experienced by the cell edge, as can be seen in the right column of Figure 4.4.

The result for large boundary anchoring and intermediate contractility best resembles the actin structures found in epithelial cells in Ref. [210] and in numerical simulations in Ref. [77]. However, an important difference is that in those studies, stress fibers align more with the non-adhesive, concave edge at the top of the pattern than with the other two edges, leading to a more horizontal actin orientation in the cell interior. This discrepancy is most likely explained by the experimental observation that stress fibers form more prominently along concave edges than along convex edges [43, 210, 211, 240], whereas our current model does not discriminate between those. Taking this difference into account will be an important step to improve the realism of our cytoskeleton model in the future.

Figure 4.5 shows cells on the crossbow pattern (Figure 4.3b), again as a function of the anchoring number (vertical axis) and contractility number (horizontal axis). For small boundary anchoring, the cytoskeleton again orients vertically, leading to perpendicular alignment at the bottom and top of the crossbow shape. Conversely, for large *An*, stress fibers orient parallel to the edge throughout the cell. Interestingly, the top row of Figure

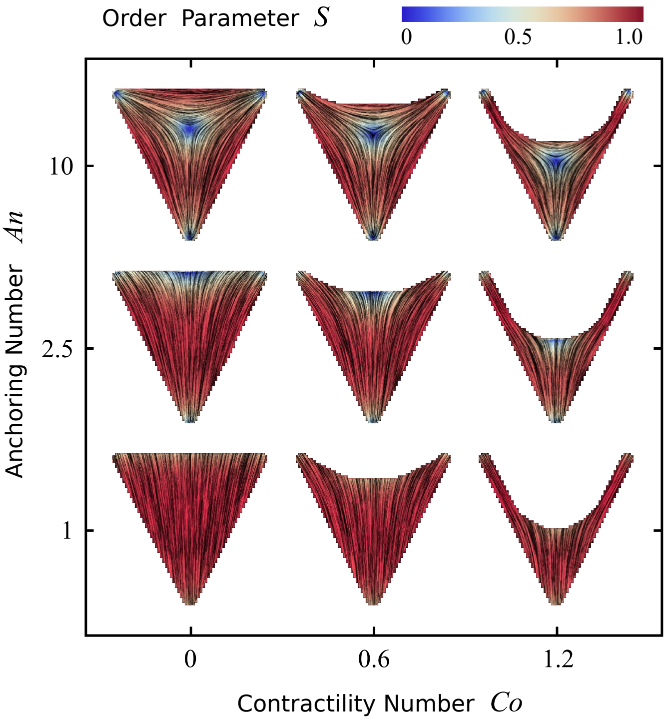

**Figure 4.4.** Cells on adhesive micropatterns in the shape of the letter V (see Figure 4.3a). The black lines in the interior of the cells represent the orientation field $\boldsymbol{n} = (\cos\theta_{\mathrm{SF}}, \sin\theta_{\mathrm{SF}})$ of the stress fibers and the background color indicates the nematic order parameter $S$. The vertical axis corresponds to the anchoring number $An = WR/K = 1, 2.5, 10$ (with $R = 60$ lattice sites) and the horizontal axis to the contractility number $Co = \sigma d/\lambda = 0, 0.6, 1.2$ (with $d = 60$ lattice sites). The spatial averages of the order parameter are given, from left to right, by: $0.76; 0.77; 0.75$ (top row), $0.83; 0.85; 0.83$ (middle row), and $0.93; 0.92; 0.91$ (bottom row). For all cells, $\delta = 9$ lattice sites, $\alpha_0/\sigma = 2$, $\mu/\lambda = 1/30$ lattice sites, $\mu/|\gamma_{\mathrm{ad}}| = 1/20$ of the area of a lattice site, and $K\Delta t/(\xi_r R^2) = 2.5 \cdot 10^{-6}$. For definitions of $\Delta t$ and $\xi_r$, see Section 4.4.2 in the Appendix.

4.5 illustrates that *Co* indirectly influences the orientation of stress fibers: increasing the bulk contractility changes the cell shape and therefore affects the boundary conditions for the orientation of the cytoskeleton. As a result, the main orientation of the stress fibers switches from vertical to horizontal, and the two topological defects of charge $+1/2$ at opposite ends of the cell are replaced by three $+1/2$ defects surrounding a $-1/2$ defect in the center. The cell shape at intermediate contractility values (middle column in Figure 4.5) resembles the shape of epithelial cells on a crossbow pattern found experimentally by Tseng *et al.* [43] and computationally by Albert and Schwarz [69], and the actin orientation reported in Tseng *et al.* is best reproduced by low to intermediate

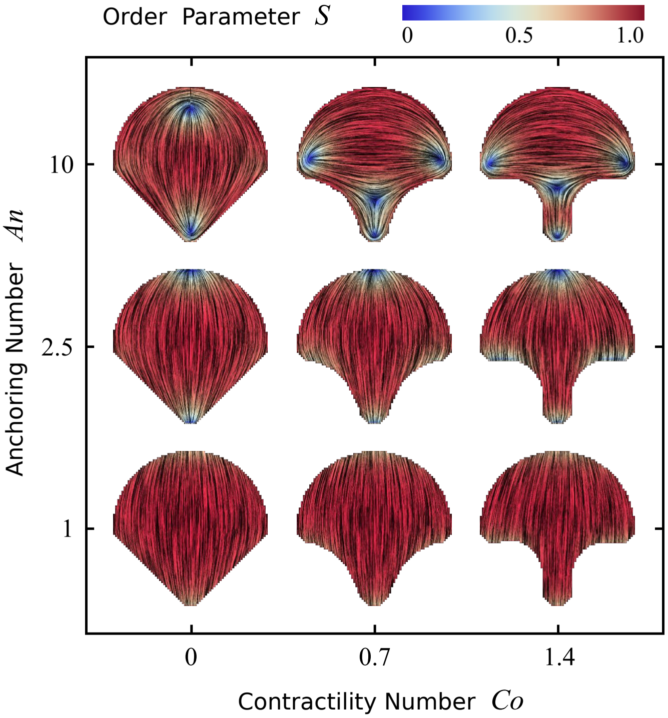

**Figure 4.5.** Cells on adhesive micropatterns in the shape of a crossbow (see Figure 4.3b). The black lines in the interior of the cells represent the orientation field $\boldsymbol{n} = (\cos\theta_{\mathrm{SF}}, \sin\theta_{\mathrm{SF}})$ of the stress fibers and the background color indicates the nematic order parameter $S$. The vertical axis corresponds to the anchoring number $An = WR/K = 1, 2.5, 10$ (with $R = 60$ lattice sites) and the horizontal axis to the contractility number $Co = \sigma d/\lambda = 0, 0.7, 1.4$ (with $d = 42$ lattice sites). The spatial averages of the order parameter are given, from left to right, by: $0.84; 0.79; 0.80$ (top row), $0.89; 0.87; 0.85$ (middle row), and $0.95; 0.94; 0.93$ (bottom row). For all cells, $\delta = 9$ lattice sites, $\alpha_0/\sigma = 2$, $\mu/\lambda = 1/30$ lattice sites, $\mu/|\gamma_{\mathrm{ad}}| = 1/20$ of the area of a lattice site, and $K\Delta t/(\xi_r R^2) = 2.5 \cdot 10^{-6}$. For definitions of $\Delta t$ and $\xi_r$, see Section 4.4.2 in the Appendix.

boundary anchoring.

### 4.2.4 Traction forces on micropatterns

The steady-state configuration of cells, as shown in Sections 4.2.1, 4.2.2, and 4.2.3, are obtained when the terms in the Hamiltonian [Eq. (4.7)] reach a mechanical equilibrium. On top of the micropatterned areas, the adhesive force applied by the substrate [last term in Eq. (4.7)] balances the contractile forces generated by the cell [first two terms in Eq. (4.7)]. The traction force that the cell edge exerts on the substrate is equal and opposite

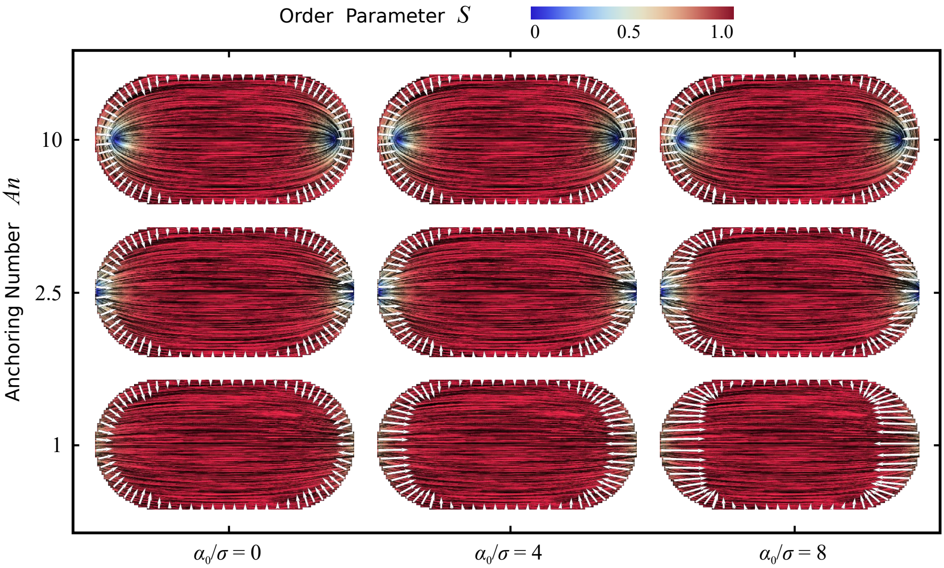

**Figure 4.6.** Traction forces of cells adhering to a micropattern in the shape of a stadium (same shape as in Figure 4.2). The black lines in the interior of the cells represent the orientation field $\boldsymbol{n} = (\cos\theta_{\mathrm{SF}}, \sin\theta_{\mathrm{SF}})$ of the stress fibers, the background color indicates the nematic order parameter $S$, and the white arrows represent the traction forces exerted on the substrate by the cell. On the vertical axis the anchoring number $An = WR/K = 1, 2.5, 10$ (with $R = 60$ lattice sites) is varied, and on the horizontal axis the ratio $\alpha_0/\sigma = 0, 4, 8$. The spatial averages of the order parameter are given, from left to right, by: $0.92; 0.92; 0.92$ (top row), $0.94; 0.94; 0.94$ (middle row), and $0.97; 0.97; 0.97$ (bottom row). For all cells, $\delta = 9$ lattice sites, $\lambda/\sigma = 60$ lattice sites, $\mu/\lambda = 1/30$ lattice sites, $\mu/|\gamma_{\mathrm{ad}}| = 1/20$ of the area of a lattice site, and $K\Delta t/(\xi_r R^2) = 2.5 \cdot 10^{-6}$. For definitions of $\Delta t$ and $\xi_r$, see Section 4.4.2 in the Appendix.

to the adhesive force applied by the substrate, and given by:

$$\boldsymbol{f}_{\mathrm{trac}} = (\lambda\kappa + \sigma)\boldsymbol{N} + \alpha_0 S(\boldsymbol{n}\cdot\boldsymbol{N})\boldsymbol{n} \ , \tag{4.13}$$

which is different from Eq. (4.2) because here we assume the line tension $\lambda$ to be constant (see Section 4.2.1). The isotropic contractility $\sigma$ and the line tension $\lambda$ generate forces normal to the cell edge [first term in Eq. (4.13)]. However, the anisotropic contractility caused by actin stress fibers, given by the last term of Eq. (4.13), points the traction forces in the direction of the local stress fiber orientation $\boldsymbol{n}$, consistent with experimental observations in Refs. [89, 90] and in Chapter 2 of this thesis. Consequently, the traction forces in Eq. (4.13) do not point purely along the surface normal $\boldsymbol{N}$, in contrast to traction forces in many previous models for cell contractility [196, 234, 235]. Hence, in our model, the degree to which the traction forces deviate from the normal direction depends on the local orientation of stress fibers $\boldsymbol{n}$, the ratio between the directed contractility $\alpha_0 S$ and the parameters $\sigma$ and $\lambda$, and on the local curvature $\kappa$ of the cell edge. For a description of how the curvature is numerically calculated, see Section 4.4.1 in the Appendix.

Figure 4.6 shows the traction forces at the cell periphery of cells on an adhesive micropattern in the shape of a stadium (see Figure 4.2), as a function of the anchoring number *An* (vertical axis) and the directed bulk contractility $\alpha_0$ (horizontal axis). Here, the micropattern shape controls the curvature $\kappa$, *An* controls the orientation of the stress fibers $\boldsymbol{n}$ (Section 4.2.2), and $\alpha_0$ sets the relative importance of directed stresses with respect to the other stresses in the cell. For $\alpha_0 = 0$ (left column of Figure 4.6), all traction forces are independent of the stress fiber orientation $\boldsymbol{n}$ and normal to the surface. At the circular caps, the larger curvature increases the effect of the line tension [Eq. (4.13)], which increases the traction forces, reproducing findings on the relation between local curvature and traction from earlier models [69, 73, 196] and from experimental observations [90, 195, 196, 241].

The other extreme, where $\alpha_0/\sigma = 8$, is shown in the right column of Figure 4.6. For *An* $= 10$ the difference with the case of zero directed contractility is negligible because the stress fibers ($\boldsymbol{n}$) are parallel to the cell boundary (perpendicular to $\boldsymbol{N}$) everywhere, hence $\alpha_0 S(\boldsymbol{n} \cdot \boldsymbol{N})\boldsymbol{n} = \boldsymbol{0}$ [Eq. (4.13)] independent of the value of $\alpha_0$. In other words, if the stress fibers are perfectly parallel to the cell edge, they cannot pull on it. For lower anchoring numbers (*An* $= 1$, *An* $= 2.5$), however, the effect of increasing $\alpha_0$ is evident, as the traction forces largely align with the local stress fiber orientation. Because of the longitudinal orientation of the stress fibers, the traction forces at the end of the circular caps increase in magnitude with respect to the forces at other locations, and this effect is strongest for *An* $= 1$ because in that case stress fibers are almost perpendicular to the ends of the circular caps. Moreover, unlike in many other traction force models [69, 196, 234, 235], the traction forces at the caps deviate significantly from the normal vector of the cell boundary. Interestingly, this deviation in orientation from the surface normal is largest for intermediate anchoring number (*An* $= 2.5$), because the tangential component of the traction force is proportional to $(\boldsymbol{n} \cdot \boldsymbol{N})(\boldsymbol{n} \cdot \boldsymbol{T})$ [Eq. (4.13)], which is maximized at a $\pi/4$ angle between the stress fibers and the boundary. In other words, the tangential component of the traction force is maximized when stress fibers are not too perpendicular to the boundary, but not too parallel either, because parallel stress fibers do not pull on the boundary.

For intermediate values of $\alpha_0$ (middle column in Figure 4.6, $\alpha_0/\sigma = 4$), traction force magnitude and orientation are determined by a combination of local boundary shape and local stress fiber orientation. The resulting traction force patterns for *An* $= 1$ and *An* $= 2.5$ qualitatively reproduce experimental traction force patterns of fibroblasts reported by Oakes *et al.* [196] and of endothelial cells reported by Roca-Cusachs *et al.* [89]. Not only are these experimentally observed traction forces larger at the spherical caps than elsewhere, as was already reproduced by the isotropic model put forward in Ref. [196], but they clearly deviate from the normal direction toward the stress fibers, which are oriented along the longitudinal direction of the stadium. Hence, our model qualitatively reproduces not only the structure of the cytoskeleton (see Section 4.2.2), but also both the magnitudes and the directions of the experimentally observed traction forces.

Next, we study traction forces on an adhesive mircropattern in the shape of a crossbow (see Figures 4.3b and 4.5). Figure 4.7 shows the cells and the traction forces at the cell boundary on the adhesive part of the substrate (Figure 4.3b) as a function of the anchoring number *An* (vertical axis) and the directed bulk contractility $\alpha_0$ (horizontal axis). For $\alpha_0 = 0$ (left column of Figure 4.7), traction forces are again independent of the stress fiber orientation and normal to the surface. Because of larger local curvature, the forces are larger at the left, bottom, and right sides of the cell. Similar to what we observed in Figure 4.6, for $An = 10$ the traction forces are independent on the directed contractility $\alpha_0$ because stress fibers parallel to the cell boundary cannot pull on it. For lower anchoring numbers, increasing the directed bulk contractility is more interesting. First, traction forces are again deviating from the cell boundary's normal vector, and are biased toward the local stress fiber orientation. This is most evident in the cells with $An = 1, An = 2.5$ and $\alpha_0/\sigma = 8$, where traction forces in the top left and top right of the crossbow point downward and forces in the bottom left and bottom right corners point upward. Moreover, the forces increase in magnitude, as a function of $\alpha_0$, at the top and bottom of the pattern, where the stress fibers orient perpendicular to the boundary. Similar to what we observed in Figure 4.6 on the stadiums, the magnitudes of the forces are largest for $An = 1$, whereas the orientations of the forces deviate most from the surface normal at $An = 2.5$.

Comparing the results for low and intermediate anchoring and nonzero directed bulk contractility in Figure 4.7 with the experimentally reported traction forces of epithelial cells on a crossbow pattern in Tseng *et al.* [43] yields a number of interesting observations. First, the general orientation of the traction forces around the boundary and the increased magnitudes of the traction forces at the bottom, left, and right sides of the pattern agree well between theory and experiment, but these features were previously explained by an isotropic Cellular Potts Model in the work of Albert and Schwarz [69]. However, Tseng *et al.* [43] additionally report an increase in traction force magnitude at the top of the pattern. This increase was not reproduced in the isotropic model of Albert and Schwarz [69], who suggested this discrepancy might be due to the presence of stress fibers along the long side of the pattern (vertical) in the experiments, which are absent in their model. Our results do show these stress fibers and a resulting increase in traction force magnitude at the top of the pattern, demonstrating that the anisotropy of the actin cytoskeleton is a likely explanation for the discrepancy between the experimental data in Ref. [43] and the simulations in Ref. [69]. Moreover, Albert and Schwarz report that the traction forces in the left and right corners of the crossbow pattern are directed more upward in the experimental data than in their model. In our numerical predictions for low and intermediate boundary anchoring, these forces do point more upward because of the directed pull of the stress fibers, although a comparison with the experimental

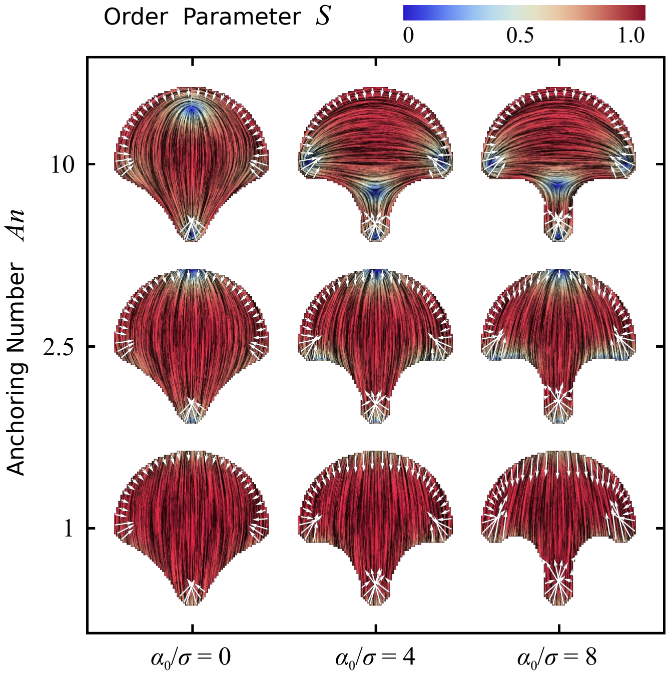

**Figure 4.7.** Traction forces of cells adhering to a micropattern in the shape of a crossbow (same shape as in Figures 4.3b and 4.5). The black lines in the interior of the cells represent the orientation field $\boldsymbol{n} = (\cos\theta_{\mathrm{SF}}, \sin\theta_{\mathrm{SF}})$ of the stress fibers, the background color indicates the nematic order parameter $S$, and the white arrows represent the traction forces exerted on the substrate by the cell. On the vertical axis the anchoring number $An = WR/K = 1, 2.5, 10$ (with $R = 60$ lattice sites) is varied, and on the horizontal axis the ratio $\alpha_0/\sigma = 0, 4, 8$. The spatial averages of the order parameter are given, from left to right, by: $0.82; 0.80; 0.81$ (top row), $0.88; 0.86; 0.84$ (middle row), and $0.94; 0.94; 0.93$ (bottom row). For all cells, $\delta = 9$ lattice sites, $\lambda/\sigma = 60$ lattice sites, $\mu/\lambda = 1/30$ lattice sites, $\mu/|\gamma_{\mathrm{ad}}| = 1/20$ of the area of a lattice site, and $K\Delta t/(\xi_r R^2) = 2.5 \cdot 10^{-6}$. For definitions of $\Delta t$ and $\xi_r$, see Section 4.4.2 in the Appendix.

data in Ref. [43] shows that they point upward too much. This discrepancy between our data and the experiments might be due to the fact that stress fibers often occur more prominently along non-adhesive cell edges (see, e.g., Refs. [43, 210, 211, 240]), which would lead to an effective downward pull at the left and right corners of the crossbow pattern. This effect was taken into account in the model of Albert and Schwarz, but is absent in our current model because we assume the line tension $\lambda$ to be constant.

## 4.3 Discussion and conclusions

In this chapter we developed a hybrid liquid crystal-Cellular Potts Model (LC-CPM) framework able to account for the effect of directed forces, originating from actin stress fibers, on cell contractility. We first verified the method by comparing the shapes of single cellular arcs in the CPM with analytical predictions. Then, we combined our model for anisotropic contractility with a model for the organization of the actin cytoskeleton that we developed in Chapter 3, where the orientation of stress fibers is governed by a competition between the tendency of stress fibers to align tangentially to the cell edges and the tendency to align parallel with one another in the cell interior. We verified that the hybrid LC-CPM method reproduces earlier numerical results on rectangular cells (Figure 3.12), and qualitatively reproduces experimentally observed stress fiber distributions on convex adhesive micropatterns in the shape of circles [215] and stadiums [196], and on non-convex patterns in the shape of a crossbow [43]. Finally, we calculated the traction forces that cells exert on adhesive micropatterns, showing that the direction of these forces is strongly influenced by the anisotropy of the stress fibers. In particular, we present a numerical method that, unlike many theoretical models [69, 196, 234, 235], produces traction forces whose orientations deviate away from the normal vector of the cell edge and toward the stress fiber orientation, in agreement with experimental observations [89, 90, 194]. Importantly, our model qualitatively predicts prominent anisotropic features in traction force patterns reported in previously published experimental data on fibroblasts and endothelial cells adhering to micropatterns with stadium shape [89, 196] and epithelial cells on micropatterns with crossbow shape [43], which were not captured by earlier models [69, 196]. Hence, our numerical approach rationalizes findings on anisotropic traction force patterns in earlier experiments, suggesting an important role for stress fibers that is worth investigating, both experimentally and theoretically, in much greater detail.

The main drawback of our current model is that it is *a priori* unclear how to adapt the phenomenological parameters of the cytoskeleton, captured in the anchoring number $An = WR/K$ [Eq. (4.11)], for different cells types, environmental conditions, or even different arcs within the same cell (see also the discussion of Figure 4.4 in Section 4.2.3). For instance, in Chapter 3 we employed this model of the cytoskeleton to study concavely shaped epithelioid and fibroblastoid cells adhering to microfabricated pillar arrays, and found that cells are best described by sufficiently large boundary anchoring of the stress fibers ($An \gtrsim 3$). In this chapter, however, we found qualitative agreement with experimental traction force patterns of fibroblasts, endothelial cells and epithelial cells, adhering to convexly shaped micropatterns, for lower boundary anchoring values ($An = 1$ and $An = 2.5$). A possible explanation for this discrepancy can be found in the fact that concave cell edges promote stress fiber formation more than convex cell edges do [43, 210, 211, 240], an effect that is not present in our current model. We emphasize, however, that our methods for implementing directed cell contractility [Eq. (4.6)] and non-normal traction forces [Eq. (4.13)] in the CPM do not crucially depend on our model for the cytoskeleton (Section 4.2.2), but can be combined with any model for the orientation of stress fibers. This offers opportunities to, in the future, include other effects into the model, such as the viscoelasticity of stress fibers and actin filament turnover [206, 207], the distinction between different subtypes of stress fibers [242], spatial variations in actin densities [176, 196, 210, 211], and the increase of cytoskeletal tension with substrate stiffness [198] or with substrate area [195–197].

We have focused our traction force analysis on the edge of the cell. Although this is not unreasonable, as traction forces are largest far away from the cell centroid [200, 228, 229] and accumulate at the cell periphery [201, 202], predicting traction forces in the cell interior would help in quantitative comparisons between theory and experiment in the future [69, 136]. Furthermore, our model could serve as a starting point for studying the role of stress fiber contractility and anisotropy in cell spreading and migration. In the framework of the Cellular Potts Model, this could be obtained by combining our model for stress fiber contractility with current CPM implementations of cell motility that depend on the formation of a lamellipodium at the cell's leading edge [124, 125]. Integrating our stress fiber description with these models could improve the realism of persistent cell motion, which crucially depends on pulling forces at the cell's rear end [243, 244]. The resulting model could then be employed to computationally study the role of cytoskeletal anisotropy in spreading of single [69, 118, 210, 230] or multiple [245] cells on micropatterns, to explore the effects of cytoskeletal anisotropy on cell-substrate interactions [136, 189], and to better understand the migration of persistent cells in complex topographies [143, 246] (see also Chapter 5). Finally, as the Cellular Potts Model is an excellent tool to computationally study multicellular systems [9], our work can serve as a starting point to study the role of cytoskeletal anisotropy in tissues [111, 217–223].

## 4.4 Appendix

### 4.4.1 Calculating cell perimeter, normal vector, and curvature

**Calculating the cell perimeter** In order to avoid lattice effects, one cannot simply compute the length of the perimeter $P$ by calculating the total edge length of the cell on the square lattice. Instead, we employ an algorithm that smoothens out lattice effects, which was developed and described in detail in Ref. [247]. Briefly, for every lattice point inside the cell a circular neighborhood of radius $R$, centered at this lattice point, is defined. For all simulations we have used $R = \sqrt{5}$. Then, the algorithm counts, for every lattice point, the number of lattice points whose center lies inside the neighborhood but outside the cell, and the resulting numbers are added up for all lattice points inside the cell. Finally the result is divided by a scaling factor, that depends on the neighborhood size used, to obtain $P$. In all simulations we have used a scaling factor of 11 [247].

**Calculating the normal vector** Again to avoid lattice effects, the normal vector of the cell $\boldsymbol{N} = (\cos\psi, \sin\psi)$ cannot be evaluated as the normal vector of an edge between

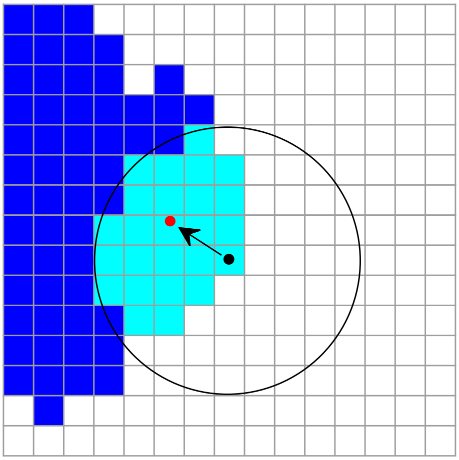

**Figure 4.8.** Schematic of the calculation of the normal vector at a lattice site (black dot) at the edge of the cell. The cell is represented by the blue lattice sites. The normal vector is calculated as the unit vector pointing from that lattice site to the center of mass (red dot) of the collection of lattice sites that are both inside the cell and inside a circular neighborhood of radius $R$ around that lattice site (cyan lattice sites).

two lattice sites. Instead, we calculate the normal vector at a given lattice site at the cell edge by again considering a circular neighborhood of radius $R$ centered at that lattice site. This is illustrated in Figure 4.8, where the black dot indicates the lattice site of interest, the lattice sites inside the cell are blue, and those outside the cell are white. Along the lines of Ref. [69], the normal vector $\boldsymbol{N}$ at a given edge lattice site is then calculated as the unit vector pointing from that lattice site to the center of mass (red dot) of the collection of lattice sites that are both inside the cell and inside the neighborhood (cyan lattice sites). In our simulations [Eq. (4.7)], we have used $R = \sqrt{5}$, whereas for the calculation of traction forces [Eq. (4.13)], we have used $R = 10.5$.

**Calculating the curvature** The curvature $\kappa$ is required to calculate traction forces [Eq. (4.13)], and is obtained by calculating the derivative of the normal angle $\psi$ to the arc length $s$, $\partial_s \psi$. This is done by first defining the boundary of the cell as the collection of lattice sites that are inside the cell but have at least one neighbor lattice site (Moore neighborhood, 8 neighbors) that is outside the cell, and labeling all boundary lattice sites with an integer $i$ such that the two neighboring (Von Neumann neighborhood, 4 neighbors) boundary lattice sites have labels $i-1$ and $i+1$. At each of these boundary lattice sites we calculate $\psi$ by calculating the normal vector using a neighborhood with $R = 10.5$. The derivative $\partial_s \psi$ is then calculated using a finite difference approximation taking into account the lattice site of interest $i$ and the boundary lattice sites $i-n$

and $i+n$, with $n$ an integer and where the distances $\Delta s_-$ (distance between lattice sites $i-n$ and $i$) and $\Delta s_+$ (distance between lattice sites $i$ and $i+n$) required for the final difference approximation are, to avoid lattice effects, the shortest distances between the centers of the two lattice sites rather than distances measured along the discrete boundary. Consequently, $\Delta s_-$ and $\Delta s_+$ are in general not equal.

The value of $n$ that produces the most accurate approximation of the curvature depends on the actual curvature of the cell boundary. Therefore, we first estimate the radius of curvature $r = 1/\kappa$ at a given lattice site using $n = 3$. Then, we calculate the curvature again using $n = 2$ if the initial radius of curvature $r < 14$ lattice sites, $n = 3$ for $14 < r < 25$ lattice sites, $n = 4$ for $25 < r < 35$ lattice sites, and $n = 5$ if $r > 35$ lattice sites. In this way we obtain the curvature at each boundary lattice site with a systematic error $< 1\%$ and a random error $< 5\%$.

### 4.4.2 Numerical methods

Here we describe the procedure, step by step, that we use to generate the numerical results shown in Figures 4.1-4.7.

**1)** Initialization.

**1a)** Define the lattice sites that are part of the adhesive micropattern. These are illustrated in Figures 4.1a, 4.2a, and 4.3.

**1b)** Define the lattice sites that are initially part of the cell. For the data in Figure 4.1 this is illustrated in Figure 4.1a. For the other data, the initial cell shape is identical to the shape of the adhesive micropattern.

**1c)** Define the cytoskeleton by defining $\hat{\boldsymbol{Q}}$ at every lattice site. In Figures 4.1b,c $S$=0 at each lattice site, and in Figures 4.1d-f $S = 1$ and $\theta_{\mathrm{SF}} = \pi/2$ at each lattice site. In the other figures, each lattice site is assigned random initial values for the orientation $-\pi/2 \leq \theta_{\mathrm{SF}} \leq \pi/2$ and the nematic order parameter $0 \leq S \leq 1$, from which $\hat{\boldsymbol{Q}}$ is calculated using Eq. (4.8). This initial cell configuration does not describe a realistic cell, but it minimizes the risk of a possible bias in the final configuration.

**2)** Cell configuration updates. Perform the following steps for a predefined number of Monte Carlo steps (MCS), which is chosen such that both the cell shape and the cytoskeleton reach a steady-state configuration. 20,000 MCS are performed for the data in Figure 4.1, 10,000 MCS are performed for the data with *An* $= 2.5$ in Figures 4.2-4.7, and 30,000 MCS are performed for the other data in Figures 4.2-4.7.

**2a)** Update the cell shape by performing one Monte Carlo step of the Cellular Potts Model using the change in Hamiltonian described by Eq. (4.7). One MCS represents a number of CPM updates equal to the number of lattice sites in the simulation. If a lattice site inside the cell is copied into the surrounding medium, the associated $\hat{\boldsymbol{Q}}$ is copied with it. If, conversely, a lattice site in the medium is copied into a lattice site that is inside the cell, $\hat{\boldsymbol{Q}}$ at that specific lattice site is discarded.

**2b)** Update the cytoskeleton. This step is skipped for the simulations reported in Figure 4.1. The free energy $F_{\mathrm{cyto}}$ in Eq. (4.9) is minimized using overdamped relaxational dynamics:

$$\partial_t Q_{ij} = -\frac{1}{\xi_r}\,\frac{\delta F_{\text{cyto}}}{\delta Q_{ij}}\ , \tag{4.14}$$

where $Q_{ij}$ represents the various components of $\hat{\boldsymbol{Q}}$, and $\xi_r$ is a rotational friction coefficient required for dimensional consistency. $\xi_r$ dictates the rate of the relaxational dynamics but does not affect the steady-state solution. To ensure the free-energy to be minimal in steady-state (i.e., when $\partial_t Q_{ij} = 0$), Eq. (4.14) is solved with Neumann boundary conditions:

$$K\boldsymbol{N}\cdot\nabla Q_{ij} - 2W\left(Q_{ij} - Q_{0,ij}\right) = 0\ . \tag{4.15}$$

At each time step $\Delta t$, $\hat{\boldsymbol{Q}}$ is updated at every lattice point by discretizing Eq. (4.14) using a forward Euler method. For details on this procedure and on the boundary conditions, see Section 3.6.2 . For every Monte Carlo step (MCS), 50 time steps of the cytoskeleton are performed.

**3)** Final configurations

**3a)** The final configurations are determined by averaging the configurations of the last 3,000 MCS of the simulation. If a lattice site was inside the cell for more than 50% of this time, it is considered inside the final configuration. Otherwise, it is considered to be outside the cell. For lattice sites inside the final configuration, the local $\hat{\boldsymbol{Q}}$ is determined by averaging $\hat{\boldsymbol{Q}}$ over all MCS (within the last 3,000 MCS of the simulation) when this lattice site was inside the cell.

**3b)** The final configurations are plotted in Figures 4.1-4.7. The cytoskeleton is visualized with Mathematica Version 11.3 (Wolfram Research, Champaign, IL) using the line integral convolution tool. When using this tool we define $S = 1$ outside the cell, while $\theta_{\text{SF}}$ is not defined outside the cell.

# Part II

# Cell migration

## CHAPTER 5

# TOPOTAXIS OF ACTIVE BROWNIAN PARTICLES

This chapter is reprinted with permission, copyright 2020 by the American Physical Society. The chapter is published as:

Koen Schakenraad, Linda Ravazzano, Niladri Sarkar, Joeri A.J. Wondergem, Roeland M.H. Merks, and Luca Giomi, 'Topotaxis of active Brownian particles', Physical Review E **101**, 032602 (2020)

## Abstract

Recent experimental studies have demonstrated that cellular motion can be directed by topographical gradients, such as those resulting from spatial variations in the features of a micropatterned substrate. This phenomenon, known as *topotaxis*, has been extensively studied for topographical gradients on the sub-cellular scale, but can also emerge as a result of topographical gradients at length scales larger than the cell. This large-scale topotaxis has recently been observed for highly motile cells that persistently crawl within a spatially varying distribution of cell-sized obstacles. In this chapter we introduce a toy model of large-scale topotaxis based on active Brownian particles constrained to move in a lattice of obstacles, with space-dependent lattice spacing. Using numerical simulations and analytical arguments, we demonstrate that topographical gradients introduce a spatial modulation of the particles' persistence, leading to directed motion toward regions of higher persistence. Our results demonstrate that persistent motion alone is sufficient to drive large-scale topotaxis and could serve as a starting point for more detailed studies on self-propelled particles and cells.

## 5.1 Introduction

Whether *in vitro* or *in vivo*, cellular motion is often biased by directional cues from the cell's micro-environment. *Chemotaxis*, i.e., the ability of cells to move in response to chemical gradients, is the best known example of this functionality and plays a crucial role in many aspects of biological organization in both prokaryotes and eukaryotes [127, 128]. Yet, it has become increasingly evident that, in addition to chemical cues, mechanical cues may also play a fundamental role in dictating how cells explore the surrounding space. *Haptotaxis* (i.e., directed motion driven by gradients in the local density of adhesion sites) and *durotaxis* (i.e., directed motion driven by gradients in the stiffness of the surrounding extracellular matrix) are well studied examples of taxa driven by mechanical cues [131, 132, 134].

*In vivo*, cells crawl through topographically intricate environments, such as the extracellular matrix, blood and lymphatic vessels, other cells, etc. Complex environments like these can significantly influence cellular migration strategies [248–255], and asymmetries in the topographical properties of the environment can serve as a directional cue for cell migration in a process called *topotaxis*. This term was used in early work on directed cell migration as a synonym for the general term “taxis” [256], but was recently redefined by Park *et al.* to describe directed motion of invasive melanoma cells on substrates with a spatial gradient in the density of nanoscale posts [140]. In general, the term “topotaxis” is suitable to describe any directional cue due to local anisotropy in the topographical properties of the surrounding environment. For instance, adhesive ratchets [137–139] and several types of anisotropic subcellular structures [137, 141, 142, 257, 258] have also been shown to lead to directed cell migration. In all of these examples, cell motion is biased due to topographical cues at sub-cellular length scales. More recently, Wondergem and coworkers demonstrated that topotaxis can also be achieved by topographical cues at length scales larger than the cell itself [143]. They studied single, highly motile, persistently migrating cells (i.e., cells performing amoeboid migration), moving on a substrate in between cell-sized micropillars that act as obstacles and consequently force the cells to move around them. If the obstacles' density smoothly varies across the substrate at length scales larger than the cell size, the cells perform *large-scale topotaxis*: the topographical gradient serves as a directional cue for the cells to move toward the regions of lower obstacle density.

Although the precise biophysical or biochemical principles behind this large-scale topotaxis, as observed in Ref. [143], are presently unknown, its occurrence for cells performing amoeboid migration suggests the possibility of cell-type-independent mechanisms that, separately from the cell's mechanosensing machinery, provide a generic route to the emergence of large-scale topotaxis. In this chapter we explore this hypothesis. Inspired by the observations on persistently migrating cells by Wondergem *et al.* [143], we study active Brownian particles (ABPs) constrained to move within a lattice of obstacles. We demonstrate that large-scale topotaxis of ABPs can result solely from the spatial modulation of persistence resulting from the interaction between the particles and the obstacles.

ABPs represent a simple stochastic model for self-propelled particles, such as active Janus particles [259], and for cell motility on flat substrates [116]. ABPs perform persistent self-propelled motion in the direction of the particle orientation in combination with rotational diffusion of this orientation. The motion of active particles has been explored in several complex geometries, including convex [260, 261] and non-convex [262] confinements, mazes [263], walls of funnels [264], interactions with asymmetric [265, 266] and chiral [267] passive objects, periodic [268] and random [269–272] obstacle lattices, and porous topographies [273]. For a review, see Refs. [144, 145]. Because of the non-equilibrium nature of active particles, local asymmetries in the environment can be leveraged to create a drift; these particles have been demonstrated to perform chemotaxis [155, 156], durotaxis [157], and phototaxis [158]. Furthermore, topographical cues, such as those obtained in the presence of arrays of asymmetric posts [149, 150] and ratchets consisting of asymmetric potentials [146–148] or asymmetric channels [151–154], have been shown to produce a directional bias in the motion of active particles reminiscent of those observed for cells.

In this chapter we study large-scale topotaxis of active Brownian particles, which we from here on simply refer to as "topotaxis". The chapter is organized as follows: in Section 5.2 we present our model for ABPs and their interaction with obstacles. In Section 5.3.1 we show that, in the presence of a gradient in the obstacle density, ABPs drift, on average, in the direction of lower density. The speed of this net drift, here referred to as topotactic velocity, increases as a function of both the density gradient and the persistence length of the ABPs. In Section 5.3.2 (numerically) and Section 5.3.3 (analytically) we study ABPs in regular obstacle lattices and demonstrate that the origin of large-scale topotaxis of active particles can be found in the altered persistence length of the particles in the presence of obstacles.

## 5.2 The model

Our model of ABPs consists of disks of radius $R_p$ self-propelling at constant speed $v_0$ along the unit vector $\boldsymbol{p} = (\cos\theta, \sin\theta)$ and subject to rotational white noise. The dynamics of the particles is governed by the following overdamped equations:

$$\frac{\mathrm{d}\boldsymbol{r}}{\mathrm{d}t} = v_0\boldsymbol{p} + \mu\boldsymbol{F} \ , \tag{5.1a}$$

$$\frac{\mathrm{d}\theta}{\mathrm{d}t} = \sqrt{2D_r}\,\xi \ , \tag{5.1b}$$

where $\boldsymbol{r} = \boldsymbol{r}(t)$ is the position of the particle, $t$ is time, and $\mu$ is a mobility coefficient. The force $\boldsymbol{F} = \boldsymbol{F}(\boldsymbol{r})$ embodies the interactions between the particles and the obstacles. $\xi = \xi(t)$ is a random variable with zero mean, i.e., $\langle\xi(t)\rangle = 0$, and time-correlation $\langle\xi(t)\xi(t')\rangle = \delta(t - t')$. The extent of rotational diffusion is quantified by the rotational diffusion coefficient $D_r$, whereas translational diffusion is neglected under the assumption of large Péclet number: $\mathrm{Pe} \gg 1$. Overall, this set-up provides a reasonable toy model for highly motile cells such as those used in experimental studies of large-scale topotaxis [117, 143, 274]. For a study on the influence of the Péclet number on the motion of ABPs around obstacles, see, for example, Ref. [268, 270].

In free space, (i.e., $\boldsymbol{F} = \mathbf{0}$), ABPs described by Eqs. (5.1) perform a persistent random walk (PRW) with mean displacement $\langle \Delta \boldsymbol{r}(t) \rangle = 0$ and mean squared displacement:

$$\left\langle |\Delta \boldsymbol{r}(t)|^2 \right\rangle = 2 v_0^2 \tau_p^2 \left( \frac{t}{\tau_p} + \mathrm{e}^{-t/\tau_p} - 1 \right) \, , \tag{5.2}$$

where $\Delta \boldsymbol{r}(t) = \boldsymbol{r}(t) - \boldsymbol{r}(0)$ and $\langle \cdots \rangle$ represents an average over $\xi$ (see, e.g., Ref. [145]). The constant $\tau_p = 1/D_r$, commonly referred to as *persistence time*, quantifies the typical timescale over which a particle tends to move along the same direction. Thus, over timescales shorter than the persistence time, $t \ll \tau_p$, ABPs move ballistically with speed $v_0$: $\left\langle |\Delta \boldsymbol{r}(t)|^2 \right\rangle \approx (v_0 t)^2$, while over timescales larger than the persistence time, $t \gg \tau_p$, ABPs diffuse, i.e., $\left\langle |\Delta \boldsymbol{r}(t)|^2 \right\rangle = 4Dt$, with $D = v_0^2 \tau_p / 2$ the diffusion coefficient. From $\tau_p$, one can define a *persistence length*, $l_p = v_0 \tau_p$, as the typical distance travelled by a particle before losing memory of its previous orientation. Consistently, the autocorrelation function of the velocity $\boldsymbol{v} = \mathrm{d}\boldsymbol{r}/\mathrm{d}t$ ($\boldsymbol{v} = v_0 \boldsymbol{p}$ in free space) is given by:

$$\langle \boldsymbol{v}(t + \Delta t) \cdot \boldsymbol{v}(t) \rangle = v_0^2 \mathrm{e}^{-\Delta t/\tau_p} \, . \tag{5.3}$$

Our ABPs roam within a two-dimensional array of circular obstacles of radius $R_o$. Following Refs. [261, 262], the interactions between particles and obstacles are modeled via a force of the form:

$$\boldsymbol{F} = \begin{cases} -\frac{v_0}{\mu} (\boldsymbol{p} \cdot \boldsymbol{N}) \, \boldsymbol{N} & \text{if } |\Delta \boldsymbol{r}_o| \le R \, , \\ \mathbf{0} & \text{otherwise} \, , \end{cases} \tag{5.4}$$

where $\boldsymbol{N}$ is a unit vector normal to the obstacle surface, $|\Delta \boldsymbol{r}_o|$ is the distance between the obstacle center and the particle center, and the effective obstacle radius $R$ is the sum of the obstacle and the particle radii: $R = R_o + R_p$. Eq. (5.4) describes a frictionless hard wall force that cancels the velocity component normal to the obstacle surface whenever the particle would penetrate the obstacle, and vanishes otherwise. Therefore, the obstacle force $\boldsymbol{F}$ is either repulsive or zero, but never attractive. We stress that the wall force does not influence the particle orientation $\boldsymbol{p}$. Thus, a particle slides along an obstacle until either the obstacle wall becomes tangential to $\boldsymbol{p}$ or rotational diffusion causes the particle to rotate away. This is consistent with experimental observations on self-propelled colloids [260] as well as various types of cells [275, 276]. For details of the numerical implementation of Eqs. (5.1) and (5.4), see Section 5.5.1 in the Appendix. In the following sections, we measure time in units of the persistence time, i.e., $\tilde{t} = t/\tau_p$, and length in units of the effective obstacle radius, i.e., $\tilde{\ell} = \ell/R$.

## 5.3 Results

The motion of ABPs in different lattices of obstacles is visualized in Figure 5.1. Each panel shows 20 simulated trajectories with persistence length $\tilde{l}_p = 5$. Figures 5.1a,b show regular square lattices with dimensionless center-to-center obstacle spacings of $\tilde{d} = 2.5$ and $\tilde{d} = 4$ respectively. In Figure 5.1, the obstacles are graphically represented as disks of radius $R$ and the ABPs as point particles. To avoid biasing the statistics of the particle trajectories, ABPs start at a random location inside the unit cell of the regular square lattice (Figure 5.1c) at $\tilde{t} = 0$ with random orientation. All trajectories are shown for a total time of $\tilde{t} = 3$. Comparing the spreading of the active particles in Figure 5.1a with that in Figure 5.1b, we observe that the more dense the obstacle lattice is, the more it hinders the diffusion of the active particles. We will quantify this later.

To study topotaxis, we define an irregular square lattice comprising a linear gradient of the obstacle spacing in the positive $x-$direction. The latter is quantified in terms of a dimensionless parameter $r$ representing the rate at which the obstacle spacing increases as $x$ increases. Thus $r = 0$ corresponds to a regular square lattice, whereas large $r$ values correspond to rapidly increasing obstacle spacing. Figure 5.1d shows this lattice for $r = 0.07$ with 20 particle trajectories, starting in the origin at $\tilde{t} = 0$ with a random orientation, plotted for a simulation time of $\tilde{t} = 5$, where $\tilde{d} = 5$ represents the obstacle spacing in the center of the gradient region. The gradient region has a finite width (not visible in Figure 5.1d) and is flanked by regular square lattices to the left, with lattice spacing $\tilde{d}_{\text{min}} = 2.1$, and to the right, with lattice spacing $\tilde{d}_{\text{max}} = 2\tilde{d} - \tilde{d}_{\text{min}}$. The minimal and maximal obstacle-to-obstacle distances ($\tilde{d}_{\text{min}}$ and $\tilde{d}_{\text{max}}$, respectively) do not depend on the steepness of the gradient, and consequently the width of the gradient region decreases for steeper gradients (larger $r$). For a detailed description of both the regular and gradient lattices as well as an image of the gradient lattice including the regular lattices on the left and right, see Section 5.5.2 in the Appendix.

### 5.3.1 The emergence of topotaxis

To quantify topotaxis, we measure the average $x$ and $y$ coordinates, $\langle \tilde{x} \rangle$ and $\langle \tilde{y} \rangle$, as a function of time for $10^6$ particles. The results are given for five values of the dimensionless density gradient $r$ in Figure 5.2a and Figure 5.6a (Section 5.5.3 in the Appendix) for $x$ and $y$ respectively. The emergence of topotaxis is clear from Figure 5.2a: the active particles move, on average, in the positive $x-$direction, hence in the direction of lower obstacle density. As expected by the symmetry of the lattice, there is no net motion in the $y$ direction independently of the value of $r$ (Figure 5.6a, Section 5.5.3 in the Appendix). To further quantify topotaxis, we define the topotactic velocity as the average velocity in the positive $x$ direction in a time interval $\Delta t$, $v_{\text{top}} = \langle \Delta x \rangle / \Delta t$, and evaluate it between $\tilde{t} = 0$ and $\tilde{t} = 30$. Figures 5.2a and 5.2b show that $\tilde{v}_{\text{top}}$ is approximatively constant in time and proportional to the density gradient $r$.

Next, we investigate the effect of the intrinsic motion of the ABPs on topotaxis. This intrinsic motion is characterized by the persistence length $l_p = v_0 \tau_p$, which uniquely

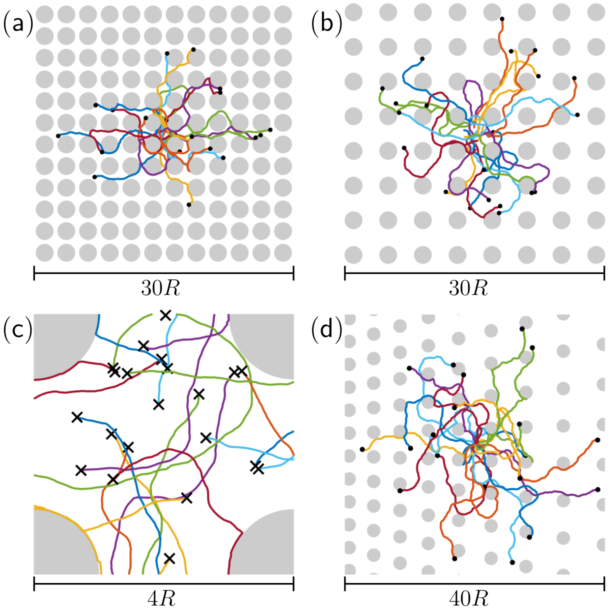

**Figure 5.1.** Simulated trajectories of 20 active Brownian particles (ABPs) with persistence length $\tilde{l}_p = v_0\tau_p/R = 5$ in different lattices of obstacles. The obstacles are graphically represented as disks of radius $R$ and the ABPs as point particles. (a,b) ABPs in regular square lattices of obstacles with center-to-center obstacle spacings $\tilde{d} = d/R = 2.5$ and $\tilde{d} = 4$ respectively. The particles start at $\tilde{t} = 0$ at a random location in the unit cell of the lattice and are simulated for a total time of $\tilde{t} = 3$. (c) The unit cell of the regular square lattice showing the starting points (crosses) of the 20 trajectories in (b). (d) ABPs in a lattice with a linear gradient in obstacle spacing, quantified by a dimensionless parameter $r = 0.07$ (see Section 5.5.2 in the Appendix), and $\tilde{d} = 5$ at the center of the gradient region. The particles start at $\tilde{t} = 0$ in the origin and are simulated for a total time of $\tilde{t} = 5$.

determines the statistics of the particle trajectory in free space. Namely, if two types of ABPs have different $v_0$ and $\tau_p$, but the same $l_p$, their trajectories have the same statistical properties, even though faster particles move along these trajectories in a shorter time. Figure 5.2c shows $\langle \tilde{x} \rangle$ as a function of time for five values of $\tilde{l}_p$. The speed of topotaxis is again approximately constant in time and increases with $\tilde{l}_p$ (Figure 5.2d). This trend partly results from the fact that increasing the persistence length corresponds either to an increment in $v_0$ or $\tau_p$, both resulting into an increase of $\tilde{v}_0$. However, Figure 5.2d shows that $\tilde{v}_{\text{top}}$ increases faster than linear as a function of $\tilde{l}_p$, suggesting an additional effect caused by the obstacle lattice. As we will see in Section 5.3.2, this effect is caused by the fact that the lattice hinders ABPs with large persistence lengths more than ABPs with smaller persistence lengths. Finally, we note that there is no net motion in the $y$

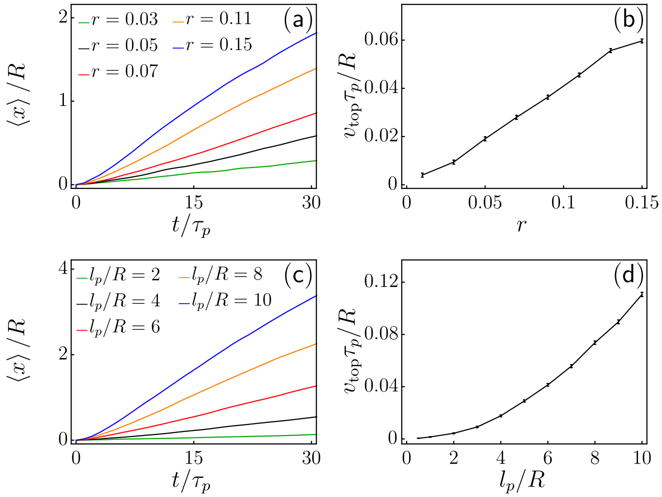

**Figure 5.2.** The emergence of topotaxis in density gradient lattices. (a) $\langle \tilde{x} \rangle = \langle x \rangle / R$ as a function of time $\tilde{t} = t/\tau_p$ for several values of the density gradient $r$, with $\tilde{d} = d/R = 5$ and $\tilde{l}_p = v_0\tau_p/R = 5$. (b) Topotactic velocity, defined in the main text, in the $x$ direction as a function of the density gradient $r$ based on the data in (a). (c) $\langle \tilde{x} \rangle = \langle x \rangle / R$ as a function of time $\tilde{t} = t/\tau_p$ for several values of the persistence length $\tilde{l}_p = v_0\tau_p/R$, with $\tilde{d} = d/R = 5$ and $r = 0.07$. (d) Topotactic velocity in the $x$ direction as a function of the persistence length $\tilde{l}_p$ based on the data in (c). Data in (a) and (c) represent averages over $10^6$ particles. Error bars in (b) and (d) are given by the standard error of $\langle x \rangle (t)/(R\, t)$ at $t = 30\ \tau_p$.

direction irrespective of the persistence length, as expected by symmetry (Figure 5.6b, Section 5.5.3 in the Appendix).

### 5.3.2 The physical origin of topotaxis

The observed occurrence of topotaxis of ABPs is intuitive, as particles migrate in the direction where there is more available space. However, the mechanism by which ABPs are guided toward the less crowded regions is not obvious from the results in Section 5.3.1. To gain more insight into the physical origin of topotaxis, we investigate how particle motility depends on the local obstacle spacing. In doing so, we take inspiration from recent works [135, 157, 277] that have shown, in the context of durotaxis, that persistent random walkers, moving in a spatial gradient of a position-dependent persistence length, show an average drift toward the region with larger persistence. As is the case in our system (Section 5.3.1), this effect is stronger in the presence of larger gradients [135, 157]. In order to understand whether or not such a space-dependent persistence might explain the observed topotactic motion, we study and characterize the motion of ABPs in regular square lattices. To do so, we measure the mean squared displacement

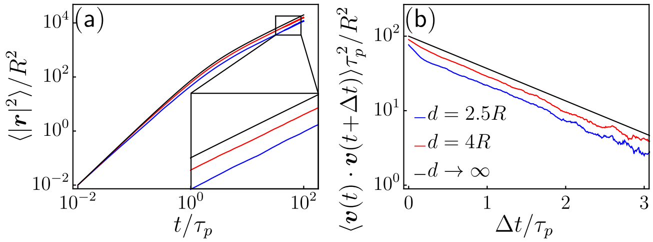

**Figure 5.3.** Regular square lattices of obstacles modify the effective parameters of the persistent random walk. (a) Dimensionless mean squared displacement $\left\langle|\Delta\tilde{\boldsymbol{r}}|^2\right\rangle = \left\langle|\Delta\boldsymbol{r}|^2\right\rangle/R^2$ as a function of dimensionless time $\tilde{t} = t/\tau_p$ for $\tilde{l}_p = v_0\tau_p/R = 10$ in free space ($d \to \infty$, black line) and in the presence of square lattices with obstacle spacings $\tilde{d} = d/R = 2.5$ (blue) and $\tilde{d} = 4$ (red). The effective diffusion coefficient $D_{\text{eff}}$ is obtained from a linear fit to the long-time ($t > \tau_p$) regime of the log-log data. (b) Dimensionless velocity autocorrelation function $\langle\tilde{\boldsymbol{v}}(t+\Delta t)\cdot\tilde{\boldsymbol{v}}(t)\rangle = \langle\boldsymbol{v}(t+\Delta t)\cdot\boldsymbol{v}(t)\rangle\,\tau_p^2/R^2$ as a function of $\Delta\tilde{t} = \Delta t/\tau_p$ for $\tilde{l}_p = v_0\tau_p/R = 10$ in free space ($d \to \infty$) and in the presence of square lattices with obstacle spacings $\tilde{d} = 2.5$ and $\tilde{d} = 4$. The effective velocity $v_{\text{eff}}$ and effective persistence time $\tau_{\text{eff}}$ are obtained from a exponential fit to the autocorrelation function. MSD and VACF data represent averages over $10^4$ particles.

(MSD) $\left\langle|\Delta\boldsymbol{r}(t)|^2\right\rangle$ as a function of time and the velocity autocorrelation function (VACF) $\langle\boldsymbol{v}(t+\Delta t)\cdot\boldsymbol{v}(t)\rangle$ as a function of the time interval $\Delta t$ for $10^4$ particles for various lattice spacings $\tilde{d}$ and persistence lengths $\tilde{l}_p$.

Figure 5.3a shows a log-log plot of the MSD for $\tilde{l}_p = 10$. The curve with $\tilde{d} \to \infty$ (black) represents the theoretical MSD in free space [Eq. (5.2)] and exhibits the well-known crossover from the ballistic regime (slope equal to 2) to the diffusive regime (slope equal to 1) around $\tilde{t} = 1$ ($t = \tau_p$). The hindrance of the obstacles is evident from the data obtained in regular lattices with $\tilde{d} = 4$ (red curve) and $\tilde{d} = 2.5$ (blue curve), as the MSD is smaller than the MSD in free space at all times (see also the inset). Moreover, the MSD is smaller for the smaller lattice spacing, as we already observed qualitatively in Figures 5.1a,b. The hindrance also manifests itself in the short-time ($t < \tau_p$) regime, where the slope of the red and blue curves is slightly smaller than that of the black curve. When not interacting with obstacles, individual ABPs still move ballistically, but interactions with obstacles prevent them from moving along straight lines. As the particles start at random locations within the unit cell (Figure 5.1c), each particle interacts with obstacles at different times, causing the MSD to show slightly sub-ballistic behavior.

The slope of the curves at timescales larger than the persistence time, on the other hand, is independent of the presence of obstacles and equal to 1 (see inset). In other words, even though the motion of the ABPs is hindered by the obstacles at all timescales, the long-time motion remains diffusive, as was also observed for ABPs in random obstacle lattices of low density [270]. Fitting the MSD at long times allows one to define an effective diffusion coefficient $D_{\text{eff}}$, namely:

$$\left\langle |\Delta \boldsymbol{r}(t)|^2 \right\rangle \xrightarrow[t \gg \tau_p]{} 4 D_{\text{eff}} t. \tag{5.5}$$

Figure 5.3b shows the velocity autocorrelation function (VACF) on a semilogarithmic plot as a function of the time interval $\Delta\tilde{t} = \Delta t/\tau_p$ for $\tilde{l}_p = 10$. The $d \to \infty$ curve again represents the theoretical curve in free space and shows exponential decay [Eq. (5.3)]. Interestingly, in the presence of increasing obstacle densities, hence for smaller lattice spacings $\tilde{d}$, the velocity autocorrelation decreases but remains, to good approximation, exponential. From this numerical evidence, we conclude that the average motion of ABPs in a two-dimensional square lattice can be described as a persistent random walk with an effective velocity $v_{\text{eff}}$ and an effective persistence time $\tau_{\text{eff}}$ [270],

$$\langle \boldsymbol{v}(t + \Delta t) \cdot \boldsymbol{v}(t) \rangle = v_{\text{eff}}^2 \, \mathrm{e}^{-\Delta t/\tau_{\text{eff}}} \; . \tag{5.6}$$

Figure 5.4 shows $D_{\text{eff}}$, $\tau_{\text{eff}}$ and $v_{\text{eff}}$, normalized by their free space values, as a function of the obstacle spacing $\tilde{d}$ for three values of the free space persistence length $\tilde{l}_p$. Starting with the effective diffusion coefficient (Figure 5.4a), we observe that, for every value of the persistence length, the effective diffusion coefficient $D_{\text{eff}}$ increases as a function of $\tilde{d}$ until it approaches the free space diffusion coefficient $D$ for large $\tilde{d}$. This is consistent with what we observed in Figures 5.1a,b and 5.3: ABPs on low density lattices spread out more than ABPs on high density lattices. Moreover, the effective diffusion coefficient deviates more from its free space value for large $\tilde{l}_p$ than it does for small $\tilde{l}_p$. This is intuitive because more persistent particles tend to move longer along the same direction and therefore are hindered more in their motion by the obstacle lattice.

The effective persistence time $\tau_{\text{eff}}$ (Figure 5.4b) and the effective velocity $v_{\text{eff}}$ (Figure 5.4c), both extracted from the velocity autocorrelation function [Eq. (5.6)], show a similar trend: they increase as a function of $\tilde{d}$ until they approach their free space values at high $\tilde{d}$, and they deviate more from their free space values for large $\tilde{l}_p$ than they do for small $\tilde{l}_p$. These data show that the obstacles cause the ABPs, on average, to move slower and change their direction of motion more quickly. We emphasize that it is the velocity $\boldsymbol{v}$ that turns more quickly, not the particle orientation $\boldsymbol{p}$, which is unaffected by the obstacles as we discussed in Section 5.2. The decreased effective velocity, with respect to free space, is intuitive given the interactions between particles and obstacles [Eq. (5.4)], which slow down the ABPs. The decreased effective persistence time, on the other hand, is less obvious as one could imagine the periodic obstacle lattice to guide ABPs along straight lines, as reported in Refs. [268, 278]. Apparently, this potential guiding mechanism is outcompeted in our system by the fact that encounters of ABPs with individual obstacles at shorter timescales cause them to change their direction of motion more quickly than in free space. In Section 5.3.3 we will study these short-timescale interactions in greater detail.

Combining the effective persistence time (Figure 5.4b) and the effective velocity (Figure 5.4c) gives the effective persistence length $l_{\text{eff}} = v_{\text{eff}}\tau_{\text{eff}}$ and the effective diffusion

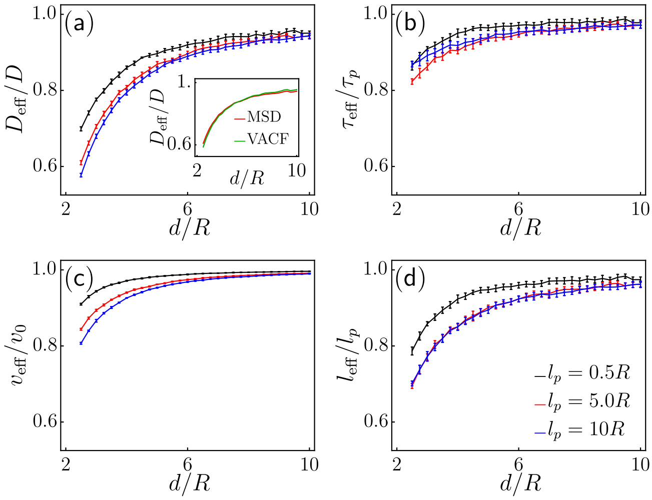

**Figure 5.4.** Effective parameters of the persistent random walk in regular lattices of obstacles. (a) Normalized effective diffusion coefficient $D_{\mathrm{eff}}/D$, obtained from the mean squared displacement [Eq. (5.5)], as a function of the normalized obstacle spacing $\tilde{d} = d/R$ for three values of the normalized persistence length $\tilde{l}_p = v_0\tau_p/R$. Inset shows $D_{\mathrm{eff}}$ for $\tilde{l}_p = 5$ obtained via the mean squared displacement (MSD) and via the velocity autocorrelation function (VACF), using $D_{\mathrm{eff}} = v_{\mathrm{eff}}^2\tau_{\mathrm{eff}}/2$. (b) Normalized effective persistence time $\tau_{\mathrm{eff}}/\tau_p$, (c) normalized effective velocity $v_{\mathrm{eff}}/v_0$, both obtained from the velocity autocorrelation function [Eq. (5.6)], and (d) normalized effective persistence length $l_{\mathrm{eff}}/l_p = v_{\mathrm{eff}}\tau_{\mathrm{eff}}/(v_0\tau_p)$ as functions of the normalized obstacle spacing $\tilde{d} = d/R$ for three values of the normalized persistence length $\tilde{l}_p = v_0\tau_p/R$. Data points represent the average of 10 independent measurements from MSD or VACF data (Figure 5.3). The error bars show the corresponding standard deviations.

coefficient $D_{\mathrm{eff}} = v_{\mathrm{eff}}^2\tau_{\mathrm{eff}}/2$. The inset of Figure 5.4a shows the effective diffusion coefficient for $\tilde{l}_p = 5$, calculated both by using the effective persistence time and effective velocity from the velocity autocorrelation function (VACF) and by a direct measurement from the mean squared displacement (MSD). The excellent agreement between $D_{\mathrm{eff}}$ measured at short and long timescales (using the VACF and MSD respectively) is another indication that the motion of the ABPs in regular square obstacle lattices can indeed be considered to be an effective persistent random walk.

The effective persistence length $l_{\mathrm{eff}} = v_{\mathrm{eff}}\tau_{\mathrm{eff}}$ is plotted in Figure 5.4d. As anticipated, the effective persistence length increases with increasing lattice spacing $\tilde{d}$, consistent with findings of ABPs in random obstacle lattices [270] and a model of persistently moving cells in a tissue of stationary cells [125]. This effect increases with the free space persistence length, as the motion of less persistent particles is randomized before they can reach an obstacle. Furthermore, the difference between data with $\tilde{l}_p = 5$ and $\tilde{l}_p = 10$ is negligible, indicating that the free space persistence length $\tilde{l}_p$ affects particle motion only when it is comparable with the lattice spacing.

These observations, combined with those in Refs. [135, 157, 277] which demonstrate a net flux of persistent random walkers toward regions of larger persistence, ultimately explain the origin of topotaxis in our system. ABPs migrate, on average, toward regions of higher persistence, hence to regions of lower obstacle density. Moreover, the dependence of the effective persistence length $l_{\text{eff}}$ on the free space persistence length $\tilde{l}_p$ (Figure 5.4d) justifies the superlinear increase of the topotactic velocity $\tilde{v}_{\text{top}}$ as a function of $\tilde{l}_p$ (Figure 5.2d). In addition to the normal speed-up due to the higher persistence, more persistent particles experience a larger gradient in persistence.

### 5.3.3 Fokker-Planck equation for regular lattices

As we explained in Section 5.3.2, topotaxis in our model of ABPs crucially relies on the fact that, even when trapped in an array of obstacles, ABPs still behave as persistent random walkers. The physical origin of this behavior is, however, less clear from the numerical simulations. In this section, we rationalize this observation using some simple analytical arguments. The probability distribution function $P = P(\boldsymbol{r}, \theta, t)$ of the position and orientation of an ABP, whose dynamics is governed by Eqs. (5.1), evolves in time based on the following Fokker-Planck equation:

$$\frac{\partial P}{\partial t} = -v_0 \boldsymbol{p} \cdot \nabla P - \mu \nabla \cdot (P \boldsymbol{F}) + D_R \frac{\partial^2 P}{\partial \theta^2} , \tag{5.7}$$

subject, at all times, to the normalization constraint:

$$\int \mathrm{d}\boldsymbol{r} \, \mathrm{d}\theta \, P(\boldsymbol{r}, \theta, t) = 1 , \tag{5.8}$$

with $\mathrm{d}\boldsymbol{r} = \mathrm{d}x \, \mathrm{d}y$. Eq. (5.7) cannot be solved exactly, but useful insights can be obtained by calculating the rate of change of the mean squared displacement $\left\langle |\Delta \boldsymbol{r}|^2 \right\rangle$. Here we assume $\boldsymbol{r}(0) = \boldsymbol{0}$, which yields $|\Delta \boldsymbol{r}|^2 = |\boldsymbol{r}|^2 = x^2 + y^2$, and

$$\frac{\partial \left\langle |\boldsymbol{r}|^2 \right\rangle}{\partial t} = \int \mathrm{d}\boldsymbol{r} \, \mathrm{d}\theta \, |\boldsymbol{r}|^2 \frac{\partial P(\boldsymbol{r}, \theta, t)}{\partial t} \tag{5.9}$$

Upon substituting Eq. (5.7) in Eq. (5.9) and integrating by parts, we obtain:

$$\frac{\partial \langle |\boldsymbol{r}|^2 \rangle}{\partial t} = 2 v_0 \langle \boldsymbol{r} \cdot \boldsymbol{p} \rangle + 2\mu \langle \boldsymbol{r} \cdot \boldsymbol{F} \rangle. \tag{5.10}$$

Analogously, the term $\langle \boldsymbol{r} \cdot \boldsymbol{p} \rangle$ evolves accordingly to:

$$\frac{\partial \langle \boldsymbol{r} \cdot \boldsymbol{p} \rangle}{\partial t} = v_0 - D_R \langle \boldsymbol{r} \cdot \boldsymbol{p} \rangle + \mu \langle \boldsymbol{p} \cdot \boldsymbol{F} \rangle \ . \tag{5.11}$$

In free space ($\boldsymbol{F} = \mathbf{0}$), Eqs. (5.10) and (5.11) can be solved exactly, using the boundary condition $\boldsymbol{r}(t = 0) = \mathbf{0}$, to find:

$$\langle \boldsymbol{r} \cdot \boldsymbol{p} \rangle_{\boldsymbol{F}=\mathbf{0}} = \frac{v_0}{D_R}\left(1 - \mathrm{e}^{-D_R t}\right) , \tag{5.12}$$

and the mean squared displacement $\langle |\boldsymbol{r}|^2 \rangle$ given by Eq. (5.2). A generic nonzero $\boldsymbol{F}$ compromises the closure of the equations, thus making the problem intractable with exact methods. Nevertheless, it is possible to use some simplifying assumptions to obtain intuitive results about $D_{\text{eff}}$ and $\tau_{\text{eff}}$ (Figure 5.4) at short ($t \ll 1/D_r = \tau_p$) and long ($t \gg 1/D_r = \tau_p$) timescales.

At short timescales, we can assume a particle to be still relatively close to its initial position $\boldsymbol{r}(0) = \mathbf{0}$. Thus one can expand the force in Eq. (5.11) at the linear order in $\boldsymbol{r}$, i.e., $\boldsymbol{F}(\boldsymbol{r}) \approx \boldsymbol{F}(\mathbf{0}) + \nabla \boldsymbol{F}(\mathbf{0}) \cdot \boldsymbol{r}$. Evidently, such an expansion is ill-defined for discontinuous forces such as that given by Eq. (5.4). However, one can imagine to smoothen the force (for instance using a truncated Fourier expansion), without altering the qualitative picture. By the symmetry of the obstacle lattice, $\boldsymbol{F}(\mathbf{0}) = \mathbf{0}$, $\partial_y F_x(\mathbf{0}) = \partial_x F_y(\mathbf{0}) = 0$, and the constant $\partial_x F_x(\mathbf{0}) = \partial_y F_y(\mathbf{0}) < 0$, as the horizontal (vertical) component of the force experienced by a particle moving in the positive $x-$direction ($y-$direction), becomes more negative as the particle moves away from the origin. Using this approximation, the short-time motion is analogous to that of ABPs confined by a harmonic trap [279–282]. The approximation allows us to write

$$\langle \boldsymbol{p} \cdot \boldsymbol{F} \rangle|_{t \ll \tau_p} = \frac{\partial F_x}{\partial x}(\mathbf{0}) \, \langle \boldsymbol{r} \cdot \boldsymbol{p} \rangle , \tag{5.13}$$

and by inserting Eq. (5.13) into Eq. (5.11) we find:

$$\left.\frac{\partial \langle \boldsymbol{r} \cdot \boldsymbol{p} \rangle}{\partial t}\right|_{t \ll \tau_p} = v_0 - \left(D_r - \mu \frac{\partial F_x}{\partial x}(\mathbf{0})\right) \langle \boldsymbol{r} \cdot \boldsymbol{p} \rangle . \tag{5.14}$$

Solving Eq. (5.14) yields:

$$\left.\langle \boldsymbol{r} \cdot \boldsymbol{p} \rangle\right|_{t \ll \tau_p} = \frac{v_0}{D_{r,\text{eff}}}\left(1 - e^{-D_{r,\text{eff}} t}\right) , \tag{5.15}$$

with $D_{r,\text{eff}} = D_r - \mu \; \partial_x F_x(\mathbf{0}) > D_r$. By comparing Eq. (5.15) with its free space equivalent [Eq. (5.12)], we identify $D_{r,\text{eff}}$ as an increased effective rotational diffusion coefficient. This implies a decreased effective persistence time, consistent with the data in Figure 5.4b. The above analysis shows that, to first order, the observed decrease in effective persistence time simply results from the short-time interactions, within a unit cell of the lattice, that cause the particles to change their direction of motion more quickly. Finally, substituting Eq. (5.15) in Eq. (5.10) and taking again the first order Taylor expansion for $\boldsymbol{F}$ allows one to solve Eq. (5.10) exactly. Expanding this exact solution at the second order in time yields:

$$\left.\langle |\boldsymbol{r}|^2 \rangle\right|_{t \ll \tau_p} = v_0^2 t^2 , \tag{5.16}$$

which is the standard ballistic regime of the mean squared displacement. Hence, the decreased effective velocity observed in Figure 5.4c originates from interactions with obstacles at larger timescales ($t \sim \tau_p$, see also Figure 5.3b).

In the long timescale ($t \gg 1/D_r = \tau_p$) the particles reach a diffusive steady state, thus $\partial_t \langle \boldsymbol{r} \cdot \boldsymbol{p} \rangle = 0$. Hence, solving Eq. (5.11) for $\langle \boldsymbol{r} \cdot \boldsymbol{p} \rangle$ and substituting in Eq. (5.10) yields:

$$\left. \frac{\partial \langle |\boldsymbol{r}|^2 \rangle}{\partial t} \right|_{t \gg \tau_p} = \frac{2v_0^2}{D_r} \left( 1 + \frac{\mu}{v_0} \langle \boldsymbol{p} \cdot \boldsymbol{F} \rangle + \frac{\mu D_r}{v_0^2} \langle \boldsymbol{r} \cdot \boldsymbol{F} \rangle \right) , \tag{5.17}$$

As the long time behavior is diffusive, the expression on the right-hand side of Eq. (5.17) is constant and equal to $4D_{\text{eff}}$. Now, according to Eq. (5.4), $\mu(\boldsymbol{p} \cdot \boldsymbol{F}) = \boldsymbol{0}$ if $|\Delta \boldsymbol{r}_o| > R$, and $\mu(\boldsymbol{p} \cdot \boldsymbol{F}) = -v_0(\boldsymbol{p} \cdot \boldsymbol{N})^2$ otherwise. Thus, $\langle \boldsymbol{p} \cdot \boldsymbol{F} \rangle < 0$. This term shows that diffusion is slowed down because the obstacle force $\boldsymbol{F}$ always slows down the particles (but never accelerates them). Moreover, for more dense obstacle lattices, particles interact with obstacles more often, which explains the observed dependence of $D_{\text{eff}}$ on the obstacle spacing in Figure 5.4a. Analogously, since particles move in an open space and, on average, away from the center, $\langle \boldsymbol{r} \cdot \boldsymbol{F} \rangle < 0$ (i.e., the repulsion forces due to the obstacles are directed more often toward the origin than toward infinity, further slowing down diffusion). Thus $D_{\text{eff}} < D$, consistent with our numerical simulations (Figures 5.3 and 5.4a).

## 5.4 Discussion and conclusions

In this chapter we investigated topotaxis, i.e., directed motion driven by topographical gradients, in a toy model of ABPs constrained to move within a two-dimensional array of obstacles of smoothly varying density. We found that ABPs migrate preferentially toward regions of lower density with a velocity that increases with the gradient in the lattice spacing and with the particles' persistence length. In our model, the origin of topotaxis crucially relies on the fact that, even when moving in a lattice of obstacles, ABPs still behave as persistent random walkers, but with renormalized transport coefficients: $\tau_{\text{eff}}$ and $v_{\text{eff}}$. As these depend on the topography of the substrate, here quantified in terms of lattice spacing, topographical gradients result into spatially varying persistence in the motion of the particles, which in turn drives directed motion toward regions of larger persistence [135, 157, 277]. We note that the motion we report here, just like the durotactic motion described in Refs. [135, 157], is perhaps better described as a "kinesis" than as a "taxis", because the underlying mechanism of transport is a nondirectional change in behavior induced by a purely positional cue. This is in contrast to the true directional bias underlying, for instance, chemotaxis of *E. coli* [126] which leads to significantly more efficient transport [277].

Several questions remain open to future investigation. For instance, how is the picture affected by translational diffusion? Is topotaxis robust against competing directional cues, such as chemotaxis [143]? How sensitive is the performance of topotaxis with respect to the obstacles' shape [149, 150, 260], the type of motion (e.g., persistent random walk, run-and-tumble, Lévy walk, etc. [260, 263, 273, 283–285]), and the details of particle-obstacle interactions [149, 271, 286–288]? Another interesting setting of the problem could be obtained by considering random arrangements of obstacles, where, unlike in the lattices studied here, particles can be trapped into convex-shaped features that can significantly alter their motion [270, 273].

Finally, although here we demonstrated that topotaxis can be solely driven by the interplay between topographical gradients and persistent random motion, whether this is sufficient to explain large-scale topotaxis of cells remains an open problem. A quantitative comparison between our numerical data and experiments on highly motile cells [143] shows, in fact, discrepancies that could be ascribed to the enormously more complex interactions between cells and their environment. Specifically, the topotactic velocity in our simulations is of the order of $1\%$ of the intrinsic particle speed (Figure 5.2), whereas in the experiments on cells this ratio is approximately $5\%$, provided that the obstacles are not spaced further apart than the cell size [143]. In order to better understand this surprising efficiency, the large-scale topotactic response of several types of persistently and individually moving cells, such as amoeba [289], invasive (amoeboid) cancer cells [290, 291], or leukocytes [292], could be compared. On the theoretical side, we are currently addressing the problem using more biologically-realistic models of cell motility based on the Cellular Potts Model [124, 125] (see also Chapter 6), which allow explicitly taking into account effects such as the resistance of cells against deformations, adhesion between cells and obstacles, and more realistic cell-obstacle interactions.

## 5.5 Appendix

### 5.5.1 Numerical methods

We numerically generate particle trajectories that perform a persistent random walk by discretizing the equations of motion as follows [157]: a particle starts at position $\boldsymbol{r}_0$ at $t = 0$, after which the particle is moved by a distance $v_0 \Delta t$ in a random initial direction $-\pi < \theta_1 < \pi$, such that the new position is $\boldsymbol{r}_1 = \boldsymbol{r}_0 + v_0 \Delta t \; \boldsymbol{p}(\theta_1)$. For all subsequent time steps, the angle at time step $n$, $\theta_n$, is updated by adding a small deviation angle to the angle of the previous time step, $\theta_n = \theta_{n-1} + \delta\theta$. Here, $-\pi < \delta\theta < \pi$ is extracted randomly from a Gaussian distribution with mean 0 and variance $\sigma^2 = 2\Delta t/\tau_p$ using the Box-Muller transform. The new position of the particle, $\boldsymbol{r}_n$, is then found by $\boldsymbol{r}_n = \boldsymbol{r}_{n-1} + v_0 \Delta t \; \boldsymbol{p}(\theta_n)$, with $\boldsymbol{r}_{n-1}$ the position at the previous time step.

If the update step moves the particle into an obstacle, however, the particle-obstacle force [Eq. (5.4)] is triggered. In that case, the normal component of the attempted displacement is subtracted, and the actual displacement is given by the tangential component of the attempted displacement, $\boldsymbol{r}_n = \boldsymbol{r}_{n-1} + v_0 \Delta t \; \left(\boldsymbol{p}(\theta_n) \cdot \boldsymbol{T}\right) \; \boldsymbol{T}$, with $\boldsymbol{T}$ the tangent unit vector of the obstacle surface at the point of the surface closest to $\boldsymbol{r}_{n-1}$. This procedure is implied by Euler integration of Eq. (5.1a) with the force $\boldsymbol{F}$ described by

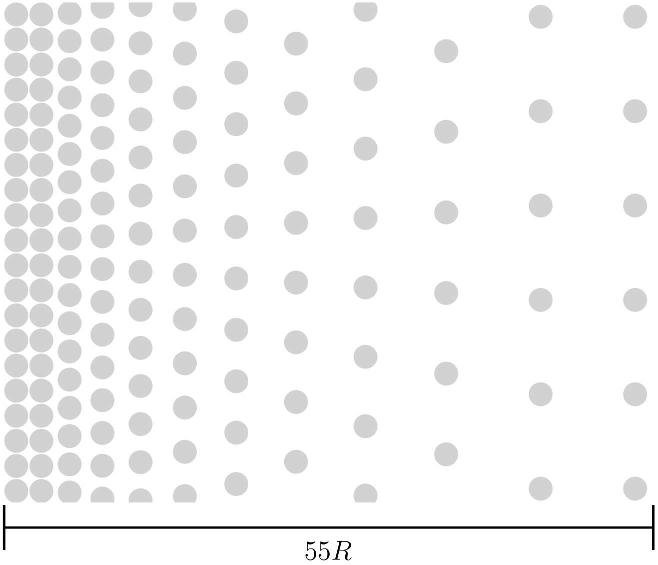

**Figure 5.5.** Snapshot of the gradient lattice as described in Section 5.5.2. The gradient region is characterized by $r = 0.15$ and $\tilde{d} = d/R = 5$. The obstacles are graphically represented as disks of radius $R$. The lattice spacing varies from $\tilde{d}_{\min} = 2.1$ to $\tilde{d}_{\max} = 7.9$ over the $x$ range $[x_{\min}, x_{\max}] = [-19, 19]$. The gradient region is flanked by a regular square lattice with $\tilde{d} = \tilde{d}_{\min}$ on the left ($x < x_{\min}$) and by a regular square lattice with $\tilde{d} = \tilde{d}_{\max}$ on the right ($x > x_{\max}$). Only the first two columns of both (infinitely large) regular lattices are shown.

Eq. (5.4). We choose the time step $\Delta t$ such that it is much smaller than the persistence time, $\Delta t \ll \tau_p$, and such that every displacement is much smaller than the obstacle radius, $v_0 \Delta t \ll R$. In all reported simulations we have used $\Delta t = 0.01\tau_p$.

### 5.5.2 Obstacle lattices

We define a regular square lattice of obstacles with the coordinates of the centers of the obstacles given by

$$x(n, m) = nd + \frac{d}{2} \tag{5.18a}$$

$$y(n, m) = md + \frac{d}{2} \tag{5.18b}$$

where $n, m \in \mathbb{Z}$ are the obstacle numbers and $d$ is the distance between the centers of two neighboring obstacles. The term $d/2$ is added to make sure that the origin of the coordinate system is in the middle of four obstacles. An illustration of this lattice is given in Figures 5.1a,b.

We define an irregular square lattice with a linear gradient of the obstacle spacing in the positive $x$ direction. The gradient region has a finite width, is centered in the origin, and is flanked by regular square lattices to the left and to the right. The coordinates of the centers of the obstacles in the gradient region are given by

$$x(n,m) = \frac{d}{1-e^{-r}}(e^{rn}-1) + \frac{d}{2} \tag{5.19a}$$

$$y(n,m) = d(m+\frac{1}{2})e^{rn} \tag{5.19b}$$

where $n, m \in \mathbb{Z}$ are again the obstacle numbers, $d$ is the distance between the centers of obstacles with $(n,m) = (0,0)$ and $(n,m) = (-1,0)$ (i.e., the lattice spacing in the origin), and $r$ is a dimensionless number that quantifies the gradient in the obstacle spacing.

Eq. (5.19) represents an obstacle lattice where the lattice spacing depends exponentially on the horizontal obstacle number $n$, such that $x(n,m) - x(n-1,m) = de^{rn}$ and $y(n,m) - y(n,m-1) = de^{rn}$. This exponential gradient in the obstacle spacing, as a function of the obstacle number $n$, leads to a linear gradient in the obstacle spacing as a function of the horizontal coordinate $x$. This can be seen by calculating the difference in obstacle distance between two adjacent pairs of obstacles, divided by the distance between those two pairs,

$$\frac{\Big(x(n+1)-x(n)\Big) - \Big(x(n)-x(n-1)\Big)}{x(n)-x(n-1)} = e^{r} - 1, \tag{5.20}$$

which is independent of $n$, as required for a linear gradient. In the limit of $r \to 0$, Eqs. (5.19) reduce to the regular square lattice given in Eqs. (5.18).

The gradient lattice is cut off on the left side at $x_{\mathrm{min}} < 0$, where the vertical distance between two neighboring obstacles, $y(n,m) - y(n,m-1)$, would otherwise become smaller than a minimal distance $d_{\mathrm{min}} = 2.1R$. At the first column of obstacles for which this is the case, the vertical coordinates [Eq. (5.19b)] are replaced by $y(n,m) = md_{\mathrm{min}} + d_{\mathrm{min}}/2$. To the left of this transition column ($x < x_{\mathrm{min}}$), a regular obstacle lattice with spacing $d_{\mathrm{min}}$ is placed such that the transition column is part of this regular lattice.

On the right side the gradient lattice is cut off at $x_{\mathrm{max}} = -x_{\mathrm{min}}$. To the right of this cut-off ($x > x_{\mathrm{max}}$), a regular obstacle lattice with spacing $d_{\mathrm{max}} = 2d - d_{\mathrm{min}}$ is placed such that the horizontal distance between the rightmost column of the gradient lattice and the leftmost column of the regular lattice is equal to $d_{\mathrm{max}}$. Thus, the gradient lattice connects two regular square lattices of lattice spacings $d_{\mathrm{min}}$ and $d_{\mathrm{max}}$. The width of the gradient region, $2x_{\mathrm{max}}$, then depends on the gradient parameter $r$. For an illustration of the gradient lattice for $r = 0.15$ and $\tilde{d} = d/R = 5$, see Figure 5.5.

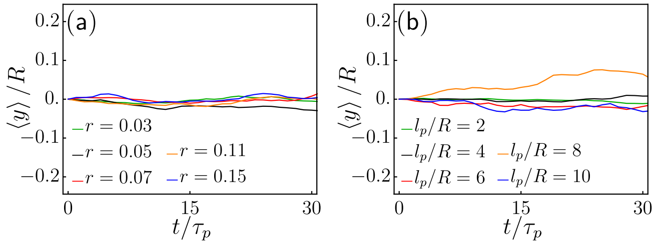

**Figure 5.6.** There is no average drift in the $y$ direction in density gradient lattices. (a) $\langle \tilde{y} \rangle = \langle y \rangle / R$ as a function of time $\tilde{t} = t/\tau_p$ for five values of the density gradient $r$, with $\tilde{d} = d/R = 5$ and $\tilde{l}_p = v_0\tau_p/R = 5$. (b) $\langle \tilde{y} \rangle = \langle y \rangle / R$ as a function of time $\tilde{t} = t/\tau_p$ for five values of the persistence length $\tilde{l}_p = v_0\tau_p/R$, with $\tilde{d} = d/R = 5$ and $r = 0.07$.

### 5.5.3 Average motion in $y$

We plot $\langle \tilde{y} \rangle (\tilde{t})$ of $10^6$ particles moving in a density gradient lattice with $\tilde{d} = 5$, starting in the origin with a random orientation, for several values of the dimensionless density gradient $r$ in Figure 5.6a, and for several values of the persistence length $\tilde{l}_p$ in Figure 5.6b. As expected, there is no average drift in the $y$ direction. The fluctuations in $\langle y \rangle$ are of the order of $10\%$ of the effective radius $R$.

### CHAPTER 6

# FINAL CONCLUSIONS AND OUTLOOK

In this thesis we studied the effects of anisotropy on two fundamental aspects of cell mechanics: the role of the actin cytoskeleton in determining cell shape and the generation of traction forces (Part I), and cell migration in an asymmetric crowded environment (Part II). In Part I we focused on the role of actin stress fibers, bundles of actin filaments that can contract under the influence of the motor protein myosin. By contracting, stress fibers can adjust the cell shape and exert forces on the environment of the cell. The structure and function of stress fibers is relatively well understood [46, 47] and several experimental studies have shown their importance in the anisotropy of the cytoskeleton and the anisotropy of traction forces [89, 90], but most theoretical models for cell contractility describe cells as isotropic objects [63, 64, 68, 73, 196, 197, 232]. In Part I we combined analytical calculations, computer simulations and *in vitro* experiments to study the geometrical and mechanical properties of cells with a highly anisotropic cytoskeleton adhering to adhesive substrates. Our findings highlight the crucial mechanical interplay between the actin cytoskeleton, which dictates the shape and traction forces of cells, and the cell shape, which, in turn, determines the structure of the actin cytoskeleton.

In Chapter 2 we studied how the orientation of the stress fibers affects the shape of the cell. We extended a previous isotropic contour model for cell contractility called the Simple Tension Model [63, 64]. When cells adhere to the substrate at a small number of discrete adhesion sites, the Simple Tension Model predicts that the cell has a concave shape and that each part of the cell edge between two adhesion sites, called a cellular arc, can be approximated by a segment of a circle. We extended this contour model by introducing the effects of anisotropic contractility due to actin stress fibers, and predict that cellular arcs of anisotropic cells are better approximated by segments of an ellipse. The aspect ratio of this ellipse is determined by the degree of anisotropy of the internal cell stresses, and the orientation of the long axis is parallel to the local orientation of stress fibers along that cellular arc. We validated our model predictions by studying epithelioid and fibroblastoid cells [173] on microfabricated elastomeric pillar arrays [55–

57]. We demonstrated that the arcs of cells with an anisotropic cytoskeleton are well approximated by a unique ellipse, which is for each cellular arc oriented parallel to the local stress fiber orientation along that arc. Additionally, we demonstrated that the traction forces that the cell exerts on the micropillar array are affected significantly by the anisotropy of the cytoskeleton. Our work shows that cells can control the anisotropy of their shape and traction forces by regulating the anisotropy of their cytoskeleton.

In Chapter 3 we reversed the question from Chapter 2, and asked how the shape of the cell affects the orientation of the stress fibers. We presented a phenomenological model for stress fiber orientation based on the continuum theory of nematic liquid crystals [91]. This model for the cytoskeleton was coupled with the model for cell shape, developed in Chapter 2, to study the mechanical interplay between cell shape and the organization of the actin cytoskeleton. Our model predicts that the orientation of the stress fibers is governed by an interplay between alignment of stress fibers with one another in the bulk of the cell and alignment of stress fibers with the cell edge. We compared our model predictions with experimental data on epithelioid and fibroblastoid cells [173] on microfabricated elastomeric pillar arrays [55–57], and demonstrated good qualitative agreement. Because our phenomenological model for the cytoskeleton does not explicitly take into account a number of biochemical pathways that are important in the generation of cytoskeletal anisotropy and traction forces [56, 176, 196, 198, 199, 206, 207, 210, 211], our theoretical predictions do not perfectly agree with the experimental data. Importantly, however, our work demonstrates that the formation and organization of the actin cytoskeleton cannot be understood from processes at the sub-cellular scale alone, but that it is crucial to take into account the boundary conditions imposed by the shape of the cell.

In Chapter 4 we build on the work in Chapters 2 and 3 and implement our model for cell shape in the framework of the Cellular Potts Model (CPM). Combining this Cellular Potts Model with the liquid crystal model for the cytoskeleton developed in Chapter 3, we study cells adhering to adhesive micropatterns that ensure reproducible cell shapes [58]. Our model predictions qualitatively reproduce experimentally observed stress fiber distributions of several cell types on differently shaped micropatterns. Additionally, this approach allowed us to calculate traction forces on micropatterned substrates. Our numerical predictions show that the traction forces are strongly biased by the local stress fiber orientation, consistent with experimental observations [89, 90] but different from many earlier models [69, 196, 234, 235]. Comparing the predictions to previously published experimental data of several cell types on different pattern shapes [43, 89, 196], we reproduce prominent anisotropic features in traction force patterns that were not captured in earlier isotropic models [69, 196]. These findings demonstrate the importance of carefully considering the configuration of the actin cytoskeleton in the study of cellular traction forces.

In Part II of this thesis we shifted our focus to cells migrating in a crowded environment, and studied large-scale topotaxis. This process was first observed by Wondergem *et al.* [143] in experiments of highly motile cells moving on a substrate in between cell-sized obstacles. In the presence of a gradient in the density of these obstacles, the cells migrate, on average, in the direction of lower obstacle densities. Inspired by these observations, in Chapter 5 we studied large-scale topotaxis of active Brownian particles (ABPs), which represent a simple model system for self-propelled particles. This allowed us to zoom out from the internal structure of the cell that we studied in Part I, and to study the role of persistent cell migration in large-scale topotaxis. We demonstrated numerically that ABPs perform topotaxis and that topotaxis is stronger for particles with larger persistence lengths and for lattices with steeper density gradients. Using a combination of numerical simulations and analytical arguments, we studied ABPs in regular obstacle lattices and showed that the origin of ABP topotaxis lies in an effective persistence length that depends on the local obstacle density. Our work demonstrates that persistent migration is on itself sufficient to drive large-scale topotaxis, even in the absence of any more complex biochemical regulatory mechanisms.

## 6.1 Outlook

Our work has revealed a number of promising directions for future work. In Part I, we identified several possibilities to extend our models with additional biochemical and biomechanical mechanisms to further improve the agreement with experimental data. These potential model extensions include spatial variations in actin densities [43, 176, 196, 210, 211, 240], the distinction between different stress fiber subtypes [242], interactions of stress fibers with the substrate in the cell interior [56, 118, 198, 199], the increase of cytoskeletal tension as a function of substrate area [195–197] or substrate stiffness [198], and the evaluation of traction forces in the cell interior [69, 136].

The most promising direction for future work is, arguably, extending our model to study the role of cytoskeletal anisotropy in cell spreading and migration. This could be achieved by taking into account, for instance, actin filament turnover and the viscoelasticity of stress fibers [206, 207], the dynamics of focal adhesions [136, 189], or cellular protrusions and retractions [216]. A natural platform for achieving this goal is the Cellular Potts Model, in which the model for stress fiber contractility we developed in Chapter 4 could be combined with previously published CPM implementations of cell migration based on the formation of a lamellipodium at the front of the cell [124, 125]. As cell migration crucially depends on pulling forces at the back of the cell [243, 244], integrating our cytoskeleton model in these existing Cellular Potts Models would be an important step forward in realistically modeling cell migration.

In Part II we were inspired by cell migration in crowded environments and demonstrated that active Brownian particles (ABPs) perform topotaxis. In the future, it is important to understand how sensitive topotaxis of active particles is with respect to the details of the model, such as the details of particle-obstacle interactions [149, 271, 286–288], the shape of the obstacles [149, 150, 260], or the type of active motion [260, 263, 273, 283–285]. From a biophysical perspective, however, the most important question is what our findings imply for cellular large-scale topotaxis. As we commented in the discussion of Chapter 5, the efficiency of ABPs to perform topotaxis is about a factor 5 lower than that of highly motile cells [143]. Investigating the origin of this large discrepancy is an important next step toward a better understanding of cellular large-scale topotaxis. Here, we speculate about a number of possible explanations for the origin of this discrepancy, and show preliminary data that presents a first step toward identifying this origin. Possible explanations include, but are not limited to:

1. ABPs in Chapter 5 are modelled as hard, non-deformable objects. Cells, on the other hand, are highly flexible and can take on many different shapes, as we have seen in Part I of this thesis. This property allows cells to squeeze themselves through narrow spaces between the obstacles [143], whereas ABPs either move through spaces effortlessly (if they fit) or not at all (if they do not fit).

2. Cells can adhere to obstacles using various physical or chemical interactions. This might guide them through an obstacle lattice in a way that is not possible for ABPs.

3. Cells respond differently to collisions with obstacles than ABPs do. As we explained in Chapter 5, obstacles in our model slow down ABPs and change the direction in which they move, but they do not change the particle orientation. In other words, obstacles affect the direction in which particles move, but they do not affect the direction in which the partcicles *try* to move. This particle-obstacle interaction is realistic for active colloids [260], but cells crawling on a substrate are likely to show a more complicated response upon encountering an obstacle.

A first step toward identifying which of the explanations above might contribute to the suprising efficiency of experimentally observed large-scale topotaxis of cells [143], is currently being undertaken by Van Steijn *et al.* [293]. They numerically study large-scale topotaxis by employing more biologically-realistic models of cell migration based on the Cellular Potts Model (CPM). In particular, they adapt the standard CPM, which we discussed in Chapters 1 and 4, in two different ways to include persistent cell motion. The first method is based on the persistent motion described in Chapter 5 of this thesis: each cell is assigned an orientation vector $\boldsymbol{p}$, which evolves in time according to Eq. (5.1). Consistent with ABPs in Chapter 5, the orientation vector is not affected by encounters with obstacles. Then, the Hamiltonian $H$ is adapted such that cell motion in the direction of $\boldsymbol{p}$ becomes more likely, whereas motion in the opposite direction becomes less likely. We call this method for cellular persistence in the CPM “vector based persistence”.

The second method of cellular persistence is based on a phenomenological description of actin polymerization at the leading edge of the cell developed by Niculescu *et al.* [125]. In this model, called the “Act model”, each lattice site in the cell is assigned an “activity value” that keeps track of the time that the lattice site was included in the cell. A term is then added to the Hamiltonian which favors the cell to expand at lattice sites that were recently added to the cell. In this way, the cell is likely to keep forming protrusions at the same side, which leads to persistent migration. However, unlike CPM cells with vector based persistence, these cells do not stubbornly keep trying to move in

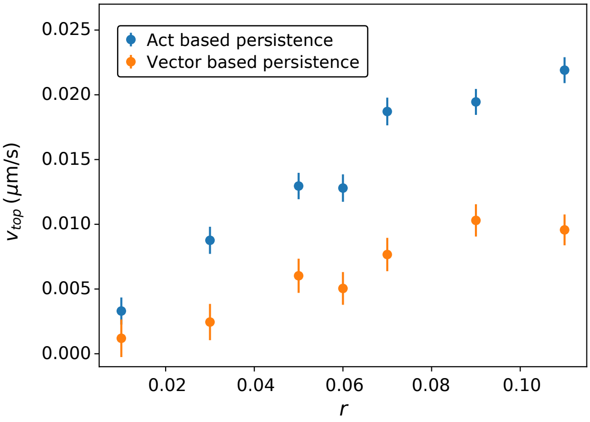

**Figure 6.1.** Topotactic velocity $v_{\mathrm{top}}$ (see Chapter 5) as a function of the dimensionless obstacle density gradient $r$ (Chapter 5) for two different models of highly motile and persistently migrating cells based on the Cellular Potts Model [293]. The model with “vector based persistence” implements persistent cell motion based on the vector $\boldsymbol{p}$ in Chapter 5, whereas cells with “Act based persistence” move persistently due to a phenomenological model of actin protrusion dynamics at the cell’s leading edge [125]. This Figure was printed with permission from Leonie van Steijn.

the same direction when they encounter an obstacle. Instead, they quickly “forget” the direction in which they were previously migrating, and start moving in a new direction.

By comparing the topotactic abilities of these two types of persistently migrating cells in the Cellular Potts Model, Van Steijn *et al.* [293] investigate to what extent explanation 3 might cause the difference in topotactic efficiency between ABPs and highly motile cells. Figure 6.1 shows the topotactic velocity $v_{\mathrm{top}}$ as a function of the dimensionless obstacle density gradient $r$ (see Chapter 5) for highly motile CPM cells with vector based persistence and highly motile CPM cells with persistence based on the Act model [293]. The cells with Act based persistence have about twice the topotactic velocity of cells with vector based persistence for all values of $r$. This result demonstrates that the “smart” way in which Act based persistent cells adapt their direction of motion upon encountering an obstacle allows them to perform topotaxis more efficiently than cells that stubbornly keep trying to move in the same direction. Returning to the results of Chapter 5, this suggests that the limited topotactic efficiency of ABPs with respect to highly motile cells can in part be explained by the fact that their orientation is not affected by interactions with obstacles. However, experimentally observed large-scale topotaxis is about five times as efficient as that of ABPs, suggesting that other explanations, such as those listed above, might also contribute to the discrepancy. In the future, it is worth investigating this in greater detail. On the theoretical side, for example, the topotactic efficiency of ABPs could be compared to that of CPM cells with vector based persistence to test explanation 1, and the adhesion affinity of cells with the obstacles can be varied in the Cellular Potts Model to test explanation 2. On the experimental side, the large-scale topotactic efficiency could be compared for different types of persistently migrating cells, such as leukocytes [292], amoeba [289], or invasive (amoeboid) cancer cells [290, 291]. Additionally, the actin dynamics within the cell could be studied during cell-obstacle interactions to shed more light on the reorientation dynamics and to inspire more realistic models of cell migration. Together, these efforts will contribute to a better biological and biophysical understanding of cell migration in crowded environments, which can potentially inspire biomedical applications in, for instance, malaria [294, 295] or cancer [251] treatments.

# Bibliography

[1] J. D. Watson and F. H. C. Crick, ‘Molecular Structure of Nucleic Acids: A Structure for Deoxyribose Nucleic Acid’, Nature **171**, 737 (1953) (pp. 1, 2).

[2] C. Monico, M. Capitanio, G. Belcastro, F. Vanzi and F. S. Pavone, ‘Optical methods to study protein-DNA interactions in vitro and in living cells at the single-molecule level’, International journal of molecular sciences **14**, 3961 (2013) (p. 1).

[3] A. Ashkin, K. Schütze, J. M. Dziedzic, U. Euteneuer and M. Schliwa, ‘Force generation of organelle transport measured in vivo by an infrared laser trap’, Nature **348**, 346 (1990) (p. 1).

[4] S. Smith, L. Finzi and C. Bustamante, ‘Direct mechanical measurements of the elasticity of single DNA molecules by using magnetic beads’, Science **258**, 1122 (1992) (p. 1).

[5] E. Florin, V. Moy and H. Gaub, ‘Adhesion forces between individual ligand-receptor pairs’, Science **264**, 415 (1994) (p. 1).

[6] K. Schakenraad, A. S. Biebricher, M. Sebregts, B. ten Bensel, E. J. G. Peterman, G. J. L. Wuite, I. Heller, C. Storm and P. van der Schoot, ‘Hyperstretching DNA’, Nature Communications **8**, 2197 (2017) (p. 1).

[7] A. M. Turing, ‘The chemical basis of morphogenesis’, Bulletin of Mathematical Biology **52**, 153 (1990) (p. 1).

[8] N. Bacaër, *A short history of mathematical population dynamics* (Springer Science & Business Media, 2011) (p. 1).

[9] A. Anderson and K. Rejniak, *Single-cell-based models in biology and medicine* (Springer Science & Business Media, 2007) (pp. 1, 7, 72, 89).

[10] A. G. Fletcher, M. Osterfield, R. E. Baker and S. Y. Shvartsman, ‘Vertex models of epithelial morphogenesis’, Biophysical Journal **106**, 2291 (2014) (p. 1).

[11] R. Pfeifer, M. Lungarella and F. Iida, ‘Self-organization, embodiment, and biologically inspired robotics’, Science **318**, 1088 (2007) (p. 1).

[12] H. Shin, S. Jo and A. G. Mikos, ‘Biomimetic materials for tissue engineering’, Biomaterials **24**, Synthesis of Biomimetic Polymers, 4353 (2003) (p. 1).

[13] I. Prigogine, *Non-equilibrium statistical mechanics* (Courier Dover Publications, 2017) (p. 1).

[14] S. Ramaswamy, 'Active matter', Journal of Statistical Mechanics: Theory and Experiment **2017**, 054002 (2017) (pp. 1, 73).

[15] A. Cavagna and I. Giardina, 'Bird flocks as condensed matter', Annual Review of Condensed Matter Physics **5**, 183 (2014) (p. 2).

[16] P. Cluzel, A. Lebrun, C. Heller, R. Lavery, J.-L. Viovy, D. Chatenay and F. Caron, 'DNA: an extensible molecule', Science **271**, 792 (1996) (p. 2).

[17] S. B. Smith, Y. Cui and C. Bustamante, 'Overstretching B-DNA: the elastic response of individual double-stranded and single-stranded DNA molecules', Science **271**, 795 (1996) (p. 2).

[18] J. F. Léger, G. Romano, A. Sarkar, J. Robert, L. Bourdieu, D. Chatenay and J. F. Marko, 'Structural transitions of a twisted and stretched DNA molecule', Physical Review Letters **83**, 1066 (1999) (p. 2).

[19] J. F. Marko and E. D. Siggia, 'Stretching DNA', Macromolecules **28**, 8759 (1995) (p. 2).

[20] M. M. Palm and R. M. H. Merks, 'Vascular networks due to dynamically arrested crystalline ordering of elongated cells', Physical Review E **87**, 012725 (2013) (pp. 2, 7).

[21] S. E. Boas and R. M. H. Merks, 'Tip cell overtaking occurs as a side effect of sprouting in computational models of angiogenesis', BMC systems biology **9**, 86 (2015) (pp. 2, 7).

[22] B. Guirao, S. U. Rigaud, F. Bosveld, A. Bailles, J. Lopez-Gay, S. Ishihara, K. Sugimura, F. Graner and Y. Bellaiche, 'Unified quantitative characterization of epithelial tissue development', Elife **4**, e08519 (2015) (pp. 2, 7).

[23] B. K. A. Nelemans, M. Schmitz, H. Tahir, R. M. H. Merks and T. H. Smit, 'Mechanical strain can increase segment number in live chick embryos', bioRxiv (2018) 10.1101/211623 (pp. 2, 7).

[24] L. Sui et al., 'Differential lateral and basal tension drive folding of drosophila wing discs through two distinct mechanisms', Nature Communications **9**, 4620 (2018) (p. 2).

[25] T. Vicsek and A. Zafeiris, 'Collective motion', Physics Reports **517**, 71 (2012) (p. 2).

[26] T. Vicsek, A. Czirók, E. Ben-Jacob, I. Cohen and O. Shochet, 'Novel type of phase transition in a system of self-driven particles', Physical Review Letters **75**, 1226 (1995) (p. 2).

[27] J. Toner and Y. Tu, 'Long-range order in a two-dimensional dynamical XY model: how birds fly together', Physical Review Letters **75**, 4326 (1995) (p. 2).

[28] A. J. Engler, S. Sen, H. L. Sweeney and D. E. Discher, 'Matrix elasticity directs stem cell lineage specification.', Cell **126**, 677 (2006) (pp. 2, 16, 34, 70).

[29] B. Alberts, A. Johnson, J. Lewis, M. Raff, K. Roberts and P. Walter, *Molecular biology of the cell* (Garland Science, 2008) (pp. 3, 4, 9).

[30] B. Trappmann et al., 'Extracellular-matrix tethering regulates stem-cell fate.', Nature Materials **11**, 642 (2012) (pp. 3, 16, 34, 70).

[31] X. Wang, X. Hu, I. Dulinska-Molak, N. Kawazoe, Y. Yang and G. Chen, 'Discriminating the independent influence of cell adhesion and spreading area on stem cell fate determination using micropatterned surfaces', Scientific Reports **6**, 28708 (2016) (p. 3).

[32] R. McBeath, D. M. Pirone, C. M. Nelson, K. Bhadriraju and C. S. Chen, 'Cell shape, cytoskeletal tension, and RhoA regulate stem cell lineage commitment', Developmental Cell **6**, 483 (2004) (pp. 3, 34).

[33] K. A. Kilian, B. Bugarija, B. T. Lahn and M. Mrksich, 'Geometric cues for directing the differentiation of mesenchymal stem cells', Proceedings of the National Academy of Sciences **107**, 4872 (2010) (pp. 3, 34, 58).

[34] N. Minc, D. Burgess and F. Chang, 'Influence of cell geometry on division-plane positioning', Cell **144**, 414 (2011) (pp. 3, 34).

[35] M. Versaevel, T. Grevesse and S. Gabriele, 'Spatial coordination between cell and nuclear shape within micropatterned endothelial cells', Nature Communications **3**, 671 (2012) (pp. 3, 34).

[36] C. S. Chen, M. Mrksich, S. Huang, G. M. Whitesides and D. E. Ingber, 'Geometric control of cell life and death', Science **276**, 1425 (1997) (pp. 3, 34).

[37] N. Jain, K. V. Iyer, A. Kumar and G. V. Shivashankar, 'Cell geometric constraints induce modular gene-expression patterns via redistribution of HDAC3 regulated by actomyosin contractility', Proceedings of the National Academy of Sciences **110**, 11349 (2013) (pp. 3, 34).

[38] S. van Helvert, C. Storm and P. Friedl, 'Mechanoreciprocity in cell migration', Nature Cell Biology **20**, 8 (2018) (p. 3).

[39] O. V. Kim, R. I. Litvinov, J. W. Weisel and M. S. Alber, 'Structural basis for the nonlinear mechanics of fibrin networks under compression', Biomaterials **35**, 6739 (2014) (p. 3).

[40] I. Pushkarsky et al., 'Elastomeric sensor surfaces for high-throughput single-cell force cytometry', Nature Biomedical Engineering **2**, 124 (2018) (pp. 3, 70).

[41] S. Suresh, 'Biomechanics and biophysics of cancer cells', Acta Materialia **55**, 3989 (2007) (p. 3).

[42] S. Kumar and V. M. Weaver, 'Mechanics, malignancy, and metastasis: the force journey of a tumor cell', Cancer and Metastasis Reviews **28**, 113 (2009) (p. 3).

[43] Q. Tseng et al., 'A new micropatterning method of soft substrates reveals that different tumorigenic signals can promote or reduce cell contraction levels', Lab Chip **11**, 2231 (2011) (pp. 3, 58, 70, 81, 82, 86–88, 114, 115).

[44] C. M. Kraning-Rush, J. P. Califano and C. A. Reinhart-King, ‘Cellular traction stresses increase with increasing metastatic potential’, PLOS ONE **7**, 1 (2012) (pp. 3, 70).

[45] V. Peschetola, V. M. Laurent, A. Duperray, R. Michel, D. Ambrosi, L. Preziosi and C. Verdier, ‘Time-dependent traction force microscopy for cancer cells as a measure of invasiveness’, Cytoskeleton **70**, 201 (2013) (pp. 3, 70).

[46] S. Pellegrin and H. Mellor, ‘Actin stress fibres.’, Journal of cell science **120**, 3491 (2007) (pp. 4, 16, 17, 38, 71, 113).

[47] K. Burridge and E. S. Wittchen, ‘The tension mounts: Stress fibers as force-generating mechanotransducers’, The Journal of Cell Biology **200**, 9 (2013) (pp. 4, 16, 17, 38, 71, 113).

[48] U. S. Schwarz and S. A. Safran, ‘Physics of adherent cells’, Reviews of Modern Physics **85**, 1327 (2013) (pp. 4–6, 16, 34, 36, 37, 44, 57, 70, 71).

[49] A. Chopra, E. Tabdanov, H. Patel, P. A. Janmey and J. Y. Kresh, ‘Cardiac myocyte remodeling mediated by n-cadherin-dependent mechanosensing’, American Journal of Physiology-Heart and Circulatory Physiology **300**, H1252 (2011) (pp. 4, 34).

[50] A. J. Engler, M. A. Griffin, S. Sen, C. G. Bönnemann, H. L. Sweeney and D. E. Discher, ‘Myotubes differentiate optimally on substrates with tissue-like stiffness’, The Journal of Cell Biology **166**, 877 (2004) (pp. 4, 34).

[51] T. Yeung et al., ‘Effects of substrate stiffness on cell morphology, cytoskeletal structure, and adhesion’, Cell Motility **60**, 24 (2005) (pp. 4, 7, 34, 45).

[52] A. Zemel, F. Rehfeldt, A. E. X. Brown, D. E. Discher and S. A. Safran, ‘Cell shape, spreading symmetry, and the polarization of stress-fibers in cells’, Journal of Physics: Condensed Matter **22**, 194110 (2010) (pp. 4, 34, 35, 43, 57).

[53] F. Grinnell, ‘Fibroblast-collagen-matrix contraction: growth-factor signalling and mechanical loading’, Trends in Cell Biology **10**, 362 (2000) (pp. 4, 7, 34, 45).

[54] K. Burridge and M. Chrzanowska-Wodnicka, ‘Focal Adhesions, Contractility, and Signaling’, Annual Review of Cell and Developmental Biology **12**, 463 (1996) (pp. 4, 16, 36, 70).

[55] H. Van Hoorn, R. Harkes, E. M. Spiesz, C. Storm, D. Van Noort, B. Ladoux and T. Schmidt, ‘The nanoscale architecture of force-bearing focal adhesions’, Nano Letters **14**, 4257 (2014) (pp. 5, 16, 20, 22, 34, 35, 50, 70, 113, 114).

[56] J. L. Tan, J. Tien, D. M. Pirone, D. S. Gray, K. Bhadriraju and C. S. Chen, ‘Cells lying on a bed of microneedles: an approach to isolate mechanical force.’, Proceedings of the National Academy of Sciences **100**, 1484 (2003) (pp. 5, 16, 20, 34, 35, 43, 44, 50, 58, 70, 113–115).

[57] L. Trichet, J. Le Digabel, R. J. Hawkins, S. R. K. Vedula, M. Gupta, C. Ribrault, P. Hersen, R. Voituriez and B. Ladoux, ‘Evidence of a large-scale mechanosensing mechanism for cellular adaptation to substrate stiffness’,

Proceedings of the National Academy of Sciences **109**, 6933 (2012) (pp. 5, 16, 20, 22, 34, 35, 50, 70, 113, 114).

[58] M. Théry, ‘Micropatterning as a tool to decipher cell morphogenesis and functions’, Journal of Cell Science **123**, 4201 (2010) (pp. 5, 22, 40, 58, 70, 114).

[59] M. Dembo and Y.-L. Wang, ‘Stresses at the cell-to-substrate interface during locomotion of fibroblasts’, Biophysical Journal **76**, 2307 (1999) (pp. 5, 70).

[60] J. P. Butler, I. M. Tolić-Nørrelykke, B. Fabry and J. J. Fredberg, ‘Traction fields, moments, and strain energy that cells exert on their surroundings’, American Journal of Physiology-Cell Physiology **282**, C595 (2002) (pp. 5, 70).

[61] B. Sabass, M. L. Gardel, C. M. Waterman and U. S. Schwarz, ‘High resolution traction force microscopy based on experimental and computational advances’, Biophysical Journal **94**, 207 (2008) (pp. 5, 70).

[62] R. Bar-Ziv, T. Tlusty, E. Moses, S. A. Safran and A. Bershadsky, ‘Pearling in cells: a clue to understanding cell shape’, Proceedings of the National Academy of Sciences **96**, 10140 (1999) (pp. 6, 7, 16, 17, 34, 36, 38, 57, 71, 74, 75).

[63] I. B. Bischofs, F. Klein, D. Lehnert, M. Bastmeyer and U. S. Schwarz, ‘Filamentous Network Mechanics and Active Contractility Determine Cell and Tissue Shape’, Biophysical Journal **95**, 3488 (2008) (pp. 6, 7, 16, 17, 20, 21, 34, 36–39, 57, 71–75, 113).

[64] I. B. Bischofs, S. S. Schmidt and U. S. Schwarz, ‘Effect of Adhesion Geometry and Rigidity on Cellular Force Distributions’, Physical Review Letters **103**, 1 (2009) (pp. 6, 7, 16, 17, 21, 34, 36–38, 42, 57, 70–75, 113).

[65] S. Banerjee and L. Giomi, ‘Polymorphism and bistability in adherent cells’, Soft Matter **9**, 5251 (2013) (pp. 6, 16, 36, 37, 42, 71).

[66] L. Giomi, ‘Softly constrained films’, Soft Matter **9**, 8121 (2013) (pp. 6, 16, 36, 71).

[67] L. Giomi, ‘Contour models of cellular adhesion’, in *Cell migrations: causes and functions*, edited by C. A. M. La Porta and S. Zapperi (Springer International Publishing, Cham, 2019), pp. 13–29 (pp. 6, 34, 36, 37, 57, 71).

[68] S. Banerjee, R. Sknepnek and M. C. Marchetti, ‘Optimal shapes and stresses of adherent cells on patterned substrates’, Soft Matter **10**, 2424 (2014) (pp. 6, 7, 70, 71, 113).

[69] P. J. Albert and U. S. Schwarz, ‘Dynamics of cell shape and forces on micropatterned substrates predicted by a Cellular Potts Model’, Biophysical Journal **106**, 2340 (2014) (pp. 6, 7, 58, 70, 72, 73, 75, 81, 82, 85, 86, 88–90, 114, 115).

[70] M. F. Coughlin and D. Stamenović, ‘A prestressed cable network model of the adherent cell cytoskeleton’, Biophysical Journal **84**, 1328 (2003) (p. 7).

[71] R. Paul, P. Heil, J. P. Spatz and U. S. Schwarz, ‘Propagation of mechanical stress through the actin cytoskeleton toward focal adhesions: model and experiment’, Biophysical Journal **94**, 1470 (2008) (p. 7).

[72] P. Guthardt Torres, I. B. Bischofs and U. S. Schwarz, 'Contractile network models for adherent cells', Physical Review E **85**, 011913 (2012) (p. 7).

[73] S. Banerjee and M. C. Marchetti, 'Controlling cell–matrix traction forces by extracellular geometry', New Journal of Physics **15**, 035015 (2013) (pp. 7, 70, 85, 113).

[74] P. Kollmannsberger and B. Fabry, 'Linear and nonlinear rheology of living cells', Annual Review of Materials Research **41**, 75 (2011) (p. 7).

[75] V. S. Deshpande, R. M. McMeeking and A. G. Evans, 'A bio-chemo-mechanical model for cell contractility', Proceedings of the National Academy of Sciences **103**, 14015 (2006) (pp. 7, 35, 43, 48, 57).

[76] V. S. Deshpande, R. M. McMeeking and A. G. Evans, 'A model for the contractility of the cytoskeleton including the effects of stress-fibre formation and dissociation', Proceedings of the Royal Society of London A: Mathematical, Physical and Engineering Sciences **463**, 787 (2007) (pp. 7, 35, 43, 48, 57).

[77] A. Pathak, V. S. Deshpande, R. M. McMeeking and A. G. Evans, 'The simulation of stress fibre and focal adhesion development in cells on patterned substrates', Journal of The Royal Society Interface **5**, 507 (2008) (pp. 7, 35, 43, 57, 58, 76, 80, 81).

[78] J. P. McGarry, J. Fu, M. T. Yang, C. S. Chen, R. M. McMeeking, A. G. Evans and V. S. Deshpande, 'Simulation of the contractile response of cells on an array of micro-posts', Philosophical Transactions of the Royal Society A: Mathematical, Physical and Engineering Sciences **367**, 3477 (2009) (p. 7).

[79] W. Ronan, V. S. Deshpande, R. M. McMeeking and J. P. McGarry, 'Cellular contractility and substrate elasticity: a numerical investigation of the actin cytoskeleton and cell adhesion', Biomechanics and Modeling in Mechanobiology **13**, 417 (2014) (pp. 7, 35, 43, 57).

[80] F. Graner and J. A. Glazier, 'Simulation of biological cell sorting using a two-dimensional extended Potts model', Physical Review Letters **69**, 2013 (1992) (p. 7).

[81] J. A. Glazier and F. Graner, 'Simulation of the differential adhesion driven rearrangement of biological cells', Physical Review E **47**, 2128 (1993) (pp. 7, 72).

[82] A. Szabó and R. M. H. Merks, 'Cellular Potts modeling of tumor growth, tumor invasion, and tumor evolution', Frontiers in oncology **3**, 87 (2013) (p. 7).

[83] B. Vianay, J. Käfer, E. Planus, M. Block, F. Graner and H. Guillou, 'Single cells spreading on a protein lattice adopt an energy minimizing shape', Physical Review Letters **105**, 128101 (2010) (pp. 7, 72).

[84] P. J. Albert and U. S. Schwarz, 'Modeling cell shape and dynamics on micropatterns', Cell Adhesion & Migration **10**, 516 (2016) (pp. 7, 58, 72).

[85] T. Vignaud, L. Blanchoin and M. Théry, 'Directed cytoskeleton self-organization', Trends in Cell Biology **22**, 671 (2012) (pp. 7, 34, 43, 45, 76).

[86] B. Ladoux, R.-M. Mège and X. Trepat, ‘Front–rear polarization by mechanical cues: from single cells to tissues’, Trends in Cell Biology **26**, 420 (2016) (pp. 7, 34, 43, 45, 76).

[87] N. T. Lam, T. J. Muldoon, K. P. Quinn, N. Rajaram and K. Balachandran, ‘Valve interstitial cell contractile strength and metabolic state are dependent on its shape’, Integrative Biology **8**, 1079 (2016) (pp. 7, 34, 43, 45, 50, 76, 79).

[88] S. K. Gupta, Y. Li and M. Guo, ‘Anisotropic mechanics and dynamics of a living mammalian cytoplasm’, Soft Matter **15**, 190 (2019) (pp. 7, 34, 43, 45, 50, 76, 79).

[89] P. Roca-Cusachs, J. Alcaraz, R. Sunyer, J. Samitier, R. Farré and D. Navajas, ‘Micropatterning of single endothelial cell shape reveals a tight coupling between nuclear volume in G1 and proliferation’, Biophysical Journal **94**, 4984 (2008) (pp. 7, 50, 70, 76, 79, 84, 85, 88, 113, 114).

[90] K. Mandal, I. Wang, E. Vitiello, L. A. C. Orellana and M. Balland, ‘Cell dipole behaviour revealed by ECM sub-cellular geometry’, Nature Communications **5**, 5749 (2014) (pp. 7, 70, 84, 85, 88, 113, 114).

[91] P.-G. De Gennes and J. Prost, *The physics of liquid crystals*, Vol. 83 (Oxford university press, 1993) (pp. 7, 8, 43, 44, 57, 76, 114).

[92] G. Meier, E. Sackmann and J. G. Grabmaier, *Applications of liquid crystals* (Springer Science & Business Media, 2012) (p. 7).

[93] D. Pauluth and K. Tarumi, ‘Advanced liquid crystals for television’, Journal of Materials Chemistry **14**, 1219 (2004) (p. 7).

[94] L. Onsager, ‘The effects of shape on the interaction of colloidal particles’, Annals of the New York Academy of Sciences **51**, 627 (1949) (p. 7).

[95] M. Nobili and G. Durand, ‘Disorientation-induced disordering at a nematic-liquid-crystal–solid interface’, Physical Review A **46**, R6174 (1992) (pp. 8, 45, 77).

[96] M. Kleman and O. D. Lavrentovich, ‘Topological point defects in nematic liquid crystals’, Philosophical Magazine **86**, 4117 (2006) (pp. 8, 79).

[97] T. Odijk, ‘Theory of lyotropic polymer liquid crystals’, Macromolecules **19**, 2313 (1986) (p. 8).

[98] P. Prinsen and P. van der Schoot, ‘Shape and director-field transformation of tactoids’, Physical Review E **68**, 021701 (2003) (p. 8).

[99] O. V. Manyuhina, K. B. Lawlor, M. C. Marchetti and M. J. Bowick, ‘Viral nematics in confined geometries’, Soft Matter **11**, 6099 (2015) (p. 8).

[100] M. Leoni, O. V. Manyuhina, M. J. Bowick and M. C. Marchetti, ‘Defect driven shapes in nematic droplets: analogies with cell division’, Soft Matter **13**, 1257 (2017) (p. 8).

[101] A. Doostmohammadi, J. Ignés-Mullol, J. M. Yeomans and F. Sagués, ‘Active nematics’, Nature Communications **9**, 3246 (2018) (p. 8).

[102] T. J. Pedley and J. O. Kessler, ‘Hydrodynamic Phenomena in Suspensions of Swimming Microorganisms’, Annual Review of Fluid Mechanics **24**, 313 (1992) (pp. 8, 17, 37, 71, 73).

[103] R. A. Simha and S. Ramaswamy, ‘Hydrodynamic Fluctuations and Instabilities in Ordered Suspensions of Self-Propelled Particles’, Physical Review Letters **89**, 058101 (2002) (pp. 8, 17, 37, 71, 73).

[104] S. P. Thampi, R. Golestanian and J. M. Yeomans, ‘Vorticity, defects and correlations in active turbulence’, Philosophical Transactions of the Royal Society A: Mathematical, Physical and Engineering Sciences **372**, 20130366 (2014) (p. 8).

[105] L. Giomi, ‘Geometry and topology of turbulence in active nematics’, Physical Review X **5**, 031003 (2015) (p. 8).

[106] L. Giomi, M. J. Bowick, P. Mishra, R. Sknepnek and M. Cristina Marchetti, ‘Defect dynamics in active nematics’, Philosophical Transactions of the Royal Society A: Mathematical, Physical and Engineering Sciences **372**, 20130365 (2014) (p. 8).

[107] T. Sanchez, D. T. N. Chen, S. J. DeCamp, M. Heymann and Z. Dogic, ‘Spontaneous motion in hierarchically assembled active matter’, Nature **491**, 431 (2012) (p. 8).

[108] V. Schaller and A. R. Bausch, ‘Topological defects and density fluctuations in collectively moving systems’, Proceedings of the National Academy of Sciences **110**, 4488 (2013) (p. 8).

[109] Z. You, D. J. G. Pearce, A. Sengupta and L. Giomi, ‘Geometry and mechanics of microdomains in growing bacterial colonies’, Physical Review X **8**, 031065 (2018) (p. 8).

[110] G. Duclos, S. Garcia, H. G. Yevick and P. Silberzan, ‘Perfect nematic order in confined monolayers of spindle-shaped cells’, Soft Matter **10**, 2346 (2014) (p. 8).

[111] T. B. Saw et al., ‘Topological defects in epithelia govern cell death and extrusion’, Nature **544**, 212 (2017) (pp. 8, 58, 89).

[112] A. Hall, ‘Rho GTPases and the actin cytoskeleton’, Science **279**, 509 (1998) (p. 8).

[113] I. Dierking and S. Al-Zangana, ‘Lyotropic liquid crystal phases from anisotropic nanomaterials’, Nanomaterials **7**, 305 (2017) (p. 8).

[114] W. R. Holmes and L. Edelstein-Keshet, ‘A comparison of computational models for eukaryotic cell shape and motility’, PLOS Computational Biology **8**, 1 (2012) (p. 9).

[115] F. Ziebert and I. S. Aranson, ‘Computational approaches to substrate-based cell motility’, Npj Computational Materials **2**, 16019 (2016) (p. 9).

[116] D. Selmeczi, S. Mosler, P. H. Hagedorn, N. B. Larsen and H. Flyvbjerg, ‘Cell motility as persistent random motion: theories from experiments’, Biophysical Journal **89**, 912 (2005) (pp. 9, 97).

[117] L. Li, E. C. Cox and H. Flyvbjerg, ‘‘Dicty dynamics’: dictyostelium motility as persistent random motion’, Physical Biology **8**, 046006 (2011) (pp. 9, 98).

[118] Y. Loosli, R. Luginbuehl and J. G. Snedeker, ‘Cytoskeleton reorganization of spreading cells on micro-patterned islands: a functional model’, Philosophical Transactions of the Royal Society A: Mathematical, Physical and Engineering Sciences **368**, 2629 (2010) (pp. 9, 89, 115).

[119] T. Shemesh, A. D. Bershadsky and M. M. Kozlov, ‘Physical model for self-organization of actin cytoskeleton and adhesion complexes at the cell front’, Biophysical Journal **102**, 1746 (2012) (p. 9).

[120] D. Shao, W.-J. Rappel and H. Levine, ‘Computational model for cell morphodynamics’, Physical Review Letters **105**, 108104 (2010) (p. 9).

[121] F. Ziebert, S. Swaminathan and I. S. Aranson, ‘Model for self-polarization and motility of keratocyte fragments’, Journal of The Royal Society Interface **9**, 1084 (2012) (p. 9).

[122] E. L. Barnhart, K.-C. Lee, K. Keren, A. Mogilner and J. A. Theriot, ‘An adhesion-dependent switch between mechanisms that determine motile cell shape’, PLOS Biology **9**, 1 (2011) (p. 9).

[123] E. Tjhung, A. Tiribocchi, D. Marenduzzo and M. E. Cates, ‘A minimal physical model captures the shapes of crawling cells’, Nature Communications **6**, 5420 (2015) (p. 9).

[124] A. F. M. Marée, V. A. Grieneisen and L. Edelstein-Keshet, ‘How cells integrate complex stimuli: the effect of feedback from phosphoinositides and cell shape on cell polarization and motility’, PLOS Computational Biology **8**, 1 (2012) (pp. 9, 58, 72, 89, 108, 115).

[125] I. Niculescu, J. Textor and R. J. de Boer, ‘Crawling and gliding: a computational model for shape-driven cell migration’, PLOS Computational Biology **11**, 1 (2015) (pp. 9, 72, 89, 104, 108, 115–117).

[126] H. C. Berg and D. A. Brown, ‘Chemotaxis in escherichia coli analysed by three-dimensional tracking’, Nature **239**, 500 (1972) (pp. 9, 107).

[127] K. F. Swaney, C.-H. Huang and P. N. Devreotes, ‘Eukaryotic chemotaxis: a network of signaling pathways controls motility, directional sensing, and polarity’, Annual Review of Biophysics **39**, 265 (2010) (pp. 9, 96).

[128] P. J. M. Van Haastert and P. N. Devreotes, ‘Chemotaxis: signalling the way forward’, Nature Reviews Molecular Cell Biology **5**, 626 (2004) (pp. 9, 96).

[129] P. A. Iglesias and P. N. Devreotes, ‘Navigating through models of chemotaxis’, Current Opinion in Cell Biology **20**, 35 (2008) (p. 9).

[130] T. Hillen and K. J. Painter, ‘A user’s guide to PDE models for chemotaxis’, Journal of Mathematical Biology **58**, 183 (2008) (p. 9).

[131] J. B. McCarthy and L. T. Furcht, ‘Laminin and fibronectin promote the haptotactic migration of B16 mouse melanoma cells in vitro.’, The Journal of Cell Biology **98**, 1474 (1984) (pp. 9, 96).

[132] C. M. Lo, H. B. Wang, M. Dembo and Y. L. Wang, ‘Cell movement is guided by the rigidity of the substrate.’, Biophysical Journal **79**, 144 (2000) (pp. 9, 16, 34, 70, 96).

[133] D. G. Mallet and G. J. Pettet, ‘A mathematical model of integrin-mediated haptotactic cell migration’, Bulletin of Mathematical Biology **68**, 231 (2006) (p. 9).

[134] G. Charras and E. Sahai, ‘Physical influences of the extracellular environment on cell migration’, Nature Reviews Molecular Cell Biology **15**, 813 (2014) (pp. 9, 96).

[135] G. Yu, J. Feng, H. Man and H. Levine, ‘Phenomenological modeling of durotaxis’, Physical Review E **96**, 010402 (2017) (pp. 9, 101, 105, 107).

[136] E. G. Rens and R. M. H. Merks, ‘Cell Shape and Durotaxis Follow from Mechanical Cell-Substrate Reciprocity and Focal Adhesion Dynamics: A Unifying Mathematical Model’, arXiv:1906.08962 (2019) (pp. 9, 35, 43, 57, 58, 89, 115).

[137] D. Caballero, J. Comelles, M. Piel, R. Voituriez and D. Riveline, ‘Ratchetaxis: long-range directed cell migration by local cues’, Trends in Cell Biology **25**, 815 (2015) (pp. 9, 96).

[138] S. E. Kim et al., ‘Cell migration according to shape of graphene oxide micropatterns’, Micromachines **7**, 186 (2016) (pp. 9, 96).

[139] E. L. Maout, S. L. Vecchio, A. Bhat and D. Riveline, ‘Chapter 7 - Directing cell migration on flat substrates and in confinement with microfabrication and microfluidics’, in *Microfluidics in cell biology part b: microfluidics in single cells*, Vol. 147, edited by M. Piel, D. Fletcher and J. Doh, Methods in Cell Biology (Academic Press, 2018), pp. 109–132 (pp. 9, 96).

[140] J. Park, D.-H. Kim, H.-N. Kim, C. J. Wang, M. K. Kwak, E. Hur, K.-Y. Suh, S. S. An and A. Levchenko, ‘Directed migration of cancer cells guided by the graded texture of the underlying matrix’, Nature Materials **15**, 792 (2016) (pp. 9, 96).

[141] J. Park, D.-H. Kim and A. Levchenko, ‘Topotaxis: a new mechanism of directed cell migration in topographic ECM gradients’, Biophysical Journal **114**, 1257 (2018) (pp. 9, 96).

[142] C. Heo, C. Jeong, H. S. Im, J. U. Kim, J. Woo, J. Y. Lee, B. Park, M. Suh and T.-i. Kim, ‘Cellular behavior controlled by bio-inspired and geometry-tunable nanohairs’, Nanoscale **9**, 17743 (2017) (pp. 9, 96).

[143] J. A. J. Wondergem, M. Mytiliniou, F. C. H. de Wit, T. G. A. Reuvers, D. Holcman and D. Heinrich, ‘Chemotaxis and topotaxis add vectorially for amoeboid cell

migration', bioRxiv (2019) 10.1101/735779 (pp. 9, 10, 89, 96, 98, 107, 108, 114, 116).

[144] C. Bechinger, R. Di Leonardo, H. Löwen, C. Reichhardt, G. Volpe and G. Volpe, 'Active particles in complex and crowded environments', Reviews of Modern Physics **88**, 045006 (2016) (pp. 10, 97).

[145] A. Zöttl and H. Stark, 'Emergent behavior in active colloids', Journal of Physics: Condensed Matter **28**, 253001 (2016) (pp. 10, 97, 98).

[146] L. Angelani, A. Costanzo and R. Di Leonardo, 'Active ratchets', Europhysics Letters **96**, 68002 (2011) (pp. 10, 97).

[147] B.-q. Ai, Q.-y. Chen, Y.-f. He, F.-g. Li and W.-r. Zhong, 'Rectification and diffusion of self-propelled particles in a two-dimensional corrugated channel', Physical Review E **88**, 062129 (2013) (pp. 10, 97).

[148] B.-Q. Ai and J.-C. Wu, 'Transport of active ellipsoidal particles in ratchet potentials', The Journal of Chemical Physics **140**, 094103 (2014) (pp. 10, 97).

[149] M. S. Davies Wykes, X. Zhong, J. Tong, T. Adachi, Y. Liu, L. Ristroph, M. D. Ward, M. J. Shelley and J. Zhang, 'Guiding microscale swimmers using teardrop-shaped posts', Soft Matter **13**, 4681 (2017) (pp. 10, 97, 108, 115).

[150] J. Tong and M. Shelley, 'Directed migration of microscale swimmers by an array of shaped obstacles: modeling and shape optimization', SIAM Journal on Applied Mathematics **78**, 2370 (2018) (pp. 10, 97, 108, 115).

[151] P. K. Ghosh, V. R. Misko, F. Marchesoni and F. Nori, 'Self-propelled janus particles in a ratchet: numerical simulations', Physical Review Letters **110**, 268301 (2013) (pp. 10, 97).

[152] X. Ao, P. Ghosh, Y. Li, G. Schmid, P. Hänggi and F. Marchesoni, 'Active Brownian motion in a narrow channel', The European Physical Journal Special Topics **223**, 3227 (2014) (pp. 10, 97).

[153] E. Yariv and O. Schnitzer, 'Ratcheting of Brownian swimmers in periodically corrugated channels: a reduced fokker-planck approach', Physical Review E **90**, 032115 (2014) (pp. 10, 97).

[154] J. Katuri, D. Caballero, R. Voituriez, J. Samitier and S. Sanchez, 'Directed flow of micromotors through alignment interactions with micropatterned ratchets', ACS Nano **12**, 7282 (2018) (pp. 10, 97).

[155] M. N. Popescu, W. E. Uspal, C. Bechinger and P. Fischer, 'Chemotaxis of active janus nanoparticles', Nano Letters **18**, 5345 (2018) (pp. 10, 97).

[156] S. Saha, S. Ramaswamy and R. Golestanian, 'Pairing, waltzing and scattering of chemotactic active colloids', New Journal of Physics **21**, 063006 (2019) (pp. 10, 97).

[157] E. A. Novikova, M. Raab, D. E. Discher and C. Storm, 'Persistence-driven durotaxis: generic, directed motility in rigidity gradients', Physical Review Letters **118**, 078103 (2017) (pp. 10, 97, 101, 105, 107, 108).

[158] C. Lozano and C. Bechinger, ‘Diffusing wave paradox of phototactic particles in traveling light pulses’, Nature Communications **10**, 2495 (2019) (pp. 10, 97).

[159] K. S. Midwood, L. V. Williams and J. E. Schwarzbauer, ‘Tissue repair and the dynamics of the extracellular matrix’, International Journal of Biochemistry and Cell Biology **36**, 1031 (2004) (p. 16).

[160] N. P. Barry and M. S. Bretscher, ‘Dictyostelium amoebae and neutrophils can swim.’, Proceedings of the National Academy of Sciences **107**, 11376 (2010) (p. 16).

[161] H. Tanimoto and M. Sano, ‘Dynamics of traction stress field during cell division’, Physical Review Letters **109**, 1 (2012) (p. 16).

[162] B. Geiger, J. P. Spatz and A. D. Bershadsky, ‘Environmental sensing through focal adhesions’, Nature Reviews Molecular Cell Biology **10**, 21 (2009) (p. 16).

[163] D. E. Discher, P. Janmey and Y.-L. Wang, ‘Tissue cells feel and respond to the stiffness of their substrate’, Science **310**, 1139 (2005) (p. 16).

[164] F. Jülicher, K. Kruse, J. Prost and J. F. Joanny, ‘Active behavior of the Cytoskeleton’, Physics Reports **449**, 3 (2007) (p. 16).

[165] B. D. Hoffman, C. Grashoff and M. A. Schwartz, ‘Dynamic molecular processes mediate cellular mechanotransduction.’, Nature **475**, 316 (2011) (p. 16).

[166] M. G. Mendez and P. A. Janmey, ‘Transcription factor regulation by mechanical stress.’, The international journal of biochemistry & cell biology **44**, 728 (2012) (p. 16).

[167] Y. Sawada, M. Tamada, B. J. Dubin-Thaler, O. Cherniavskaya, R. Sakai, S. Tanaka and M. P. Sheetz, ‘Force sensing by mechanical extension of the Src family kinase substrate p130Cas’, Cell **127**, 1015 (2006) (pp. 16, 34, 70).

[168] C. A. Reinhart-King, M. Dembo and D. A. Hammer, ‘Cell-cell mechanical communication through compliant substrates’, Biophysical Journal **95**, 6044 (2008) (pp. 16, 34).

[169] R. D. Sochol, A. T. Higa, R. R. R. Janairo, S. Li and L. Lin, ‘Unidirectional mechanical cellular stimuli via micropost array gradients’, Soft Matter **7**, 4606 (2011) (pp. 16, 34, 70).

[170] M. Ghibaudo, L. Trichet, J. Le Digabel, A. Richert, P. Hersen and B. Ladoux, ‘Substrate topography induces a crossover from 2D to 3D behavior in fibroblast migration.’, Biophysical journal **97**, 357 (2009) (pp. 16, 34).

[171] D. A. Fletcher and R. D. Mullins, ‘Cell mechanics and the cytoskeleton’, Nature **463**, 485 (2010) (pp. 16, 34).

[172] H. E. Balcıoğlu, H. van Hoorn, D. M. Donato, T. Schmidt and E. H. J. Danen, ‘The integrin expression profile modulates orientation and dynamics of force transmission at cell-matrix adhesions.’, Journal of Cell Science **128**, 1316 (2015) (pp. 16, 22, 27).

[173] E. H. J. Danen, P. Sonneveld, C. Brakebusch, R. Fässler and A. Sonnenberg, 'The fibronectin-binding integrins $\alpha 5\beta 1$ and $\alpha \mathrm{v}\beta 3$ differentially modulate RhoA–GTP loading, organization of cell matrix adhesions, and fibronectin fibrillogenesis', The Journal of Cell Biology **159**, 1071 (2002) (pp. 16, 17, 22, 34, 50, 113, 114).

[174] L. Giomi, N. Hawley-Weld and L. Mahadevan, 'Swarming, swirling and stasis in sequestered bristle-bots', Proceedings of the Royal Society A: Mathematical, Physical and Engineering Sciences **469**, 20120637 (2013) (p. 17).

[175] E. Kassianidou, C. A. Brand, U. S. Schwarz and S. Kumar, 'Geometry and network connectivity govern the mechanics of stress fibers', Proceedings of the National Academy of Sciences **114**, 2622 (2017) (p. 18).

[176] M. Théry, V. Racine, M. Piel, A. Pépin, A. Dimitrov, Y. Chen, J.-B. Sibarita and M. Bornens, 'Anisotropy of cell adhesive microenvironment governs cell internal organization and orientation of polarity', Proceedings of the National Academy of Sciences **103**, 19771 (2006) (pp. 22, 44, 45, 52, 57, 58, 76, 81, 89, 114, 115).

[177] OrientationJ, *http://bigwww.epfl.ch/demo/orientation*, 1999 (pp. 23, 25, 32, 63).

[178] T. Panciera, L. Azzolin, M. Cordenonsi and S. Piccolo, 'Mechanobiology of yap and taz in physiology and disease', Nature Reviews Molecular Cell Biology **18**, 758 (2017) (p. 34).

[179] S. Walcott and S. X. Sun, 'A mechanical model of actin stress fiber formation and substrate elasticity sensing in adherent cells', Proceedings of the National Academy of Sciences **107**, 7757 (2010) (pp. 35, 43, 57).

[180] A. Zemel, F. Rehfeldt, A. E. X. Brown, D. E. Discher and S. A. Safran, 'Optimal matrix rigidity for stress-fibre polarization in stem cells', Nature Physics **6**, 468 (2010) (pp. 35, 43, 57).

[181] N. Nisenholz, M. Botton and A. Zemel, 'Early-time dynamics of actomyosin polarization in cells of confined shape in elastic matrices', Soft Matter **10**, 2453 (2014) (pp. 35, 43, 57).

[182] M. Raab, J. Swift, P. D. P. Dingal, P. Shah, J.-W. Shin and D. E. Discher, 'Crawling from soft to stiff matrix polarizes the cytoskeleton and phosphoregulates myosin-ii heavy chain', The Journal of Cell Biology **199**, 669 (2012) (pp. 35, 43, 57).

[183] V. Schaller, C. Weber, C. Semmrich, E. Frey and A. R. Bausch, 'Polar patterns of driven filaments', Nature **467**, 73 (2010) (pp. 35, 43, 57).

[184] P. Kraikivski, R. Lipowsky and J. Kierfeld, 'Enhanced ordering of interacting filaments by molecular motors', Physical Review Letters **96**, 258103 (2006) (pp. 35, 43, 57).

[185] S. Swaminathan, F. Ziebert, D. Karpeev and I. S. Aranson, 'Motor-mediated alignment of microtubules in semidilute mixtures', Physical Review E **79**, 036207 (2009) (pp. 35, 43, 57).

[186] M. Soares e Silva, J. Alvarado, J. Nguyen, N. Georgoulia, B. M. Mulder and G. H. Koenderink, 'Self-organized patterns of actin filaments in cell-sized confinement', Soft Matter **7**, 10631 (2011) (pp. 35, 43, 45, 48, 50, 57).

[187] J. Alvarado, B. M. Mulder and G. H. Koenderink, 'Alignment of nematic and bundled semiflexible polymers in cell-sized confinement', Soft Matter **10**, 2354 (2014) (pp. 35, 43, 45, 48, 50, 57).

[188] S. Deshpande and T. Pfohl, 'Hierarchical self-assembly of actin in micro-confinements using microfluidics', Biomicrofluidics **6**, 034120 (2012) (pp. 35, 43, 57).

[189] V. S. Deshpande, M. Mrksich, R. M. McMeeking and A. G. Evans, 'A bio-mechanical model for coupling cell contractility with focal adhesion formation', Journal of the Mechanics and Physics of Solids **56**, 1484 (2008) (pp. 35, 43, 57, 58, 89, 115).

[190] A.-C. Reymann, J.-L. Martiel, T. Cambier, L. Blanchoin, R. Boujemaa-Paterski and M. Théry, 'Nucleation geometry governs ordered actin networks structures', Nature Materials **9**, 827 (2010) (pp. 35, 43, 57).

[191] G. Letort, A. Z. Politi, H. Ennomani, M. Théry, F. Nedelec and L. Blanchoin, 'Geometrical and mechanical properties control actin filament organization', PLOS Computational Biology **11**, 1 (2015) (pp. 35, 43, 57).

[192] A. P. Liu, D. L. Richmond, L. Maibaum, S. Pronk, P. L. Geissler and D. A. Fletcher, 'Membrane-induced bundling of actin filaments', Nature Physics **4**, 789 (2008) (pp. 35, 43, 57).

[193] S. Thomopoulos, G. M. Fomovsky and J. W. Holmes, 'The development of structural and mechanical anisotropy in fibroblast populated collagen gels', Journal of Biomechanical Engineering **127**, 742 (2005) (p. 35).

[194] W. Pomp, K. Schakenraad, H. E. Balcıoğlu, H. van Hoorn, E. H. J. Danen, R. M. H. Merks, T. Schmidt and L. Giomi, 'Cytoskeletal anisotropy controls geometry and forces of adherent cells', Physical Review Letters **121**, 178101 (2018) (pp. 36, 37, 70, 71, 74, 75, 88).

[195] A. D. Rape, W.-H. Guo and Y.-L. Wang, 'The regulation of traction force in relation to cell shape and focal adhesions', Biomaterials **32**, 2043 (2011) (pp. 42, 44, 58, 70, 85, 89, 115).

[196] P. W. Oakes, S. Banerjee, M. C. Marchetti and M. L. Gardel, 'Geometry regulates traction stresses in adherent cells', Biophysical Journal **107**, 825 (2014) (pp. 42, 44, 50, 52, 58, 70, 76, 79, 80, 84, 85, 88, 89, 113–115).

[197] J. Hanke, D. Probst, A. Zemel, U. S. Schwarz and S. Köster, ‘Dynamics of force generation by spreading platelets’, Soft Matter **14**, 6571 (2018) (pp. 42, 44, 58, 70, 89, 113, 115).

[198] J. Fu, Y.-K. Wang, M. T. Yang, R. A. Desai, X. Yu, Z. Liu and C. S. Chen, ‘Mechanical regulation of cell function with geometrically modulated elastomeric substrates.’, Nature Methods **7**, 733 (2010) (pp. 43, 44, 58, 89, 114, 115).

[199] G. L. Lin, D. M. Cohen, R. A. Desai, M. T. Breckenridge, L. Gao, M. J. Humphries and C. S. Chen, ‘Activation of beta 1 but not beta 3 integrin increases cell traction forces’, FEBS Letters **587**, 763 (2013) (pp. 43, 44, 58, 114, 115).

[200] C. Roux, A. Duperray, V. M. Laurent, R. Michel, V. Peschetola, C. Verdier and J. Étienne, ‘Prediction of traction forces of motile cells’, Interface Focus **6**, 20160042 (2016) (pp. 43, 70, 89).

[201] D. Riveline, E. Zamir, N. Q. Balaban, U. S. Schwarz, T. Ishizaki, S. Narumiya, Z. Kam, B. Geiger and A. D. Bershadsky, ‘Focal contacts as mechanosensors: externally applied local mechanical force induces growth of focal contacts by an mDia1-dependent and ROCK-independent mechanism’, The Journal of Cell Biology **153**, 1175 (2001) (pp. 43, 70, 89).

[202] N. Q. Balaban et al., ‘Force and focal adhesion assembly: a close relationship studied using elastic micropatterned substrates’, Nature Cell Biology **3**, 466 (2001) (pp. 43, 70, 89).

[203] B. Wehrle-Haller and B. A. Imhof, ‘Actin, microtubules and focal adhesion dynamics during cell migration’, The International Journal of Biochemistry & Cell Biology **35**, 39 (2003) (p. 44).

[204] R. De, A. Zemel and S. A. Safran, ‘Dynamics of cell orientation’, Nature Physics **3**, 655 (2007) (p. 44).

[205] A. Livne, E. Bouchbinder and B. Geiger, ‘Cell reorientation under cyclic stretching’, Nature Communications **5**, 3938 (2014) (p. 44).

[206] J. Étienne, J. Fouchard, D. Mitrossilis, N. Bufi, P. Durand-Smet and A. Asnacios, ‘Cells as liquid motors: mechanosensitivity emerges from collective dynamics of actomyosin cortex’, Proceedings of the National Academy of Sciences **112**, 2740 (2015) (pp. 44, 58, 89, 114, 115).

[207] P. W. Oakes, E. Wagner, C. A. Brand, D. Probst, M. Linke, U. S. Schwarz, M. Glotzer and M. L. Gardel, ‘Optogenetic control of rhoa reveals zyxin-mediated elasticity of stress fibres’, Nature Communications **8**, 15817 (2017) (pp. 44, 58, 89, 114, 115).

[208] S. B. Khatau, C. M. Hale, P. J. Stewart-Hutchinson, M. S. Patel, C. L. Stewart, P. C. Searson, D. Hodzic and D. Wirtz, ‘A perinuclear actin cap regulates nuclear shape’, Proceedings of the National Academy of Sciences **106**, 19017 (2009) (p. 44).

[209] K. Nagayama, Y. Yahiro and T. Matsumoto, ‘Apical and basal stress fibers have different roles in mechanical regulation of the nucleus in smooth muscle cells cultured on a substrate’, Cellular and Molecular Bioengineering **6**, 473 (2013) (p. 44).

[210] M. Théry, A. Pépin, E. Dressaire, Y. Chen and M. Bornens, ‘Cell distribution of stress fibres in response to the geometry of the adhesive environment’, Cell Motility **63**, 341 (2006) (pp. 44, 45, 52, 57, 58, 76, 81, 87–89, 114, 115).

[211] J. James, E. D. Goluch, H. Hu, C. Liu and M. Mrksich, ‘Subcellular curvature at the perimeter of micropatterned cells influences lamellipodial distribution and cell polarity’, Cell Motility **65**, 841 (2008) (pp. 44, 50, 52, 58, 76, 79, 81, 87–89, 114, 115).

[212] J. Galanis, D. Harries, D. L. Sackett, W. Losert and R. Nossal, ‘Spontaneous patterning of confined granular rods’, Physical Review Letters **96**, 028002 (2006) (p. 48).

[213] Y. H. Tee et al., ‘Cellular chirality arising from the self-organization of the actin cytoskeleton’, Nature Cell Biology **17**, 445 (2015) (pp. 49, 58, 80).

[214] G. Duclos, C. Blanch-Mercader, V. Yashunsky, G. Salbreux, J.-F. Joanny, J. Prost and P. Silberzan, ‘Spontaneous shear flow in confined cellular nematics’, Nature Physics **14**, 728 (2018) (pp. 49, 58).

[215] S. Jalal, S. Shi, V. Acharya, R. Y.-J. Huang, V. Viasnoff, A. D. Bershadsky and Y. H. Tee, ‘Actin cytoskeleton self-organization in single epithelial cells and fibroblasts under isotropic confinement’, Journal of Cell Science **132** (2019) (pp. 58, 80, 88).

[216] F. J. Segerer, F. Thüroff, A. Piera Alberola, E. Frey and J. O. Rädler, ‘Emergence and persistence of collective cell migration on small circular micropatterns’, Physical Review Letters **114**, 228102 (2015) (pp. 58, 115).

[217] M. Eastwood, V. C. Mudera, D. A. McGrouther and R. A. Brown, ‘Effect of precise mechanical loading on fibroblast populated collagen lattices: morphological changes.’, Cell Motility and the Cytoskeleton **40**, 13 (1998) (pp. 58, 89).

[218] D. W. J. Van der Schaft, A. C. C. Van Spreeuwel, H. C. Van Assen and F. P. T. Baaijens, ‘Mechanoregulation of Vascularization in Aligned Tissue-Engineered Muscle: A Role for Vascular Endothelial Growth Factor’, Tissue Engineering Part A **17**, 2857 (2011) (pp. 58, 89).

[219] O. Wartlick, P. Mumcu, F. Jülicher and M. Gonzalez-Gaitan, ‘Understanding morphogenetic growth control - lessons from flies.’, Nature Reviews Molecular Cell Biology **12**, 594 (2011) (pp. 58, 89).

[220] R. F. M. Van Oers, E. G. Rens, D. J. LaValley, C. A. Reinhart-King and R. M. H. Merks, ‘Mechanical Cell-Matrix Feedback Explains Pairwise and

Collective Endothelial Cell Behavior In Vitro', PLoS Computational Biology **10**, e1003774 (2014) (pp. 58, 73, 89).

[221] P. Santos-Oliveira, A. Correia, T. Rodrigues, T. M. Ribeiro-Rodrigues, P. Matafome, J. C. Rodríguez-Manzaneque, R. Seiça, H. Girão and R. D. M. Travasso, 'The Force at the Tip - Modelling Tension and Proliferation in Sprouting Angiogenesis', PLoS Computational Biology **11**, 1 (2015) (pp. 58, 89).

[222] D. S. Vijayraghavan and L. A. Davidson, 'Mechanics of neurulation: From classical to current perspectives on the physical mechanics that shape, fold, and form the neural tube', Birth Defects Research **109**, 153 (2017) (pp. 58, 89).

[223] D. L. Barton, S. Henkes, C. J. Weijer and R. Sknepnek, 'Active vertex model for cell-resolution description of epithelial tissue mechanics', PLOS Computational Biology **13**, 1 (2017) (pp. 58, 89).

[224] C. A. Reinhart-King, M. Dembo and D. A. Hammer, 'The dynamics and mechanics of endothelial cell spreading', Biophysical Journal **89**, 676 (2005) (p. 70).

[225] I. M. Tolić-Nørrelykke and N. Wang, 'Traction in smooth muscle cells varies with cell spreading', Journal of Biomechanics **38**, 1405 (2005) (p. 70).

[226] N. Wang, E. Ostuni, G. M. Whitesides and D. E. Ingber, 'Micropatterning tractional forces in living cells', Cell Motility **52**, 97 (2002) (p. 70).

[227] J. P. Califano and C. A. Reinhart-King, 'Substrate stiffness and cell area predict cellular traction stresses in single cells and cells in contact', Cellular and Molecular Bioengineering **3**, 68 (2010) (p. 70).

[228] C. A. Lemmon and L. H. Romer, 'A predictive model of cell traction forces based on cell geometry', Biophysical Journal **99**, L78 (2010) (pp. 70, 89).

[229] C. M. Edwards and U. S. Schwarz, 'Force localization in contracting cell layers', Physical Review Letters **107**, 128101 (2011) (pp. 70, 89).

[230] M.-C. Kim, D. M. Neal, R. D. Kamm and H. H. Asada, 'Dynamic modeling of cell migration and spreading behaviors on fibronectin coated planar substrates and micropatterned geometries', PLOS Computational Biology **9**, 1 (2013) (pp. 70, 89).

[231] B. L. Bangasser and D. J. Odde, 'Master equation-based analysis of a motor-clutch model for cell traction force', Cellular and Molecular Bioengineering **6**, 449 (2013) (p. 70).

[232] S. Lin, M. C. Lampi, C. A. Reinhart-King, G. Tsui, J. Wang, C. A. Nelson and L. Gu, 'Eigenstrain as a mechanical set-point of cells', Biomechanics and Modeling in Mechanobiology **17**, 951 (2018) (pp. 70, 113).

[233] P. W. Oakes, 'Balancing forces in migration', Current Opinion in Cell Biology **54**, 43 (2018) (p. 70).

[234] D. Ben-Yaakov, R. Golkov, Y. Shokef and S. A. Safran, ‘Response of adherent cells to mechanical perturbations of the surrounding matrix’, Soft Matter **11**, 1412 (2015) (pp. 70, 84, 85, 88, 114).

[235] R. Golkov and Y. Shokef, ‘Elastic interactions between anisotropically contracting circular cells’, Physical Review E **99**, 032418 (2019) (pp. 70, 84, 85, 88, 114).

[236] M. Newman and G. Barkema, *Monte carlo methods in statistical physics* (Oxford University Press: New York, USA, 1999) (p. 72).

[237] E. G. Rens and L. Edelstein-Keshet, ‘From energy to cellular force in the Cellular Potts Model’, bioRxiv (2019) 10.1101/601781 (p. 72).

[238] N. J. Savill and P. Hogeweg, ‘Modelling morphogenesis: from single cells to crawling slugs’, Journal of Theoretical Biology **184**, 229 (1997) (p. 73).

[239] K. Schakenraad, J. Ernst, W. Pomp, E. H. J. Danen, R. M. H. Merks, T. Schmidt and L. Giomi, ‘Mechanical interplay between cell shape and actin cytoskeleton organization’, arXiv:1905.09805 (2019) (p. 75).

[240] K. A. Kilian, B. Bugarija, B. T. Lahn and M. Mrksich, ‘Geometric cues for directing the differentiation of mesenchymal stem cells’, Proceedings of the National Academy of Sciences **107**, 4872 (2010) (pp. 81, 87, 88, 115).

[241] C. Labouesse, A. B. Verkhovsky, J.-J. Meister, C. Gabella and B. Vianay, ‘Cell shape dynamics reveal balance of elasticity and contractility in peripheral arcs’, Biophysical Journal **108**, 2437 (2015) (p. 85).

[242] S. Lee, E. Kassianidou and S. Kumar, ‘Actomyosin stress fiber subtypes have unique viscoelastic properties and roles in tension generation’, Molecular Biology of the Cell **29**, 1992 (2018) (pp. 89, 115).

[243] E. Barnhart, K.-C. Lee, G. M. Allen, J. A. Theriot and A. Mogilner, ‘Balance between cell-substrate adhesion and myosin contraction determines the frequency of motility initiation in fish keratocytes’, Proceedings of the National Academy of Sciences **112**, 5045 (2015) (pp. 89, 115).

[244] C. Abaurrea-Velasco, T. Auth and G. Gompper, ‘Vesicles with internal active filaments: self-organized propulsion controls shape, motility, and dynamical response’, New Journal of Physics **21**, 123024 (2019) (pp. 89, 115).

[245] P. J. Albert and U. S. Schwarz, ‘Dynamics of cell ensembles on adhesive micropatterns: bridging the gap between single cell spreading and collective cell migration’, PLOS Computational Biology **12**, 1 (2016) (p. 89).

[246] K. Schakenraad, L. Ravazzano, N. Sarkar, J. A. J. Wondergem, R. M. H. Merks and L. Giomi, ‘Topotaxis of active Brownian particles’, Physical Review E **101**, 032602 (2020) (p. 89).

[247] R. Magno, V. A. Grieneisen and A. F. Marée, ‘The biophysical nature of cells: potential cell behaviours revealed by analytical and computational studies of cell surface mechanics’, BMC Biophysics **8**, 8 (2015) (p. 89).

[248] D.-H. Kim, K. Han, K. Gupta, K. W. Kwon, K.-Y. Suh and A. Levchenko, 'Mechanosensitivity of fibroblast cell shape and movement to anisotropic substratum topography gradients', Biomaterials **30**, 5433 (2009) (p. 96).

[249] D. Arcizet, S. Capito, M. Gorelashvili, C. Leonhardt, M. Vollmer, S. Youssef, S. Rappl and D. Heinrich, 'Contact-controlled amoeboid motility induces dynamic cell trapping in 3d-microstructured surfaces', Soft Matter **8**, 1473 (2012) (p. 96).

[250] X. Sun, M. K. Driscoll, C. Guven, S. Das, C. A. Parent, J. T. Fourkas and W. Losert, 'Asymmetric nanotopography biases cytoskeletal dynamics and promotes unidirectional cell guidance', Proceedings of the National Academy of Sciences **112**, 12557 (2015) (p. 96).

[251] C. D. Paul, P. Mistriotis and K. Konstantopoulos, 'Cancer cell motility: lessons from migration in confined spaces', Nature Reviews Cancer **17**, 131 (2016) (pp. 96, 118).

[252] N. D. Bade, T. Xu, R. D. Kamien, R. K. Assoian and K. J. Stebe, 'Gaussian curvature directs stress fiber orientation and cell migration', Biophysical Journal **114**, 1467 (2018) (p. 96).

[253] L. Pieuchot et al., 'Curvotaxis directs cell migration through cell-scale curvature landscapes', Nature Communications **9**, 3995 (2018) (p. 96).

[254] D.-H. Kim et al., 'Biomechanical interplay between anisotropic re-organization of cells and the surrounding matrix underlies transition to invasive cancer spread', Scientific Reports **8**, 14210 (2018) (p. 96).

[255] B. Winkler, I. S. Aranson and F. Ziebert, 'Confinement and substrate topography control cell migration in a 3D computational model', Communications Physics **2**, 82 (2019) (p. 96).

[256] R. Nossal, 'Mathematical theories of topotaxis', in *Biological growth and spread* (Springer, 1980), pp. 410–439 (p. 96).

[257] D.-H. Kim, C.-H. Seo, K. Han, K. W. Kwon, A. Levchenko and K.-Y. Suh, 'Guided cell migration on microtextured substrates with variable local density and anisotropy', Advanced Functional Materials **19**, 1579 (2009) (p. 96).

[258] D.-H. Kim, P. P. Provenzano, C. L. Smith and A. Levchenko, 'Matrix nanotopography as a regulator of cell function', The Journal of Cell Biology **197**, 351 (2012) (p. 96).

[259] S. J. Ebbens and D. A. Gregory, 'Catalytic janus colloids: controlling trajectories of chemical microswimmers', Accounts of Chemical Research **51**, 1931 (2018) (p. 97).

[260] G. Volpe, I. Buttinoni, D. Vogt, H.-J. Kümmerer and C. Bechinger, 'Microswimmers in patterned environments', Soft Matter **7**, 8810 (2011) (pp. 97, 98, 108, 115, 116).

[261] Y. Fily, A. Baskaran and M. F. Hagan, ‘Dynamics of self-propelled particles under strong confinement’, Soft Matter **10**, 5609 (2014) (pp. 97, 98).

[262] Y. Fily, A. Baskaran and M. F. Hagan, ‘Dynamics and density distribution of strongly confined noninteracting nonaligning self-propelled particles in a nonconvex boundary’, Physical Review E **91**, 012125 (2015) (pp. 97, 98).

[263] M. Khatami, K. Wolff, O. Pohl, M. R. Ejtehadi and H. Stark, ‘Active Brownian particles and run-and-tumble particles separate inside a maze’, Scientific Reports **6**, 37670 (2016) (pp. 97, 108, 115).

[264] P. Galajda, J. Keymer, P. Chaikin and R. Austin, ‘A wall of funnels concentrates swimming bacteria’, Journal of Bacteriology **189**, 8704 (2007) (p. 97).

[265] L. Angelani and R. Di Leonardo, ‘Geometrically biased random walks in bacteria-driven micro-shuttles’, New Journal of Physics **12**, 113017 (2010) (p. 97).

[266] S. A. Mallory, C. Valeriani and A. Cacciuto, ‘Curvature-induced activation of a passive tracer in an active bath’, Physical Review E **90**, 032309 (2014) (p. 97).

[267] L. Angelani, R. Di Leonardo and G. Ruocco, ‘Self-starting micromotors in a bacterial bath’, Physical Review Letters **102**, 048104 (2009) (p. 97).

[268] S. Pattanayak, R. Das, M. Kumar and S. Mishra, ‘Enhanced dynamics of active Brownian particles in periodic obstacle arrays and corrugated channels’, The European Physical Journal E **42**, 62 (2019) (pp. 97, 98, 103).

[269] C. Reichhardt and C. J. Olson Reichhardt, ‘Active matter transport and jamming on disordered landscapes’, Physical Review E **90**, 012701 (2014) (p. 97).

[270] M. Zeitz, K. Wolff and H. Stark, ‘Active Brownian particles moving in a random Lorentz gas’, The European Physical Journal E **40**, 23 (2017) (pp. 97, 98, 102–104, 108).

[271] A. Morin, D. Lopes Cardozo, V. Chikkadi and D. Bartolo, ‘Diffusion, subdiffusion, and localization of active colloids in random post lattices’, Physical Review E **96**, 042611 (2017) (pp. 97, 108, 115).

[272] O. Chepizhko and T. Franosch, ‘Ideal circle microswimmers in crowded media’, Soft Matter **15**, 452 (2019) (p. 97).

[273] G. Volpe and G. Volpe, ‘The topography of the environment alters the optimal search strategy for active particles’, Proceedings of the National Academy of Sciences **114**, 11350 (2017) (pp. 97, 108, 115).

[274] H. Takagi, M. J. Sato, T. Yanagida and M. Ueda, ‘Functional analysis of spontaneous cell movement under different physiological conditions’, PLOS ONE **3**, 1 (2008) (p. 98).

[275] P. Denissenko, V. Kantsler, D. J. Smith and J. Kirkman-Brown, ‘Human spermatozoa migration in microchannels reveals boundary-following navigation’, Proceedings of the National Academy of Sciences **109**, 8007 (2012) (p. 98).

[276] V. Kantsler, J. Dunkel, M. Polin and R. E. Goldstein, ‘Ciliary contact interactions dominate surface scattering of swimming eukaryotes’, Proceedings of the National Academy of Sciences **110**, 1187 (2013) (p. 98).

[277] C. R. Doering, X. Mao and L. M. Sander, ‘Random walker models for durotaxis’, Physical Biology **15**, 066009 (2018) (pp. 101, 105, 107).

[278] T. Chinnasamy, J. L. Kingsley, F. Inci, P. J. Turek, M. P. Rosen, B. Behr, E. Tüzel and U. Demirci, ‘Guidance and self-sorting of active swimmers: 3D periodic arrays increase persistence length of human sperm selecting for the fittest’, Advanced Science **5**, 1700531 (2018) (p. 103).

[279] A. Pototsky and H. Stark, ‘Active Brownian particles in two-dimensional traps’, Europhysics Letters **98**, 50004 (2012) (p. 106).

[280] M. Hennes, K. Wolff and H. Stark, ‘Self-induced polar order of active Brownian particles in a harmonic trap’, Physical Review Letters **112**, 238104 (2014) (p. 106).

[281] A. P. Solon, M. E. Cates and J. Tailleur, ‘Active brownian particles and run-and-tumble particles: a comparative study’, The European Physical Journal Special Topics **224**, 1231 (2015) (p. 106).

[282] O. Dauchot and V. Démery, ‘Dynamics of a self-propelled particle in a harmonic trap’, Physical Review Letters **122**, 068002 (2019) (p. 106).

[283] I. Berdakin, Y. Jeyaram, V. V. Moshchalkov, L. Venken, S. Dierckx, S. J. Vanderleyden, A. V. Silhanek, C. A. Condat and V. I. Marconi, ‘Influence of swimming strategy on microorganism separation by asymmetric obstacles’, Physical Review E **87**, 052702 (2013) (pp. 108, 115).

[284] M. Mijalkov and G. Volpe, ‘Sorting of chiral microswimmers’, Soft Matter **9**, 6376 (2013) (pp. 108, 115).

[285] T. Bertrand, Y. Zhao, O. Bénichou, J. Tailleur and R. Voituriez, ‘Optimized diffusion of run-and-tumble particles in crowded environments’, Physical Review Letters **120**, 198103 (2018) (pp. 108, 115).

[286] O. Chepizhko and F. Peruani, ‘Diffusion, subdiffusion, and trapping of active particles in heterogeneous media’, Physical Review Letters **111**, 160604 (2013) (pp. 108, 115).

[287] D. Takagi, J. Palacci, A. B. Braunschweig, M. J. Shelley and J. Zhang, ‘Hydrodynamic capture of microswimmers into sphere-bound orbits’, Soft Matter **10**, 1784 (2014) (pp. 108, 115).

[288] T. Jakuszeit, O. A. Croze and S. Bell, ‘Diffusion of active particles in a complex environment: role of surface scattering’, Physical Review E **99**, 012610 (2019) (pp. 108, 115).

[289] T. Bretschneider, H. G. Othmer and C. J. Weijer, ‘Progress and perspectives in signal transduction, actin dynamics, and movement at the cell and tissue level: lessons from dictyostelium’, Interface Focus **6**, 20160047 (2016) (pp. 108, 118).

[290] E. Sahai, ‘Illuminating the metastatic process’, Nature Reviews Cancer **7**, 737 (2007) (pp. 108, 118).

[291] P. Friedl and S. Alexander, ‘Cancer invasion and the microenvironment: plasticity and reciprocity’, Cell **147**, 992 (2011) (pp. 108, 118).

[292] P. Friedl, S. Borgmann and E.-B. Bröcker, ‘Amoeboid leukocyte crawling through extracellular matrix: lessons from the dictyostelium paradigm of cell movement’, Journal of Leukocyte Biology **70**, 491 (2001) (pp. 108, 118).

[293] L. Van Steijn, J. A. J. Wondergem, K. Schakenraad, D. Heinrich and R. M. H. Merks, ‘Modeling topotaxis with the Cellular Potts Model’, in preparation (pp. 116, 117).

[294] C. M. de Korne et al., ‘Regulation of plasmodium sporozoite motility by formulation components’, Malaria Journal **18**, 155 (2019) (p. 118).

[295] B. M. F. Winkel et al., ‘Quantification of wild-type and radiation attenuated plasmodium falciparum sporozoite motility in human skin’, Scientific Reports **9**, 13436 (2019) (p. 118).

# Samenvatting

Wat hebben natuurkunde en biologie met elkaar te maken? Hoewel dit oorspronkelijk twee onafhankelijke wetenschappen waren, kunnen beide vakgebieden veel van elkaar leren. Enerzijds vormen de complexe en ingenieuze structuren en materialen waaruit levende organismen zijn opgebouwd een enorme inspiratie voor nieuwe technologische toepassingen. Je kunt hierbij bijvoorbeeld denken aan het ontwerpen van operatierobots die tijdens het opereren van vorm moeten kunnen veranderen. Anderzijds vinden er in levende organismen een hoop natuurkundige processen plaats, waardoor het bestuderen van het leven met een natuurkundige bril leidt tot een beter begrip van biologische processen op verschillende schalen. Zo speelt de mechanica, de tak van de natuurkunde die zich bezighoudt met de relatie tussen krachten, vervorming en beweging, een belangrijke rol bij het aflezen en kopiëren van de erfelijke code in het DNA, bij de embryonale ontwikkeling, en zelfs bij het collectieve gedrag van een school vissen of een zwerm vogels. Op de langere termijn kunnen deze natuurkundige inzichten ook leiden tot nieuwe medische toepassingen, zoals het verbeteren van behandelingen van astma, malaria en kanker.

In dit proefschrift kijken we niet direct naar deze medische toepassingen, maar leveren we een bijdrage aan de fundamentele kennis van de biofysica, het snijvlak van natuurkunde en biologie. Dit doen we door cellen te bestuderen. Alle levende organismen zijn opgebouwd uit cellen, die vaak gespecialiseerd zijn als bijvoorbeeld spiercellen of levercellen. Om hun taken uit te voeren produceren cellen allerlei stoffen. Je kunt hier bijvoorbeeld denken aan speeksel of maagzuur, maar ook aan hersencellen die met elkaar communiceren via neurotransmitters. Cellen worden dan ook vaak bestudeerd vanuit het perspectief van de biochemie. Er zijn echter ook veel cellen die mechanische taken uit moeten voeren, zoals rondlopen om op een ziekteverwekker te jagen of aan weefsel trekken om een wond te dichten. Het vakgebied dat probeert te begrijpen hoe cellen dit soort mechanische taken uitvoeren, heet de celmechanica. In dit proefschrift bestuderen we celmechanica met behulp van theoretisch onderzoek: we gebruiken wiskundige modellen om biofysische processen te beschrijven. Theoretisch natuurkundig onderzoek met behulp van wiskundige modellen is zo oud als de natuurkunde zelf, maar in de biologie is theoretisch onderzoek relatief nieuw. De invloed van de zogenoemde mathematische biologie wordt echter steeds groter. In dit proefschrift combineren we methoden uit de theoretische natuurkunde en de mathematische biologie. Het is daarbij heel belangrijk dat de theorie altijd hand in hand gaat met het experiment, omdat theoretisch werk juist in samenwerking met experimenten zijn meest nuttige bijdrage kan leveren. Zo kunnen met behulp van modellen kwantitatieve (zoals in Hoofdstukken 2 en 3) of kwalitatieve (Hoofdstuk 4) voorspellingen gedaan worden die weer als inspiratie kunnen dienen voor nieuwe experimenten. Bovendien kunnen verschillende verschijnselen in modellen eenvoudig worden toegevoegd of juist weggelaten, waardoor modellen kunnen helpen de uitkomsten van experimenten te interpreteren (Hoofdstuk 5).

In dit proefschrift kijken we naar het effect van *anisotropie* op de celmechanica. Dat is het tegenovergestelde van *isotropie*, wat letterlijk ‘gelijk in elke richting’ betekent. Een materiaal is isotroop als je het verschil niet zou kunnen zien als het gedraaid wordt, zoals bij zand. Anisotrope materialen bestaan vaak uit langwerpige deeltjes, waardoor je het wel kunt zien als ze gedraaid worden. Zie bijvoorbeeld Figuur 1.4b in Hoofdstuk 1. De technologie van een LCD-scherm maakt hier bijvoorbeeld gebruik van, maar je zou ook iets alledaags als een doosje lucifers anisotroop kunnen noemen. Dit proefschrift bevat twee delen, die twee verschillende aspecten van anisotropie in de celmechanica bestuderen. In **Deel I** (Hoofdstukken 2, 3, en 4) bestuderen we het cytoskelet van de cel. Het cytoskelet is een complex netwerk van filamenten in de cel dat de cel stevig maakt maar ook laat bewegen. Met andere woorden, het cytoskelet is voor een cel wat de combinatie van botten en spieren zijn voor het menselijk lichaam. We concentreren ons hierbij op een specifiek soort filament dat actine heet. Actinefilamenten kunnen in grote hoeveelheden allerlei complexe structuren vormen. Wij hebben vooral gekeken naar zogenaamde stress fibers, dikke bundels van parallelle actinefilamenten. De actinefilamenten hierin kunnen ten opzichte van elkaar schuiven, waardoor stress fibers aan hun omgeving kunnen trekken. In Deel I bestuderen we hoe cellen deze stress fibers gebruiken om hun eigen vorm te reguleren en om krachten op hun omgeving uit te oefenen. De typen cellen die wij bestuderen, bevatten veel stress fibers die vaak dezelfde oriëntatie hebben als de naastgelegen stress fibers. Dit is zichtbaar in bijvoorbeeld Figuur 1.4a en geïllustreerd met lijnen op de kaft. Omdat de stress fibers dus parallel aan elkaar liggen, is het cytoskelet van deze cellen anisotroop. Daardoor trekken deze cellen niet even hard in alle richtingen, maar wordt de kracht in één richting geconcentreerd. We bestuderen dus hoe de anisotropie van het cytoskelet de mechanica van de cel beïnvloedt.

We beginnen in **Hoofdstuk 2** met de vraag hoe het cytoskelet de vorm van de cel bepaalt. We doen dit door samen te werken met collega’s die experimenten doen waarbij ze cellen op een chemisch bewerkt oppervlak leggen dat we het substraat noemen. Deze cellen spreiden zich over het substraat uit en binden er op een aantal plaatsen aan. Omdat de rand van deze cellen nu door de stress fibers in hun cytoskelet naar binnen getrokken wordt, heeft elk stuk van de rand tussen twee bindingsplaatsen een naar binnen gekromde vorm. Zie bijvoorbeeld Figuren 1.2, 1.3, 2.1 en 2.2 in Hoofdstukken 1 en 2 en de illustratie op de kaft. Bij cellen met een isotroop cytoskelet, dus zonder parallelle stress fibers, kan de vorm van dit stuk celrand goed benaderd worden met een stuk van een cirkel. De vorm van de celrand is dus ook isotroop: je zou het verschil niet kunnen zien als een cirkel wordt gedraaid. Bij cellen met een anisotroop cytoskelet, dus met parallelle stress fibers, blijkt echter uit de experimenten dat de vorm van de cel niet meer met cirkels benaderd kan worden. Om dat te verklaren, hebben wij eerdere modellen voor de celvorm uitgebreid met het effect van stress fibers. Ons model voorspelt dat bij cellen met een anisotroop cytoskelet elk stuk naar binnen gekromde rand de vorm van een ellips heeft. Een ellips is een cirkel die in één richting is uitgerekt, zie bijvoorbeeld Figuur 2.2. Deze vorm is dus, net als de stress fibers, anisotroop omdat je het kan zien als een ellips gedraaid wordt. Het model voorspelt daarnaast dat de richting waarin de cirkel is uitgerekt precies gelijk is aan de richting van de stress fibers in de cel. Uit de experimentele data van onze collega's blijkt dat beide voorspellingen van het model correct zijn. Daarmee hebben we dus laten zien dat cellen de anisotropie van hun binnenkant, in de vorm van parallelle stress fibers, kunnen gebruiken om hun vorm aan de buitenkant ook anisotroop te maken. Dit is relevant voor cellen die zich in het lichaam door nauwe openingen moeten wringen zoals cellen die op een ziekteverwekker jagen, cellen die wondjes genezen, of kankercellen tijdens een uitzaaiing.

In **Hoofdstuk 3** draaien we de vraag om, en bestuderen we hoe de vorm van de cel de structuur van het cytoskelet beïnvloedt. We hebben een model ontwikkeld dat beschrijft hoe de celvorm de oriëntatie van de stress fibers in de hele cel beïnvloedt. Ons model laat zien dat de stress fibers in de cel enerzijds dezelfde oriëntatie 'willen' hebben als de naastgelegen stress fibers, en anderzijds dezelfde oriëntatie als de dichtstbijzijnde celrand. De voorspellingen van ons model tonen veel overeenkomsten met de experimentele data van onze collega's. Hiermee hebben we laten zien dat de structuur van het cytoskelet niet volledig begrepen kan worden door de vorming van individuele stress fibers te bestuderen, maar dat de vorm van de cel waarin de stress fibers zich bevinden ook een belangrijke rol speelt.

In **Hoofdstuk 4** implementeren we het model uit Hoofdstuk 3 in het *Cellular Potts Model*, een veel gebruikt computermodel uit de mathematische biologie voor het simuleren van celmechanica. Met behulp van het Cellular Potts Model bestuderen we de krachten die cellen uitoefenen op het substraat waar ze op liggen. Deze krachten worden tractiekrachten genoemd. Er bestaan al veel modellen om deze krachten uit te rekenen, maar deze modellen gebruiken doorgaans de aanname dat het cytoskelet isotroop is. In Hoofdstuk 4 bestuderen we hoe de tractiekrachten veranderen als het cytoskelet veel parallelle stress fibers bevat, en dus anisotroop is. De voorspellingen van ons model laten zien dat de tractiekrachten sterk afhangen van de specifieke structuur van het cytoskelet: de oriëntatie van de stress fibers bepaalt zowel de richting van de tractiekrachten als de plek waar de cel de grootste krachten op het substraat uitoefent. Onze voorspellingen reproduceren experimentele observaties uit de literatuur die eerdere isotrope modellen niet konden verklaren.

In **Deel II** van dit proefschrift verleggen we onze aandacht naar een ander aspect van celmechanica, en bestuderen we de migratie van cellen over een substraat. Er zijn veel mechanismen bekend die cellen kunnen stimuleren om in een specifieke richting te bewegen. Het bekendste voorbeeld hiervan is *chemotaxis*, een proces waarbij cellen naar een hogere of juist een lagere concentratie van een bepaalde stof bewegen. Er zijn echter ook veel mechanische stimuli bekend die cellen een specifieke kant op kunnen sturen. De belangrijkste voorbeelden hiervan zijn *haptotaxis*, waarbij cellen richting gebieden migreren waar ze makkelijker aan het substraat kunnen binden, en *durotaxis*, waarbij cellen van zachte naar harde substraten bewegen. Omdat de cellen in deze processen een voorkeur hebben voor één specifieke richting, zou je het kunnen waarnemen als het substraat gedraaid werd. Deze processen zijn dus ook anisotroop. Studies naar deze anisotrope stimuli worden vanwege reproduceerbaarheid en praktische overwegingen vaak op volledig vlakke substraten gedaan. In het menselijk lichaam komen migrerende cellen echter voortdurend obstakels tegen, zoals andere cellen of bloedvaten, maar het is onbekend hoe deze obstakels de gerichte beweging van cellen beïnvloeden. Om dit op een systematische manier te onderzoeken, bestuderen onze experimentele collega's de beweging van cellen over substraten waar ze kunstmatige obstakels op hebben aangebracht. Daarbij deden ze een interessante ontdekking: als de dichtheid van de obstakels varieert over het substraat, zorgen de obstakels zelf voor een anisotrope stimulus. De cellen bewegen dan vaak van gebieden met veel obstakels naar gebieden met minder obstakels: ze vertonen *topotaxis*. Uit de experimenten is het echter lastig op te maken waardoor de cellen hiertoe in staat zijn. Daar komen wij in beeld.

In **Hoofdstuk 5** bestuderen we topotaxis met behulp van computersimulaties van bewegende deeltjes, een sterk vereenvoudigd model voor celmigratie. De kern van dit model is dat de voortbeweging van de deeltjes, net als die van de echte cellen, *persistent* is: de deeltjes bewegen altijd een stuk in dezelfde richting voordat ze in een willekeurige richting afbuigen. Als ze echter een obstakel tegenkomen, moeten ze eromheen bewegen. Wanneer we deze deeltjes laten rondbewegen in een obstakellandschap met een variatie in de obstakeldichtheid, observeren wij ook topotaxis: de deeltjes bewegen vaker van gebieden met veel obstakels naar gebieden met weinig obstakels dan andersom. Hiermee hebben we laten zien dat persistente voortbeweging op zichzelf al voldoende is voor het optreden van topotaxis, ook in de afwezigheid van complexere biologische processen of 'intelligentie' van de cellen. Wel blijkt uit een vergelijking tussen de experimenten en onze simulaties dat cellen een stuk sneller in de richting van lage obstakeldichtheid bewegen dan de gesimuleerde deeltjes, wat suggereert dat er ook andere natuurkundige en/of biologische processen een rol spelen bij topotaxis. In **Hoofdstuk 6** bespreken we lopend vervolgonderzoek waarin we proberen deze andere processen te identificeren. Dit onderzoek laat onder andere zien dat de verklaring voor de hogere snelheid van topotaxis bij cellen wellicht te vinden is in de manier waarop deeltjes en cellen reageren op botsingen met obstakels. De gesimuleerde deeltjes zijn 'dom' en proberen altijd rechtdoor te lopen, ook als er iets in de weg staat. Cellen lijken echter mechanismen te gebruiken om hun richting van voortbeweging snel aan te passen als ze een obstakel tegenkomen. Verder onderzoek zal moeten uitwijzen of dit inderdaad het verschil in snelheid van topotaxis tussen deeltjes en cellen verklaart.

# Publication List

## Work presented in this thesis

- Wim Pomp[*], **Koen Schakenraad**[*], Hayri E. Balcıoğlu, Hedde van Hoorn, Erik H.J. Danen, Roeland M.H. Merks, Thomas Schmidt, and Luca Giomi, 'Cytoskeletal Anisotropy Controls Geometry and Forces of Adherent Cells', Physical Review Letters 121, 178101, **2018** (Chapter 2).
- **Koen Schakenraad**, Jeremy Ernst, Wim Pomp, Erik H.J. Danen, Roeland M.H. Merks, Thomas Schmidt, and Luca Giomi, 'Mechanical interplay between cell shape and actin cytoskeleton organization', arXiv:1905.09805, **2019** (Chapter 3).
- **Koen Schakenraad**, Bente H. Bakker, Gaia I. Martorana, Luca Giomi, and Roeland M.H. Merks, 'A hybrid Cellular Potts Model predicts stress fiber orientations and traction forces on micropatterned substrates', *in preparation* (Chapter 4).
- **Koen Schakenraad**, Linda Ravazzano, Niladri Sarkar, Joeri A.J. Wondergem, Roeland M.H. Merks, and Luca Giomi, 'Topotaxis of active Brownian particles', Physical Review E 101, 032602, **2020** (Chapter 5).

## Other work

- **Koen Schakenraad**[*], Andreas S. Biebricher[*], Maarten Sebregts, Brian ten Bensel, Erwin J.G. Peterman, Gijs J.L. Wuite, Iddo Heller, Cornelis Storm, and Paul van der Schoot, 'Hyperstretching DNA', Nature Communications 8, 2197, **2017**.
- Ludwig A. Hoffmann, **Koen Schakenraad**, Roeland M.H. Merks, and Luca Giomi, 'Chiral stresses in nematic cell monolayers', Soft Matter 16, 764-774, **2020**.
- Joeri A.J. Wondergem, Maria Mytiliniou, Patrick Witzel, **Koen Schakenraad**, Caspar J. Schmeits, Martijn A. Janse, Franz L. Edel, and Doris Heinrich, 'Cell trajectories reveal environmental topographic structure through jump-distance distributions', *in preparation.*

---

[*] These authors contributed equally to this work

- Leonie van Steijn, Joeri A.J. Wondergem, **Koen Schakenraad**, Doris Heinrich, and Roeland M.H. Merks, ‘Modeling topotaxis with the Cellular Potts Model’, *in preparation.*

# Curriculum Vitae

I was born in 1990 in Venray, where I grew up and received my secondary education at Raayland College. I specialized in the natural sciences and got interested in physics. During my final year, I won the third prize in the National Physics Olympiad and an honorable mention at the International Physics Olympiad in Hanoi, Vietnam.

In 2008 I enrolled in the BSc program Applied Physics at Eindhoven University of Technology (TU/e). In 2011 I finished the program cum laude with an experimental thesis on atomic layer deposition, and enrolled in the MSc program Applied Physics at TU/e. As part of my master's program, I went abroad for seven months to perform an experimental internship on laser-plasma wakefield acceleration of electrons at the Lawrence Berkeley National Laboratory in Berkeley, California. During my master's program I got interested in theory and wrote a theoretical thesis on the mechanical properties of DNA under supervision of prof. dr. Kees Storm and prof. dr. Paul van der Schoot. In 2014 I completed the program cum laude, and received an Academic Award from TU/e and the Lorentz prize for theoretical physics from the *Koninklijke Hollandsche Maatschappij der Wetenschappen* for my master's thesis. During these six years I discovered how much I enjoy teaching, and worked as a teaching assistant at TU/e and as a mathematics teacher at *Stichting Studiebegeleiding Leiden*. I was also an active member of study association *S.V.T.N. J.D. van der Waals*, and I participated in national (PION) and international (PLANCKS) physics competitions for student teams, winning the first prize in PION and the second prize in PLANCKS.

In 2015 I was awarded a Leiden/Huygens PhD fellowship and started as a PhD candidate at Leiden University in a joint project between the Soft and Biomechanics group of dr. Luca Giomi and the Mathematical Biology group of prof. dr. Roeland Merks. I studied several anisotropic aspects of cell mechanics, the results of which are presented in this thesis. During my PhD, I supervised three master students and collaborated with colleagues from various theoretical and experimental disciplines. I was actively involved in communicating science by presenting my work at several national and international conferences and workshops, as a teaching assistant and guest lecturer in physics and mathematics courses, and in outreach activities such as the *Avond van Wetenschap & Maatschappij* and the *Klokhuis vragendag*. In 2016 I won the Best Presentation Prize at the Casimir Spring School. Furthermore, I was a member of the Institute council of the Leiden Institute of Physics and the Casimir PhD platform, where I focused on monitoring and improving the general well-being of PhD candidates during their PhD.

# Acknowledgements

I would like to thank everyone who helped me in any way with writing this thesis. First of all, I would like to thank my supervisors, Luca and Roeland. Thank you for all the enjoyable scientific discussions and for giving me the opportunity to explore my own ideas during my PhD. Luca, thank you for your dedication to our work and for always making time for me. Roeland, bedankt voor je aanstekelijke enthousiasme en voor je steun. Next, I would like to thank my students: Jeremy, Linda, and Gaia. Without your great work I could not have written this thesis. Supervising your master projects was a great experience from which I learned a lot. I also thank Wim, Thomas, Joeri, Niladri, Bente Hilde, and Leonie for their scientific contributions to my thesis. Joeri, jou wil ik in het bijzonder bedanken voor de gezellige en productieve samenwerking, je enthousiasme, en je goede ideeën die me hebben geholpen het topotaxisproject op te zetten. Ik wil hier ook mijn afstudeerbegeleiders Paul en Kees noemen. Jullie hebben me geïnspireerd om te gaan promoveren.

Alle (oud)-leden van het Casimir PhD platform: bedankt voor al jullie goede werk en voor alle lol die we tijdens onze vergaderingen hebben gehad. Ik ben echt trots op wat we samen bereikt hebben op het gebied van promovendiwelzijn. Gesa, jou ben ik daarnaast dankbaar voor de goede gesprekken, de gezelligheid, je oprechte interesse en alle inzichten die je me gegeven hebt. Marije en Eric, jullie bedank ik voor jullie inzet voor promovendizaken en voor de persoonlijke steun. I would also like to thank everyone I met in the Giomi group, the Merks group, the Instituut-Lorentz, at the tenth floor, in the Instituutsraad, and during teaching. Thanks for being great colleagues. In particular, I thank Zhihong for being a fantastic office mate, Melissa and Ireth for their support, and Casper, Vera, and Peter for always making me feel welcome at the tenth floor. Furthermore, I thank Fran, Manon, and Marianne for their support with administration and the Doctorate Committee for reading my thesis.

Ik wil al mijn vrienden bedanken die er in de afgelopen jaren voor me geweest zijn, in het bijzonder de Tapirs en Bart. Tapirs, bij jullie kon ik met mijn voeten spreken toen mijn armen dat niet konden. Bart, jij was er voor me toen je het nog moeilijker had dan ik. We missen je. Ik ben al mijn (stief/schoon)-broers, -zussen en -ouders dankbaar voor hun steun en liefde. Dorien en Marijn, ik vind het super leuk dat jullie samen de kaft voor dit proefschrift hebben ontworpen. Jan-Hein en Imca, betere stiefouders had ik me niet kunnen wensen. Pap en mam, dankjulliewel dat ik altijd bij jullie terecht kan voor advies en om mijn hart te luchten, en dat jullie er los van elkaar toch samen voor me zijn. Tot slot, lieve Christa, je bent er altijd voor me als ik je nodig heb. Dankjewel voor je luisterend oor, je geduld, je lach, je interesse, je vertrouwen, je troost, je aanmoediging en je liefde.